Electronic Structure Calculations of Materials for Photovoltaic, Electrochemistry and Single Molecule Magnet Applications

A THESIS

SUBMITTED TO THE FACULTY OF THE GRADUATE SCHOOL

OF THE UNIVERSITY OF MINNESOTA

BY

Debmalya Ray

IN PARTIAL FULFILLMENT OF THE REQUIREMENTS

FOR THE DEGREE OF

DOCTOR OF PHILOSOPHY

ADVISOR: Laura Gagliardi

May, 2021

Acknowledgements

First and foremost I want to thank my adviser Prof. Laura Gagliardi for her encouragement and support throughout my PhD.She always encouraged me to explore new directions in the field of computational materials science and also gave me opportunity to present my research at various conferences.

I would also like to thank Prof. Christopher J. Cramer, Prof. Ilja Siepmann, Prof. Wayne J Gladfelter and Prof. Turan Birol for examining the thesis and providing useful feedback. I would specially like to thank Prof. Christopher J. Cramer and Prof. Turan Birol for being a great mentor throughout my PhD.

I want to thank all the past and present members of Gagliardi group for all the encouragement and support provided throughout my PhD. I want to thank Melanie Burns for all the help regarding official paperwork. I would specially like to thank Hung, Prachi, Carlo, Jing, Jingyun, Jenny, Davide, Riddhish, Abhisekh for all the friendship.

I want to thank all my experimental collaborators and coauthors: Dr. Bryan Voigt, Dr. Catherine Clark, Dr. Subhadip Goswami, Dr. Meagan S Oakley, Xiaojing Bai, Prof. Chris Leighton, Prof. Michael Manno, Prof. Eray S Aydil, Prof. Russel J Holmes, Prof. Omar K Farha, Prof. Joseph T. Hupp for providing tremendous guidance regarding all my works and explaining there experimental results clearly. I specially want to thank Bryan, Chris, Michael and Eray for painstakingly editing my papers.

Last but not the least I would like to thank all my friends and family members for helping me to survive the graduate school.

Abstract

One of the key scientific challenges of modern era is the efficient development of sustainable energy sources. Towards this goal, efficient production of solar energy has garnered considerable importance within the scientific community. Photovoltaic systems convert the sunlight to electrical energy. Perovskites and pyrite are largely explored for photovoltaic application. In this thesis we discuss strategies to computationally design and understand perovskite- and pyrite-based solar cell materials and predict ways to enhance their performance.We also focuses on computational understanding of structural and electronic properties of conductive metal-organic frameworks for electrochemistry and battery applications and lanthanide and actinide-based materials for single-molecule magnet applications.

Contents

List of Tables

List of Figures

List of Abbreviations

DFT	(Kohn-Sham) density functional theory
CASSCF	Complete active space self-consistent field
XMS-CASPT2	Extended multi-state complete active space with second-order perturbation theory
GGA	Generalized gradient approximation
NGA	Non-separable gradient approximation
CT	Charge-transfer
HS	High spin
IS	Intermediate spin
LS	Low spin
$E_{\mathbf{g}}$	bandgap
$E_{\mathbf{b}}$	Binding energy of defects
$E_{\mathbf{a}}$	Activation energy
VBM	Valence band maxima
CBM	Conduction band minima
DOS	Density of states
PDOS	Partial density of states

Chapter 1

Introduction

One of the key scientific challenges of the modern era is the efficient development of sustainable energy resources. Towards this goal, efficient production of solar energy has garnered considerable importance within the scientific community. Photovoltaic (PV) systems convert sunlight to electrical energy by taking the advantage of the photoelectric effect.[1] The efficiency of solar cell is directly related with the band gap of the material used in the cell. This is due to two factors:

- The photon energy of light varies according to the different wavelengths of light. The solar spectrum, from infrared to ultraviolet, covers a a range of 0.5 eV to 2.9 eV.The semiconductor material chosen for solar cell applications should to have a low band gap so that it can absorb the maximum of the solar energy.
- However, the desire to have a large built-in voltage requires a material with a large band gap. Therefore as a compromise, materials having a band gap between 1.0 and 1.7 eV are effective solar cell material.

In 1961, William Shockley and Hans Queisser, theoretically showed that the maxium efficiency of a single junction solar cell is around 33% and materials that have a band gap of 1.3 eV will have the highest efficiency for solar cell applications.

The most commonly used solar cell material is based on crystalline silicon (Si). Si solar cells reached efficiencies upto 20% [2] but their production remains expensive. Moreover, crystalline Si doesn't absorb light well, hence it requires a very thick film to absorb a good fraction of light.

The second generation solar cell materials such as cadmium telluride (CdTe) and copper indium gallium diselenide (CIGS) absorb more light than Si and also have low cost compared to it. However, indium(In) and telurium(Te) are not abundant and cadmium(Cd) is highly toxic, making them unfavorable materials for solar cell application. Thus the search for ideal low-cost solar cell materials with suitable band gap is of fundamental importance. In this thesis we explored two classes of materials namely perovskite and pyrite and their suitability for photovoltaic application.

Perovskites a class of compounds with the general formula ABX_3, where A is a divalent or monovalent cation, B is a tetravalent or divalent cation and X is either an oxide or halide. Hybrid organic-inorganic lead and tin-based perovskites are commonly used in solar cell devices.[3, 4, 5, 6, 7, 8, 9, 10, 11, 12] One such lead-based perovskite, $CH_3NH_3PbI_3$, has an efficiency of 22.1%.[13] Unfortunately, due to the presence of lead, this is a toxic material. [14, 15, 16] One possibility to reduce toxicity would be to completely replace lead with tin or germanium, which lie above lead in the periodic table. However, tin and germanium perovskites are not stable due to the oxidation of Sn(II) to Sn(IV) and Ge(II) to Ge(IV). [17, 18] Thus, in Chapter 2 of this thesis we used computational modeling methods, especially density functional theory, to predict possible replacements of Pb that would form perovskite structures with suitable band gaps for solar cell applications. We screened p-block and s-block elements such as Ge, Sn, Pb, Mg, Ca, Ba and Sr as an alternative B site cation in the $CsMI_3$ perovskite structure. We tested various density functionals and their effect on the structural, electronic and thermodynamic properties of $CsMI_3$ perovskite.

Pyrite, FeS_2, is one of the most suitable materials for photovoltaic applications due to its high absorbance of light and its earth-abundant, inexpensive (0.0019 ¢/kw) and non-toxic components.[19, 20] It was extensively studied during 80's for solar cell applications. However, it never exceeded a disappointing efficiency of 2.8%. [21] This poor performance is mainly due to the inability to control defects and doping in FeS_2. [21, 22, 23, 24, 25, 26]. Thus, in this thesis we explored S-vacancy related defects and 3d transition metal doping in pyrite.

In Chapter 3 of the thesis, we discussed how complex S-vacancy related defects can dope pyrite n-type. We also discussed the thermodynamic vs kinetic pathway of formation of these

complex S-vacancy related defects.

In Chapter 4 of the thesis, we discussed the effect of 3d transition metal doping in pyrite.

In this thesis, we also discuss a novel class of material called metal organic frameworks (MOFs) for their potential application in the field of electrochemistry. In general, MOFs are insulating in nature. Recently, electrical conductivity in MOFs has become an interesting topic of research because it can be utilized to build MOF-based field-effect transistors, chemiresistive sensors, electrochromic devices, supercapacitors, batteries and solar cells. In our recent work,[27] we showed that by introducing a fullerene C_{60} molecule within the Zr(IV)-based MOF NU-901 the conductivity of the host-guest system can be enhanced by 11 orders of magnitude compared to NU-901 alone. This enhancement in electrical conductivity is driven by the donor (organic linker of the MOF) – acceptor (C_{60} molecule) interaction. In Chapter 5 of the thesis, we discuss how the electrical conductivity of Zr(IV) based MOF can be further enhanced by incoporating heterofullernes.

Finally, we also explored the electronic and magnetic properties lanthanide and actinide based molecules which has potential applications in the field of single-molecule magnets. In Chapter 6 of the thesis, we used wavefunction based methods to study the electronic and magnetic properties of Dy(III) and Cf(III) based single-molecule magnets.

Chapter 2

A Computational Study of Structural and Electronic Properties of Lead-Free $CsMI_3$ Perovskites (M = Ge, Sn, Pb, Mg, Ca, Sr, Ba)

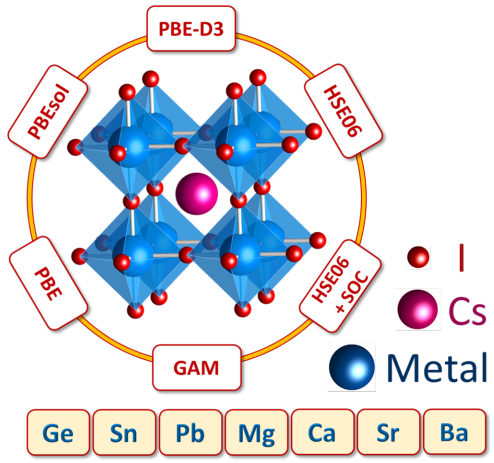

Reproduced with permission from the acticle by Debmalya Ray, Catherine Clark, Hung Q. Pham, Joshua Borycz, Russell J. Holmes, Eray S. Aydil and Laura Gagliardi, *J. Phys. Chem. C* 2018, 122, 14, 7838–7848.

2.1 Introduction

Inorganic and hybrid organic-inorganic halide perovskites have emerged in the last decade as promising materials for efficient, low-cost, thin film solar cells that can be deployed on a large-scale.[3, 4, 5, 6, 7, 8, 9, 10, 11, 12] Devices based on lead halide perovskites have reached power conversion efficiencies of >22%,[13] rivaling established solar cell materials including cadmium telluride (CdTe), copper indium gallium selenide (CIGS), and single-crystal Si. The archetypal hybrid organic-inorganic halide perovskite, $CH_3NH_3PbI_3$, has a bandgap near the Shockley-Quessier optimum,[28, 29] strong absorption in the visible spectrum,[6, 30, 31, 32] long carrier lifetimes,[33, 34] and high charge carrier mobilities.[10, 35, 36] Consequently, $CH_3NH_3PbI_3$ can act both as a light absorber and as an efficient charge transporting layer in a solar cell. One of the major concerns, however, is the toxicity of lead. The use of lead is particularly problematic because lead perovskites tend to decompose in ambient conditions, releasing harmful compounds such as PbI_2.[14, 15, 16]

In an effort to find novel non-toxic perovskites for photovoltaics, significant experimental and computational work has sought to identify metal cation replacements for lead.[36, 37, 38, 39, 40, 41, 42, 43, 44, 45, 46] Experimentally, the most well-studied alternative to lead is tin (e.g. $CH_3NH_3SnI_3$). While tin is electronically similar to lead and can exist in the +2 oxidation state, tin favors the +4 oxidation state. So far, tin halide solar cells have only achieved a reported maximum efficiency of 9.0%,[47] considerably lower than devices based on lead. These low efficiencies are thought to be due to oxidation of Sn(II) to Sn(IV).[17, 18] No other lead-free perovskites have approached the high efficiencies realized in lead-based solar cells.

Computationally, a broad array of potential lead cation replacements have been explored.[41, 48, 49] However, most studies typically examine only one crystal structure (e.g., tetragonal or cubic), without comparing the formation energies between different structures. Since many of these compounds have not been experimentally synthesized, comparison between multiple crystal structures is necessary to help identify the structural properties of those that may be stable and synthesized in the laboratory. Furthermore, computational studies use different types

of functionals, but often only one in a single study, making it difficult to compare results from different investigations.

Herein, we report the results of a systematic computational study that elucidates the electronic structures of inorganic $CsMI_3$ (M = Pb, Sn, Ge, Mg, Ca, Sr, Ba) perovskites across five crystallography-imitated structures. We compute these results using several Kohn-Sham density functionals, namely generalized gradient approximation (GGA), non-separable gradient approximation (NGA), and hybrid functionals. We also investigated the effect of spin-orbit coupling (SOC) on the bandgaps of all the $CsMI_3$ structures and show the importance of including SOC on the bandgap for different s-block and p-block metals. While it is well known that the predicted values of the bandgap can depend on the functional used, few studies report the formation energy for different crystal structures and their relative stabilities[50] and even fewer consider the dependence of formation energy on the choice of the functional. To the best of our knowledge, this is the first comprehensive DFT study that compares formation energy and relative stability across several functionals for halide perovskites. We consider the alkaline earth metals Mg, Ca, Sr, Ba as potential replacements for lead in an ABX_3 perovskite, and compare the results with those from calculations for Ge, Sn, and Pb. We focus on the structural and electronic properties, the formation energies, and the relative stabilities of the different perovskite phases. We explore how predictions of these properties depend on the choice of the density functional. Finally, we reconcile these predictions with experimental data.

2.2 Computational Methods

The perovskites (see Figure 2.1a) modeled in this work are $CsMI_3$ (M = Pb, Sn, Ge, Mg, Ca, Sr, Ba). Cesium was chosen for the A-site due to significant recent interest in all-inorganic perovskites.[51, 52] Additionally, modeling perovskites with the spherically symmetric cesium cation is much more computationally affordable than with its similarly-sized organic counterpart $CH_3NH_3^+$, allowing extensive comparisons between different combinations of functionals and structures.[48]

We considered five different initial structures as the starting atomic configuration in the

geometry optimization. These were constructed using the perovskite platonic model[48, 53] (the high symmetry point of platonic model are shown Figure 2.1b) where the $CsMI_3$ crystal structure consists of corner-sharing MI_6 octahedra. Following Filip et al.,[48] the metal-iodide bond lengths were initially set at 3.1 Å and different values of apical (α_a) and equatorial (α_e) metal-halide-metal bond angles were used in order to create different orientations of the MI_6 octahedra, resulting in five crystallographically-imitated structures: cubic, tetragonal 1, tetragonal 2 (out-of-plane tetragonal), orthorhombic 1, and orthorhombic 2 (see Figure 2.1c).[48, 53] The "conventional unit cells" in the platonic perovskite model are tetragonal, and are composed of four $CsMI_3$ units. To facilitate the comparison of calculated and experimentally determined lattice parameters, the computationally determined structures were transformed into standard conventional unit cells. With the exception of $CsGeI_3$, the space groups of the computationally determined structures matched the experimental data when such data were available. For $CsGeI_3$, the computationally determined structure was cubic with space group $Pm\bar{3}m$, whereas the reported experimental structure is trigonal with space group R3m.49 The $Pm\bar{3}m$ $CsGeI_3$ structure was further transformed into the R3m space group by using the transformation matrix [(1, 0, -1); (-1, 1, 0); (1, 1, 1)]. All transformations were done using the Material Studio 6.1 software.

Periodic density functional theory (DFT) calculations of the $CsMI_3$ (M = Pb, Sn, Ge, Mg, Ca, Sr, Ba) structures were performed using the Vienna Ab Initio Simulation Package (VASP).[54, 55, 56, 57] Starting with initial guesses of the atomic coordinates in each of the five structures shown in Figure 2.1c, the crystal structures were determined by minimizing the energy while retaining the symmetry of the initial guess. These structural relaxation calculations were repeated using different functionals, including PBE,[58, 59] PBE-D3,[60] PBEsol,[61] GAM,[62] and HSE06.[63, 64, 65] Among these functionals PBE, PBE-D3, PBEsol are GGA functionals, while GAM is a NGA functional and HSE06 is a hybrid functional. In the GGA approximation, the total energy of the system is expressed in terms of the electron density and its gradient. In NGA functionals, the total exchange and the correlation part are not separated, and instead are treated together. Hybrid functionals like HSE06 account for the non-local exchange interactions by including a

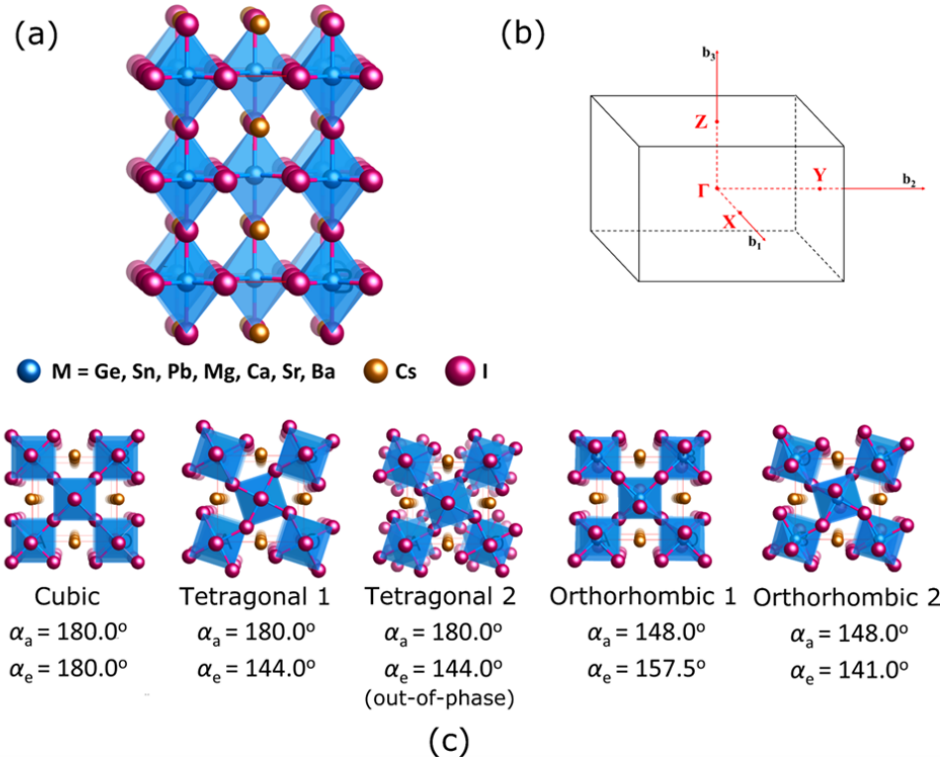

Figure 2.1: Cesium metal iodide perovskites ($CsMI_3$, M = Ge, Sn, Pb, Mg, Ca, Sr, Ba): (a) Generic $CsMI_3$ crystal structure viewed along the [100] direction; (b) First Brillouin zone (FBZ) of a tetragonal cell and its high symmetry points (Γ, X, Y, Z); (c) Five starting structures of perovskite viewed along the [001] direction: cubic, tetragonal 1, tetragonal 2, orthorhombic 1, orthorhombic 2. α_a and α_e are the initial apical and equatorial metal-halide-metal bond angles used to construct five different phases of perovskite.

percent of Hartree-Fock exchange (25% Hartree-Fock exchange for HSE06). The projected augmented wave (PAW) [66, 67] potentials were used to describe the interactions between the core and the valence electrons. A plane-wave kinetic energy cutoff of 670 eV was used for all the functionals except for HSE06, for which the cutoff was set to 400 eV to reduce the computational time (as HSE06 calculations are computationally intense). The structural relaxation was done by sampling the Brillouin zone over a 6×6×6 k-point grid centered at the Γ point. An energy convergence criterion of 10^{-5} eV was used in the geometry optimization. The atomic positions were relaxed until the forces were less than 0.02 eV/Å. The effect of spin-orbit coupling64 on the $CsMI_3$ bandgaps was investigated using the HSE06 functional with a 4×4×4 k-point mesh. Since we use a tetragonal unit cell with four $CsMI_3$ units for all perovskite phases studied here,

we are able to explore their Brillouin zones using the same paths, i.e. Y-Γ and Γ-Z, as defined in Figure 2.1b. The band structures computed by HSE06 and GAM were plotted along these paths to benchmark the capability of the GAM functional in computing the band dispersions of halide perovskites against HSE06.

2.3 Results and Discussions

2.3.1 Structural Characterization

It is well known that hybrid DFT functionals such as HSE06 can accurately predict certain experimentally measured structural properties such as lattice parameters.[68] In our calculations, we used HSE06 as a benchmark, and found that all other functionals perform similarly in predicting the lattice parameters, with PBEsol and PBE-D3 underestimating them by 1-2$\%$. We compared the HSE06 predictions to experimentally determined lattice parameters, when available, and found that they are within the experimentally reported range for the cubic phase of $CsPbI_3$ and within 1$\%$ or less of the experimental values for the cubic and tetragonal phases of $CsSnI_3$ (Table 2.1). The calculated orthorhombic 1 and orthorhombic 2 lattice parameters are different, due to different tilting of the MI_6 octahedra (see Table A.1-A.7). The experimentally synthesized orthorhombic phase is expected to exhibit dynamic disorder of the MI_6 units,[69] making head-to-head comparison with calculations difficult. Perhaps for this reason the deviation between some of the experimentally measured and predicted parameters is slightly worse for the orthorhombic phases (1-2$\%$ as opposed to <1$\%$). Metals with similar ionic radii result in perovskites with similar lattice parameters. For example, the ionic radii of Pb^{2+} and Sr^{2+} are 1.19 Å and 1.18 Å, respectively, which result in orthorhombic 2 phase perovskites with a= 9.02 Å, b= 8.66 Å, c= 12.62 Å and a= 9.17 Å, b= 8.72 Å, c= 12.74 Å, respectively. Detailed structural information is reported in Table A.1-A.7.

Table 2.1: . Comparison between HSE06 and available experimental lattice parameters (Å) for $CsMI_3$ (M = Ge, Sn, Pb, Mg, Ca, Sr, Ba). The orthorhombic and tetragonal phases reported here are the results of the orthorhombic 2 and tetragonal 1 phases from our DFT calculations.The calculated $Pm\bar{3}m$ $CsGeI_3$ structure was transformed into the R3m space group to match the experimental structure by using the transformation matrix [(1, 0, -1); (-1, 1, 0); (1, 1, 1)]. All transformations were done using the Material Studio 6.1 software.

$CsMI_3$	Experimental			HSE06
	Crystal system	Space group	Lattice parameters	Lattice parameters
$CsGeI_3$	Trigonal[70]	R3m [70]	a/b=8,3582 [70] c=10.6098[70]	a/b=8.40 c=10.29
$CsSnI_3$	Cubic [40]	$Pm\bar{3}m$ [40]	a=6.219 [40]	a=6.23
	Tetragonal [40]	P4/mbm [40]	a/b=8.772 [40] c=6.261[40]	a/b=8.67 c=6.32
	Orthorhombic [40]	Pnma [40]	a=8.6885[40] b=8.6384 [40] c=12.3775[40]	a=8.89 b=8.61 c=12.45
$CsPbI_3$	Cubic [71]	$Pm\bar{3}m$	a=6.1769 [71] a=6.2894 [38] a=6.40[37]	a=6.36
$CsCaI_3$	Orthorhombic [72]	Pnma [72]	a=8.6226[72] b=12.2823[72] c=8.5548[72]	a=8.75 b=12.39 c=8.61

2.3.2 Electronic Structure Calculations

It is well-known that predicting bandgaps of semiconductors is challenging for DFT.[73] Commonly used GGA functionals tend to underestimate bandgaps due to the poor treatment of electronic correlation by these functionals. Hybrid functionals such as HSE06 usually predict bandgaps that agree better with experiments, however they are computationally more expensive.[73] High levels of theory such as quasiparticle self-consistent GW (QSGW) are commonly used for predicting bandgaps that agree more closely with experiments, but they are even more computationally expensive than hybrid functionals. Here, we computed the bandgaps of different $CsMI_3$ phases using various functionals and compared them to experimentally determined values and to QSGW predictions from the literature (Table 2.2). We also estimated the effect of spin orbit coupling (SOC) in the HSE06 calculations for all the phases of $CsMI_3$ perovskites. Figure 2.2 compares the predicted bandgaps for the five $CsMI_3$ structures using different functionals. The numerical values and character of the predicted bandgaps (direct or indirect) are reported in Table A.8.

Table 2.2: Comparison between calculated bandgaps (in eV) and available experimental and QSGW bandgap values for $CsMI_3$ (M = Ge, Sn, Pb, Mg, Ca, Sr, Ba). In the HSE06 and QSGW cases values with and without spin orbit coupling are reported. The orthorhombic and tetragonal phases reported here are the results of the orthorhombic 2 and tetragonal 1 phases from our DFT calculations.The calculated $Pm\bar{3}m$ $CsGeI_3$ structure was further transformed into the R3m space group to match the experimental structure by using the transformation matrix [(1, 0, -1); (-1, 1, 0); (1, 1, 1)].

	$CsGeI_3$ (trigonal)	$CsSnI_3$ (orthorhombic)	$CsSnI_3$ (tetragonal)	$CsSnI_3$ (cubic)	$CsPbI_3$ (cubic)
PBEsol	0.274	0.504	0.271	0.003	1.161
PBE	0.647	0.817	0.682	0.459	1.485
PBED3	0.433	0.635	0.475	0.242	1.334
GAM	1.241	1.469	1.250	1.076	1.976
HSE06	0.872	1.127	0.923	0.694	1.938
HSE06+SOC	0.691	0.804	0.709	0.344	0.755
Experimental	1.6 [70]	1.3 [74]			1.73[71]
QSGW	1.404 [42]		1.494 [41]	1.354 [41]	2.288 [42]
QSGW+SOC	1.199 [42]	1.3 ± 0.1 [41]	1.288 [41]	1.008 [41]	1.331 [42]

For $CsPbI_3$, HSE06, GAM and PBE predict bandgaps within 10-15% of the experimental value. For the orthorhombic phase of $CsSnI_3$, the bandgaps predicted by HSE06 and GAM are similar compared to experiments and QSGW predictions (error is within 14%). For the cubic and tetragonal phases of $CsSnI_3$, all functionals except GAM underestimate the bandgap significantly when compared with the QSGW predictions. For cubic $CsSnBr_3$, Shi et al.[75] used HSE06 with 43% Hartree-Fock exchange instead of the original 25% to get agreement with experiment. In our calculation, we also observe that for cubic and tetragonal $CsSnI_3$ HSE06 with 25% HF-exchange underestimates the bandgap when compared to QSGW bandgap. On the other hand, according to our calculations, GAM is in better agreement with experimental and QSGW values. Moreover, GAM agrees with HSE06 for Pb perovskites. For $CsGeI_3$, the bandgap predicted by GAM is the closest among all the functionals when compared to experimental and QSGW bandgap. The experimentally determined bandgap for $CsGeI_3$ (R3m), 1.6 eV, is closest to the prediction by GAM for the cubic $CsGeI_3$, while HSE06 underestimates the bandgap. Ming et al.[49] matched the experimental value (1.6 eV) by using HSE06 with 45% HF exchange instead of the standard 25% HF-exchange in the HSE06 functional. Thus, for p-block $CsMI_3$ (M = Pb, Sn, Ge) perovskites, GAM predicts similar bandgaps compared to experiments and QSGW methods.

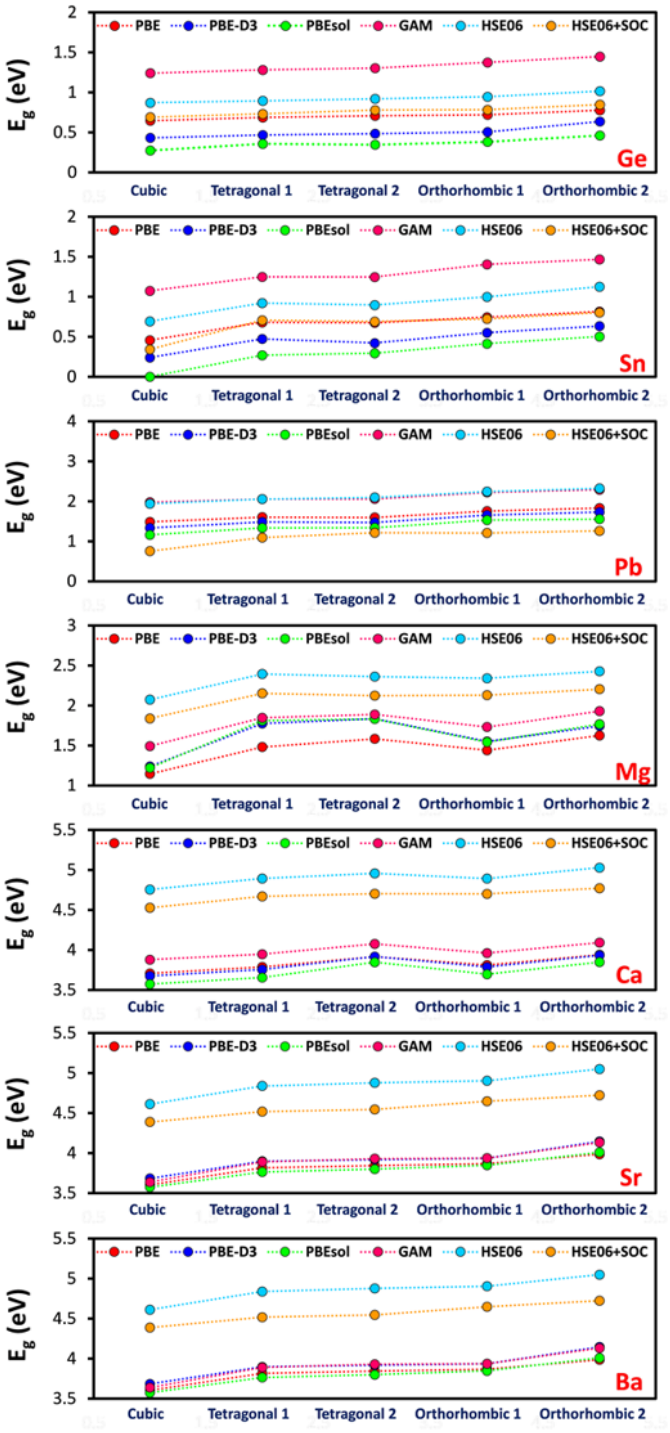

Figure 2.2: Bandgaps for different $CsMI_3$ structures (M = Ge, Sn, Pb, Mg, Ca, Sr, Ba) calculated using five functionals: PBE, PBE-D3, PBEsol, GAM, and HSE06.

Table 2.3: A comparison between calculated bandgaps of $CsMX_3$ (M= Pb, Sn, Ge) perovskites using the platonic perovskite model (This Work) and using the conventional cubic, tetragonal and orthorhombic unit cells from the literature.

$CsMX_3$ M = Pb, Sn, Ge)	PBE Bandgap (eV) (This Work)	PBE Bandgap (eV) (Previous Work)
Cubic $CsPbI_3$	1.485	1.48,[76] 1.44,[77] 1.49 [78]
Cubic $CsSnI_3$	0.459	0.44,[45] 0.48 [78]
Cubic $CsGeI_3$	0.647	0.62 [45]
Tetragonal $CsPbI_3$	1.604	1.60 [78]
Tetragonal $CsSnI_3$	0.682	0.62 [78]
Orthorhombic $CsPbI_3$	1.831	1.82 [78]
Orthorhombic $CsSnI_3$	0.817	0.81 [78]

In contrast, GAM predictions are similar to GGA functionals (see Table A.8) for s-block $CsMI_3$ (M = Mg, Ca, Sr, Ba), for which the available experimental data are limited. Thus, we expect that the bandgaps of these s-block perovskites, if formed, would be between the bandgaps predicted by the GGA/NGA functionals and the HSE06 functional. However, even the bandgap values predicted by GGA and NGA are already high enough to make s-block perovskites (M = Ca, Ba, Sr) unlikely candidates for solar cell absorber materials, though there are plenty of other applications for wide bandgap semiconductors. To summarize, GAM predicts the highest bandgaps and closest to the experimentally determined values for Pb, Sn and Ge, i.e. the p-block perovskites. In contrast, for s-block perovskites, the highest bandgaps are predicted by HSE06 while GAM gives values similar to those predicted by GGA methods.

The effect of SOC in combination with the HSE06 functional in bandgap calculations was also investigated because previous calculations concluded that including SOC improved the band structure.[41, 42, 79] Among the p-block perovskites, Pb has the highest SOC followed by Sn and Ge, in order of decreasing atomic number. Upon adding SOC for Pb perovskites the bandgap decreases by 1 eV compared to bandgap computed without SOC. It should be noted that including spin-orbit coupling result in the underestimation of the bandgap of $CsPbI_3$: the bandgap predicted by HSE06 (with 25$\%$ HF exchange) with SOC for cubic $CsPbI_3$ is 0.55 eV.[80] From our platonic model we observed that the bandgap of $CsPbI_3$ using HSE06 + SOC (with 25$\%$ HF exchange) is predicted to be 0.755 eV. This difference is due to the fact we computed the effect of SOC of the HSE06 optimized structure whereas Hendon et al.[80] computed the effect of SOC at the PBEsol optimized geometry. The decrease in bandgap is 0.3 eV and 0.2 eV for Sn and Ge perovskites, respectively, when SOC is included.

Among the s-block CsMI3 perovskites, the differences in bandgap predictions due to SOC varies between 0.20 to 0.33 eV when compared to bandgap predictions without SOC, and as such, the effect of SOC on bandgap is much smaller than that in $CsPbI_3$. The bandgap decreases from Ca to Ba for all structures when SOC is included. No such consistent trend is observed with all the functionals when SOC is not included. The SOC effects on bandgaps are reported in Table A.8.

In order to validate the use of the platonic perovskite model, we compare the PBE functional predicted bandgaps of different phases of Pb, Sn and Ge perovskites using the platonic perovskite model to bandgaps using conventional cubic, tetragonal and orthorhombic unit cells as reported in the literature. The predicted bandgaps obtained using platonic perovskites are in good agreement compared to the bandgaps predicted by conventional cubic, tetragonal and orthorhombic unit cells (see Table 2.3).

DFT functionals typically predict qualitatively similar band dispersions for $CsMI_3$ perovskites. Thus, in Figure 2.3 we report the band structures for all $CsMI_3$ phases calculated using GAM and HSE06 (with 25$\%$) functionals.[81, 82]78,79 In general, there is qualitative agreement between the two methods. The values of the bandgaps at the Γ points are, however, slightly different for the same structure and metal. For the p-block metals (Ge, Sn, Pb), the conduction bands of the tetragonal structures are more dispersive (larger band width) along Γ-Z compared with those of other structures. For all other structures of p-block metals, the curvature is similar along Γ-Z and Y-Γ for both the valence and conduction bands. Effective mass of holes and electrons along Γ-Z and Y-Γ direction for different phases of $CsMI_3$ perovskites are reported in Table A.9-A.12. For p-block metals, the band projection at the Γ point shows that the valence bands are comprised of and ca. 40$\%$ metal s-orbitals and ca. 60$\%$ iodine p-orbitals (see Table A.13-A.17), while the conduction bands are comprised of ca. 80$\%$ metal p-orbitals and ca. 20$\%$ iodide s- and d-orbitals. This observation is consistent with previous calculations.[37, 39, 42, 43] The s-block metals (Ca, Sr, Ba) exhibit bandgaps wider than 4 eV, with the exception of Mg having 2.5 eV bandgap. The gap widening in $CsCaI_3$, $CsSrI_3$, and $CsBaI_3$ can be attributed to the large contribution of I-6s and Cs-6s orbitals to the conduction bands (see Table A.13-A.17), which does not exist in $CsMgI_3$. For $CsMgI_3$, the conduction band has a major contribution from Mg-3s, some contribution from I-6s and no contribution from Cs-6s orbitals. Moreover, the valence bands of s-block metals are flat around the Γ point, indicating heavy holes. The projected valence bands at the Γ point show 100$\%$ iodine p-orbital character. The lack of hybridization in the s-block metals results in less disperse valence bands as shown in Figure 2.3, and this results in large hole effective masses in the valence bands.

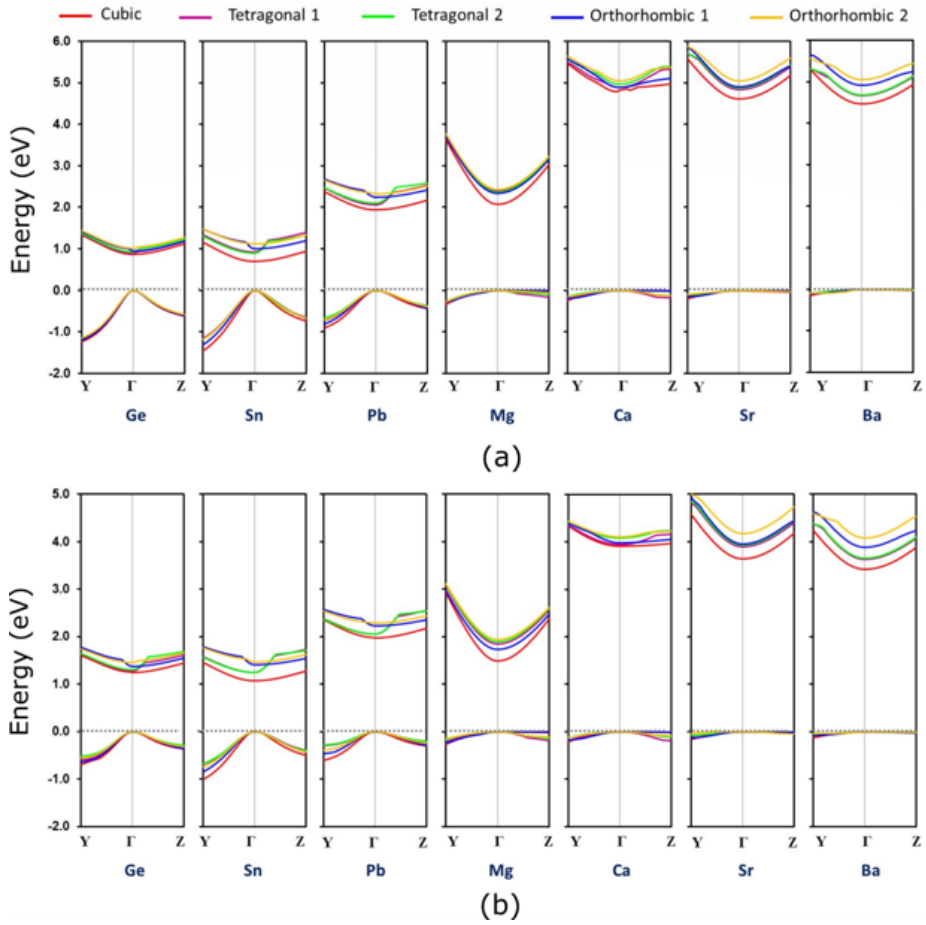

Figure 2.3: Band structures alongthe Y-Γ-Z path for $CsMI_3$ (M= Ge, Sn, Pb, Mg, Ca, Sr and Ba) calculated by HSE06 (a) and GAM (b). The valence band maxima are set to zero energy.

2.3.3 Formation Energy and Relative Stability of Different Crystal Structures

In the platonic model, each perovskite unit cell contains four $CsMI_3$ formula units. Accordingly, the formation energy (E_{form}) was calculated using[50]

$$E_{form} = E\left(Cs_4M_4I_{12}\right) - 4 \times E(CsI) - \frac{4}{y}E\left(M_yI_{2y}\right) \tag{2.1}$$

where $E(Cs_4M_4I_{12})$, $E(CsI)$, $E(M_yI_{2y})$ are the electronic energies of four perovskite formula units, CsI, and the corresponding metal-iodide salt, respectively, and y is the number of formula units of the metal-iodide salt required to synthesize one unit cell.

Figure 2.4 shows the formation energies for all five perovskite structures in Figure 2.1 calculated using HSE06. Several trends can be observed across different metals. For cations with similar ionic radii, the relative stability of different phases is similar. For example, for both Pb and Sr, the orthorhombic 2 phase is the most stable structure, whereas the cubic phase is the least stable. $CsCaI_3$ also shows a similar trend in relative stability where the orthorhombic γ-phase is the most stable and the other phases are close in energy. An orthorhombic-to-cubic phase transition with increasing temperature is observed in both $CH_3NH_3PbI_3$[83] and $CsSrBr_3$[84], consistent with the order of stability predicted by our calculations, which rank the relative stability of these structures at 0 K. For $CsPbI_3$, $CsSrI_3$, and $CsCaI_3$, the cubic structure has the smallest negative energy of formation and is less stable than the orthorhombic and tetragonal structures. Based on these calculations, we also expect the possibility of an orthorhombic-to-cubic phase transition for $CsSrI_3$.

We also studied the effect of different functionals on predicting the formation energy. Compared to other functionals, PBE-D3 gives smaller negative values of the formation energy for all cases except $CsMgI_3$. For $CsMgI_3$, PBE-D3 predicts negative formation energy, whereas all the other functionals predict positive formation energy. For $CsBaI_3$, PBE-D3 predicts a larger positive formation energy compared to other functionals. A detailed comparison of the formation energies of all the structures using different functionals is reported in Table A.18.

As seen in Figure 2.4, all the p-block halide perovskites studied here ($CsGeI_3$, $CsSnI_3$,

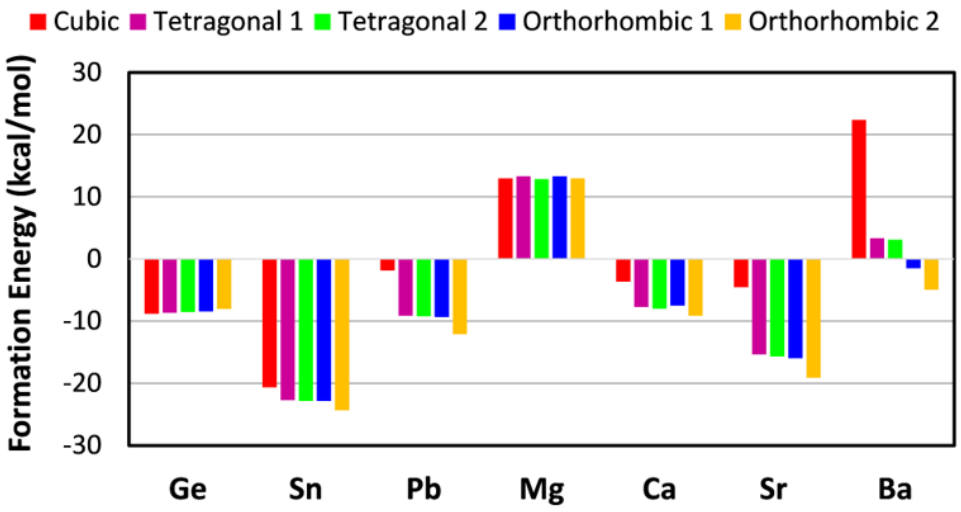

Figure 2.4: Formation energy of cesium metal iodide perovskites ($CsMI_3$, M = Ge, Sn, Pb, Mg, Ca, Sr, Ba) for cubic, tetragonal 1, tetragonal 2, orthorhombic 1, orthorhombic 2 phases using the HSE06 functional.

and $CsPbI_3$) have negative formation energies with respect to the CsI and MI_2 precursors. This aligns well with experimental results reported in the literature, as $CsGeI_3$,[33, 45, 70] $CsSnI_3$,[36, 74, 85, 86, 87, 88, 89] and $CsPbI_3$[71, 90, 91, 92, 93, 94] have all been successfully synthesized in at least one phase.

For $CsPbI_3$, experiments have established that an edge-sharing orthorhombic phase is stable at room temperature, but transforms into the cubic corner-sharing phase upon heating above 563 K.[38] Recently, several publications have demonstrated a stabilized, cubic corner-sharing $CsPbI_3$ structure at room temperature.[71, 90, 91, 92, 93, 94] A corner-sharing orthorhombic phase has not yet been observed experimentally for $CsPbI_3$, but is well known for $CH_3NH_3PbI_3$. Given that our calculations show that the tetragonal and orthorhombic corner-sharing phases are more stable than the cubic phase at 0 K, it would be interesting to see if these structures could be synthesized experimentally.

For M = Sn, all five structures in Figure 2.4 have negative formation energies at 0 K. Cubic (α-phase), tetragonal (β-phase), and orthorhombic (γ-phase) $CsSnI_3$ have all been synthesized

and experiments have established that the orthorhombic phase transforms to the tetragonal and cubic phases, sequentially, as the temperature is increased.[36, 40, 43] This experimental trend in stability is consistent with the trend in the formation energies of the phases calculated here.

For $CsGeI_3$, all five structures are close in energy at 0 K and thus is it challenging to predict which phase might be observed at experimentally realistic temperatures. Experimentally, $CsGeI_3$ is known to form in the R3m space group at room temperature.[70] The cubic phase of $CsGeI_3$ can be transformed via the matrix transformation as discussed in the computational details section.

As for the alkaline earth metal perovskites where M = Mg, Ca, Sr, and Ba, the formation energies are much more varied, as can be seen in Figure 2.4. Significantly fewer experimental results have been published for these inorganic alkaline earth metal halide perovskites. The majority of the work on $CsMI_3$ exists in the scintillator field, where $CsMI_3$ serves as a wide gap host for emissive dopants such as Eu^{2+} or Tm^{2+}.[84, 95, 96, 97, 98, 99, 100, 101] However, perhaps due to the primary function of $CsMI_3$ perovskites as host materials, these papers often include little or no optical or structural characterization of phase-pure $CsMI_3$.

In our calculations, $CsMgI_3$ has positive formation energy in all the phases and all functionals except PBE-D3 (see Table A.18). This high positive formation energy follows from the small coordination factor of 0.33 for the MgI_6 octahedra, which is significantly lower than the octahedral coordination factor (0.41), and the empirical stability limit established for halide perovskites (0.442).[102] This high formation energy is also validated by experiments, which have shown that $CsMgI_3$ does not adopt a corner-sharing MX6 octahedral network like the prototypical halide perovskite $MAPbI_3$; instead it $CsMgI_3$ adopts a face-sharing $CsNiCl_3$ type structure with space group P63/mmc.[101, 103] Based on experimental observations in the literature and the calculations performed here, it appears unlikely that $CsMgI_3$ will adopt a corner-sharing perovskite structure.

The formation energy of $CsCaI_3$ is slightly negative for all five phases calculated. There is some experimental evidence of a corner-sharing orthorhombic $CsCaI_3$ crystal,[72] however most reports of $CsCaI_3$ include a dopant such as Eu^{2+}, and limited optical and structural

characterization of $CsCaI_3$ exists.[101]

Of the alkaline earth metal perovskites, our calculations show that $CsSrI_3$ has the largest negative formation energy. However, $CsSrI_3$ has been shown experimentally to form an orthorhombic structure (space group Cmcm), where the SrI_6 octahedra are arranged in linear chains instead of a 3D corner-sharing octahedral network.[72, 101]

For $CsBaI_3$, the formation energies of the orthorhombic 1 and orthorhombic 2 phases are slightly negative, whereas the cubic and tetragonal phases are positive. This may indicate that if formed experimentally, corner-sharing $CsBaI_3$ may adopt an orthorhombic crystal structure. Interestingly, the synthesis of $CsBaI_3$, and very recently $CH_3NH_3BaI_3$, have been claimed, but these studies have limited characterization of structural, optical, and stability properties.[104, 105] In our experimental work, we were unable to synthesize either of these compounds.

Given the limited available experimental data on $CsMX_3$ (M = Mg, Ca, Sr, Ba), we attempted to synthesize several perovskites ($CsCaI_3$, $CsBaI_3$, and $CsSrBr_3$) to corroborate the calculations performed here. The predicted negative formation energy of $CsCaI_3$ (Figure 2.4) makes it a promising candidate for comparison between experiment and computation, and to the best of our knowledge, no optical or stability data is published for undoped $CsCaI_3$. In contrast, experimentally synthesizing and performing structural characterization on $CsBaI_3$ would test the accuracy of the large dependence of formation energy on crystal structure presented in Figure 2.4. $CsSrBr_3$ was synthesized as an alternative due to the known non-corner-sharing structure of $CsSrI_3$, as well as the toxicity of SrI_2. $CsSrBr_3$ is known to form an orthorhombic Pnma structure,[72] but the authors are unaware of any published optical or stability data on undoped $CsSrBr_3$. Details and results can be found in the Experimental Results Section.

2.3.4 Experimental Results

The synthesis of $CsCaI_3$, $CsBaI_3$, and $CsSrBr_3$ proved challenging due to the significant hygroscopicity of the alkaline earth metal halide precursors (CaI_2, BaI_2, and $SrBr_2$). Initially, we attempted to synthesize thin films of $CsCaI_3$, $CsBaI_3$, and $CsSrBr_3$ using the “one-step” and “two-step” spin-coating techniques commonly used in the perovskite literature.[106, 107, 108, 109,

110]103–107 Even when encapsulated, these thin films visibly and measurably decomposed on the order of minutes, prohibiting structural and optical characterization. We pursued synthesis using a more robust precursor melting technique as described in Section A.1. All synthesis steps were performed in an N_2 atmosphere, and all characterization was done without exposing the samples to ambient conditions.

Figure 2.5 shows the x-ray diffraction (XRD) patterns for the products obtained from the attempted synthesis of $CsBaI_3$ using a variety of CsI and BaI_2 precursor stoichiometric ratios. The 1:3 CsI:BaI_2 molar stoichiometry formed the known double-salt iodide $CsBa_2I_5$, with some unreacted BaI_2.[111] Increasing the molar ratio of CsI resulted in the disappearance of the $CsBa_2I_5$ phase, appearance of significant CsI precursor peaks, and also the appearance of two unknown peaks near 2θ=30°. These may be shifted BaI_2 peaks due to the incorporation of Cs interstitial or substitutional defects. Notably, however, none of the experimental XRD patterns have peaks below 2θ=20°, which would be expected for a perovskite of this unit cell size. Taken together, the lack of peaks below 2θ=20° and the fact that nearly all peaks can be matched with $CsBa_2I_5$, BaI_2, or CsI, suggest the inability to synthesize a $CsBaI_3$ perovskite in any measurable quantity. Furthermore, none of the patterns shown in Figure 2.5 resemble the simulated $CsBaI_3$ XRD patterns for any of the 5 structures studied herein. For example, the simulated orthorhombic 1 and orthorhombic 2 XRD patterns are shown in Figure 2.5 and represent the lowest energy $CsBaI_3$ structures (see Figure 2.4). The lattice parameters of these structures can be found in Table A.1-A.7. The formation energy of $CsBa_2I_5$ calculated using HSE06 is -24.5 kcal/mol, which is much more negative than that of $CsBaI_3$ phases as shown in Figure 2.4, corroborating these observations. Computed lattice parameters and formation energy of $CsBa_2I_5$ using different functionals are reported in Table A.19.

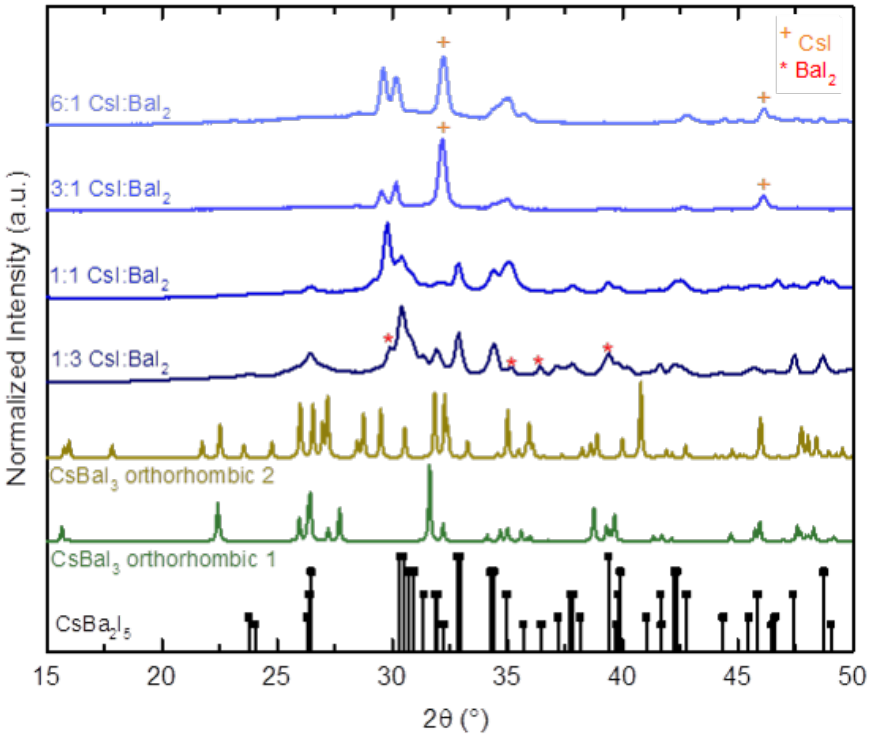

Figure 2.5: X-ray diffraction patterns for different stoichiometries of CsI and BaI_2 precursors used in an attempt to synthesize $CsBaI_3$. The 1:3 CsI:BaI_2 ratio (darkest blue trace) formed the known $CsBa_2I_5$ double-salt iodide (black sticks) with residual BaI_2 precursor (red asterisks). Increasing the molar ratio of CsI resulted in the disappearance of the $CsBa_2I_5$ phase and the appearance of significant CsI precursor peaks (orange crosses). Two unknown peaks near 2θ=30°, hypothesized to be shifted BaI_2 peaks due to the incorporation of Cs interstitial or substitutional defects, are evident in the 3:1 and 6:1 CsI:BaI_2 traces. Notably, no peaks match simulated $CsBaI_3$ patterns (green and yellow traces), which suggests that $CsBaI_3$ perovskite was not formed in a measurable quantity.

The attempted synthesis of $CsCaI_3$ was similarly unsuccessful, possibly due to the extreme hygroscopicity of CaI_2. All XRD patterns measured showed peaks that could be entirely matched by CsI, CaI_2, or hydrated versions of CaI_2 such as $CaI_2{\cdot}H_2O$.

In contrast, $CsSrBr_3$ was readily synthesized using the precursor melt method described in Section A.1. Figure 2.6 shows XRD patterns for 1:2, 1:1, and 2:1 molar ratios of CsBr and $SrBr_2$ precursors, all which resulted in significant formation of $CsSrBr_3$, with some residual precursor in the 1:2 and 2:1 ratios. UV-vis absorption measurements were performed on $CsSrBr_3$ powder suspended in silicone oil (see Section A.1, Figure A.1). No appreciable absorption was detected in this suspension down to a wavelength of 200 nm, suggesting a bandgap >6.2 eV. To support our experimental observation, an HSE06 calculation was performed for the orthorhombic 2 phase of $CsSrBr_3$ yielding a formation energy of -21.8 kcal/mol, similar to that of $CsSrI_3$. The calculated XRD pattern using the orthorhombic 2 phase is similar to the pattern of the XRD peaks obtained by experimental synthesized peaks, however, all the predicted XRD peaks obtained using HSE06 optimized orthorhombic 2 structure are shifted towards left. This is due to the fact that HSE06 optimized orthorhombic 2 structure overestimates the lattice parameter by 0.1 Å when compared to experimental values. Similar disagreements in lattice parameters between theory and experiment are not uncommon and, in fact, are observed in the literature for different perovskites and perovskite like compounds.[42, 46, 112, 113] The orthorhombic 2 structure showed a bandgap of 5.7 eV using the HSE06 functional. Comparison of lattice parameters, formation energy and bandgap using different functionals are reported in Table A.20.

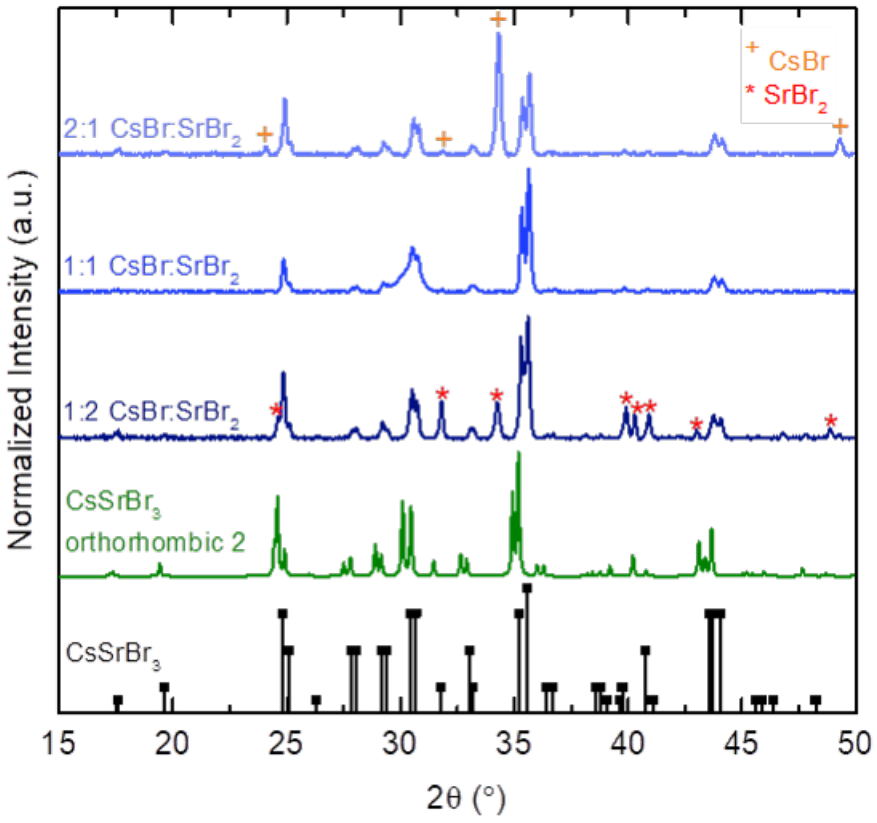

Figure 2.6: X-ray diffraction patterns for different stoichiometries of CsBr and $SrBr_2$ precursors used to synthesize $CsSrBr_3$. All three ratios (blue traces) show the formation of the $CsSrBr_3$ perovskite (black sticks). As expected, the 1:2 ratio also contains excess $SrBr_2$ (red asterisks), and the 2:1 ratio contains excess CsBr (orange crosses).

The stability of $CsSrBr_3$ in ambient conditions (Section A.1, Figure A.2) was evaluated as a function of air exposure time via in situ XRD. A significant change in the diffraction pattern was observed after only 15 minutes of air exposure. Within 60 minutes, the XRD pattern was almost completely that of $SrBr_2 \cdot 6H_2O$. This rapid degradation in the presence of moisture, along with its large optical bandgap, indicates this material is unlikely to be useful in PV applications.

2.4 Conclusion

We computed formation energies, structural and electronic properties of $CsMI_3$ perovskites, where M = Ge, Sn, Pb, Mg, Ca, Sr, Ba, using several density functionals. We found that Mg and Ba perovskites are unlikely to form in cubic, tetragonal or orthorhombic perovskite phases, which is corroborated by experimental evidence presented here and in the literature. We also found that the formation energy of Sr perovskites is more negative than that of Pb perovskites. While their predicted wide bandgap makes them unlikely candidates as solar absorbers, they may find other applications where wider gaps are desired. However, extreme hygroscopicity of Sr perovskites is a significant challenge. Finally, we showed that the local functional GAM performed similar to the hybrid functional HSE06 for p-block element perovskites, but had less satisfactory performance for s-block perovskites.

Chapter 3

Sulfur Vacancy Clustering and its Impact of Electronic Properties in Pyrite FeS_2

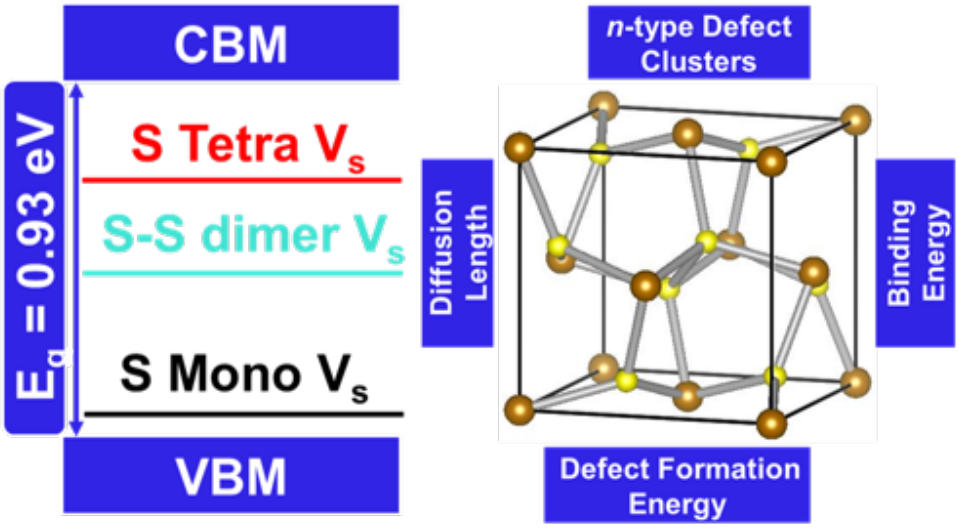

3.1 Introduction

Notwithstanding the impressive successes of commercial Si solar cells, there has always been a steady interest in developing alternative photovoltaic devices based on thin films of materials that are cheaper than silicon and are comprised of abundant and nontoxic elements.[19, 20] Pyrite FeS_2 has been an ideal candidate in this regard,[19] as it has a suitable band gap ($E_g \approx 0.95$ eV), [21] strong light absorption ($\alpha \geq 10^5$ cm^{-1} for $h\nu \geq 1.0$ eV), [21] and a favorable minority carrier diffusion length, [114] and is comprised of earth-abundant, nontoxic, inexpensive elements.

Unfortunately, solar cells employing pyrite FeS_2 as the photoabsorber perform poorly, generating power conversion efficiencies of only $\sim$ 3% [21], a factor of 10 below the Shockley-Queisser limit.[115] Of the proposed factors contributing to this disappointing performance, two have proven particularly persistent: anomalous surface electronic properties [21, 114, 116, 117] and a lack of understanding and control of doping.[21, 22, 23, 24, 25, 26] There has been steady progress during the past decade, however, in resolving both of these issues.[116, 117, 22, 118] In terms of pyrite's surface behavior, it has recently been established that an electrically conductive, typically p-type, nanoscopic surface layer forms on unintentionally doped n-type pyrite single crystals,[116, 117] consistent with earlier reports of surface band bending and Fermi level pinning.[21, 114, 119, 120, 121] The existence of this surface layer, which may be due to intrinsic surface states, was not fully appreciated during earlier studies of Schottky-type solar cells [21, 122] and has since been implicated in their poor performance.[116] For example, an internal p-n junction created by the p-type surface inversion layer has been hypothesized as a potential explanation for poor efficiency,[116] and indeed a leaky internal junction could explain low open circuit voltages. [123]

Lack of doping understanding and control, the second enduring issue with pyrite, has prevented the fabrication of p-n homojunctions, the simplest potential route to pyrite solar cells. Here too, however, significant recent progress has been made.[22, 118] It is now known, for example, just as with single crystals, that unintentionally-doped pyrite thin films with sufficiently

high carrier mobility are in fact n-type and not p-type as previously believed.[22] A common origin for the n-type behavior in unintentionally-doped pyrite single crystals and thin films is thus implicated. Building on numerous literature suggestions, over many years,[21, 25, 116] a recent experiment has implicated S vacancy-related defects as this n-type dopant.[118] Specifically, by systematically decreasing the S vapor pressure during crystal growth, Voigt et al.[118] observed monotonic increases in Hall electron density, conductivity, and mobility, independent of the concentration of various impurities, providing strong evidence for a native S vacancy-related donor. The activation energy ($\Delta E_{\text{activation}}$) associated with this donor state, i.e., the energy difference between the donor level and the conduction band minimum (CBM), was measured to be 0.23 eV.[118] This large $\Delta E_{\text{activation}}$ (i.e., a deep donor state) is widely observed in unintentionally-doped single crystals, regardless of the synthesis method.[21, 116, 117, 25, 118] It should be emphasized, however, that the measurements of Voigt et al.[118] only show that the free electron density increases with decreasing S vapor pressure, implicating a S-vacancy-related defect; the measurements cannot distinguish, however, between a simple S vacancy and S vacancy-containing clusters, or complexes.

Notably, computational studies do not uniformly support simple S vacancies as the deep donors in pyrite. The neutral S mono-vacancy (V_S), for example, has been the focus of several density functional theory (DFT) studies.[24, 124, 125, 126] These studies do not find an occupied (i.e., donor) state near 0.23 eV below the CBM (i.e., with $\Delta E_{\text{activation}}$ = 0.23 eV) at temperature T = 0 K, but instead find a filled state 0.80 eV below the CBM.[124, 127] This implies that S mono-vacancies in pyrite produce donor states that are too far beneath the CBM to efficiently n-dope the material, in disagreement with the experimentally observed $\Delta E_{\text{activation}}$ = 0.23 eV.[116, 25, 118] Charged S mono-vacancies have also been investigated;[24, 124, 126] the neutral vacancy, however, was identified as the predominant charge state, although the nature of dopant states (i.e., donors vs. acceptors) created by charged S mono-vacancies, and their locations in the gap, were not reported. Moreover, DFT-calculated V_S formation energies $\Delta E_{\text{formation}}$ are in the 2.4 – 3.5 eV range, depending on the functional employed and the sulfur chemical potential (μ_S).[24, 123, 124, 125, 126] These large $\Delta E_{\text{formation}}$ values imply that V_S would form in only

very low equilibrium concentrations at experimentally relevant temperatures (pyrite crystals are typically grown at 900 K, for example [116, 118]). DFT could overestimate $\Delta E_{\text{formation}}$,[128] however, or, alternatively, V_S could be incorporated via non-equilibrium routes during growth, e.g., through surface vacancy formation (which may have a lower $\Delta E_{\text{formation}}$ in pyrite)[129, 130] and diffusion-limited trapping processes. Hu et al.[125] and Krishnamoorthy et al.[124] also investigated whether removing a S-S dimer, a trademark of the pyrite structure, could yield a native deep donor. Creating this S-S dimer vacancy, however, required an even larger $\Delta E_{\text{formation}}$ of >4 eV, and was thus ruled out as a possibility.

Importantly, while $\Delta E_{\text{formation}}$ values of this magnitude may prohibit isolated S-S dimer vacancies from forming in reasonable concentrations at experimentally relevant temperatures, clustering remains a possibility in FeS_2. If S mono-vacancies are introduced during growth, for example (via either equilibrium or non-equilibrium routes, as discussed above), and have sufficient mobility, then an energetic driving force to cluster could result in agglomeration, sequestering the initial V_S. This possibility has not been explored in pyrite FeS_2, nor has a detailed theoretical study of the donor state energies for a broad range of potential native S defect complexes been performed. With recent experimental evidence strongly supporting a S vacancy-related defect as the origin of the universal n-type doping in unintentionally-doped pyrite, such a theoretical study seems overdue. Elucidation of precisely which defect(s) could be responsible for n-doping in pyrite, how they form, and their corresponding $\Delta E_{\text{activation}}$ and $\Delta E_{\text{formation}}$, is clearly needed, and could point the way to defect control and mitigation strategies.

In this article, we report on a detailed and comprehensive DFT investigation of $\Delta E_{\text{formation}}$, $\Delta E_{\text{activation}}$, and their implications for electronic properties of pyrite, for a broad variety of S vacancy-derived native defects. Our goal is to thoroughly examine the formation energies of possible S vacancy-related defects, and the energy levels they introduce into the band gap, in order to assess the likelihood that such defect clusters could account for the unintentional n-doping observed in experiment. S vacancy clusters are specifically highlighted, examining the potential driving forces for such, and the trends in $\Delta E_{\text{activation}}$ with the number of vacancies involved. After reproducing the known crystal and electronic structures of defect-free pyrite, we

first confirm that S mono-vacancies indeed do not explain the experimentally observed donor state. By considering four different configurations of S di-vacancies, we then show that the S-S dimer vacancy produces a donor state with $\Delta E_{\text{activation}} \approx 0.55$ eV, i.e., 0.25 eV closer to the CBM than the S mono-vacancy or any of the other S di-vacancies explored. Calculating formation energies, we find that there is a significant enthalpic benefit for S mono-vacancies to cluster into two di-vacancies, namely the S-S dimer vacancy and the trans-S di-vacancy (two mono-vacancies situated across an FeS_6 coordination octahedron from each other in a trans-configuration). By combining these two di-vacancies to form a tetra-vacancy (two S-S dimer vacancies situated trans across an Fe coordination center), we obtain a donor state with$\Delta E_{\text{activation}} \approx 0.41$ eV. This is closer to the experimental $\Delta E_{\text{activation}} \approx 0.23$ eV than other V_S-based defects, and suggests a clear trend of better agreement with experiment with increasing cluster size. In combination with formation energy and diffusion arguments that suggest S mono-vacancies are incorporated in large enough concentration, and with sufficient mobility to cluster upon cooling from typical growth temperatures, we assert that these results can explain experimental observations of S vacancy-based doping in pyrite FeS_2.[118] Clearly, these findings highlight the importance of defect clusters and complexes in this promising photovoltaic material.

3.2 Computational Methods

Spin-polarized DFT calculations were performed using the Vienna ab initio Simulation Package (VASP)[54, 55, 56, 57] and projected augmented wave (PAW) potentials.[66, 67] The Perdew-Burke-Ernzerhof (PBE)[58, 59] exchange-correlation functional was employed, with the generalized gradient approximation (GGA) and a Hubbard U correction [131] of 1.8 eV for Fe 3d electrons. As described below, these methods were chosen after extensive benchmarking of pyrite crystal and electronic structure parameters vs. various choices of functional and U value. A kinetic energy cutoff of 350 eV was used for structure optimizations and band structure calculations; total energies converged to within 0.0002 eV/atom (see Table B.1) with this cutoff. A 7×7×7 k-point grid mesh centered at the Γ point was used to sample the Brillouin zone of the unit cell, and Gaussian smearing with a width of 0.01 eV was used when plotting the resulting

density-of-states (DOS). Pyrite FeS_2 adopts a simple cubic structure (space group: $Pa\bar{3}$, Figure 3.1a,b), which can be visualized as a NaCl-like structure, with Fe situated on the face-centered cubic (FCC) sites and <111>-oriented S dimers (S-S) in the anion positions (i.e., the octahedral interstices of the FCC Fe sub-lattice). Each Fe is thus bound to six S atoms in an octahedral coordination, and each S is tetrahedrally-coordinated to three Fe atoms and the other S atom in its dimer.

After initial calculations, the defect-free structure was modified by introducing various S-vacancy-derived defects. All structures (including defect-free pyrite FeS_2) were relaxed using energy and force convergence criteria of 10^{-5} eV and 0.02 eV/Å, respectively. To calculate corresponding band structures and defect formation energies, 3×3×3 supercells were typically used, unless otherwise stated (2×2×2 supercells were used for comparison in some cases). For structural optimization of supercells and DOS calculations, the Brillouin zone was sampled using a 3×3×3 k-point grid mesh centered at the Γ point and the band structure was extracted along the R-Γ-X-M-R trajectory. To compare with defect state energies obtained using the PBE+U functional, 2×2×2 pyrite supercell calculations with the HSE06 functional (with 7% Hartree-Fock exchange, a)[63, 64, 65] were also performed, including a Γ-centered 2×2×2 k-point grid mesh for Brillouin zone sampling. We also verified convergence of the defect formation energy and activation energy with respect to the kinetic energy cutoff (see Table B.2). CM5[132, 133] and Bader[134, 135, 136, 137] charge analysis was performed based on charge density obtained from VASP calculation. All band structures and DOS reported in the article were calculated using 3×3×3 supercells, but defects are depicted in 2×2×2 supercells to aid visualization. The importance of defect-defect self-interaction was evaluated by comparing the results calculated using 2×2×2 and 3×3×3 supercells (Tables B.3-B.5). Band structures and various calculated values for all defects reported in this manuscript, except the S tetra-vacancy (as discussed below), are well converged with respect to supercell size and do not show significant self-interaction effects in $\Delta E_{\text{activation}}$, $\Delta E_{\text{formation}}$, binding energy ($E_{\text{b}}$), or band structure dispersity. S tetra-vacancy calculations with a 3×3×3 supercell also do not exhibit significant self-interaction effects, although 2×2×2 supercell calculations do (Table B.3), likely due to the size of the tetra-vacancy

relative to the other defects. We also evaluated if fixing vs. relaxing the lattice parameter influenced the defect $\Delta E_{\text{activation}}$. The lattice parameter was either fixed at the bulk pyrite lattice parameter or allowed to relax prior to band structure and DOS calculations. Atomic positions were always relaxed, and the PBE+(U = 1.8 eV) functional and a 3×3×3 k-point grid mesh centered at the Γ point were employed. As shown in Table B.6, whether the lattice parameter is fixed or relaxed does not influence the $\Delta E_{\text{activation}}$ of any defect in this study.

For calculations of defect formation energy, we adopt the notation of Van de Walle et al.[138] The formation energy ($\Delta E_{\text{formation}}$) of a vacancy V is given by

$$\Delta E_{formation}\left(\mu_{\alpha}\right) = E_V - E_0 - \sum_{\alpha} n_{\alpha}\left(\mu_{\alpha}^{0} + \Delta\mu_{\alpha}\right) + q\left(E_{VBM} + E_F + \Delta V\right) \tag{3.1}$$

where E_V is the total electronic energy of the supercell with the vacancy V, E_0 is the total electronic energy of a defect-free supercell, α is the identity of the atom removed to create V, n_{α} is the number of these removed atoms per supercell (note: n_{α} < 0 when removing atoms, i.e., creating V), μ_{α}^{0} is the standard state chemical potential of atom α, and $\Delta\mu_{\alpha}$ is the difference between μ_{α}^{0} and the chemical potential of α. In our case, S_8 was taken as the standard state of sulfur, and thus the energy of one sulfur atom in S_8 was taken as the chemical potential in the sulfur-rich ($\Delta\mu_S = 0$) condition. In equation 3.1, q represents the charge state of V, E_{VBM} represents the energy eigenvalue of the valence band maximum (VBM) and E_{F} represents the Fermi level relative to the VBM. To determine the predominant charge state of the S mono-vacancy, i.e., that which is present in highest concentration, a self-consistent solution for the Fermi level was obtained using the SC-Fermi code of J. Buckeridge, available on GitHub.[139] Yang et al.[140] outline the equations necessary to calculate this self-consistent solution. A frozen defect approximation (assuming 10^{20} cm^{-3} vacancies, as estimated from experimental Hall electron densities in pyrite single crystals)[116, 118] was used in these calculations. Finally, ΔV is a DFT post-processing correction to align the reference electrostatic potential of the defect-containing supercell to that of the bulk, and is computed using the recently-developed sxdefectalign code.[141, 142]

In general, $\Delta E_{\text{formation}} \leq 0$ indicates spontaneous defect formation. In contrast, when $\Delta E_{\text{formation}}$ is positive, defect formation is not spontaneous, but rather occurs via a Boltzmann

distribution at T > 0 K (i.e., with an exponential T dependence). In particular, the concentration (c) of a defect or defect complex is given by[138]

$$c = N_{sites} N_{config} exp\left(-\frac{\Delta E_{formation}}{K_B T}\right) \tag{3.2}$$

where N_{sites} is the concentration (per unit volume) of the sites at which the defect can be incorporated (e.g., for a V_S in pyrite FeS_2, N_{sites} = 5.03 × 10^{22} cm^{-3}, i.e., the concentration of S sites), N_{config} is the number of equivalent configurations in which a defect can be incorporated (for point defects, N_{config} = 1), and K_B is Boltzmann's constant. While equation 3.2 can be used to calculate equilibrium concentrations of point defects as well as defect complexes/clusters, the likelihood of forming defect complexes can be quantified by the binding energy (E_b) of these defects. This is defined by Van de Walle et al.[138] as

$$E_b = \sum_i \Delta E_{formation}(i) - \Delta E_{formation}(defect - cluster) \tag{3.3}$$

where $\Delta E_{formation}(i)$ is the formation energy of the i-th isolated point defect participating in a cluster and $\Delta E_{formation}(defect - cluster)$ is the formation energy of the entire cluster. With this definition, a negative E_b indicates an energetic penalty for point defect clustering, whereas a positive E_b indicates that a stable bound defect cluster is favorable. For a given complex to form spontaneously at a larger concentration than its constituent point defects in thermal equilibrium, $\Delta E_{formation}(defect - cluster) \leq \Delta E_{formation}(i)$ is required, thus implying E_b must be greater than all $\Delta E_{formation}(i)$. As Van de Walle et al.[138] outline, this is caused by a loss in configurational entropy that occurs when defects cluster, requiring an overwhelming energetic benefit in formation energy (i.e., $\Delta E_{formation}(defect - cluster) \leq \Delta E_{formation}(i)$ to drive the total Gibbs free energy towards clustering.

While E_b must be greater than $\Delta E_{formation}(i)$ for clustering to occur in equilibrium, clustering can also occur out of equilibrium when 0 < E_b < $\Delta E_{formation}(i)$. Using the example of Mg-H complexes in GaN, Van de Walle et al.[138] describe how clustering can occur in this E_b range if defects are kinetically trapped, or "frozen in" when cooling from growth conditions. Critically, this can only occur when defects are kinetically trapped such that their concentration is not dictated

by equilibrium conditions while cooling, but defects are still mobile enough to diffuse on the nanometer scale and thus combine with other defects to form the cluster.

It should be noted that the formation energies (equation 3.1) and binding energies (equation 3.3) computed by the above approach do not include effects such as zero point energy, or finite temperature effects such as thermal expansion, or vibrational and configurational entropy. As described in section B.2 we thus also evaluated the influence of these effects. Thermal expansion was found to impact calculated energies by only $\approx$2 meV, while zero point energy and vibrational entropy were found to impact calculated energies by $\approx$0.1 eV (B.7). These effects were thus ignored. Configurational entropy, on the other hand, was found to have a non-negligible effect on formation energies (Table B.8 and Table B.9) and resulting binding energies (Table B.10 and Table B.11), as discussed below.

3.3 Results and Discussions

3.3.1 Defect-Free Pyrite

The crystal structure of defect-free pyrite FeS_2 is shown in Figure 3.1 a,b, with the octahedral coordination of Fe and tetrahedral coordination of S showcased in 3.1a and 3.1b, respectively. As noted above, various density functionals were used to calculate the defect-free, relaxed bulk pyrite Fe-S and S-S bond lengths, lattice parameter, and band gap. These were then compared to experimentally determined quantities (Figures B.1-B.4) to identify the most suitable functional for further study. Among the various functionals, the PBE functional with a Hubbard U correction of 1.8 eV for Fe 3d orbitals yields a lattice parameter of 5.418 Å (experiment: 5.418 Å),[21] an Fe-S bond distance of 2.26 Å (experiment: 2.26 Å),[21] and a S-S bond distance of 2.16 Å (experiment: 2.14 Å),[21, 143, 144] all of which agree well with experiment and previous theoretical studies.[125, 126, 145, 146] Figure 3.1c shows the calculated band structure of defect-free pyrite, yielding an indirect band gap (E_{g}) of 0.93 eV that agrees well with both theoretical [125, 126, 145, 146] and experimental studies.[21, 147, 148, 149, 150, 151, 152, 153] The PBE+U (U = 1.8 eV) functional was thus used for all subsequent calculations, unless specified

otherwise. Note that the HSE06 functional with 7% Hartree-Fock exchange (a) also predicted an accurate band gap; calculations using this functional will be briefly discussed below for comparison with PBE+U (U = 1.8 eV) results. Figure 3.1c shows that the VBM occurs near the X point, while the CBM is located at the Γ point. The disperse CBM is characteristic of pyrite and is due to S 3p states.[154] These are evident in Figure 3.1c and also in the spin-resolved DOS shown in Figure 3.1d, which exhibits a weak tail of states in the bottom portion of the conduction band. The states nearest the VBM, in contrast, create relatively large DOS, due to their Fe 3d t_{2g} nature.[125] Using this band structure of defect-free pyrite, we obtain an isotropic electron effective mass of 0.56m_e and anisotropic hole effective masses of 1.46m_e (along the VBM to Γ direction) and 1.95m_e (along the VBM to X direction). These are in agreement with past theory[125] and experiment (see Table B.12 for a detailed comparison).[26, 143, 149]

CM5[132, 133] and Bader[134, 135, 136, 137](reported in parenthesis) charge analysis of defect-free pyrite shows that the charges on Fe and S are +0.32e (+0.90e) and -0.16e (-0.45e) (where e = 1.6×10^{-19} C), respectively, confirming a mixed ionic/covalent nature. The calculation summarized in Figure 3.1c,d also predicts a non-ferromagnetic ground state in defect-free pyrite, which is in agreement with both experiment and theory.[23, 125, 145, 155, 156]

3.3.2 Sulfur Mono-Vacancy

Using the PBE+U (U = 1.8 eV) functional, S vacancies were then investigated. To introduce the simplest S vacancy into pyrite, i.e., the S mono-vacancy (V_S), a single neutral S atom was removed from a supercell (Figure 3.2a), the structure was relaxed, and the band structure and DOS calculated. Note that a 2×2×2 supercell is shown in Figure 3.2a for illustration, but the calculation results shown in Figure 3.2b,c are for a larger 3×3×3 supercell. Figure 3.2b,c shows that, in addition to some small increases in empty DOS above the CBM, the V_S produces two occupied states in the band gap, as highlighted in Figure 3.2c. These states are found at 0.04 eV and 0.15 eV above the VBM, i.e., they have $\Delta E_{\text{activation}}$ = 0.91 eV and 0.80 eV, respectively; this is generally consistent with previous calculations.[124, 125] Note that a slight increase in band gap, from 0.93 to 0.95 eV, is observed in all calculations that include S vacancies; this

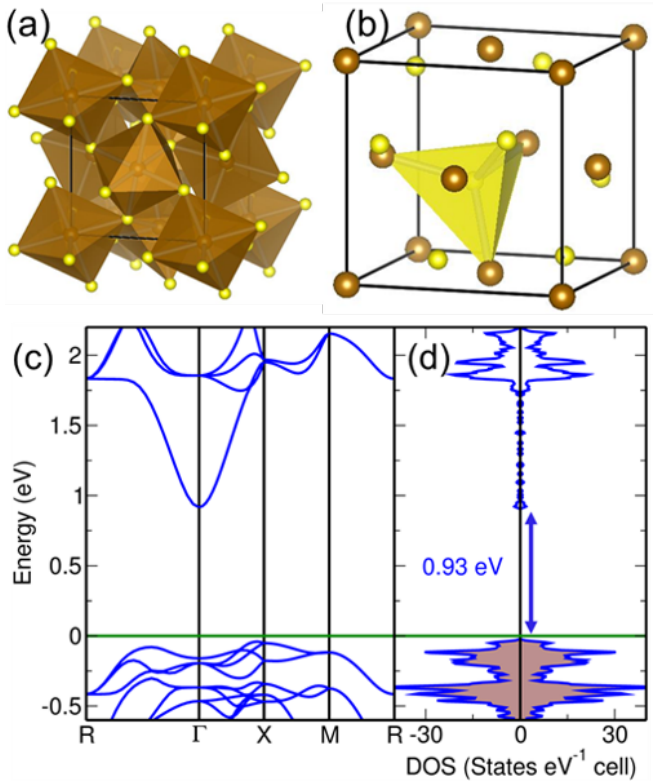

Figure 3.1: Crystal Structure of Pyrite FeS_S ($Pa\bar{3}$ space group); illustrations of (a) the octahedral Fe coordination and (b) tetrahedral S coordination. Fe and S atoms are represented by brown and yellow spheres, respectively. Spin-resolved DFT results for the (c) band structure and (d) density-of-states (DOS) of a defect-free single pyrite FeS_2 unit cell using the PBE+U (U = 1.8 eV) functional. The green line at 0 eV represents the Fermi level, and the band gap, E_g (0.93 eV), is shown in (d).

increase is well within DFT's uncertainty of about ±0.04 eV and thus is not discussed further. Upon addition of the V_S, both CM5 and Bader (reported in parenthesis) charge analyses reveal a near-doubling in charge on the S atom nearest the VS (green atom, Figure 3.2a), from -0.16e (-0.45e) to -0.25e (-0.80e), demonstrating that negative charge moves to the S nearest the V_S, as also in agreement with previous calculations.[125] This is consistent with the expectation that, in a simple ionic picture, the reduction of S^- to S^{2-} is more favorable than the reduction of Fe(II) to Fe(I). Charge density analysis of the highest occupied defect state ($\Delta E_{activation}$ = 0.80 eV) reveals S p_z character derived from the S atom nearest the V_S (likely associated with the increase in negative charge discussed above) and Fe t_{2g} character from the three Fe atoms bound to

this S (Figure B.5). The minor contribution of Fe t_{2g} orbitals to this state can be explained by crystal field theory. Specifically, creating a V_S pulls the remaining S (green atom, Figure 3.2a) towards the original dimer center-of-mass by 0.2 Å. This elongates the Fe-S bonds of the three Fe atoms bound to this S, distorting their octahedral coordination, breaking the degeneracy of the t_{2g} orbitals, and lifting one of them into the band gap. A qualitative schematic of this process is shown in Figure B.6. Note that we also verified that the positions of the defect states, their dispersion in energy, and the CM5 and Bader charges do not depend on the supercell size; thus, only the 3×3×3 supercell calculations are presented here. These results, all consistent with literature,[124, 125] indicate that the occupied state in the band gap produced by a neutral V_S is too low in energy, and thus $\Delta E_{\text{activation}}$ is too large, to explain the S vacancy-related donor observed in experiment.

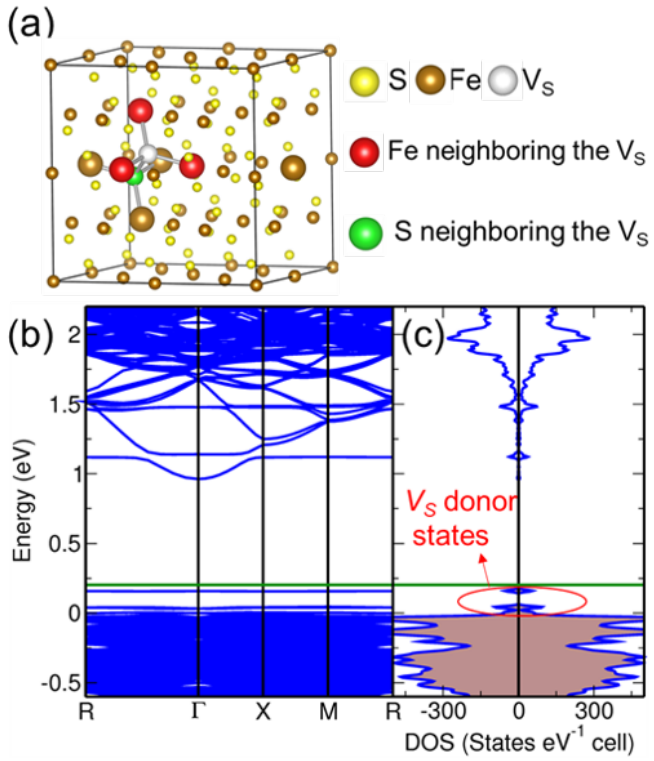

Figure 3.2: DFT analysis of the S mono-vacancy in pyrite FeS_2. (a) 2×2×2 supercell of pyrite containing one S mono-vacancy. Spin-resolved band structure (b) and density-of-states (DOS) (c) of one S mono-vacancy in a 3×3×3 pyrite supercell using the PBE+U (U = 1.8 eV) level of theory. The horizontal green line represents the Fermi level. The donor states induced by the S vacancy in the band gap are labeled.

For completeness, and to explore the likelihood of formation, we also calculated $\Delta E_{\text{formation}}$ for S mono-vacancies. This was done not only for the neutral V_S, but also for various possible charge states, as a function of the Fermi level. Figure 3.3 shows $\Delta E_{\text{formation}}$ vs. E_F (the VBM is at E_F = 0 here) at an illustrative $\Delta\mu_S$ = -0.6 eV, i.e., S-poor conditions, for V_S charges (q) of 0, ±1, and ±2. The positively and negatively charged defects trend upwards and downwards with E_F, respectively, as expected from equation (3.1). Most importantly, the neutral (q = 0) V_S can be seen to have the lowest $\Delta E_{\text{formation}}$, unless the Fermi level is above 0.94 eV (i.e., above the CBM, vertical dashed line) or below 0.22 eV. Using the experimentally deduced Fermi level location (0.23 eV below the conduction band minimum at T = 0 K)[118], in conjunction with Figure 3.3, we conclude that the neutral S mono-vacancy has the lowest formation energy in the E_F range of greatest relevance to experiment. This is certainly true for most high quality FeS_2 single crystals, which are S-deficient and n-type, but non-degenerately doped. More quantitatively, assuming a frozen V_S concentration of 10^{20} cm^{-3}, self-consistent Fermi level calculations indicate that E_F resides 0.52 eV and 0.66 eV above the VBM at 300 K and 860 K (near typical crystal growth temperatures),[116, 156] respectively. This is in reasonable agreement with past theoretical studies showing that E_F lies 0.46 eV above the VBM when various charge states of Fe- and S-related defects are considered.[24, 123] All of these E_F positions are safely in the range in which the neutral V_S has the lowest $\Delta E_{\text{formation}}$, and thus the neutral vacancy should be present in the highest concentrations. Based on these findings, we discuss only neutral S vacancies in the remainder of this manuscript. The DOS for the various charge states of the S mono-vacancy are reported in (Figure B.7).

3.3.3 Sulfur Di-Vacancies

As isolated V_S appear not to generate a $\Delta E_{\text{activation}}$ that can be reconciled with the S vacancy-related n-dopant observed in pyrite crystals, but given the aforementioned suspicion of clustering tendencies, we moved on to considering S di-vacancies. Figure 3.4 shows the four different S di-vacancies considered: two separate S mono-vacancies (Figure 3.4a), a S-S dimer vacancy (Figure 3.4b), a cis-S di-vacancy (Figure 3.4c), and a trans-S di-vacancy (Figure 3.4d).

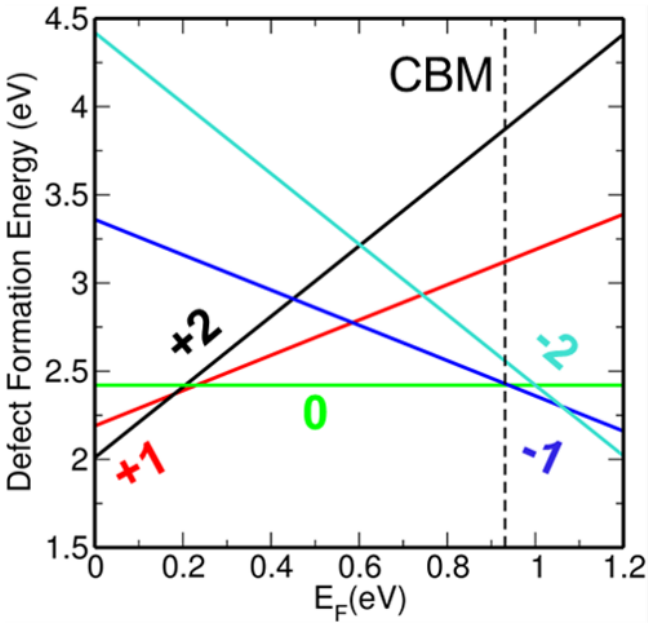

Figure 3.3: The formation energy ($\Delta E_{\text{formation}}$) of the S mono-vacancy (V_S) in different charge states V_S. the Fermi level (E_F). $\Delta\mu_S$ = -0.6 eV is assumed, and E_F = 0 eV is defined as the valence band maximum (VBM) of pyrite. The conduction band minimum (CBM) is depicted with a vertical dashed line.

Again, the supercell size (varied from 2×2×2 to 3×3×3, corresponding to VS concentrations of 1.6 × 10^{21} cm^{-3} to 4.8 × 10^{20} cm^{-3}, respectively) had no significant effect on the resultant defect state position or its dispersion in energy, for any di-vacancy (see Table B.3). Consequently, only the results obtained with the 3×3×3 supercell are discussed here; Figure 3.4 nevertheless depicts 2×2×2 supercells, simply for ease of inspection.

Shown in Figure 3.4 a are two separate S mono-vacancies, i.e., vacancies coordinated to different Fe atoms within a supercell and not part of the same S-S dimer. As shown in Figure 3.5b, this situation results in occupied states emerging at 0.04 eV and 0.15 eV above the VBM (i.e., with $\Delta E_{\text{activation}}$ = 0.91 eV and 0.80 eV, respectively), identical to the single V_S discussed above (Figure 3.2c). CM5 and Bader (reported in parenthesis) charge analyses again show a near-doubling in negative charge (from -0.16e (-0.45e) to -0.26e (-0.82e)) on the S atoms nearest each vacancy (green atoms, Figure 3.4a), confirming that the negative charge left by vacancy creation moves to these S atoms. Somewhat unsurprisingly, this di-vacancy can thus be viewed simply as two non-interacting V_S, and, like V_S, it does not generate a $\Delta E_{\text{activation}}$ consistent with

experiment. For completeness, the DOS shown in Figure 3.5b is expanded upon in Figure B.8, which also includes the calculated band structure.

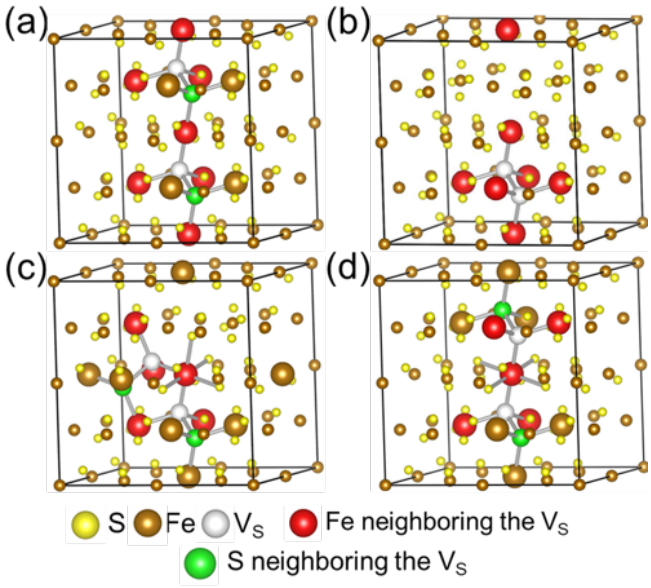

Figure 3.4: Supercell configurations of four possible S di-vacancies: (a) two S mono-vacancies, (b) a S-S dimer vacancy, (c) a cis-S di-vacancy and (d) a trans-S di-vacancy. These configurations are described further in the text.

Of higher interest, the S-S dimer vacancy, shown in Figure 3.4b, results in the DOS plotted in Figure 3.5c. A single occupied defect state forms in the band gap in this situation, at 0.40 eV above the VBM, corresponding to $\Delta E_{\text{activation}} \approx 0.55$ eV. Significantly, this is much higher in energy than the states resulting from a single V_S (Figure 3.2c) or two non-interacting V_S (Figure 3.5b), and is thus closer to the $\Delta E_{\text{activation}}$ seen in experiment. Since both S atoms in the dimer have been removed, the negative charge left by the vacancy creation is partially transferred to the six Fe atoms nearest the defect (red atoms, Figure 3.4b), as illustrated in B.99; the change in CM5 and Bader (reported in parenthesis) charge amounts to -0.01e (-0.05e) per Fe atom. The remainder of the negative charge is then accommodated by the S atoms coordinated to these six Fe. In contrast to the mono-vacancy case, partial charge density analysis of the highest occupied defect state (see Figure B.9) created by the S-S dimer vacancy reveals almost entirely Fe e_g character. This can again be rationalized via crystal field arguments: these six Fe atoms now have square pyramidal coordination, breaking the degeneracy of the Fe e_g orbitals and

lowering the Fe d_{Z^2} orbital energy. This orbital is in turn partially filled by the negative charge provided by the S-S dimer vacancy, as schematically shown in Figure B.10. This correlation between charge transferring to Fe (not S) atoms and a higher energy donor state (and thus lower $\Delta E_{\text{activation}}$) will be returned to below when discussing more complex defects. A detailed band structure and DOS for this S-S dimer vacancy are shown in Figure B.11.

Moving on, the cis-S di-vacancy and trans-S di-vacancy are shown in Figures 3.4c and 3.4d, respectively. Two V_S are introduced on the same FeS_6 coordination octahedron, either along different axes, sharing an edge of an octahedron (cis-S di-vacancy, Figure 3.4c), or across the Fe atom from each other and along the same axis (trans-S di-vacancy, Figure 3.4d). As shown in Figure 3.5d, the cis-S di-vacancy results in three occupied defect states within 0.2 eV of the VBM. The trans-S di-vacancy (Figure 3.5e), on the other hand, induces two defect states, also within 0.2 eV of the VBM and strikingly similar to those in the VS case (Figure 3.2c). Calculated band structures and more detailed views of the resulting DOS for the cis-S di-vacancy and the trans-S di-vacancy cases are shown in Figures B.12 and B.13, respectively. In both cases CM5 and Bader (reported in parenthesis) charge analyses confirm an increase in negative charge on the S atoms nearest the respective mono-vacancies, from -0.16e (-0.45e) to -0.26e (-0.80e), indicating once again that the charge shifts to the S dimer partners of each respective V_S. Again, this association between negative charge transferring to S and corresponding donor states yielding $\Delta E_{\text{activation}} \geq$ 0.75 eV suggests that S vacancies must be configured in a way that transfers charge to Fe, not S, to generate defect states near the experimental $\Delta E_{\text{activation}}$ of 0.23 eV. Of the four di-vacancies investigated here, this occurs only for the S-S dimer vacancy. In the other cases, even if two S atoms are removed from the same Fe coordination octahedron, almost no charge transfer to Fe and the corresponding eg states is observed, and there is thus little increase in the donor state energy towards the experimentally observed value. Interestingly, mild spin polarization is observed 0.2 eV above the CBM when either the cis- or trans-S di-vacancy are introduced. Partial DOS analysis indicates that these states have predominantly Fe d character, and thus the origin of this mild spin polarization likely stems from the reconfigured ligand field of the Fe atom that has both mono-vacancies as nearest neighbors in each respective defect. For

example, in the trans-S di-vacancy case, the ligand field around this Fe becomes square planar, which lifts and lowers the dxy and dz2 orbitals, respectively, allowing unpaired electrons and, if exchange is sufficient, polarization.

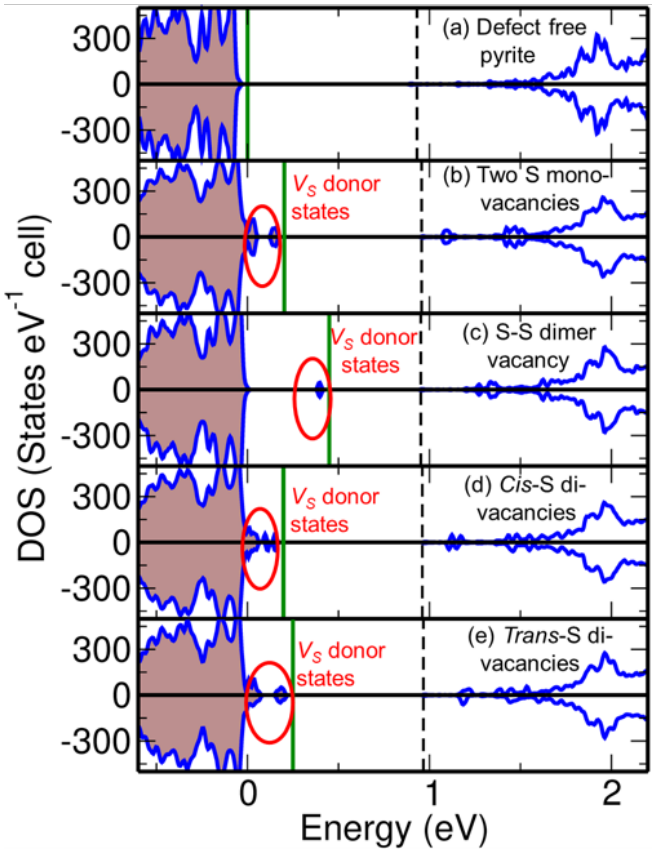

Figure 3.5: DFT-calculated spin-resolved density-of-states (DOS) of pyrite that is (a) defect-free, or contains (b) two S mono-vacancies, (c) a S-S dimer vacancy, (d) a cis-S di-vacancy, or (e) a trans-S di-vacancy in a 3×3×3 supercell. Vertical green lines represent the Fermi level, the black dashed line represents the conduction band minimum (CBM), and donor states within the gap created by defect inclusion are circled. The small apparent DOS below the CBM in (a) is an artifact of the Gaussian smearing function (0.01 eV width) used to smooth the calculated DOS of defect-free pyrite. When we examine the eigenvalues of occupied and unoccupied states at each k-point for these calculations we do not find any state corresponding to these small intensities in the DOS.

For completeness, and to understand if the donor levels in the gap created by these S vacancies depend on the functional, these calculations were also performed with the HSE06 (a = 0.07) functional. As shown in Table B.3, the $\Delta E_{\text{activation}}$ of the highest occupied defect level induced by each vacancy agrees very well between PBE+U (U =1.8 eV) and HSE06 (a = 0.07),

confirming that the S-S dimer vacancy is the only mono- or di-vacancy studied thus far that shifts the resulting donor state towards that which is experimentally observed.

3.3.4 Vacancy Formation and Binding Energies

Corresponding values of $\Delta E_{\text{formation}}$ were calculated for the defects studied above, and are plotted as a function of the S chemical potential (relative to S8) in Figure 3.6. It should be noted, as discussed in Section 2 above, that the $\Delta E_{\text{formation}}$ (Table B.9) reported here reflect a correction due to configurational entropy, as this was found non-negligible; the literature values of $\Delta E_{\text{formation}}$ that we compare our results to do not include this correction. For isolated V_S, $\Delta E_{\text{formation}}$ decreases linearly from 2.88 eV to 1.98 eV with decreasing $\Delta\mu_S$ (i.e., moving from a S-rich to a S-poor environment), in agreement with previous studies.10,19,20 Corresponding $\Delta E_{\text{formation}}$ values for the di-vacancies exhibit similar linear dependencies on $\Delta\mu_S$, but with larger absolute values. The trans-S di-vacancy has the lowest $\Delta E_{\text{formation}}$ at a given $\Delta\mu_S$, followed by the S-S dimer vacancy, and the cis-S di-vacancy; the two S mono-vacancies (Figure 3.4a) then have nearly identical $\Delta E_{\text{formation}}$ to twice the S mono-vacancy, as expected from the above discussion (Section 3.3). Critically, Figure 3.6 thus illustrates that the $\Delta E_{\text{formation}}$ of various S di-vacancies are less than twice that of the S mono-vacancy. This has important implications for vacancy clustering, which is returned to below. First, however, we discuss these $\Delta E_{\text{formation}}$ values in the context of isolated vacancies.

While earlier studies[124, 125, 126] suggested that such high $\Delta E_{\text{formation}}$ values (2-3 eV for mono-vacancies) would yield V_S concentrations too low to either play a significant role in electronic properties or to cluster into di-vacancies (and/or other defect complexes), we contend that these possibilities should not be excluded, particularly given the compelling new evidence for S vacancy-related n-doping in pyrite.13 Naively applying equation (3.2) with a $\Delta E_{\text{formation}}$ of 1.98 eV, for example, yields a V_S concentration of 1.27×10^{11} cm^{-3}, assuming $N_{\text{config}} = 1$, $N_{\text{sites}} = 5 \times 10^{22}$ cm^{-3}, and T = 860 K (a typical growth temperature for FeS^2 single crystals).6,13 While this is below the intrinsic carrier density at 300 K (3×10^{11} cm^{-3}), and thus electronically

insignificant, DFT has been known to overestimate $\Delta E_{\text{formation}}$.22 In TiO_2, for example, DFT-calculated $\Delta E_{\text{formation}}$ values for O vacancies are well above 3.0 eV, although they are understood to be present experimentally.22 Similar overestimations are observed for O vacancy formation in lanthanide62 and actinide oxides too.63–65 To rule out possible inaccuracies associated with a particular functional, we also calculated $\Delta E_{\text{formation}}$ using the HSE06 functional and found good agreement (Table B.4) with values from PBE+U. While this consistency suggests that there is no significant variation across reasonable choices of functional, overestimation of $\Delta E_{\text{formation}}$ may be an inherent, or deeper, problem with DFT. It is relevant in this regard that DFT (using the PBE+U functional) overestimates the $\Delta E_{\text{formation}}$ of V_S on the FeS_2(100) surface. Calculated values range from 0.4-2.1 eV,19,21,23,24 compared to experimental formation enthalpies of 0.10 ± 0.03 eV from X-ray photoelectron spectroscopy (XPS).24 Such overestimation may occur in bulk pyrite also, in which case S mono-vacancies could potentially form in significant equilibrium concentrations.

Surface S vacancy formation and/or kinetic processes driving vacancy incorporation into pyrite crystals during growth should also be considered. For example, a small formation enthalpy of only 0.10 ± 0.03 eV24 could generate high densities of S vacancies on the surface of pyrite crystals that can be kinetically trapped, or "frozen in," during crystal growth. This hypothesis gains further credence when the poor diffusivity of S and VS in pyrite is considered.13,65 In a dynamic crystal or film growth process, this poor diffusivity could inhibit vacancy motion, out-diffusion, and annihilation, after initial creation on the surface. As an example, a typical chemical vapor transport growth of pyrite yields crystals of order 1 mm thickness in around 10 days; this corresponds to an average growth rate of 1 nm s-1. By assuming either experimental S self-diffusion coefficients66 or DFT-calculated V_S diffusion coefficients,23 the relation $l = \sqrt{Dt}$ (where l is diffusion length, D is diffusion coefficient, and t is time) yields V_S diffusion lengths of 0.01-2 nm in 1 s at growth T (860 K13). The upper end of this range is on the order of typical growth rates, meaning that pyrite crystals grow as fast as (or faster than) V_S can diffuse in the bulk, supporting the idea of kinetic trapping.

Moving on to di-vacancies, and the important possibility of clustering, the first point to

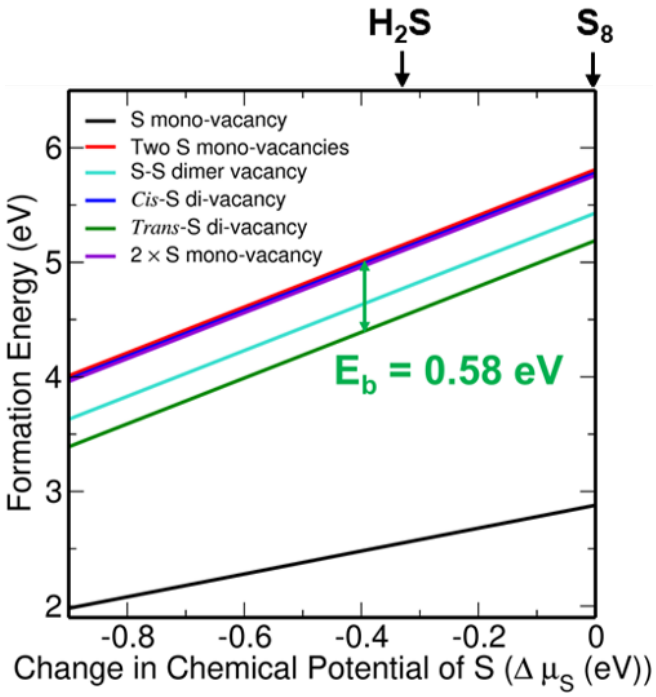

Figure 3.6: Dependence of the defect formation energy ($\Delta E_{\text{formation}}$) on the S chemical potential ($\Delta\mu_{\text{S}}$) for S mono- and di-vacancies in pyrite FeS_2. S_8 is taken as the standard state of S, and thus defined as $\Delta\mu_{\text{S}}$ = 0. As an example, the energy difference (0.58 eV) between the trans-S di-vacancy and 2×$\Delta E_{\text{formation}}$ (V_{S}) is shown to directly visualize the binding energy (E_{b}) associated with this defect. As noted in the text, $\Delta E_{\text{formation}}$ and E_{b} reflect corrections due to configurational entropy.

emphasize is that the di-vacancy $\Delta E_{\text{formation}}$ values shown in Figure 3.6 are all above 3.5 eV, even under S-poor conditions, about 1.4 eV above S mono-vacancies. While this may preclude equilibrium formation of these defects in significant concentrations at T < 740 ℃ (above which pyrite decomposes3), it is nevertheless possible for di-vacancies to form via clustering of VS.43 As outlined in Section 2, defect clusters can form via two routes if the binding energy (E_{b}, the energy gained by the clustering reaction between point defects) is positive: in thermal equilibrium during growth (if $E_{\text{b}} \geq \Delta E_{\text{formation}}(i)$, where $\Delta E_{\text{formation}}(i)$ are the formation energies of the individual point defects), or upon cooling from growth conditions (if E_{b} is not $\geq \Delta E_{\text{formation}}(i)$, but is still significantly larger than $k_{\text{B}}T$). The latter, however, requires defect concentrations to both be “frozen in” upon cooling (i.e., unable to diffuse out of the sample and thus unable to maintain thermal equilibrium concentrations, which is possible in pyrite), yet mobile enough to diffuse and

reach other defects (on the nanoscale) in order to cluster. For formation of S di-vacancies, the relevant reaction is two individual S mono-vacancies transforming to a di-vacancy, i.e., V_S +V_S $\leftrightarrow$ V_S-V_S. This reaction is possible for all four of the geometries discussed above (Figure 3.4), for which E_b can be computed from the calculated formation energies (Figure 3.6) using (3). It is important to note here that for clustering of point defects of the same type (as in the current case), E_b is independent of the chemical potential of the defect i.

For S di-vacancies, E_b can be easily visualized as the difference between $2\Delta E_{\text{formation}}(V_S)$ and the $\Delta E_{\text{formation}}$ of the di-vacancy in question (see Figure 3.6). For example, in the case of two S mono-vacancies coordinated to different Fe atoms within the same supercell (Figure 3.4a), $\Delta E_{\text{formation}}$ is essentially unchanged relative to $2\Delta E_{\text{formation}}(V_S)$ (Figure 3.6), yielding E_b = -0.05 eV. As noted in Section 3.3.3, this defect is essentially two independent, non-interacting V_S, and there is thus no E_b associated with forming this "di-vacancy". The $\Delta E_{\text{formation}}$ of the cis-S di-vacancy (Figure 3.4c) is lower than $2\Delta E_{\text{formation}}(V_S)$ by about -0.02 eV. The E_b of this di-vacancy is therefore negative and thus the di-vacancy is unlikely to form. In contrast, the E_b values for the S-S dimer vacancy and the trans-S di-vacancy are much higher, at 0.34 eV and 0.58 eV, respectively. For completeness, E_b was also calculated using different supercell sizes (3×3×3 vs. 2×2×2) and functionals (PBE+U vsS. HSE06). As shown in Supplemental Information (Tables B.5 and B.11), E_b agrees well between different supercell sizes in PBE+U calculations and between different functionals using 2×2×2 supercells. Once again, these E_b values are less than $\Delta E_{\text{formation}}(V_S)$, and thus significant concentrations are not expected in equilibrium. With the condition $E_b >> k_BT$ satisfied, however, there is now a significant energetic "driving force" for V_S to cluster into these di-vacancies upon cooling. In fact, and as noted in the Introduction, the notion that S vacancies could cluster in pyrite is not new; prior work by Herbert et al.[130] combined XPS and scanning tunneling microscopy with kinetic Monte Carlo calculations to show that S and Fe vacancies cluster on pyrite crystal surfaces, eventually forming pits $\sim$ 5 nm in diameter. Additionally, based on positron lifetimes in both synthetic and natural crystals, Puff et al.[157] suggested that di-vacancies or larger defect clusters are present in pyrite. These studies did not, however, elucidate the specific geometries of the defect complexes/clusters, or elaborate

on how these influence electronic properties of pyrite; this is the situation we hope to improve upon here. S vacancy clustering is thus returned to below, after discussing a next logical step: the S tetra-vacancy.

3.3.5 Sulfur Tetra-Vacancy

Motivated by the findings that: (i) there is an energetic benefit for V_S to cluster in S-S dimer and trans- configurations, and (ii) the S-S dimer vacancy produces a donor state relatively close to the CBM, we investigated a S tetra-vacancy complex. This is composed of two S-S dimer vacancies oriented in a trans-fashion across a common Fe, as shown in Figure 3.7a. The primary Fe center has square planar coordination, and the 10 other Fe atoms that are nearest-neighbors to one of the V_S (also shown as red atoms in Figure 3.7a) have square pyramidal coordination. The calculated band structure and DOS of such a defect, in a 3×3×3 supercell, is shown in Figure 3.7b,c, again using the PBE+U approach. Significantly, the highest occupied in-gap energy level produced corresponds to a $\Delta E_{\text{activation}}$ of 0.41 eV. This is the highest donor level energy of any S vacancy-based defect in this study, the lowest $\Delta E_{\text{activation}}$, and thus the closest agreement to date with the single crystal experimental $\Delta E_{\text{activation}}$. More importantly, the trend of $\Delta E_{\text{activation}}$ values becoming progressively closer to the experimental result with increasing S vacancy cluster size becomes yet clearer. In addition, the CM5 and Bader charge on each nearest-neighbor Fe atom increase by -0.01e and -0.05e respectively, further confirming the hypothesis of an elevated donor state energy when the negative charge induced by S vacancy creation primarily goes to Fe. No significant change in CM5 and Bader charges occur on the primary Fe center, however. The donor state in the gap is also both spin-polarized (quite likely for the same reason as the trans-S di-vacancy described in Section 3.3.3) and mildly dispersive in energy, suggesting that this V_S concentration (9.3×10^{20} cm^{-3}) is large enough to initiate donor band broadening and thus an evolution towards an insulator-metal transition (IMT), as was also observed recently in experiment.[118] Consistent with this, when calculated in a 2×2×2 supercell (corresponding to a V_S concentration of 3.1×10^{21} cm^{-3}), the defect band further broadens, indicating increased proximity to the IMT (see Figure B.1414).

When calculated using a 3×3×3 supercell, the corresponding tetra-vacancy $\Delta E_{\text{formation}}$ is 6.84 eV under S-poor conditions ($\Delta\mu_S$ = -0.9 eV). With this defect cluster being composed of four V_S, E_S is thus 1.08 eV. This is larger than any of the di-vacancies studied, suggesting that there is a driving force for clustering V_S beyond di-vacancies, into tetra-vacancies, and likely yet more complex defects. This E_b, however, remains smaller than $\Delta E_{\text{formation}}(V_S)$ = 1.98 eV (again, under the most S-deficient conditions), indicating that vacancy complex formation still likely requires "freezing-in" of V_S during growth, followed by clustering upon cooling.

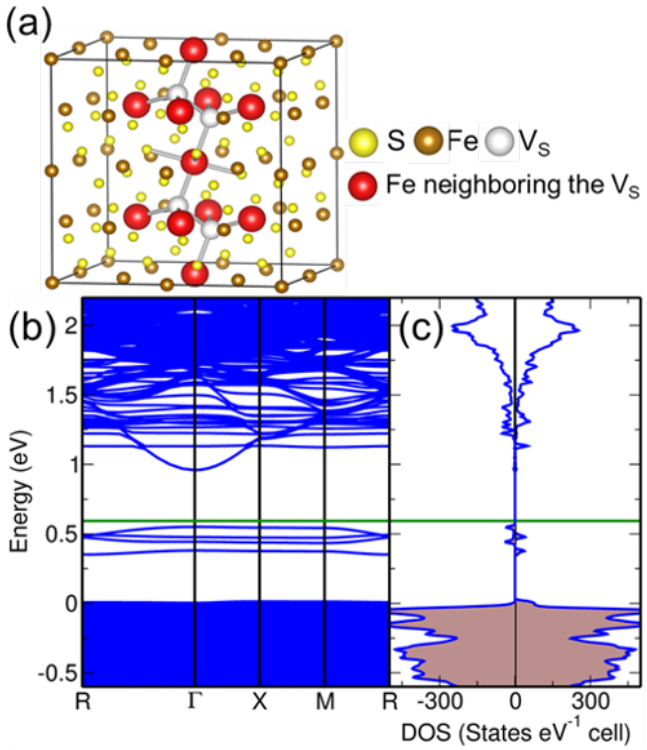

Figure 3.7: (a) 2×2×2 pyrite supercell containing a S tetra-vacancy. Band structure (b) and spin-resolved density-of-states (DOS) of the S tetra-vacancy at the PBE+U (U = 1.8eV) level of theory, calculated using a 3×3×3 supercell. The horizontal green line represents the Fermi level.

In a recent review, Van de Walle et al.[138] outlined how to calculate the relative concentration of defect complexes formed upon cooling from the growth conditions, where point defects are kinetically trapped. For clustering upon cooling to be feasible in our case, the V_S must be able to diffuse at least the average separation distance between vacancies ($d \simeq [V_S]^{-\frac{1}{3}}$, where [$V_S$] is the V_S concentration), yet be unable to diffuse the dimensions of the sample (1 mm for a

single crystal) so as to prevent equilibrium conditions. Kinetically-trapped defect clustering then requires only that E_b substantially exceed $k_B T$. Using an analogous treatment to that for Mg-H defect clusters in GaN,43 the concentration of a given S vacancy cluster can be calculated via mass action, using (2) for each defect (including the clusters). For example, considering the reaction of two V_S to form a S-S dimer vacancy, i.e., V_S+V_S $\leftrightarrow$ V_S-V_S, mass action yields

$$\frac{c_{V_S}^2}{c_{V_S-V_S}^2} = \frac{N_{sites}}{N_{configs}} e^{-\frac{E_b}{k_B T}} \tag{3.4}$$

where c_{V_S} and $c_{V_S-V_S}$ are the concentrations of V_S and the S-S dimer vacancy (denoted with V_S-V_S), respectively, and E_b is the binding energy associated with this event (0.34 eV). Assuming an initial concentration of S mono-vacancies ($c_{V_s}^{tot}$) and conserving their concentration (i.e., putting $c_{V_S} + 2c_{V_S-V_S}$ = $c_{V_s}^{tot}$, the fraction of V_S involved in the S-S dimer vacancy can be calculated as a function of T (see Figure B.15). In a similar fashion, the fraction of V_S participating in tetra-vacancies was also calculated as a function of T, assuming an analogous reaction, 4V_S $\leftrightarrow$ $V_{tetra\text{-}V_S}$ (where $V_{tetra\text{-}V_S}$ denotes the tetra-vacancy cluster). The results are shown in Figure 3.8, with $\frac{c_{tetra-V_S}}{c_{V_S}^{tot}}$ denoting the fraction of V_S involved in tetra-vacancies upon cooling. Total V_S concentrations of 10^{20} cm^{-3} was chosen as relevant to recent single crystal experiments.[116, 118] Since E_b is large and positive in this case (1.08 eV), the fraction of V_S involved in tetra-vacancies approaches 1 as T is decreased from the growth temperature (assumed here to be 860 K). This, however, assumes that the V_S can diffuse at least their average separation at all relevant T. To assess the relevant diffusion length (l) as a function of T, also plotted in Figure 3.8 (right axis, green) is an estimated range for $l(T)$. This was calculated via $l = \sqrt{Dt}$, as in Section 3.3.4, although t is now the time spent at a given temperature while cooling (10 min was chosen as a simple estimate). A DFT-calculated V_S $D(T)$ was used as an upper bound,[129] while $D(T)$ from an experimental S self-diffusion study was used as a lower bound.[158] Where the approximate separation distance (green dashed line) exits the green shaded range of $l(T)$ upon cooling ($\approx$ 710 K), the V_S can be considered "frozen-in", and unable to continue clustering, even though an energetic driving force to do so remains. In this simple picture, 24% of the V_S participate in the tetra-vacancy when initially present at

concentrations of 10^{20} cm^{-3}, respectively. (Note that this value will further increase under slower cooling conditions). This is direct evidence that the energetic gain realized by clustering is large enough, and the diffusivity sufficient, to enable significant clustering of V_S into tetra-vacancies. Recall, critically, that this is also the defect for which DFT calculates a defect level 0.41 eV below the CBM, in closest agreement with recent single crystal experiments.[118]

Combining the trends of improved agreement between experimental and DFT-calculated $\Delta E_{\text{activation}}$ and increasing E_b with increasing defect size (from S mono- to di- to, finally, tetra-vacancies), we expect $\Delta E_{\text{activation}}$ to continue decreasing for even larger S vacancy clusters. Calculating $\Delta E_{\text{activation}}$ and E_b of these defects, while quickly becoming both prohibitively expensive and difficult, would clearly be worthwhile, as would investigating the possible involvement of native Fe defects in these clusters. Experimentally, careful cooling treatments of pyrite crystals and films is one potential route to further evidence defect clustering in pyrite FeS_2.

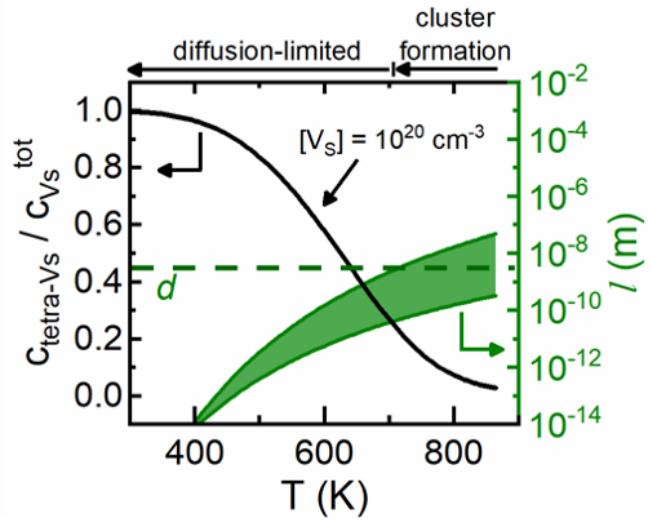

Figure 3.8: The temperature (T) dependence of (left axis) the fraction of S mono-vacancies (V_S) participating in a tetra-vacancy cluster for total initial S mono-vacancy concentrations of 10^{20} cm^{-3}, assuming a binding energy of 1.08 eV. Also plotted (right axis, green) is the T-dependence of a range of S vacancy diffusion lengths (l) estimated assuming $l = \sqrt{Dt}$, where D is the vacancy diffusion coefficient and t is time (10 min). As upper and lower bounds, DFT-calculated V_S diffusion and experimental S self-diffusion coefficients were used, respectively. The average separation distance between V_S (assuming a concentration of 10^{19}-10^{20} cm^{-3}) is 2-5 nm, and is marked with a green dashed line.

3.4 Conclusion

In summary, comprehensive density functional theory calculations have been used to study various types of S vacancies and vacancy clusters in pyrite and assess which S vacancy-related defect could account for the unintentional n-doping observed in experiment. The S mono-vacancy (in any charge state) is found not to generate the experimentally observed behavior, with its primary (neutral) charge state having a very deep donating nature (i.e., too large an activation energy) and high formation energy, although the latter could be overestimated by density functional theory. Additional calculations reveal, however, that a S-S dimer vacancy drives partial reduction of Fe atoms nearest the defect, raising the donor energy level towards the conduction band minimum, in closer agreement with experiment. Importantly, defects such as the S-S dimer vacancy and trans-S di-vacancy also have significant binding energies, driving vacancy clustering. Combining these findings, a S tetra-vacancy cluster was constructed, with S-S dimer vacancies oriented in a trans-fashion across an Fe coordination center. The defect state generated by this tetra-vacancy rises to within 0.41 eV of the conduction band minimum, the best agreement obtained to date with the experimental value of 0.23 eV from recent single crystal work. Calculations based on the binding energy of this defect and known S diffusivities support the idea that significant clustering of S vacancies into defect clusters such as the tetra-vacancy is likely in pyrite FeS_2. This work thus advances S vacancy clusters, rather than simple defects such as mono- or di-vacancies, as the defects potentially responsible for the native n-type doping effects observed in pyrite FeS_2. Based on the discovered trends of increasing binding energy and donor energy level with increasing cluster size, further clustering of S vacancies, past tetra-vacancies, is probable, and is expected to further decrease the donor activation energy, approaching the experimental value. Such defect clusters are expected to be relevant beyond single crystals, in polycrystalline thin films also.

Chapter 4

Effect of 3d Transition Metal Doping on Pyrite (FeS_2)

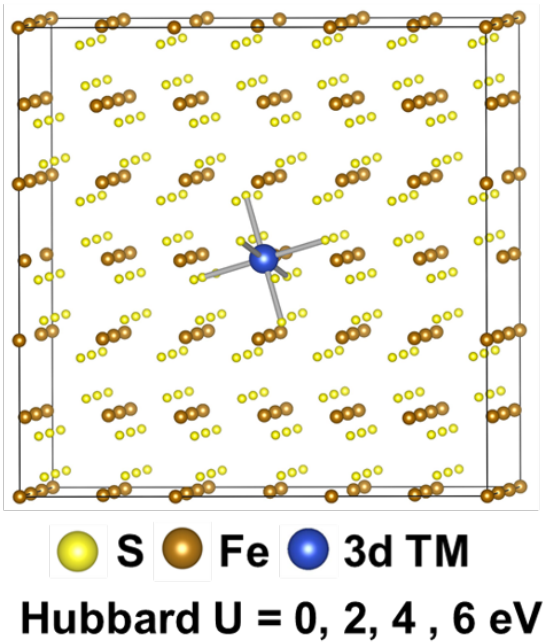

4.1 Introduction

Pyrite (FeS_2) and its use as a potential solar energy materials has been a topic of research for decades. Theoretically pyrite is an ideal solar cell material as it has an ideal semiconductor bandgap of 0.95 eV, [21] strong light absorption ($\alpha \geq 10^5$ cm^{-1} for $h\nu \geq 1.0$ eV), [21] and a favorable minority carrier diffusion length, [114] and it is also made of low cost, non-toxic, earth abundant elements like Fe and S.[19, 20] Despite of all the potentials the photoconversion efficiency of pyrite solar cell never exceeded beyond $\sim$ 3%. [21]

Pyrites' lack of performance as a photovoltaic material is mainly due to poor understanding and control of defects and dopants in it. [21, 22, 23, 24, 25, 26] Recent experimental and computational work from our group has made significant progress in this regard.[22, 118, 159] In our experimental works [22, 118] we showed that both single crystal and unintentionally doped pyrite thin films are n-type in nature and there is a common origin of n-type behavior on them. Historically, origin of this n-type behavior is believed to be due to the presence of S-vacancy related defects that is present in this materials.[21, 25, 116] Recent experimental work by Voigt et al. [118] conclusively proved that S-vacancies are indeed the origin of n-type behavior in this materials. This was further consolidated by the computational work of Ray et al. [159] which showed that complex S-vacancy clusters can be formed kinetically during the crystal growth of pyrite and can be the origin of n-type behavior in pyrite. Both experimental and computational work also revealed that S-vacancies are deep donors in pyrite i.e. has a higher activation energy (i.e. the energy difference between the defect band and conduction band minima).

Although the origin of n-type behavior is mainly due to S-vacancy related defects there can be other possible impurities (such as transition metal (TM) impurities) that can be present in pyrite. In this work, we focused on the effect of 3d TM in their II oxidation state and evaluated their effect on the electronic and electrical properties of Pyrite (FeS_2). The purpose of this study is two fold. First, we would like to understand the how these 3d TM metal dopings affect the electronic properties of FeS_2. Second, Fe is in the middle of the 3d TM series. Thus, our working hypothesis is metals that are on the right side of Fe in the periodic table can dope pyrite as

n-type whereas metals on the left hand side can dope Pyrite as p-type semiconductor. Moreover, finding metals that can dope pyrite p-type can be useful to make p-n homojunction solar cells of pyrite.

Computational modeling of 3d TM doping is not straight forward due to the delocalization errors involved with 3d electrons when treated using density functional theory (DFT). Thus, in this work we used DFT with Hubbard U correction in order to study the effect of 3d TM doping on Pyrite. For the dopant metals various Hubbard U values were tested and the variations of the results were reported as a function of Hubbard values.

4.2 Computational Methods

We started with the crystal structure of Pyrite (FeS_2) and optimized using VASP package.[54, 55, 56, 57] Projected augmented wave (PAW) pseudopotentials [66, 67] and PBE functional [58, 59] with Hubbard U correction[131] was used for all the calculations. Based on our previous studies we used a Hubbard U value of 1.8 eV for Fe 3d electrons. Further, we made a 3×3×3 supercell of FeS_2 and replaced one of the Fe centers with 3d transition metals (Sc, Ti, V, Cr, Mn, Co, Ni, Cu and Zn). We used Hubbard U values of 0, 2, 4 and 6 eV for these 3d transition metals. We used a range of Hubbard U values for various 3d metals in order to get an idea how the DFT results may vary as a function of Hubbard U values used in this calculation (since there is not much experimental data available for the position of dopant state(s) arising from the doping 3d transition metals in pyrite). All the geometry optimizations were performed with energy convergence criteria of 10^{-5} eV and force convergence criteria of -0.02 eV/Å. A planewave energy cut off of 350 eV and Γ-centered 3×3×3 k-point grid was used for geometry optimization and density of state calculations.

4.3 Results and Discussions

4.3.1 Electronic Properties of Pyrite (FeS_2)

The structureal and electronic properties of FeS_2 is discussed in details in Section 3.3.1 of the thesis. In pyrite the Fe(II) centers have electronic configuration of $3d^6$ and they have low spin $t_{2g}^6 e_g^0$) electronic configuration. From density of state (DOS) analysis we found the computed bandgap of pyrite is 0.93 eV which is similar to the previously reported experimental and theoretical bandgaps of FeS_2.[21, 147, 148, 149, 150, 151, 152, 153, 125, 126, 145, 146] Partial density of state (PDOS) analysis revealed (Figure 4.1) that the valence band maxima (VBM) is made of Fe t_{2g} bands whereas the conduction band consists of S 3p tails which is again consistent with previous literature. [154]

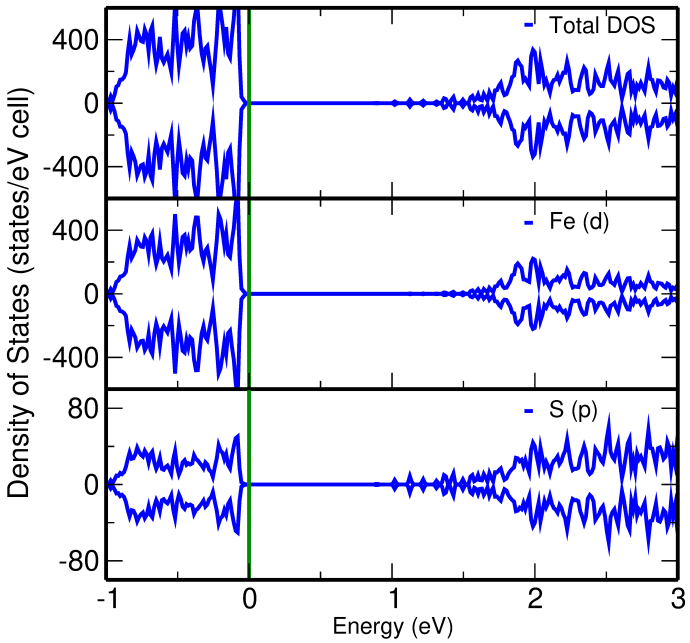

Figure 4.1: Comparison of total density of states and partial density of states of a 3×3×3 supercell of pyrite (FeS_2 computed using PBE+U(=1.8 eV) method. Fermi level is taken as zero.

4.3.2 Effect of Sc Doping

The electronic configuration of Sc(II) is $3d^1$ (i.e. $t_{2g}{}^1e_g{}^0$). Upon doping with Sc(II) we found the 3d electron of Sc completely shifts to the 6 neighboring S atom (oxidizing Sc(II) to Sc(III)), which in turn fills up the empty 3p states of S. This creates an occupied level around 1.11 eV for all the Hubbard the U values (Figure 4.2). These results suggests Sc(II) doping can be an effective n-type dopant. The movement of 3d electron from Sc to neighboring S centers were further confirmed by PDOS analysis as shown in Figure C.1. PDOS analysis shows presence of Sc 3p orbitals near the VBM and Sc 3d orbitals are completely empty.

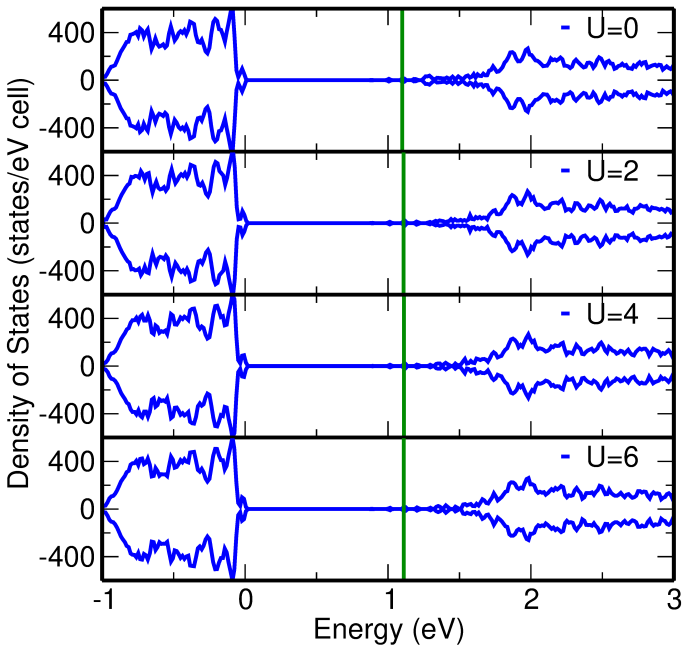

Figure 4.2: Effect of Sc doping on the density of states of pyrite (FeS_2 as a function of Hubbard U value. Energy eigenvalue of the VBM the pyrite is taken as zero.

4.3.3 Effect of Ti Doping

The electronic configuration of Ti(II) is $3d^2$ (i.e. $t_{2g}{}^2e_g{}^0$). Upon doping with Ti(II) we found that the 3d electrons of Ti is localized on Ti centers predominantly (Figure C.2). For U= 0 eV the occupied defect level (Figure 4.3) is located 0.84 eV above the VBM and with increasing U values the position of the occupied defect level moves toward the VBM (i.e. for U =6 eV the

position of the defect band is around 0.07 eV above the VBM). More importantly the defect band arising from the Ti(II) doping is an occupied state and hence Ti(II) will not be able to make p-type FeS_2.

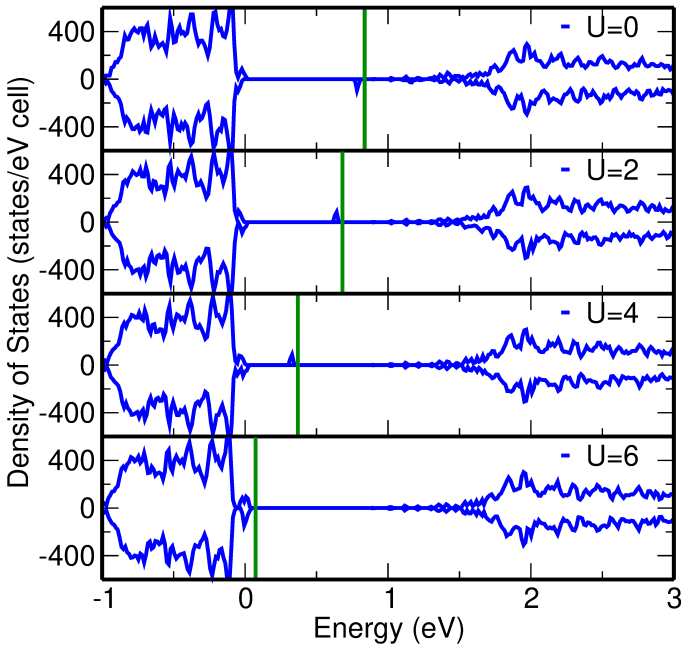

Figure 4.3: Effect of Ti doping on the density of states of pyrite (FeS_2 as a function of Hubbard U value. Energy eigenvalue of the VBM the pyrite is taken as zero.

4.3.4 Effect of V Doping

The electronic configuration of Ti(II) is $3d^3$ (i.e. $t_{2g}{}^3e_g{}^0$). Similar to Ti(II) case we found that the 3d electrons of V is also localized predominantly on the V center (see Figure C.3). The occupied defect level is around 0.56 eV above the VBM for Hubbard U value of 0 eV and it goes down to 0.05 eV above the VBM for Hubbard U value of 6 eV (Figure 4.4). Similar to Ti(II), V(II) also creates an occupied level within the bandgap of FeS_2 which makes it an unsuitable candidate for p-type doping. For each Hubbard U value the occupied defect state arising from Ti(II) is higher in energy from the VBM than that of V(II). This is probably due to the half-filled nature of the t_{2g} electrons in the V(II) compared to the partially filled t_{2g} bands of Ti(II).

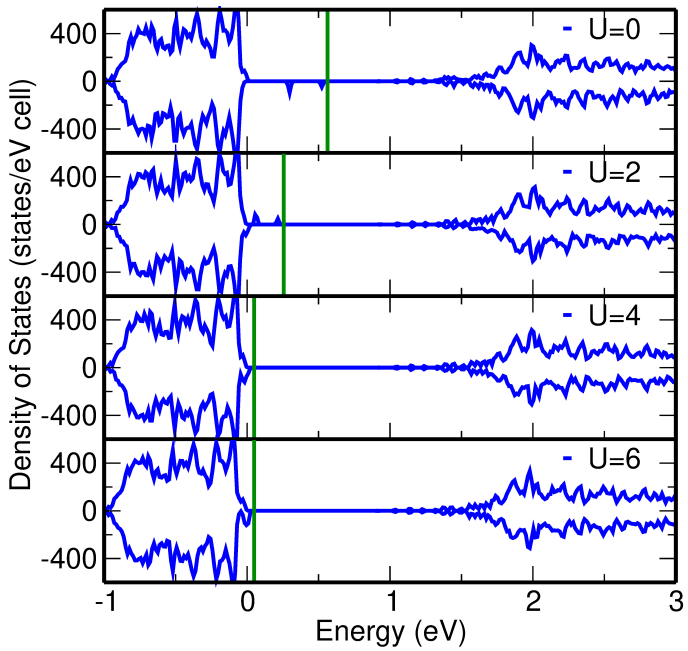

Figure 4.4: Effect of V doping on the density of states of pyrite (FeS_2 as a function of Hubbard U value. Energy eigenvalue of the VBM the pyrite is taken as zero.

4.3.5 Effect of Cr Doping

The electronic configuration of Cr(II) is $3d^4$. Thus, Cr(II) can have two potential spin states namely $t_{2g}^3e_g^1$ (high spin or HS) and $t_{2g}^4e_g^0$ (low spin spin or LS). For U=0 eV we found the $t_{2g}^4e_g^0$ LS state is the ground state. However, for higher U value we found that Cr(II) is partially oxidized to Cr(III) ($t_{2g}^3e_g^0$) and donates the excess electron to the S 3p states (Figure C.4). Interestingly for all the Hubbard U values Cr creates occupied donor states near the conduction band minima (see Figure 4.5). Thus, we believe Cr can be an efficient n-type donor of pyrite.

4.3.6 Effect of Mn Doping

The electronic configuration of Mn(II) is $3d^5$. This gives rise to three potential spin states namely $t_{2g}^3e_g^2$ (high spin or HS), $t_{2g}^4e_g^1$ (intermediate spin or IS), $t_{2g}^5e_g^0$ (low spin or LS). From our calculation we found that at U = 0 and 2 eV the LS Mn(II) center is more stable whereas for U = 4 and 6 eV the HS Mn(II) is the ground state. For U = 0 and 2 eV the position of the defect bands are 0.38 and 0.28 eV above the VBM respectively whereas for U = 4 and 6 eV the

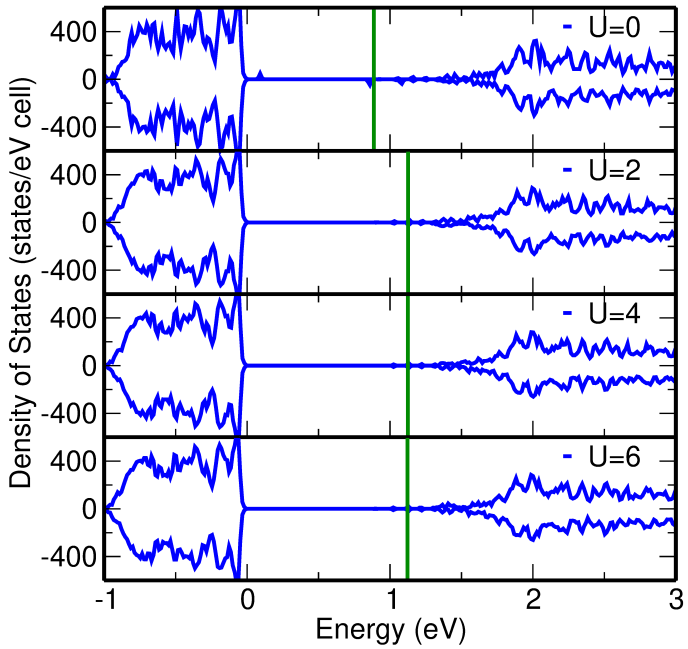

Figure 4.5: Effect of Cr doping on the density of states of pyrite (FeS_2 as a function of Hubbard U value. Energy eigenvalue of the VBM the pyrite is taken as zero.

position of the defect bands are 0.72 and 0.59 eV above the VBM respectively (Figure 4.6). The position of the defect bands are higher for the HS case as in the HS case the electrons are also populating the e_g orbitals of Mn(II). Most importantly for both LS and HS cases the defect bands are occupied irrespective of Hubbard U value this makes Mn(II) an unsuitable p-type dopant for FeS_2. PDOS analysis for Mn doped FeS_2 is shown in Figure C.5.

4.3.7 Effect of Co Doping

The electronic configuration of Co(II) is $3d^7$. This gives rise to two potential spin states namely $t_{2g}^4e_g^3$ (high spin or HS), $t_{2g}^6e_g^1$ (low spin or LS). Experimentally Co is known to be a n-type dopant and the spin state of Co is S=1/2 in the Co doped pyrite.[160] From our calculation we found, that at U=0 and 2 eV the e_g electron of the Co is delocalized over S 3p states. The e_g electron becomes localized on the Co center for U value of 4 eV and makes the LS electronic configuration more stable. For U= 6 eV we found that HS Co electronic configuration becomes more stable.(see Figure 4.7 and Figure C.6) For all the U values Co doping produces occupied

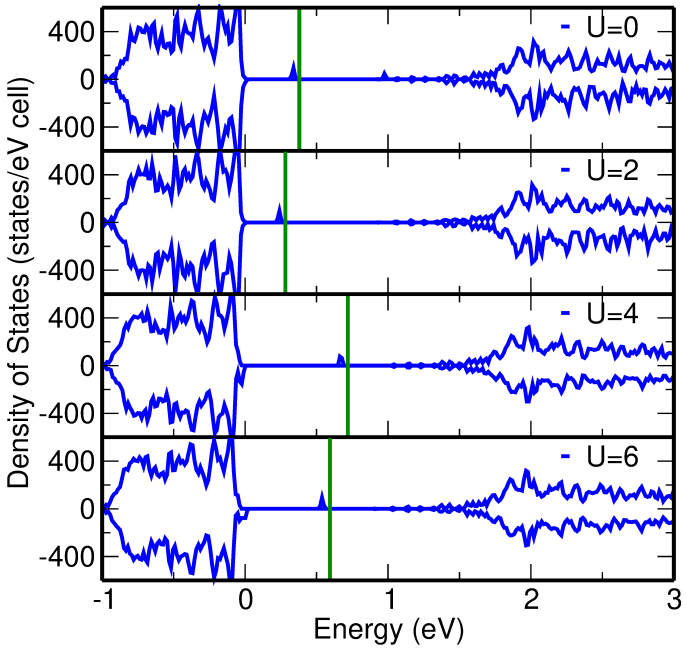

Figure 4.6: Effect of Mn doping on the density of states of pyrite (FeS_2 as a function of Hubbard U value. Energy eigenvalue of the VBM the pyrite is taken as zero.

defect state in the bandgap which makes it a donor type defect. Since, U = 4 eV predicts the spin state of Co center correctly we believe that Co will be an efficient electron donor (n-type dopant) for pyrite.

4.3.8 Effect of Ni Doping

The electronic configuration of Ni(II) is $3d^8$. In the octahedral crystal field Ni(II) has high spin (HS) $t_{2g}^6 e_g^2$ configuration. From our caculation we found that, upon doping with Ni(II) occupied defect states are created within the bandgap of FeS_2. The position of the defect state is around 0.87 eV higher than the VBM for Hubbard U value of 0 eV and becomes closer to the VBM as a function of increasing Hubbard U value (Figure 4.8 and Figure C.7) on the Ni center (the occupied defect level is around 0.45 eV above the VBM for U= 6 eV). It should be noted that defect states are occupied irrespective of Hubbard U value which is not surprising as Ni has two excess electrons compared to Fe and hence Ni doping is expected to make FeS_2 n-type. However, the efficiency of n-type doping with Ni is poor compared to that of Co which has one

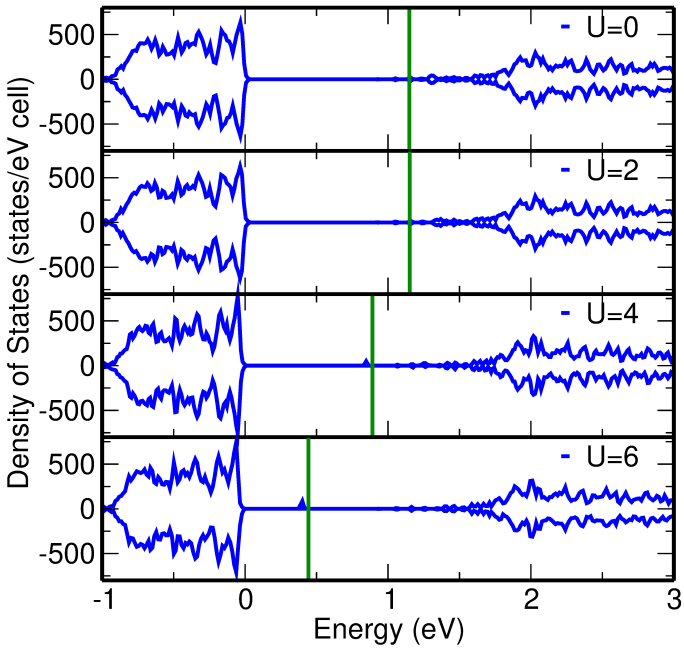

Figure 4.7: Effect of Co doping on the density of states of pyrite (FeS_2 as a function of Hubbard U value. Energy eigenvalue of the VBM the pyrite is taken as zero.

less electron than Ni. This is due to lack of hybridization between the Ni 3d bands and S 3p states.

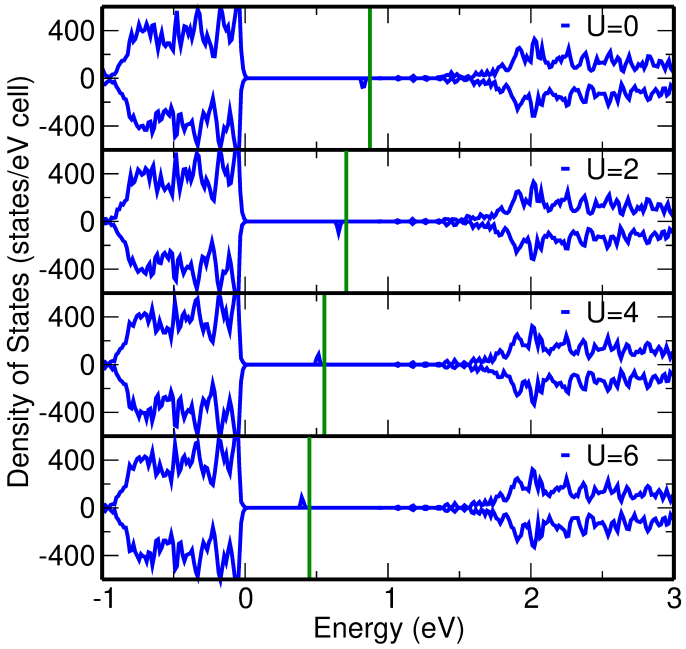

Figure 4.8: Effect of Ni doping on the density of states of pyrite (FeS_2 as a function of Hubbard U value. Energy eigenvalue of the VBM the pyrite is taken as zero.

4.3.9 Effect of Cu Doping

The electronic configuration of Cu(II) is $3d^9$ (i.e. $t_{2g}{}^6e_g{}^3$). From our calculation we found for all the U values Cu doping creates an occupied defect state near the CBM of pyrite (see Figure 4.9). PDOS analysis show that the occupied defect bands have dominant Cu 3d character (Figure C.8).The position of the defect band is around 0.82 eV above the VBM for U= 0 eV and it gradually decreases to 0.69 eV above the VBM for U = 6 eV.

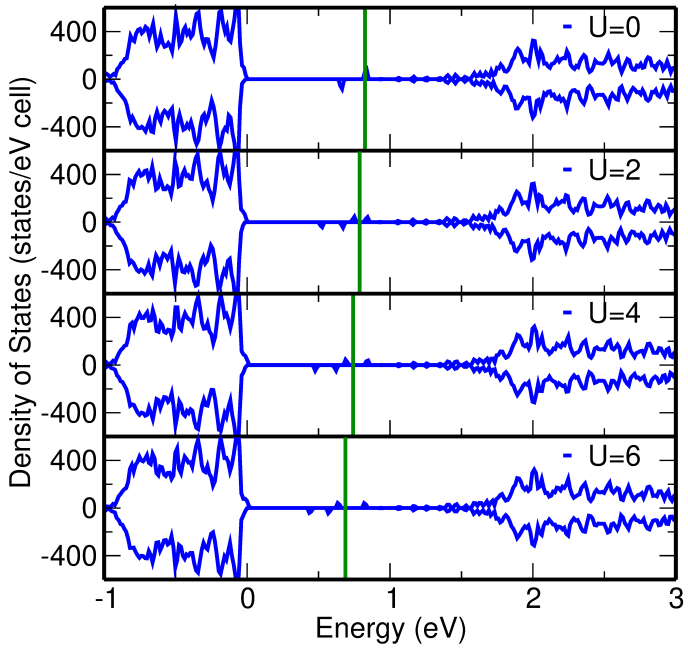

Figure 4.9: Effect of Cu doping on the density of states of pyrite (FeS_2 as a function of Hubbard U value. Energy eigenvalue of the VBM the pyrite is taken as zero.

4.3.10 Effect of Zn Doping

Upon doping with Zn(II) we observe that an occupied defect level appears above 0.32 eV of the VBM irrespective of the Hubbard U value we choose (see Figure 4.10). Further PDOS analysis suggests that this occupied defect state arises from filled Zn centers (Figure C.9). Since the occupied defect states are around far away from the CBM we believe Zn cannot dope pyrite n-type or p-type efficiently.

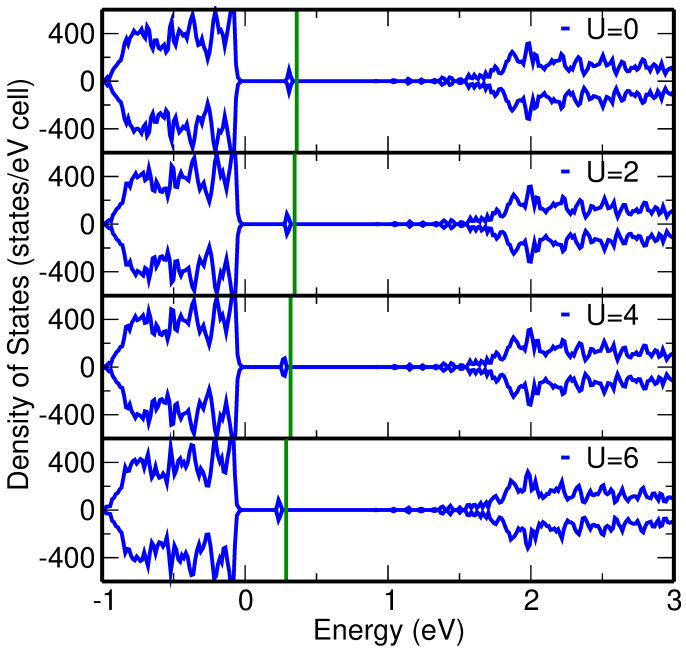

Figure 4.10: Effect of Zn doping on the density of states of pyrite (FeS_2 as a function of Hubbard U value. Energy eigenvalue of the VBM the pyrite is taken as zero.

4.4 Conclusion

In conclusion, in this work we studied the effect of 3d transition metal doping on pyrite using density functional theory. Our study shows metals that are on the right side of Fe in the periodic table can dope pyrite n-type efficiently (except Zn). However, none of the metals on the left hand side of Fe in the periodic table can dope pyrite p-type. In fact, Sc and Cr can be potential n-type donor of pyrite.

Chapter 5

Tuning the Conductivity of Hexa- Zirconium(IV) Metal-Organic Frameworks by Encapsulating Heterofullerenes

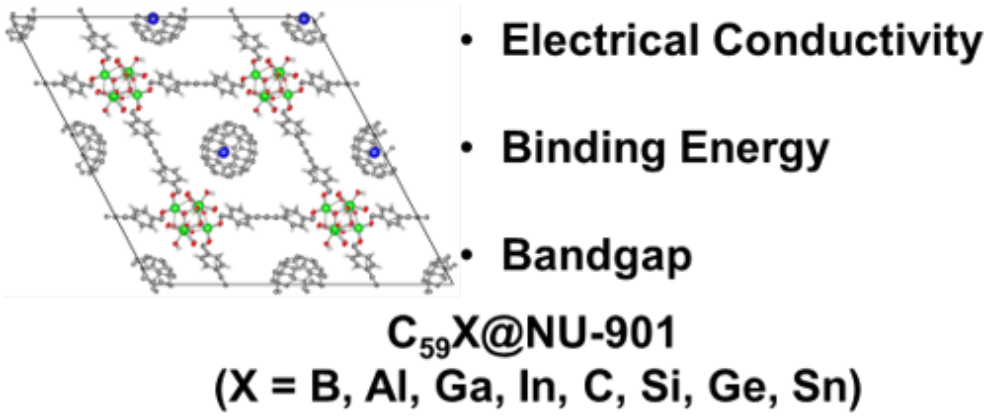

Reproduced with permission from the acticle by Debmalya Ray,Subhadip Goswami, Jiaxin Duan, Joseph T. Hupp, Christopher J. Cramer and Laura Gagliardi *Chem. Mater.* 2021, 33, 4, 1182–1189.

5.1 Introduction

Metal-organic frameworks (MOFs) are porous crystalline materials formed by precise combinations of metal ions/metal-oxide nodes and organic linkers that are employed in various fields such as gas storage and release,[161, 162] chemical separations,[163, 164, 165] catalysis,[166, 167, 168, 169, 170] drug delivery,[171] chemical sensors,[172] energy transfer[173, 174, 175] and solar fuel production.[176, 177, 178] Electrical conductivity in MOFs has attracted the attention for potential applications in field-effect transistors,[179] batteries,[180] chemiresistive sensors,[181] electrochromic devices[182, 183] and supercapacitors.[184, 185] In general the majority of the MOFs comprises redox-inactive metal nodes and organic linkers being responsible for poor conductivity. However, some recent progress towards electrical conductivity in MOFs[186, 187, 188, 189] makes it an open topic of research.

Electrical conductivity in MOFs can be achieved in several ways,[190] such as judicious choice of redox-active linkers,[191, 192, 193, 194, 195] mixed-valence metal nodes,[196, 197, 198] π-stacking of organic linkers within the MOF framework,[199] formation of MOFs as 2D conjugated compounds,[200] and by engineering frontier orbital energies of the metal ions and organic linkers.[201]

The free pore space in the MOF enables an alternate route for tuning the electrical conductivity via the incorporation of guest molecules which can act as electron acceptors or electron donors facilitating host-guest type charge-transfer (CT) interaction within the MOF framework. For example, Talin et al.[189] introduced electron accepting tetracyanoquinodimethane (TCNQ) in the HKUST-1 MOF and observed six orders of magnitude (i.e. from 10^{-8} S/cm to 0.07 S/cm) enhancement in electrical conductivity compared to the host MOF. Recently, Kung et al.[188] showed that nickel(IV) bis(dicarbollide) (NiCB) can be easily incorporated in the triangular pore of NU-1000 giving rise to electrical conductivity of 2.7×10^{-7} S/cm (compared to the electrical conductivity of 9.1×10^{-12} S/cm for the NU-1000 MOF).

The introduction of fullerene C_{60}[202] in MOFs has also been previously reported.[203, 204, 205, 206, 207, 208] Unlike most MOFs, C_{60} is a semiconducting material; it has a variety of

applications ranging from molecular optoelectronics to biomedical devices, due to its exceptional electrochemical and photophysical properties.[209, 210] A basic understanding of electron donor acceptor CT in C_{60} is critical in the field of organic photovoltaics.[210] In our previous study we showed that the incorporation of C_{60} enhances the electrical conductivity (i.e. from 10^{-14} S/cm to 10^{-3} S/cm) of Zr(IV) based MOFs such as NU-901, which is an insulator.[27] The electron transfer happens between the 1,3,6,8-tetrakis(p-benzoate)pyrene ($TBAPy^{4-}$) linkers (they act as electron donors) of the MOF and the guest C_{60} molecule (it acts as an electron acceptor), which in turn gives rise to electrical conductivity in MOFs. Recently a study by Souto et al.[206] showed that the electrical conductivity of MUV-2 MOF can be increased by two orders of magnitude (i.e. from 3.7×10^{-11} S/cm to 4.7×10^{-9} S/cm) upon incorporation of C_{60}. A theoretical study by Pratik et al.[207] showed that the electrical conductivity of porphyrin-based MOFs can also be enhanced upon incorporation of C_{60}.

Like for other semiconducting materials, the electronic properties of fullerene (C_{60}) can be modulated by introducing one or more heteroatoms in the fullerene structure. These compounds are known as heterofullerenes[211, 212, 213, 214, 215] and have distinct electronic properties compared to their all-carbon analogues.[216] Boron and nitrogen are the preferred elements for making heterofullerenes due to the similar size and electronegativity to carbon.[216] Several other heterofullerenes have been made experimentally.[213, 214, 215, 216, 217, 218, 219]

NU-901, a Zr(IV) based MOF, consists of $Zr_6(\mu_3\text{-}O)_4(\mu_3\text{-}OH)_4(H_2O)_4(OH)_4$ metal nodes and tetratopic $TBAPy^{4-}$ linkers in scu topology. The diamond pore of NU-901 is suitable to host C_{60} due to appropriate size matching. This in turn facilitates the CT from electronic rich linkers of NU-901 MOF to the electron deficient host molecules such as C_{60}.

In this study, we explored the effect of fullerene and heterofullerene encapsulation on the electronic properties of the NU-901 MOF using density functional theory. We investigated the probability of formation of heterofullerenes as well as their binding energy to NU-901. Our findings suggest that $C_{59}B$, $C_{59}Sn$ and $C_{59}Ge$ can further improve the electrical conductivity of NU-901 compared to C_{60}.

5.2 Computational Methods

We started from the crystal structure of NU-901 as reported by Liu et al.[220] and incorporated C_{60} as shown in the Figure 5.1. Periodic density functional theory (DFT) geometry optimizations of NU-901 with and without $C_{59}X$ (X = B, Al, Ga, In, C, Si, Ge, Sn) were performed using the Vienna Ab Initio Simulation Package (VASP/5.3.5).[54, 55, 56, 57] The structural relaxation was performed by sampling the Brillouin zone over a 2 ×2×2 k-point grid centered at the Γ point. The geometries of fullerene, heterofullerene, corannulene and heterocorannulene was optimized by the putting the molecules in a 25 Å cubic box and Γ point only sampling. The PBE[58, 59] exchange correlation functional along with Becky-Johnson dispersion (D3-BJ)[60, 221] correction was employed for all the geometry optimizations. Further single-point HSE06[63, 64, 65] calculations were performed to determine the bandgap and density of states (DOS) of the systems under consideration at the PBE-D3-BJ optimized geometry. The projected augmented wave (PAW) [66, 67] potentials were used to describe the interactions between the core and the valence electrons. A plane-wave kinetic energy cutoff of 520 eV was used for all the calculations. An energy convergence criterion of 10^{-5} eV was used in the geometry optimization. The atomic positions were relaxed until the forces were less than 0.02 eV/Å.

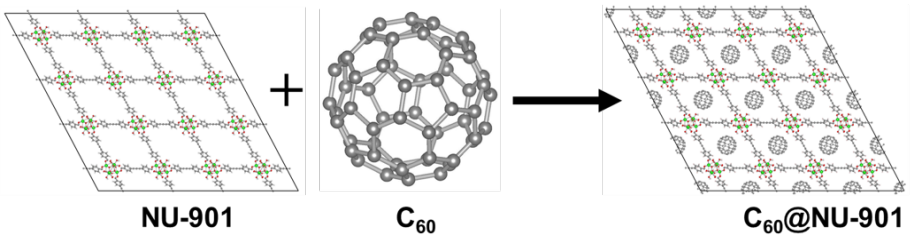

Figure 5.1: Schematic representation of C_{60} encapsulation in NU-901. Color code: Zr (green), O (red), C (grey), H (white).

Linker-linker and linker-fullerne charge-transfer integrals are computed using the ADF2016 [222, 223, 224] software package and the M06-2X [225] functional. In the literature Patwardhan et al.[226] also used M06-2X functional to compute charge transfer integrals between linkers of the NU-901 MOF. The TZP polarization basis sets were used for all the calculations.

The binding energy ($\Delta E_{binding}$) of $C_{59}X$ to NU-901 was calculated using the following equation:

$$\Delta E_{binding} = E\left(C_{59}X@NU-901\right) - E\left(NU-901\right) - E\left(C_{59}X\right) \tag{5.1}$$

where, E($C_{59}X$@NU-901), E(NU-901) and E($C_{59}X$) are the electronic energies of $C_{59}X$@NU-901, NU-901 and $C_{59}X$ respectively. In principle one could use the zero-point energy corrected energies, but this is not the case in this study because the calculation of vibrational frequencies are very expensive in periodic calculations.

In donor-acceptor type MOF conductivity, the electrical conductivity scales as the square-root of the product of the numbers of positive and negative charge carriers, i.e. (holes × electrons)1/2 and with their mobilities.[227] The number of charge carriers is directly proportional to $exp\left(-\frac{E_{DA}}{2K_BT}\right)$, where E_{DA} is the energy gap between an acceptor-derived conduction band and a donor-derived valence band and can be measured by electronic absorption spectroscopy.[227] From DFT calculations E_{DA} can be estimated as the difference of energy eigenvalue of donor state ($i.e.$ energy of the highest occupied crystalline orbitals) and acceptor state (i.e. energy of the lowest unoccupied crystalline orbitals), i.e., the bandgap (E_g) of the system. K_B is the Boltzmann constant and T is the temperature at which the experiment is performed. Thus, the relative conductivity of $\frac{C_{59}X@NU-901}{C_{60}@NU-901}$ can be obtained as follows:

$$\frac{\sigma_{C_{59}X@NU-901}}{\sigma_{C_{60}@NU-901}} = exp\left(\frac{E_g(C_{60}@NU-901) - E_g(C_{59}X@NU-901)}{2K_BT}\right) \tag{5.2}$$

where, $\sigma_{C_{59}X@NU-901}$ is the electrical conductivity of $C_{59}X$@NU-901 and $\sigma_{C_{60}@NU-901}$ is the electrical conductivity of C_{60}@NU-901.

The formation energies ($\Delta E_{\text{formation}}$) of the heterofullerenes were calculated using the PBE-D3-BJ functional electronic energies as computed from the periodic calculations. The following reaction was used to compute the formation energy of $C_{59}X$ similar to that presented by Bai et al.[228] (see Figure D.1).

$$\Delta E_{formation} = E\left(C_{59}X\right) + E\left(corannulene\right) - E\left(C_{60}\right) - E\left(corannulene-X\right) \tag{5.3}$$

Where, $E(C_{59}X)$, $E(corannulene)$, $E(C_{60})$ and $E(corannulene-X)$ are the electronic energies of $C_{59}X$, corannulene, C_{60} and corannulene-X respectively. Corannulene is an aromatic

compound with chemical formula $C_{20}H_{10}$ and can be considered as a building block of C_{60}. Thus, we used corannulene and corannulene-X (i.e. heterocorannulene) to compute the formation energy of heterofullerenes.

5.3 Results and Discussions

5.3.1 Structural and Electronic Properties of Pristine NU-901 and NU-901 with C_{60}

The lattice parameters of the optimized NU-901 structure using PBE-D3-BJ agrees well with the previously reported computational[220] and experimental[183] lattice parameters of NU-901 as shown in Table D.1. This suggests that PBE-D3-BJ can describe the structural properties of NU-901 accurately. We then computed the electronic properties of NU-901 (as shown in Figure 5.2). The computed bandgap of NU-901 using HSE06 functional is 2.62 eV, which agrees well with the experimental bandgap of 2.53 eV.[27] Partial DOS (PDOS) analysis reveals that both the valence band maxima (VBM) and conduction band minima (CBM) arise from the linker C and O p orbitals. There is no hybridization between the node and linker orbitals. Thus, in pristine NU-901 CT happens from linker π orbitals to linker π^* orbitals. This is similar to what has been reported in the literature for NU-901.[27, 226] We also investigated the favorable charge-transfer pathways in pristine NU-901 MOF (see Figure D.2). Similar to Patwardhan et al.,[226] we also found that charge transfer between linkers happens along the ab plane and also along the c-direction of the MOF. Along the ab plane the charge transfer happens faster between the linkers when the angle between them is acute ($a + b$ direction, shown in blue in Figure D.2(a)) and happens slower when the angle between the linkers is obtuse ($a - b$ direction, shown in green in Figure D.2(a)). Hole-transfer integral values along the c-direction (shown in red in Figure D.2(b)) are similar to those along the $a + b$ direction. The values of hole-transfer integrals along different directions are summarized in Table D.2.

We then incorporated the C_{60} molecule inside NU-901. There are two possible ways in which C_{60} can be incorporated in NU-901 which we refer to C_{60}@NU-901 (ST) (stacked) and

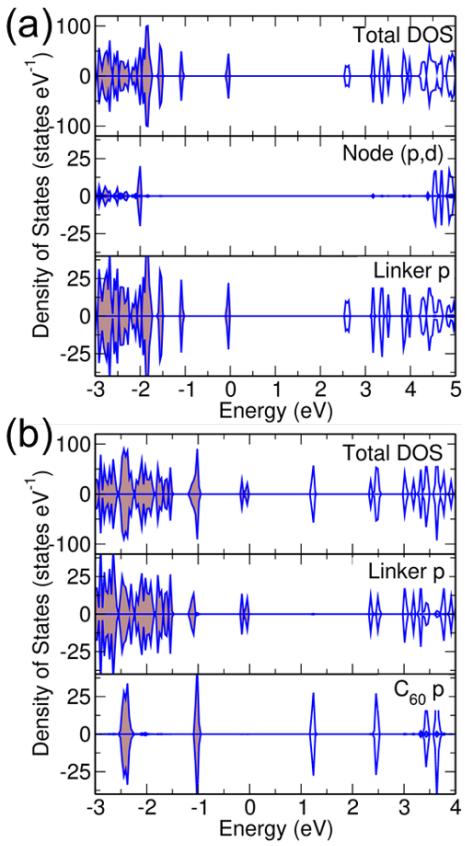

Figure 5.2: Total DOS and projected DOS of (a) NU-901 and (b) C_{60}@NU-901 (ST) computed using the HSE06 functional. The valence band maxima are shifted to zero.

C_{60}@NU-901 (NST) (non-stacked) as shown in Figure 5.3. In the C_{60}@NU-901 (ST) structure the fullerene molecule is directly stacked with the pyrene ring of the $TBAPy^{4-}$ organic linker of the NU-901 MOF whereas in the C_{60}@NU-901 (NST) structure the fullerene molecule in the NU-901 pore is not directly stacked with the electron rich pyrene ring of the $TBAPy^{4-}$ linker. Similar geometric conformations for the C_{60}@NU-901 host-guest system using PBE-D3-BJ functionals are reported in literature by Goswami et al.[27] In this work we also computed the binding energy of C_{60} in both stacked and non-stacked conformation as discussed in the following paragraph.

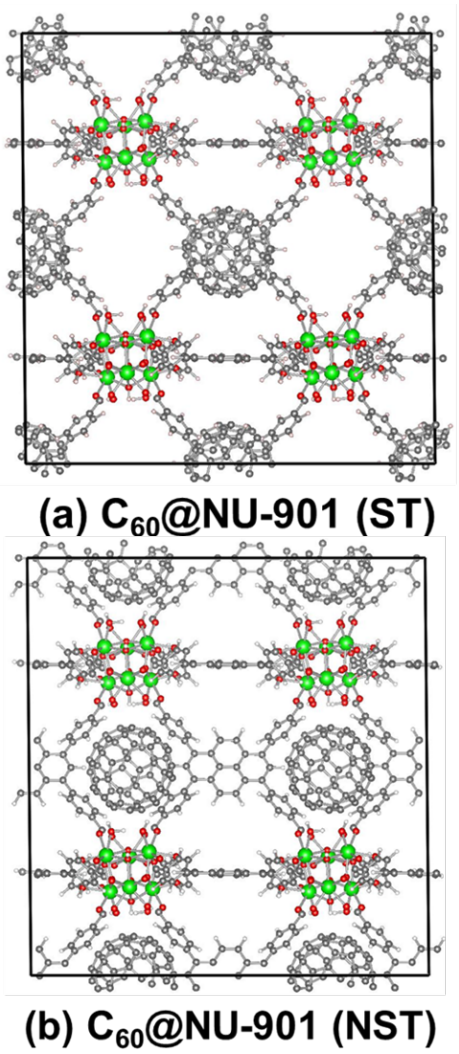

Figure 5.3: Structure of (a) C_{60} stacked with organic linker (C_{60}@NU-901 (ST)) and (b) C_{60} non-stacked with organic linker (C_{60}@NU-901 (NST)) along the crystallographic b-direction. Color code: Zr (green), O (red), C (grey), H (white).

Our calculation showed that C_{60}@NU-901 (ST) is energetically more favorable by 19.7 kcal/mol compared to C_{60}@NU-901 (NST). However, in the case of C_{60}@NU-901 (ST) we observed a distortion in the lattice of NU-901 compared to the pristine MOF. This distortion in the lattice parameters is perhaps unsurprising given the strong CT interaction between 1,3,6,8-tetrakis(p-benzoate)pyrene($TBAPy^{4-}$) organic linkers with C_{60} in the stacked configuration. Moreover, in our calculation we considered 1:1 loading of NU-901 and C_{60} whereas experimentally only 60% of the diamond pores of NU-901 are filled up with C_{60}. In the pristine NU-901 the distance between two parallel linkers in the diamond pore is 19 Å, whereas the diameter of C_{60} molecule is 7 Å. Thus, when C_{60} is incorporated in the center of the diamond pore of undistorted NU-901(i.e. in the initial structure before geometry optimization) the distances between the electron donating $TBAPy^{4-}$ linker and electron accepting fullerene (C_{60}) are 6 Å, a value that is not favorable for charge transfer (CT). In order to have electron hopping between the organic linker and C_{60}, the CT distance has to be between 2.5 Å and 3.5 Å. In the C_{60}@NU-901 (ST) structure (after geometry optimization) we indeed observe a 3.4 Å distance between the $TBAPy^{4-}$ linker and C_{60} (Figure D.3). This distortion in the structure of the NU-901 MOF in the presence of fullerene happens due to the strong $\pi - \pi^{\star}$ interaction between the $TBAPy^{4-}$ linker and C_{60}. This strong interaction is absent in C_{60}@NU-901 (NST), which explains the lower stability of C_{60}@NU-901 (NST) compared to C_{60}@NU-901 (ST). Hole-transfer integrals between the linkers and fullerene are reported in Table D.2.

We computed the binding energy of C_{60} with NU-901 in both C_{60}@NU-901 (ST) and C_{60}@NU-901 (NST) configurations using equation (5.1). The binding energy for the stacked and non-stacked conformations are -35.1 and -15.4 kcal/mol, respectively. This suggests that there is a strong driving force for C_{60} to be incorporated in the NU-901 diamond pore especially in the stacked conformation.

The HSE06 bandgaps of C_{60}@NU-901 (ST) (Figure 5.2) and C_{60}@NU-901 (NST) are 1.27 eV and 1.56 eV respectively, to be compared to the bandgap of 2.62 eV pristine NU-901. Experimentally upon encapsulation of C_{60} the bandgap decreased from 2.53 eV to 1.77 eV.[27] This reduction of bandgap qualitatively agrees also with previously reported calculations[27]

performed using the PBE-D3 functional and can explain the eleven orders of increase in magnitude of electrical conductivity of fullerene incorporated NU-901 compared to that of pristine NU-901 (using equation (5.2)). The difference in bandgap between the C_{60}@NU-901 (ST) and C_{60}@NU-901 (NST) structures of 0.29 eV is due to the strong interaction of C_{60} in the stacked structure with the electron-donating $TBAPy^{4-}$ linker.

The DOS analysis shows that the VBM in C_{60}@NU-901 (both ST and NST) arises from the linker π orbitals, while the CBM from the C_{60} π^* orbitals. This is expected due to the electron accepting nature of C_{60} and the electron donating nature of the $TBAPy^{4-}$ linker. Thus, incorporation of C_{60} favors CT in NU-901. Moreover, the large decrease in bandgap upon incorporation of C_{60} enhances the probability of direct charge transfer from linker to C_{60} orbitals.

5.3.2 Electronic Properties of $C_{59}X$@NU-901(X = B, Al, Ga, In, Si, Ge, Sn)

Motivated by the fact that C_{60} enhances the electrical conductivity of NU-901, we incorporated heterofullerenes ($C_{59}X$, X = B, Al, Ga, In, Si, Ge, In) in NU-901 by considering two possible stacked conformations as shown in Figure 5.4. In the first conformation the heteroatom (X) is closer to the $TBAPy^{4-}$ linker ($C_{59}X$@NU-901 conformation 1), whereas in second conformation the heteroatom (X) is towards the c-direction of the NU-901 ($C_{59}X$@NU-901 conformation 2). We also incorporated the $C_{59}X$ in non-stacked conformation ($C_{59}X$@NU-901 (NST)) and found that, similarly to the C_{60} case, the non-stacked structure is less stable compared to the stacked conformations of $C_{59}X$. We computed the relative stability of all the conformations and reported it in Table D.3. Except for Al and In, in all the other cases both conformations are very close in energy. For Al and In, the heteroatom in conformation 2 interacts strongly with the terminal OH and H_2O group attached to the Zr_6 node of NU-901. However, the electronic properties of both conformations are similar and thus we report the DOS of conformation 2 only (as in general this conformation is slightly more stable from our calculation) in the main manuscript and DOS of conformation 1 in the Figure D.4-D.10.

Among the four group-V heterofullerenes ($C_{59}B$, $C_{59}Al$, $C_{59}Ga$, $C_{59}In$), $C_{59}B$ is known

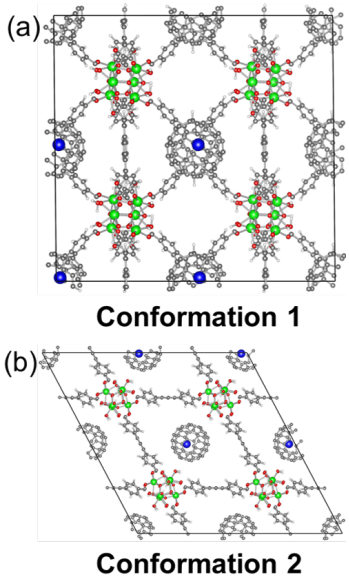

Figure 5.4: Represents two possible conformations in which $C_{59}X$ can be incorporated in the NU-901 structure in stacked conformation. (a) Heteroatom of $C_{59}X$ is near the $TBAPy^{4-}$ organic linker and (b) Heteroatom of $C_{59}X$ is pointing towards the c-direction. Color code: Zr (green), O (red), C (grey), H (white), heteroatom X (blue).

experimentally. Since group-V elements have one less electron compared to carbon (i.e. a hole), the corresponding heterofullerenes are expected to be more electron deficient compared to C_{60}. From our calculations we observed that only $C_{59}B$ reduces the bandgap drastically by 1 eV compared to C_{60}@NU-901 stacked. The densities of states of $C_{59}X$@NU-901 (X = B, Al, Ga, In) are shown in Figure 5.5.

In the case of $C_{59}B$@NU-901 the unoccupied state is only 0.2 eV above the VBM. Thus, we believe that the introduction of $C_{59}B$ in the NU-901 enhances the electrical conductivity by several orders of magnitudes compared to C_{60}@NU-901 (ST) and C_{60}@NU-901 (NST). Moreover, the unoccupied state $C_{59}X$@NU-901 is highly spin-polarized compared to C_{60}@NU-901 (ST/NST) because one electron is missing. Hence these $C_{59}X$@NU-901 systems can have possible applications in the field of spintronics. Interestingly for Al, Ga and In the unoccupied state (arising from the heteroatom) remains in the same position as that of C_{60}@NU-901 (ST). This is possibly due to poor overlap of Al, Ga and In, 3p, 4p and 5p orbitals, respectively, with the linker 2p orbitals and C 2p orbitals of $C_{59}X$. We also noticed that in these three cases the VBM

does not arise from the linker 2p orbitals, but from the $C_{59}X$ p-orbitals. On the other hand, for $C_{59}B$@NU-901 the VBM still arises from linker 2p orbitals. The $C_{59}B$ 2p orbitals are lower in energy than the linker 2p orbitals and hence CT can take place from the linker 2p orbital to $C_{59}B$ empty 2p* orbital. Since in the cases of Al, Ga and In the VBM arises from the $C_{59}X$ (X= Al, Ga, In) moiety, CT cannot take place between the linker 2p orbital to the 3p*, 4p* and 5p* orbitals of Al, Ga and In respectively. This lack of CT in turn explains the lack of decreasing bandgap in $C_{59}X$@NU-901 when X is Al, Ga and In.

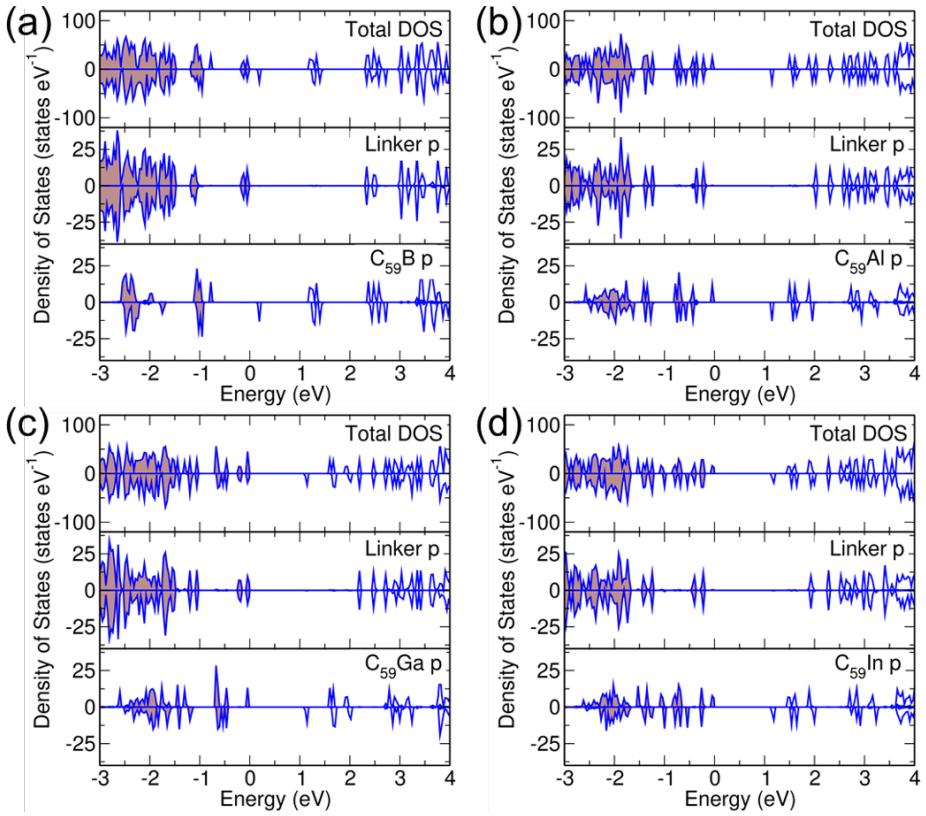

Figure 5.5: Total DOS and projected DOS on linker and $C_{59}X$ of (a) $C_{59}B$@NU-901, (b) $C_{59}Al$@NU-901, (c) $C_{59}Ga$@NU-901, and (d) $C_{59}In$@NU-901 conformation 2 computed using HSE06 functional. Valence band maxima is shifted to zero.

Group-VI elements have the same valence electronic configuration as carbon. However, going down along the group, the electronegativity of the element decreases, which in turn lowers the energy of the CBM or lowest unoccupied crystalline orbital. Thus, upon doping with Si, Ge and Sn, we observed that for $C_{59}Si$ the empty state remains similar to that of C_{60}@NU-901 (ST).

However, for $C_{59}Ge$ and $C_{59}Sn$ the bandgap decreases by 0.41 and 0.51 eV, respectively. These results suggest that doping with $C_{59}Ge$ and $C_{59}Sn$ will enhance the electrical conductivity of NU-901 MOF. The DOS of $C_{59}X$@NU-901 (X = Si, Ge and Sn) are reported in Figure 5.6.

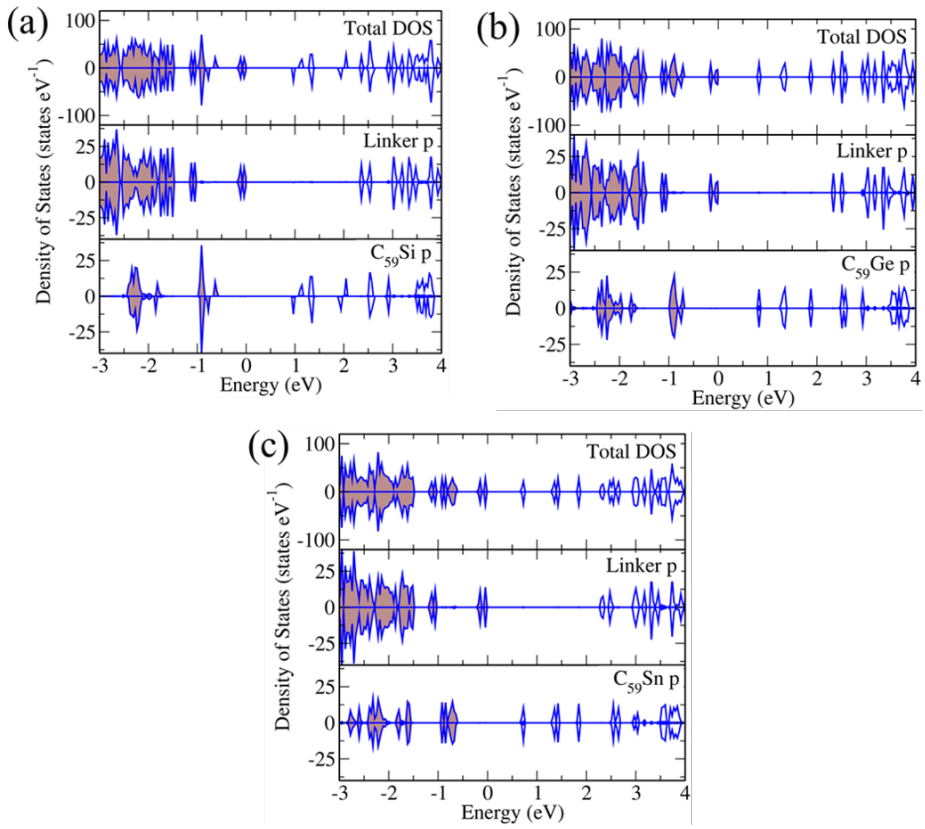

Figure 5.6: Total DOS and projected DOS on linker and $C_{59}X$ of (a) $C_{59}Si$@NU-901, (b) $C_{59}Ge$@NU-901, and (c) $C_{59}Sn$@NU-901 conformation 2 computed using HSE06 functional. Valence band maxima is shifted to zero.

5.3.3 Relative Electrical Conductivity of C_{60}@NU-901 and C_{59}X@NU-901 (X = B, Al, Ga, In. C, Si, Ge, Sn)

We estimated the electrical conductivity of C_{59}X@NU-901 relative to that of C_{60}@NU-901 (ST) using equation 5.2 and reported it in Table 5.1.

Table 5.1: Comparison of bandgap (eV) and relative conductivity (at T = 298 K) of conformation 1 and conformation 2 of C_{59}X@Nu-901 w.r.t C_{60}@NU-901 (ST) using the HSE06 functional.

C_{59}X	Conformation 1		Conformation 2	
	E_g (eV)	Relative Conductivity	E_g (eV)	Relative Conductivity
C_{60}	1.27	1	-	-
C_{59}B	0.21	1×10^{9}	0.22	8×10^{8}
C_{59}Al	1.15	11	1.18	6
C_{59}Ga	1.15	12	1.16	9
C_{59}In	1.21	4	1.20	4
C_{59}Si	1.34	3×10^{-1}	1.16	10
C_{59}Ge	0.86	3×10^{3}	0.86	3×10^{3}
C_{59}Sn	0.65	2×10^{5}	0.75	2×10^{4}

The introduction of C_{60} enhances the electrical conductivity by 10^{11} times as reported in the experimental literature.[27] This eleven-order increase in electrical conductivity can be explained using equation 5.2. However, the relative electrical conductivity not only depends on the donor-acceptor gap (E_g), but also depends on the mobility of the samples. Since the mobility of NU-901 and fullerene/heterofullerene incorporated NU-901 can be different we decided not to use the electrical conductivity of pristine NU-901 as our reference. Different heterofullernes have different acceptor levels. Thus, upon incorporation of heterofullerenes on NU-901 the C_{59}X@NU-901 systems have different bandgap (Table 5.1). This gives rise to different electrical conductivity (using equation 5.2). Our study shows that heterofullerenes can enhance the electrical conductivity by 10^9 times. As expected from the smallest bandgaps, C_{59}B will enhance the electrical conductivity of NU-901 the most.

5.3.4 Binding Energy and Formation Energy of Heterofullerenes

Similar to the C_{60} case, we also calculated the binding energy of $C_{59}X$ for both conformations. Interestingly all of the heterofullerenes strongly bind to NU-901 compared to fullerene itself as shown in Table 5.2. This suggests these heterofullerenes can easily be incorporated in the NU-901 structure.

Further, the formation energies of heterofullerenes, computed using equation 5.3, are reported in Table D.4. Our calculated formation energies are negative for all the cases except for $C_{59}In$ suggesting the instability of $C_{59}In$ to form in the gas phase. This is due to the large size of In compared to other Group V heteroatoms.

Table 5.2: Binding energy (kcal/mol) of conformation 1 and conformation 2 of $C_{59}X$@NU-901 using the PBE-D3-BJ functional computed using equation 5.1.

$C_{59}X$	C_{60}	$C_{59}B$	$C_{59}Al$	$C_{59}Ga$	$C_{59}In$	$C_{59}Si$	$C_{59}Ge$	$C_{59}Sn$
Conformation 1	-35.1	-35.8	-62.3	-58.7	-62.5	-47.6	-36.3	-42.9
Conformation 2	-35.1	-36.4	-92.3	-62.9	-83.8	-38.3	-36.7	-38.3

5.4 Conclusion

We investigated the effect of fullerene- and heterofullerene-doping on the structural and electronic properties of NU-901 by using density functional theory. Our study confirms that introducing C_{60} enhances the electrical conductivity of NU-901 by means of donor-acceptor charge transfer between the organic linker and fullerene. We further showed that the electrical conductivity of NU-901 can be tuned by introducing heteroatoms such as B, Sn and Ge in the C_{60} structure. The negative binding energies of NU-901 and $C_{59}X$ (X = B, Al, Ga, In. C, Si, Ge, Sn) complexes also suggest that heterofullerenes can be easily incorporated in the NU-901 framework. This study will guide subsequent experimental studies to design metal organic frameworks with enhanced electrical conductivity.

Chapter 6

Theoretical Investigation of Single-molecule Magnet Behaviour in Mononuclear Dysprosium and Californium Complexes

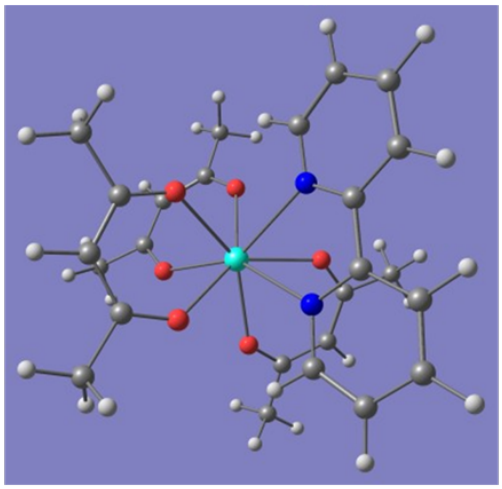

Magnetic Susceptibility, g- Tensor
Blocking Barrier

6.1 Introduction

Single-molecule magnets (SMMs) characteristically exhibit magnetic hysteresis, a process in which a material becomes magnetized through exposure to a magnetic field and slowly relaxes upon removal of the field.[229] SMMs can favour magnetization in one of two states depending on the direction of the magnetic field, resulting in a magnetic bistability. The effective magnetic relaxation energy barrier, U_{eff}, which separates these two states, scales with the total spin, *S*, and size of anisotropy, *D*.[230] Early SMMs composed of polynuclear transition metal clusters to maximize *S* but magnetic hysteresis was observed at only very low temperatures (4 K).[231, 232, 233]

In the case of transition metals, the ligand-field effect dominates in the splitting of the ground and excited states, therefore the nature of the magnetic bistability is defined by spin substates, m_s. For lanthanides, spin-orbit coupling dominates (although the ligand-field effect also plays a significant but smaller role[234]) and the nature of the magnetic bistability is composed of m_J microstates. The energy gap between the ground and first excited m_J states can be increased further through crystal field splitting, and thus U_{eff} may also be increased.[235, 236, 237, 238] Larger magnetic moments and the unquenched orbital angular momentum of lanthanides are both crucial properties in designing SMMs with much higher magnetic blocking temperatures (T_B). Dysprosium metallocenes have been at the forefront of lanthanide SMM research,[239, 240, 241] with large U_{eff} barriers (up to 1541 cm^{-1}) and magnetic blocking temperatures above liquid nitrogen temperature (T_B=80 K).[242]

An extensive amount of work has been done to understand how to engineer lanthanide-based SMMs with ideal magnetic properties,[243, 244, 245, 246] but less has been done with actinides. Since actinides have much larger spin-orbit coupling than do the lanthanides, actinide-based SMMs can potentially produce greater magnetic barriers and magnetic moments.[247] Additionally, the greater radial extent of the 5f orbitals compared to that of the 4f[248] increases the likelihood of covalency between actinide and ligand (and therefore partial quenching of angular momentum), which can produce strong magnetic exchange.[249] These unique features

make the guidance outlined for lanthanides difficult to apply, so new engineering techniques must be developed specifically for actinide-based SMMs.

Uranium-based SMMs are the most studied but they have yet to reach the success of the lanthanide-based SMMs.[236, 250] It is important to note that there are much higher challenges associated to synthesizing and characterizing actinides since they are less accessible, expensive, and are dangerous to handle. However, computational chemistry provides a safe alternative to experimental actinide chemistry and the opportunity to determine and understand design criteria for actinide SMMs, allowing this field to grow more rapidly.

Certain precautions must be taken when modelling complicated systems containing large relativistic and spin-orbit coupling effects, and are multireference in nature, such as the *f*-block elements. Benchmark studies using density functional theory (DFT) show serious limitations of this method when studying ground and excited states of uranium complexes.[251] Previous studies in our group have shown that complete active space self-consistent field (CASSCF) method with spin-orbit coupling has been successful in predicting magnetic properties of actinide-based SMMs.[252, 253, 254] In the literature, there are very few experimental examples of Cf(III)-based compounds and their magnetic properties.[255, 256, 257] There are few computational studies of Cf(III)-based complexes which only report the electronic properties,[255, 258, 259] and to the best of our knowledge, there are no computational studies of the magnetic properties of Cf(III)-based magnets.

In this work, we focused on late actinide elements, namely Cf(III), and compared the magnetic properties to that of isoelectronic Dy(III)-based magnets. Cf(III) can easily undergo $\alpha - decay$ and convert to Cm(III), so an isostructural Cm(III) complex was also studied.[255] Our study shows the magnetic properties of Cf(III) and Dy(III) based compounds are very similar. However, the performance of Cf(III) magnet can be degraded via the $\alpha - decay$ of Cf(III) to Cm(III).

6.2 Computational Methods

6.2.1 DFT Calculations

The systems studied in this work were generated from the experimental crystal structure of the Dy(III) complex (Figure 6.1a) reported in literature (will be referred as Dy-Ph in the manuscript).[260] In order to reduce computational cost, the phenyl rings of the dibenzoylmethanoate linkers in the Dy-Ph complex were replaced with methyl groups. We will refer to this truncated complex as Dy-Me in this article (Figure 6.1b). Additionally, we replace Dy with both Cf and Cm in the truncated complex to generate the Cf-Me and Cm-Me structures. Geometry optimizations of the highest spin state (sextet for Dy and Cf, octet for Cm) for the Dy-Ph, Dy-Me, Cf-Me, and Cm-Me complexes were performed with DFT using the BP86 functional,[261] which has been shown previously to give reasonable geometries for actinide complexes.[252, 253] Analytical frequencies were computed to ensure all geometries were at a global minimum. The TZ2P basis set was used for the metal centers (Dy, Cf, and Cm) and the DZP basis set was used for C, H, O and N atoms.[262] The zero-order regular approximation (ZORA) was used to include scalar relativistic effects.[263, 264, 265] All DFT computations were done using the ADF2016 software package.[222, 223, 224]

6.2.2 Multireference Calculations

The electronic structures of Dy-Ph, Dy-Me, Cf-Me, and Cm-Me complexes were analyzed using the complete active space self-consistent field (CASSCF) method[266, 267] implemented in *OpenMolcas* (version 19.11, tag 1312-g91e1abe) software package.[268] All metals are in the 3+ oxidation state, and Dy(III), Cf(III) and Cm(III) have valence electronic configurations of $4f^9$, $5f^9$ and $5f^7$ respectively. Thus, for the SA-CASSCF calculations, we include all f-electrons and f-orbitals in the active space, which results in a (9,7) active space for the Dy and Cf complexes and a (7,7) active space for the Cm complex. For the Dy and Cf complexes, the (9,7) active space gives rise to 21 sextet, 224 quartet and 490 doublet states, and all configurations were included in the SA-CASSCF calculations. For the Cm complex there are 1 octet, 48 sextet, 392

quartet and 784 doublet configurations possible for the (7,7) active space choice, where all of the octet, sextet, quartet configurations and first 600 roots of the doublet spin state are included in the SA-CASSCF calculation.

State interaction was included via the restricted active space self interaction (RASSI) method.[269] For Dy and Cf complexes, 21 sextet, 128 quartet and 130 doublet roots were included in the RASSI calculation and for the Cm complex, 1 octet, 21 sextet, 119 quartet and 41 doublet roots were included in the RASSI calculation. Spin-orbit coupling was added using an effective one-electron spin-orbit Hamiltonian (SA-CASSCF-SO).[270] The SINGLE_ANISO program[271, 272, 273] was used to compute powder magnetic susceptibility (χ T) curves using the van-Vleck formalism from the energy eigenvalues (ϵ) and magnetic moments (μ) of the spin-orbit coupled states.

The resolution of identity Cholesky decomposition[274] (RICD) was used for computing the two electrons integrals at a reduced cost. The Douglas-Kroll-Hess (DKH) Hamiltonian was used to incorporate scalar relativistic effects. Two different basis set choices were used: the first was the cc-pVDZ-DK3 basis set on the metal centers (Dy, Cf and Cm)[275, 276] and the cc-pVDZ-DK basis set was used for H, C, N and O atoms[277, 278] (referred as BS1 in the manuscript). The second basis set consists of cc-pVTZ-DK3 basis sets for the metal centers (Dy, Cf and Cm),[275, 276] cc-pVTZ-DK basis set for N and O atoms [277, 278] and cc-pVDZ-DK basis sets for C and H atoms (referred as BS2 in the manuscript).

Further, the effect of dynamic correlation was included using extended multi-state complete active-space second-order perturbation (XMS-CASPT2) theory.[279, 280, 281] Recent work on Dy(III) complexes by Reta et. al. [282] showed that when only 21 sextet roots from the SA-CASSCF calculation (referred as SA-CASSCF-low in the text) are used with RASSI (SA-CASSCF-SO-low), they give similar results in terms of magnetic properties compared to similar calculations using 21 sextet, 128 quartet and 130 doublet roots. Thus, in order to reduce the computational cost in the XMS-CASPT2 level we use the above protocol and compute only 21 sextet roots for the Dy-Me and Cf-Me complexes. These XMS-CASPT2 calculations were performed using the 'NOMULT' keyword in *OpenMolcas* which only corrects the eigenvalue

of these states but does not mix the CASSCF eigenstates with dynamic electron correlation. Moreover, the states chosen in the XMS-CASPT2 calculations are divided into three groups of 11, 7 and 3 (total 21 states) based on energy of the free Dy(III) ion at the SA-CASSCF level in order to retain state degeneracy and then these energies were used to account for the spin orbit coupling using RASSI module (XMS-CASPT2-SO). This approach has been used previously with other multireference studies with Dy(III) in the literature. [242]

6.3 Results and discussion

6.3.1 Structural Analysis of Dy-Ph, Dy-Me, Cf-Me and Cm-Me Complexes

In order to determine the accuracy of our computed structures, we first compared the Dy-N and Dy-O bond lengths of the Dy-Ph complex to the experimental structure. A detailed comparison of important bond lengths of these compounds is shown in Table 6.1. Our results show that the computed bond lengths are within 0.02 Å of the experimental bond lengths. Further, we also noticed that truncation of phenyl ring to a methyl group does not significantly change the Dy-N and Dy-O bond lengths in these complexes. This suggests that BP86 functional and linker truncation gives results similar to experiment and we will use this protocol for obtaining the structures of Cf-Me and Cm-Me compound. Cf-N, Cf-O, Cm-N and Cm-O bond lengths are summarized in Table 6.1.

Table 6.1: Comparison of M-N (Å) and M-O (Å) bond lengths of Dy-Ph (experimental and DFT), Dy-Me, Cf-Me, Cm-Me. DFT bond lengths are obtained using the BP86 functional.

Compound	M-N (Å)	M-O (Å)
Dy-Ph (Expt.)	2.576	2.314
Dy-Ph (DFT)	2.599	2.323
Dy-Me	2.604	2.327
Cf-Me	2.636	2.368
Cm-Me	2.672	2.394

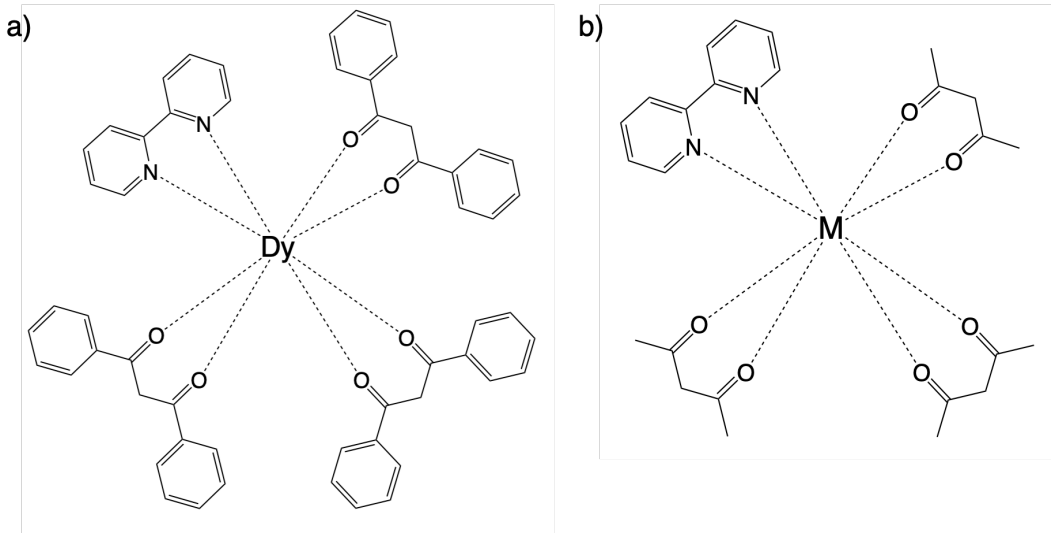

Figure 6.1: A schematic representation of Dy-Ph and M-Me (M = Dy, Cf and Cm) compounds.

6.3.2 Magnetic Properties of Dy-Ph Complex

We first studied the magnetic properties of the experimentally synthesized Dy-Ph complex as shown in 6.1 using both the experimental geometry and the DFT optimized geometry. In the structure Dy(III) has 9 4f electrons and ground state term symbol of $^6H_{15/2}$. The relative energies of various roots for different spin states of the Dy-Ph (expt.) complex are computed using SA-CASSCF method and shown in Figure E.1. The sextet ground state is 24966 cm^{-1} and 37470 cm^{-1} more stable than the first root of the quartet and doublet spin states, respectively. The sextet, quartet, and doublet spin states are spanned over an energy range of 0-35327, 24966-107293 and 37470-180563 cm^{-1}, respectively. We also found that for Dy-Ph (expt.) complex in the SA-CASSCF level there is a 12081 cm^{-1} gap between the 128th and 129th roots of the quartet spin state and a 2749 $^{-1}$ gap between the 130th and 131st roots of the double spin state. Thus, for the RASSI calculation we included first 21 sextet, 128 quartet and 130 doublet roots (upto 50000 cm^{-1} in the overall energy window). For the Dy-Ph (DFT) complex also we observed a similar energy spectrum. At the SA-CASSCF-SO level we observed a 3000 cm^{-1} gap between the 8th and 9th Kraemer's doublets (KDs) (Table 6.2 and thus only first 8 KDs were considered when computing the magnetic properties. We then computed the magnetic

susceptibility of the computed and experimental Dy-Ph structures and in both the cases the susceptibility curve overestimates the magnetic susceptibility at 0 K when compared to the experimental magnetic susceptibility (Figure 6.2). We also found that the effective blocking barrier height for the Dy-Ph (expt.) complex is 299.4 cm^{-1} and that of Dy-Ph (DFT) complex is 235.6 cm^{-1} as computed using BS2. The blocking barrier plots for both the complexes are shown in Figure 6.3. We further noticed that the g-tensor values for the ground state KD is highly anisotropic, which is one of the necessary criteria for good single molecule magnet behaviour. The g-tensor values for first 8 KDs using BS2 are summarized in Table 6.3. We also noticed both BS1 and BS2 gave very similar results (Figure 6.2, Table E.1). Thus, only the BS2 results were discussed in the main manuscript and BS1 results were presented in the supplementary information (Table E.1-E.2).

In order to understand the various competing magnetic relaxation processes we further looked in to $ab-initio$ blocking barrier plots using the transverse magnetic moments between connecting doublets. The largest value between the connecting doublets indicate the most probable pathway of magnetic relaxation. For both Dy-Ph (expt.) and Dy-Ph (DFT) complexes, the ground state is $|\pm 15/2\rangle$ and the transverse magnetic moment between $|+15/2\rangle$ to $|-15/2\rangle$ is on the order of 10^{-3} μ_B (see Figure 6.3). which is small and hence quantum tunneling magnetization (QTM) mechanism for magnetic relaxation via ground state is likely suppressed at low temperature. QTM in the ground state is completely suppressed when the transverse moment magnetization values are in the order of 10^{-3} μ_B.[283] The transverse magnetic moments are higher between $|\pm m_J\rangle$ states to $|\pm m_{J+1}\rangle$ states compared to that of ground state QTM which suggests that at higher temperatures, excited states will be accessible and magnetic relaxation may take place via thermally assisted quantum tunneling of magnetization (TA-QTM) via higher excited states. We further noticed that beyond the first excited state the Orbach processes between $\pm m_J$ to $\pm m_{J+1}$ also become competitive with TA-QTM mechanism$_s$.

Table 6.2: Relative energies (cm^{-1}) of the lowest 9 Kraemer's doublets of Dy-Ph (expt.) and Dy-Ph (DFT) using SA-CASSCF-SO and BS2 basis sets.

	Dy-Ph (expt)	Dy-Ph (DFT)
KD1	0.0	0.0
KD2	159.7	117.3
KD3	220.5	155.7
KD4	251.4	197.6
KD5	299.4	235.6
KD6	341.8	288.8
KD7	407.6	380.1
KD8	493.4	496.1
KD9	3636.7	3590.1

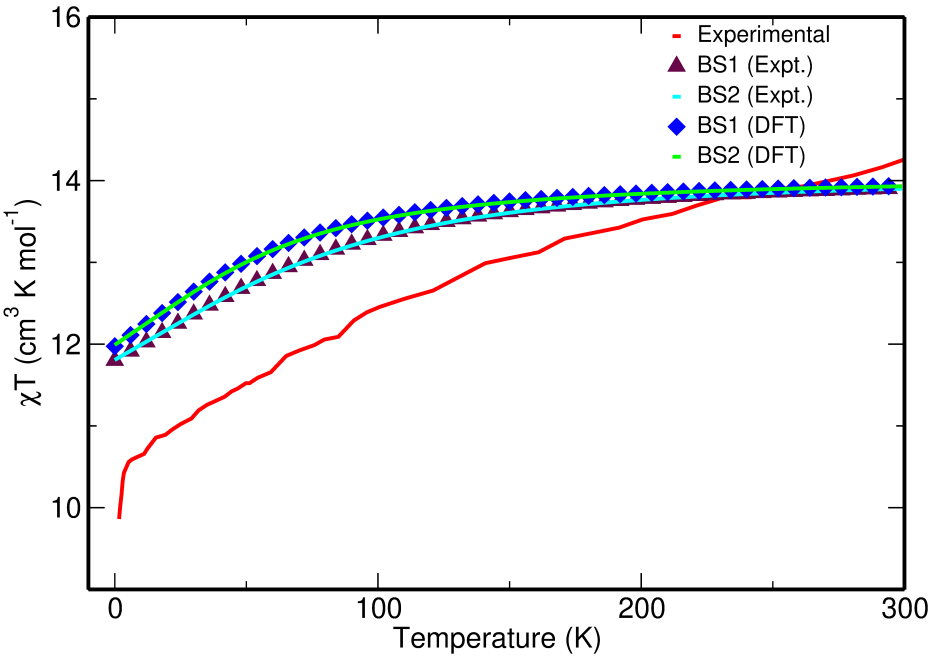

Figure 6.2: Comparison of experimental and computed χT curve using both experimental and DFT optimized geometries of Dy-Ph using SA-CASSCF-SO and the BS1 and BS2 basis sets.

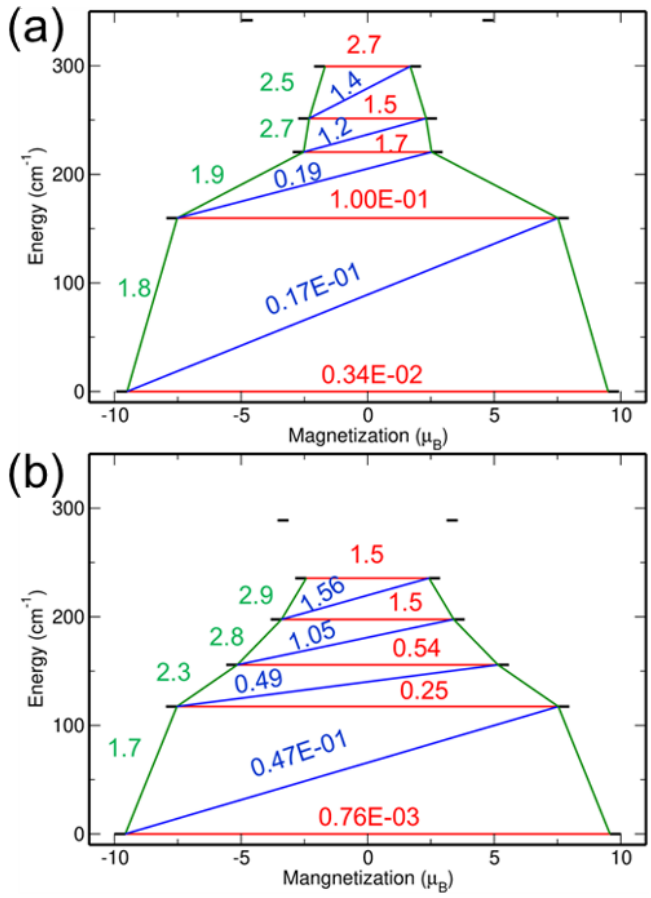

Figure 6.3: Comparison of the blocking barriers of (a) Dy-Ph (expt.) and (b) Dy-Ph (DFT) using SA-CASSCF-SO and the BS2 basis set. The red line indicates QTM between $|\pm m_J\rangle$ states. The green line indicates the transitions between $|+m_J\rangle$ to $|+m_{J+1}\rangle$ states which will proceed via direct magnetic relaxation between states. The blue line represents possible Orbach processes.

Table 6.3: Comparison of g-tensor values for Dy-Ph (expt.) and Dy-Ph (DFT) computed with SA-CASSCF-SO and the BS2 basis set.

	Dy-Ph (expt.)			Dy-Ph (DFT)		
	g_x	g_y	g_z	g_x	g_y	g_z
KD1	0.00	0.01	19.43	0.00	0.00	19.58
KD2	0.23	0.36	15.63	0.62	0.80	16.84
KD3	2.46	3.40	13.72	0.97	1.78	13.52
KD4	8.93	5.81	1.33	3.47	4.94	8.11
KD5	2.08	3.72	12.97	2.69	4.21	9.88
KD6	0.84	1.30	17.47	0.12	0.32	17.39
KD7	0.09	0.28	18.58	0.07	0.13	18.43
KD8	0.02	0.06	19.39	0.01	0.02	19.48

6.3.3 Effect of Linker Truncation

In order to reduce the computational cost we truncated the phenyl linkers of dibenzoylmethanoate to methyl groups. As shown in Table 6.1 truncation of linkers from phenyl to methyl has minor effects on the electronic structure around the metal center. We further investigated the effect of linker truncation on the magnetic properties of Dy(III) complexes. As shown in Figure 6.4 the linker truncation barely affects the magnetic susceptibility curves using both BS1 and BS2 at the SA-CASSCF-SO level of theory. Energies of the first nine Kraemer's doublets and g-tensor values for both the Dy-Ph (DFT) and Dy-Me complex are reported in the supplementary information in Tables E.3-E.5. These tables show that linker truncation does not affect the magnetic properties of these Dy(III) magnets and hence this truncation scheme can serve as good model for exploring the magnetic properties of complexes containing other metals such as Cf(III) and Cm(III) while maintaining computational efficiency.

6.3.4 Comparison of Magnetic Properties of Dy-Me, Cf-Me and Cm-Me

Both Dy and Cf are in the +3 oxidation state and has a f^9 valence electronic configuration. From our calculations, we also found that ground state term symbol for both Dy(III) and Cf(III) is $^6H_{15/2}$ and the ground spin state is a sextet. In the SA-CASSCF level of theory we found that

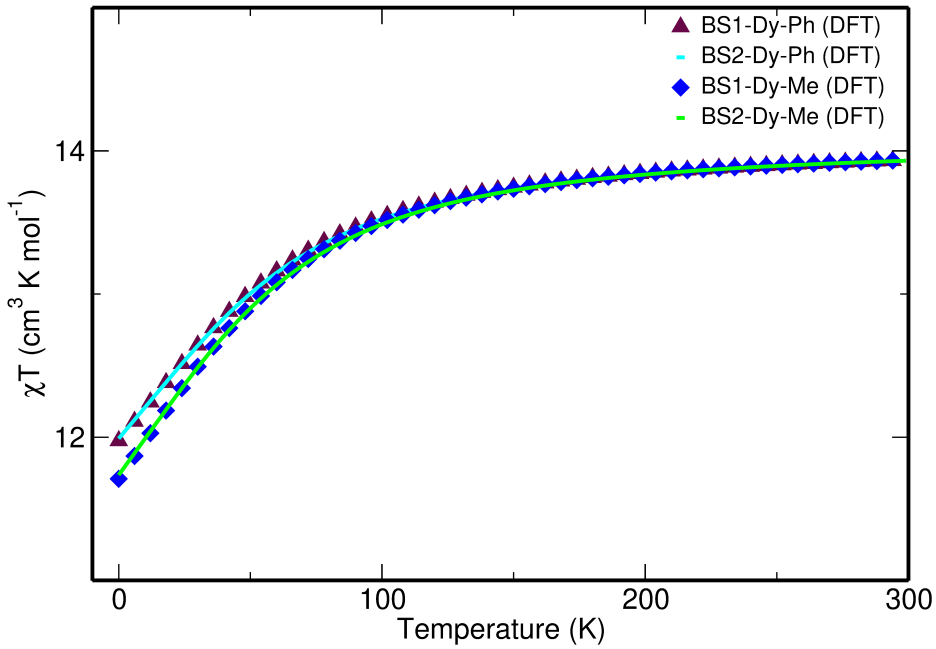

Figure 6.4: Comparison of experimental and computed χT curves using DFT optimized geometry of Dy-Ph and Dy-Me complexes using SA-CASSCF-SO and the BS1 and BS2 basis sets.

energy spectrum of the Dy-Me complex, including all sextet, quartet and doublet roots, spanned over 0-35315, 24953-107279 and 37439-180547 cm^{-1}, respectively, which is similar to that of the Dy-Ph complex. For Cf-Me complex in the SA-CASSCF level the energy spectra window for sextet, quartet and doublet spin states are 0-25981, 18857-78804, 28562-132354 cm^{-1}, respectively (Figure 6.5). For both Dy-Me and Cf-Me complex there is a gap of 12906 and 7907 cm^{-1} between the 128th and 129th root of the quartet spin state and a gap of 2805 and 985 cm^{-1} between the 130th and 131st roots of the doublet spin state. Similar to the Dy-Ph complexes we also included 21 sextet, 128 quartet and 130 doublet roots in the RASSI-SO calculation in order to include the effect of spin-orbit coupling for the Dy-Me and Cf-Me complexes. Energies of the lowest 9 KDs are reported in Table 6.4. As shown in Table 6.4, the effect of spin-orbit splitting between the ground state and first excited state is larger in the Cf-Me complex by 200 cm^{-1} compared to that of Dy-Me complex. This is expected due to the larger spin-orbit coupling effects in actinides compared to that of lanthanides. Similar to Dy-Ph complexes, we also noticed a large gap in energy between the 8th and 9th KD for both Dy-Me and Cf-Me

complex (see Table 6.4). Thus, we included first 8 KDs only when computing magnetic properties of the Cf-Me complex.

We then compared the magnetic susceptibility curves of Dy-Me and Cf-Me complexes (see Figure 6.6). At the SA-CASSCF-SO level of theory, the χT values of Cf-Me complexes are slightly lower than that of the Dy-Me complexes at all temperatures, which is consistent with the fact that the magnetic susceptibility of Cf_2O_3 is less that of Dy_2O_3[256]. Moreover, the magnetic susceptibility of free Cf(III) ion is 9.7 whereas that of Dy metal is 10.2.[256] However, compared to other actinide complexes, the χT values of the Cf-Me complex is at least 10 times higher.[252, 253, 254] This suggests that the lower magnetic susceptibility of actinide-based SMMs are not generic of 5f electrons but it is rather a problem of early actinide compounds. A careful look of the relative energies of first few KDs (see Table 6.4) also reveal that blocking barrier of Dy-Me and Cf-Me complexes are around 232 and 398 cm^{-1}, respectively. The g-tensor values corresponding to the ground state KD of the Dy-Me complex is g_x=g_y=0.01 and g_z=19.37 and that of Cf-Me complex is g_x=g_y=0.0 and g_z=18.95 which is again similar and highly anisotropic (see Table 6.5). We believe in terms of magnetic behaviour, both Dy-Me and Cf-Me complexes will perform similarly, and compared to other actinide SMMs, Cf-Me is capable of being a more suitable candidate for SMM applications.

We also looked at the blocking barrier plots for both the Dy-Me and Cf-Me complexes (see Figure 6.7. The QTM value at ground state (shown in red in Figure 6.7) for both complexes, is in the order of 10^{-3} μ_B and thus at low T, QTM via the ground state will most likely be suppressed.[283] In both cases, the transverse magnetic moments between $|\pm m_J\rangle$ to $|\pm m_{J+1}\rangle$ states (shown in green in Figure 6.7) are higher than ground state transverse magnetic moment of the QTM process. Moreover, the TA-QTM and Orbach transverse magnetic moments are quite large. Thus, at higher T, both TA-QTM (shown in red in Figure 6.7) and Orbach processes (shown in blue in Figure 6.7) will be more likely to be responsible for the main magnetic relaxation pathways. For Dy-Me complex the magnetic relaxation will likely take place via the 4th excited state where as for Cf-Me complex the magnetic relaxation will take place via the 2nd excited state. Further the magnetic blocking barrier of Cf-Me is 166 cm^{-1} higher than that of Dy-Me

suggesting the magnetic relaxation will be slower in the case of the Cf-Me complex.

We also investigated the effect of basis set dependence of magnetic susceptibility, relative energy of KDs, g-tensor and blocking barrier values using BS1 and BS2 set of basis sets (see supplementary information Figures E.2-E.3, Table E.6-E.7). Our study shows these results are not dependent on the choice of basis set used here.

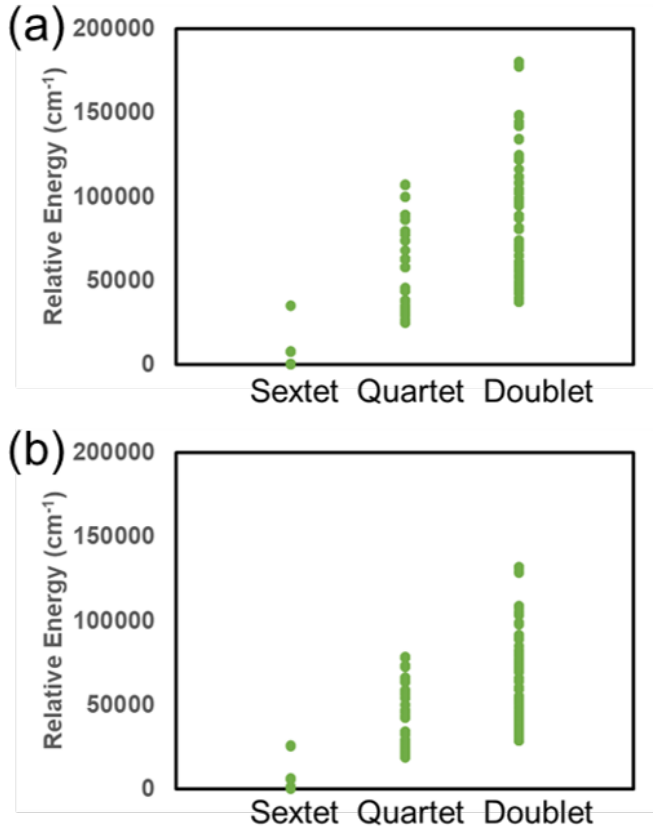

Figure 6.5: Relative energies (cm^{-1}) of all the roots of the Dy-Me and Cf-Me complexes as computed using SA-CASSCF. The BS2 basis set was used for these calculations. The first sextet root is taken as the ground state.

Table 6.4: Relative energies (cm^{-1}) of the lowest 9 Kraemer's doublets of Dy-Me, Cf-Me, Cm-Me using SA-CASSCF-SO and the BS2 basis set.

	Dy-Me	Cf-Me	Cm-Me
KD1	0.0	0.0	0.0
KD2	118.3	329.0	5.8
KD3	169.6	398.9	9.4
KD4	199.9	481.0	13.2
KD5	232.0	544.8	26141.2
KD6	278.3	664.2	26296.3
KD7	356.7	813.7	26411.7
KD8	490.8	1107.7	26681
KD9	3599.4	8280.9	28414.6

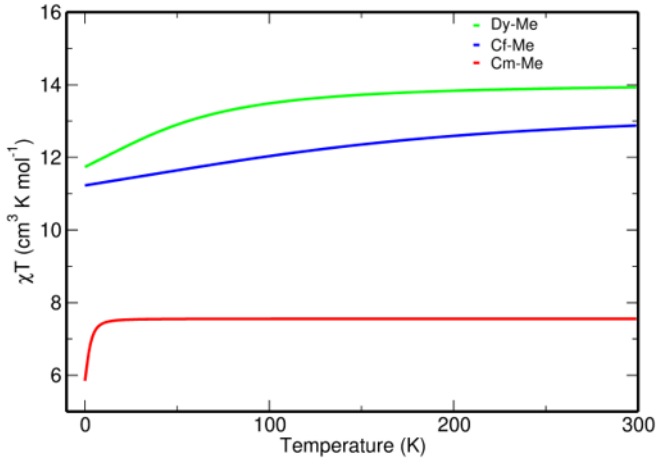

Figure 6.6: Comparison of the computed χT vs T curves using the DFT optimized geometry of Dy-Me, Cf-Me and Cm-Me complexes using SA-CASSCF-SO and the BS2 basis set.

Cf(III) readily undergoes α-decay and converts to Cm(III).[255] Thus, we also explored the magnetic properties of an analogous Cm-Me complex. Our study shows that for Cm(III), the octet spin state is very stable and the J=7/2 state is the ground state with the term symbol $^8S_{7/2}$. The computed magnetic susceptibility (Figure 6.6) of the Cm-Me complex is significantly lower than that of the Cf-Me complex and the g-tensor values are also less anisotropic (see Table 6.5). Moreover, the first 4 KDs are extremely close in energy (within 13 cm^{-1}). This suggests that magnetic properties of Cf-Me complex will be lost if converted to Cm(III).

Table 6.5: Comparison of g-tensor values for Dy-Me, Cf-Me and Cm-Me computed using SA-CASSCF-SO and the BS2 basis set.

	Dy-Me			Cf-Me			Cm-Me		
	g_x	g_y	g_z	g_x	g_y	g_z	g_x	g_y	g_z
KD1	0.01	0.01	19.37	0.00	0.00	18.95	0.15	0.17	13.67
KD2	0.43	0.53	15.93	0.86	1.41	14.54	1.47	1.78	9.51
KD3	1.35	1.80	14.25	1.13	2.13	15.22	3.94	4.69	6.74
KD4	1.79	4.22	8.78	1.21	4.89	8.97	0.63	1.21	12.78
KD5	3.07	5.25	9.99	3.25	4.18	10.01	0.04	1.27	8.57
KD6	0.24	0.45	18.34	0.27	0.44	17.72	0.78	2.94	7.77
KD7	0.02	0.05	19.02	0.03	0.04	18.28	1.22	2.72	6.21
KD8	0.00	0.00	19.68	0.01	0.02	19.04	0.07	1.08	7.98

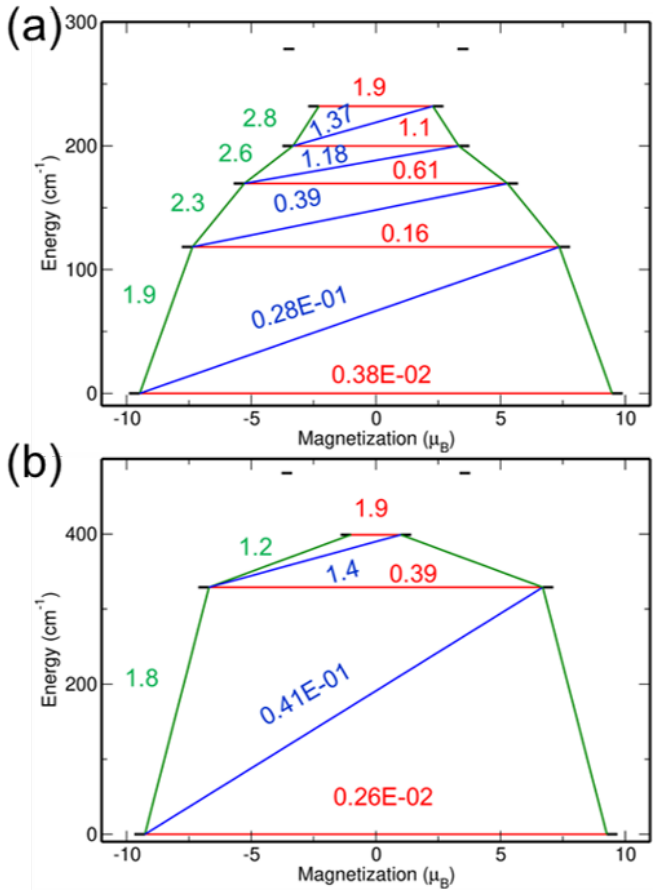

Figure 6.7: Comparison of the blocking barriers for (a) Dy-Me and (b) Cf-Me computed using SA-CASSCF-SO and the BS2 basis set. The red line indicates QTM between $|\pm m_J\rangle$ states. The green line indicates the transitions between $|+m_J\rangle$ to $|+m_{J+1}\rangle$ states which will proceed via direct magnetic relaxation between states. The blue line represents possible Orbach processes.

6.3.5 Effect of Dynamic Correlation on the Magnetic Properties of Dy-Me and Cf-Me Complexes

Similar to Reta et. al. [282] we first compared the magnetic properties of Dy-Me and Cf-Me complexes using SA-CASSCF-SO and SA-CASSCF-SO-low level of theory. Our results show negligible change in magnetic susceptibility (see supplementary Figure E.4) and energies of lowest 8 KDs (see supplementary information Table E.8). There is a slight difference in the energy of the 9th KD for both the complexes at the SA-CASSCF-SO and SA-CASSCF-SO-low levels of theory. However, the energy of the 9th KD is still higher by 3000 cm^{-1} (for Dy-Me) and 5700 cm^{-1} (for Cf-Me) in the SA-CASSCF-SO-low level of theory and hence it is not important to include in the magnetic property calculation. Thus, we also think computing the 21 sextet roots in the XMS-CASPT2 level is sufficient to capture the magnetic properties of Dy-Me and Cf-Me complexes.

We first looked at the energy spectrum of the 21 sextet roots using XMS-CASPT2 and compared that with that of SA-CASSCF. Our results show that the energy window of the sextet decreases by 7000 cm^{-1} and 6400 cm^{-1} for Dy-Me and Cf-Me complex, respectively, at the XMS-CASPT2 level when compared to that of SA-CASSCF level of theory (see supplementary information Table E.9).

The magnetic susceptibility curve obtained using the XMS-CASPT2-SO level of theory is very similar to that obtained using the SA-CASSCF-SO-low level of theory (see Figure 6.8). We also noted the energy of the first 8 KDs are very similar using above mentioned level of theories (see Table 6.6. Similar to SA-CASSCF-SO level of theory, in the SA-CASSCF-SO-low and XMS-CASPT2-SO level of theory also the Dy-Me and Cf-Me complex undergoes magnetic relaxation via 4th and 2nd excited state KD. The effective barrier heights obtained using XMS-CASPT2-SO level are 304.3 and 473.2 cm^{-1} whereas the effective barrier using the SA-CASSCF-SO-low level of theory are lower at 233.7 and 406.3 cm^{-1} for Dy-Me and Cf-Me complexes respectively. Thus, we can conclude that the effective blocking barrier of Cf-Me complex will be higher than that of the Dy-Me complex. Further comparison of g-tensor values also shows that at the XMS-CASPT2-SO level of theory both Dy-Me and Cf-Me complexes are highly anisotropic (see Table 6.7.

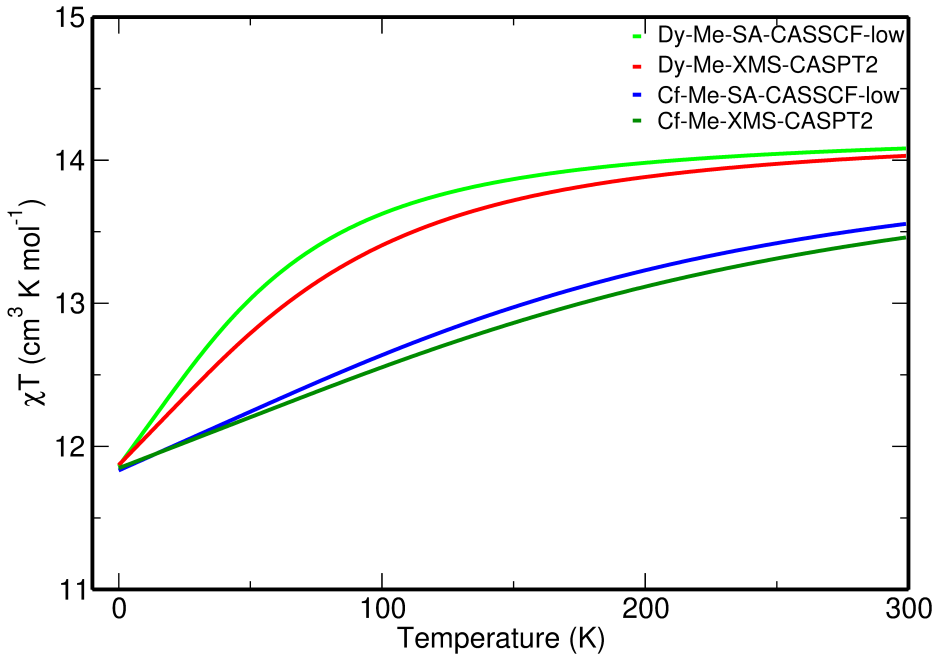

Figure 6.8: Comparison of the computed χT vs T curves of Dy-Me and Cf-Me complexes using SA-CASSCF-SO-low and XMS-CASPT2-SO method and the BS2 basis set.

Table 6.6: Relative energies (cm^{-1} of first 9 KDs of Dy-Me and Cf-Me using SA-CASSCF-SO-low and XMS-CASPT2-SO level of theory.

	Dy-Me		Cf-Me	
	SA-CASSCF-SO-low	XMS-CASPT2-SO	SA-CASSCF-SO-low	XMS-CASPT2-SO
KD1	0.0	0.0	0.0	0.0
KD2	120.1	162.0	363.1	418.6
KD3	171.3	232.2	406.3	473.2
KD4	201.9	265.4	516.6	599.4
KD5	233.7	304.3	581.5	675.6
KD6	283.1	374.5	741.3	854.8
KD7	363.0	464.3	911.2	1049.7
KD8	499.2	622.7	1238.6	1404.3
KD9	3045.4	3076.5	5864.6	5904.4

Table 6.7: Computed g-tensor values of Dy-Me and Cf-Me complex using SA-CASSCF-SO-low and XMS-CASPT2-SO level of theory.

	Dy-Me						Cf-Me					
	SA-CASSCF-SO-low			XMS-CASPT2-SO			SA-CASSCF-SO-low			XMS-CASPT2-SO		
	g_x	g_y	g_z	g_x	g_y	g_z	g_x	g_y	g_z	g_x	g_y	g_z
KD1	0.01	0.01	19.48	0.01	0.01	19.48	0.00	0.00	19.45	0.00	0.00	19.47
KD2	0.43	0.54	15.99	0.32	0.43	15.88	0.84	2.25	14.02	0.75	1.79	14.54
KD3	1.39	1.89	14.43	1.65	2.72	14.27	0.49	2.03	15.53	0.70	1.86	16.05
KD4	1.69	4.21	8.68	1.61	4.72	8.24	2.04	4.86	9.49	2.15	5.15	9.18
KD5	3.01	5.55	10.08	2.81	5.38	10.62	2.74	4.73	11.65	2.56	4.64	11.79
KD6	0.21	0.38	18.54	0.18	0.30	18.67	0.11	0.19	18.54	0.10	0.22	18.45
KD7	0.02	0.06	19.15	0.03	0.05	19.18	0.04	0.09	18.95	0.03	0.09	18.98
KD8	0.00	0.01	19.78	0.00	0.01	19.78	0.02	0.04	19.58	0.02	0.04	19.59

6.3.6 Conclusion

In this work, we explored the magnetic properties of Dy(III) complexes with multireference theory and compared them to the magnetic properties of analogous Cf(III) complexes. Our study reveals that both Dy-Me and Cf-Me complexes show similar magnetic behavior in terms of magnetic susceptibility and anistropy, providing the first example of a potential Cf(III)-based single molecule magnet. We also investigated the impact of α-decay on the Cf-Me complex by studying the magnetic properties of a Cm-Me complex. The effective blocking barrier of Cf-Me is higher than that of Dy-Me. However, the magnetic properties of Cf-Me complex can be compromised if it undergoes α-decay and converts to Cm-Me complex.

References

[1] A. Einstein. Concerning an Heuristic Point of View Toward the Emission and Transformation of Light. *Annalen der Physik*, 17:132–148, 1905.

[2] J. Zhao, A. Wang, F. Yun, G. Zhang, D.M. Roche, S.R. Wenham, and M. A. Green. 20,000 PERL Silicon Cells for the "1996 World Solar Challenge" Solar Car Race. *Prog Photovolt Res. Appl.*, 5:269–276, 1997.

[3] J. S. Manser, A. Christians, and P. V Kamat. Intriguing optoelectronic properties of metal halide perovskites. *Chem. Rev.*, 116:12956–13008, 2016.

[4] P. P. Boix, K. Nonomura, N. Mathews, and S. G. Mhaisalkar. Current progress and future perspectives for organic/inorganic perovskite solar cells. *Mater. Today*, 17:16–23, 2014.

[5] M. He, D. Zheng, M. Wang, C. Lin, and Z. Lin. High efficiency perovskite solar cells: from complex nanostructure to planar heterojunction. *J. Mater. Chem. A*, 2:5994–6003, 2014.

[6] M. A. Green, A. Ho-Baillie, and H. J. Snaith. The emergence of perovskite solar cells. *Nat. Photonics*, 8:506–514, 2014.

[7] Guan Zhang, Gang Liu, Lianzhou Wang, and John T. S. Irvine. Inorganic perovskite photocatalysts for solar energy utilization. *Chem. Soc. Rev.*, 45:5951–5984, 2016.

[8] J. S. Manser, M. I. Saidaminov, J. A. Christians, O. M. Bakr, and P. V. Kamat. Making and breaking of lead halide perovskites. *Acc. Chem. Res.*, 49:330–338, 2016.

[9] P. P. Boix, S. Agarwala, T. M. Koh, N. Mathews, and S. G. Mhaisalkar. Perovskite solar cells: Beyond methylammonium lead iodide. *J. Phys. Chem. Lett.*, 6:898–907, 2015.

[10] M. Grätzel. The light and shade of perovskite solar cells. *Nat. Mater*, 13:838–842, 2014.

[11] D. H. Fabini, J. G. Labram, A. J. Lehner, J. S. Bechtel, H. A. Evans, A. Van der Ven, F. Wudl, M. L. Chabinyc, and R. Seshadri. Main-group halide semiconductors derived from perovskite: Distinguishing chemical, structural, and electronic aspects. *Inorg. Chem.*, 56:11–25, 2017.

[12] W. Zhang, G. E. Eperon, and H. J. Snaith. Metal halide perovskites for energy applications. *Nat. Energy*, 1:16048–16055, 2016.

[13] W. S. Yang, B.-W. Park, E. H. Jung, N. J. Jeon, Y. C. Kim, D. U. Lee, S. S. Shin, J. Seo, E. K. Kim, J. H. Noh, and S. I. Seok. Iodide management in formamidinium-lead-halide–based perovskite layers for efficient solar cells. *Science*, 356:1376–1379, 2017.

[14] A. Babayigit, D. D. Thanh, A. Ethirajan, J. Manca, M. Muller, H. G. Boyen, and B. Conings. Assessing the toxicity of Pb- and Sn-based perovskite solar cells in model organism Danio rerio. *Sci. Rep.*, 6:18721–18731, 2016.

[15] G. E. Eperon, S. N. Habisreutinger, T. Leijtens, B. J. Bruijnaers, J. J. van Franeker, D. W. deQuilettes, S. Pathak, R. J. Sutton, G. Grancini, D. S. Ginger, R. A. J. Janssen, A. Petrozza, and H. J. Snaith. The importance of moisture in hybrid lead halide perovskite thin film fabrication. *ACS Nano*, 9:9380–9393, 2015.

[16] A. Babayigit, A. Ethirajan, M. Muller, and B. Conings. Toxicity of organometal halide perovskite solar cells. *Nat. Mater*, 15:247–251, 2016.

[17] E. S. Parrott, R. L. Milot, T. Stergiopoulos, H. J. Snaith, M. B. Johnston, and L. M. Herz. Effect of structural phase transition on charge-carrier lifetimes and defects in $CH_3NH_3SnI_3$ perovskite. *J. Phys. Chem. Lett.*, 7:1321–1326, 2016.

[18] F. Hao, C. C. Stoumpos, D. H. Cao, R. P. H. Chang, and M. G. Kanatzidis. Lead-free solid-state organic–inorganic halide perovskite solar cells. *Nat. Photonics*, 8:489–494, 2014.

[19] C. Wadia, A. P. Alivisatos, and D. M. Kammen. Materials availability expands the opportunity for large-scale photovoltaics deployment. *Environ. Sci. Technol.*, 43:2072, 2009.

[20] C. A. Wolden, J. Kurtin, J. B. Baxter, I. Repins, S. E. Shaheen, J. T. Torvik, A. A. Rockett, V. M. Fthenakis, and E. S. Aydil. Photovoltaic manufacturing: Present status, future prospects, and research needs. *J. Vac. Sci. Technol. A*, 29:030801, 2011.

[21] A Ennaoui, S Fiechter, C Pettenkofer, N Alonsovante, K Buker, M Bronold, C Hopfner, and H Tributsch. Iron Disulfide for Solar-Energy Conversion. *Sol. Energy Mater. Sol. Cells*, 29:289, 1993.

[22] X. Zhang, M. Li, J. Walter, L. O'Brien, M. Manno, B. Voigt, F. Mork, S. V. Baryshev, J. Kakalios, E. S. Aydil, and C. Leighton. Potential resolution to the doping puzzle in iron pyrite: Carrier type determination by Hall effect and thermopower. *Phys. Rev. Mater.*, 1:015402, 2017.

[23] Xin Zhang, Michael Manno, Andrew Baruth, Melissa Johnson, Eray S. Aydil, and Chris Leighton. Crossover from nanoscopic intergranular hopping to conventional charge transport in pyrite thin films. *ACS Nano*, 7:2781, 2013.

[24] R. Sun, M K Y Chan, S. Kang, and G Ceder. Intrinsic stoichiometry and oxygen-induced p -type conductivity of pyrite FeS_2. *Phys. Rev. B*, 84:035212, 2011.

[25] Miguel Cabán-Acevedo, Nicholas S. Kaiser, Caroline R. English, Dong Liang, Blaise J. Thompson, Hong En Chen, Kyle J. Czech, John C. Wright, Robert J. Hamers, and Song Jin. Ionization of high-density deep donor defect states explains the low photovoltage of iron pyrite single crystals. *J. Am. Chem. Soc.*, 136:17163, 2014.

[26] P. P. Altermatt, T. Kiesewetter, K. Ellmer, and H. Tributsch. Specifying targets of future research in photovoltaic devices containing pyrite (FeS_2) by numerical modelling. *Sol. Energy Mater. Sol. Cells*, 71:181, 2002.

[27] S. Goswami, D. Ray, K. I. Otake, C. W. Kung, S. J. Garibay, T. Islamoglu, A. Atilgan, Y. Cui, C. J. Cramer, O. K. Farha, and J. T. Hupp. A porous, electrically conductive hexa-zirconium(iv) metal-organic framework. *Chem. Sci.*, 9:4477–4482, 2018.

[28] Marina R. Filip and Feliciano Giustino. GW quasiparticle band gap of the hybrid organic-inorganic perovskite $CH_3NH_3PbI_3$: Effect of spin-orbit interaction, semicore electrons, and self-consistency. *Phys. Rev. B*, 90:245144, 2014.

[29] T. Baikie, Y. Fang, J. M. Kadro, M. Schreyer, F. Wei, S. G. Mhaisalkar, M. Grätzel, and T. J. White. Synthesis and crystal chemistry of the hybrid perovskite $CH_3NH_3PbI_3$ for solid-state sensitised solar cell applications. *J. Mater. Chem. A*, 1:5628–5641, 2013.

[30] Stefaan De Wolf, Jakub Holovsky, Soo-Jin Moon, Philipp Löper, Bjoern Niesen, Martin Ledinsky, Franz-Josef Haug, Jun-Ho Yum, and Christophe Ballif. Organometallic halide perovskites: Sharp optical absorption edge and its relation to photovoltaic performance. *J. Phys. Chem. Lett.*, 5(6):1035–1039, 2014.

[31] K. Tvingstedt, O. Malinkiewicz, A. Baumann, C. Deibel, H. J. Snaith, V. Dyakonov, and H. J. Bolink. Radiative efficiency of lead iodide based perovskite solar cells. *Sci. Rep.*, 4:6071–6077, 2014.

[32] D. Shi, V. Adinolfi, R. Comin, M. Yuan, E. Alarousu, A. Buin, Y. Chen, S Hoogland, A. Rothenberger, K. Katsiev, Y. Losovyj, X. Zhang, P. A. Dowben, O. F. Mohammed, E. H. Sargent, and O. M. Bakr. Low trap-state density and long carrier diffusion in organolead trihalide perovskite single crystals. *Science*, 347:519–522, 2015.

[33] S. D. Stranks, G. E. Eperon, G. Grancini, C. Menelaou, M. J. P. Alcocer, T. Leijtens, L. M. Herz, A. Petrozza, and H. J. Snaith. Electron-hole diffusion lengths exceeding 1 micrometer in an organometal trihalide perovskite absorber. *Science*, 342:341–344, 2013.

[34] Guichuan Xing, Nripan Mathews, Swee Sien Lim, Yeng Ming Lam, Subodh Mhaisalkar, and Tze Chien Sum. Long-Range Balanced Electron- and Hole-Transport Lengths in Organic-Inorganic $CH_3NH_3PbI_3$. *Science*, 342:344–347, 2013.

[35] C. Wehrenfennig, G. E. Eperon, M. B. Johnston, H. J. Snaith, and L. M. Herz. High charge carrier mobilities and lifetimes in organolead trihalide perovskites. *Adv. Mater.*, 26(10):1584–1589, 2014.

[36] C. C. Stoumpos, C. D. Malliakas, and M. G. Kanatzidis. Semiconducting tin and lead iodide perovskites with organic cations: Phase transitions, high mobilities, and near-infrared photoluminescent properties. *Inorg. Chem.*, 52:9019–9038, 2013.

[37] Yaguang Guo, Qian Wang, and Wissam A. Saidi. Structural Stabilities and Electronic Properties of High-Angle Grain Boundaries in Perovskite Cesium Lead Halides. *J. Phys. Chem. C*, 121:1715–1722, 2017.

[38] D. M. Trots and S. V. Myagkota. High-temperature structural evolution of caesium and rubidium triiodoplumbates. *J. Phys. Chem. Solids*, 69:2520–2526, 2008.

[39] M. Ahmad, G. Rehman, L. Ali, M. Shafiq, R. Iqbal, R. Ahmad, T. Khan, S. Jalali-Asadabadi, M. Maqbool, and I. Ahmad. Structural, electronic and optical properties of $CsPbX_3$ (X=Cl, Br, I) for energy storage and hybrid solar cell applications. *J. Alloys Compd.*, 705:828–839, 2017.

[40] Koji Yamada, Shinya Funabiki, Hiromi Horimoto, Takashi Matsui, Tsutomu Okuda, and Sumio Ichiba. Structural phase transitions of the polymorphs of $CsSnI_3$ by means of rietveld analysis of the X-ray diffraction. *Chem. Lett.*, 20(5):801–804, 1991.

[41] Ling Yi Huang and Walter R L Lambrecht. Electronic band structure, phonons, and exciton binding energies of halide perovskites $CsSnCl_3$, $CsSnBr_3$, and $CsSnI_3$. *Phys. Rev. B*, 88:165203, 2013.

[42] Ling Yi Huang and Walter R L Lambrecht. Electronic band structure trends of perovskite halides: Beyond Pb and Sn to Ge and Si. *Phys. Rev. B*, 93:195211, 2016.

[43] Ivo Borriello, Giovanni Cantele, and Domenico Ninno. Ab initio investigation of hybrid organic-inorganic perovskites based on tin halides. *Phys. Rev. B*, 77:235214, 2008.

[44] Li-Chuan Tang, Chen-Shiung Chang, Li-Chuan Tang, and Jung Y Huang. Electronic structure and optical properties of rhombohedral $CsGeI_3$. *J. Phys. Condens. Mater.*, 12(43):9129–9143, 2000.

[45] T. Krishnamoorthy, H. Ding, C. Yan, W. L. Leong, T. Baikie, Z. Zhang, M. Sherburne, S. Li, M. Asta, N. Mathews, and S. G. Mhaisalkar. Lead-free germanium iodide perovskite materials for photovoltaic applications. *J. Mater. Chem. A*, 3:23829–23832, 2015.

[46] G Shwetha and V Kanchana. Optical isotropy in structurally anisotropic halide scintillators : Ab initio study. *Phys. Rev. B*, 86:115209, 2012.

[47] Shuyan Shao, Jian Liu, Giuseppe Portale, Hong-Hua Fang, Graeme R. Blake, Gert H. ten Brink, L. Jan Anton Koster, and Maria Antonietta Loi. Highly reproducible sn-based hybrid perovskite solar cells with 9% efficiency. *Adv. Energy Mater.*, 8(4):1702019, 2018.

[48] M. R. Filip and F. Giustino. Computational screening of homovalent lead substitution in organic - inorganic halide perovskites. *J. Phys. Chem. C*, 120:166–173, 2016.

[49] W. Ming, H. Shi, and M.-H. Du. Large dielectric constant, high acceptor density, and deep electron traps in perovskite solar cell material $CsGeI_3$. *J. Mater. Chem. A*, 4:13852–13858, 2016.

[50] J. T. Jacobsson, M. Pazoki, A. Hagfeldt, and T. Edvinsson. Goldschmidt Rules and Strontium Replacement in Lead Halogen Perovskite Solar Cells: Theory and Preliminary Experiments on $CH_3NH_3SrI_3$. *J. Phys. Chem. C*, 119:25673–25683, 2015.

[51] E. M. Hutter, R. J. Sutton, S. Chandrashekar, M. Abdi-Jalebi, S. D. Stranks, H. J. Snaith, and T. J. Savenije. Vapour-deposited cesium lead iodide perovskites: Microsecond charge carrier lifetimes and enhanced photovoltaic performance. *ACS Energy Letters*, 2:1901–1908, 2017, https://doi.org/10.1021/acsenergylett.7b00591.

[52] Jingru Zhang, Qian Wang, Xisheng Zhang, Jiexuan Jiang, Zhenfei Gao, Zhiwen Jin, and Shengzhong (Frank) Liu. High-performance transparent ultraviolet photodetectors based on inorganic perovskite cspbcl3 nanocrystals. *RSC Adv.*, 7:36722–36727, 2017.

[53] M. R. Filip, G. E. Eperon, H. J. Snaith, and F. Giustino. Steric Engineering of Metal-Halide Perovskites with Tunable Optical Band Gaps. *Nat. Commun.*, 5:5757–5765, 2014.

[54] G. Kresse and J. Furthmüller. Efficient iterative schemes for ab initio total-energy calculations using a plane-wave basis set. *Phys. Rev. B*, 54:11169–11186, 1996.

[55] G. Kresse and J. Furthmüller. Efficiency of ab-initio total energy calculations for metals and semiconductors using a plane-wave basis set. *Comput. Mater. Sci.*, 6(1):15–50, 1996.

[56] G. Kresse and J. Hafner. Ab initio molecular dynamics for liquid metals. *Phys. Rev. B*, 47:558–561, 1993.

[57] G. Kresse and J. Hafner. Ab initio molecular-dynamics simulation of the liquid-metal–amorphous-semiconductor transition in germanium. *Phys. Rev. B*, 49:14251–14269, 1994.

[58] John P. Perdew and Yue Wang. Accurate and simple analytic representation of the electron-gas correlation energy. *Phys. Rev. B*, 45:13244–13249, 1992.

[59] John P. Perdew, Kieron Burke, and Matthias Ernzerhof. Generalized gradient approximation made simple. *Phys. Rev. Lett.*, 77:3865–3868, 1996.

[60] S. Grimme, J. Antony, S. Ehrlich, and H. Krieg. A consistent and accurate ab initio parametrization of density functional dispersion correction (dft-d) for the 94 elements h-pu. *J. Chem. Phys.*, 132:154104, 2010.

[61] John P. Perdew, Adrienn Ruzsinszky, Gábor I. Csonka, Oleg A. Vydrov, Gustavo E. Scuseria, Lucian A. Constantin, Xiaolan Zhou, and Kieron Burke. Restoring the density-gradient expansion for exchange in solids and surfaces. *Phys. Rev. Lett.*, 100:136406, 2008.

[62] H. S. Yu, W. Zhang, P. Verma, X. He, and D. G. Truhlar. Nonseparable exchange–correlation functional for molecules, including homogeneous catalysis involving transition metals. *Phys. Chem. Chem. Phys.*, 17:12146–12160, 2015.

[63] Jochen Heyd, Gustavo E. Scuseria, and Matthias Ernzerhof. Hybrid Functionals Based on a Screened Coulomb Potential. *J. Chem. Phys.*, 118(18):8207–8215, 2003.

[64] Jochen Heyd and Gustavo E. Scuseria. Efficient Hybrid Density Functional Calculations in Solids: Assessment of the Heyd-Scuseria-Ernzerhof Screened Coulomb Hybrid Functional. *J. Chem. Phys.*, 121(3):1187–1192, 2004.

[65] Aliaksandr V. Krukau, Oleg A. Vydrov, Artur F. Izmaylov, and Gustavo E. Scuseria. Influence of the Exchange Screening Parameter on the Performance of Screened Hybrid Functionals. *J. Chem. Phys.*, 125(22), 2006.

[66] P. E. Blöchl. Projector augmented-wave method. *Phys. Rev. B*, 50:17953–17979, 1994.

[67] G. Kresse and D. Joubert. From ultrasoft pseudopotentials to the projector augmented-wave method. *Phys. Rev. B*, 59:1758–1775, 1999.

[68] Minliang Lai, Qiao Kong, Connor G. Bischak, Yi Yu, Letian Dou, Samuel W. Eaton, Naomi S. Ginsberg, and Peidong Yang. Structural, optical, and electrical properties of phase-controlled cesium lead iodide nanowires. *Nano Res.*, 10:1107–1114, 2017.

[69] Lucy D. Whalley, Jarvist M. Frost, Young-Kwang Jung, and Aron Walsh. Perspective: Theory and simulation of hybrid halide perovskites. *J. Chem. Phys.*, 146(22):220901, 2017.

[70] C. C. Stoumpos, L. Frazer, D. J. Clark, Y. S. Kim, S. H. Rhim, A. J. Freeman, J. B. Ketterson, J. I. Jang, and M. G. Kanatzidis. Hybrid germanium iodide perovskite semiconductors: Active lone pairs, structural distortions, direct and indirect energy gaps, and strong nonlinear optical properties. *J. Am. Chem. Soc.*, 137:6804–6819, 2015.

[71] Giles E. Eperon, Giuseppe M. Paternò, Rebecca J. Sutton, Andrea Zampetti, Amir Abbas Haghighirad, Franco Cacialli, and Henry J. Snaith. Inorganic caesium lead iodide perovskite solar cells. *J. Mater. Chem. A*, 3:19688–19695, 2015.

[72] G. Schilling and G. Meyer. Ternäre bromide und iodide zweiwertiger lanthanide und ihre erdalkali-analoga vom typ AMX_3 and AM_2X_5. *Zeitschrift für anorganische und allgemeine Chemie*, 622(5):759–765, 1996.

[73] A. J. Garza and G. E. Scuseria. Predicting band gaps with hybrid density functionals. *J. Phys. Chem. Lett.*, 7(20):4165–4170, 2016.

[74] I. Chung, J.-H. Song, J. Im, J. Androulakis, C. D. Malliakas, H. Li, A. J. Freeman, J. T. Kenney, and M. G. Kanatzidis. $CsSnI_3$: Semiconductor or metal? high electrical conductivity and strong near-infrared photoluminescence from a single material. high hole mobility and phase-transitions. *J. Am. Chem. Soc.*, 134:8579–8587, 2012.

[75] Hongliang Shi and Mao-Hua Du. Shallow halogen vacancies in halide optoelectronic materials. *Phys. Rev. B*, 90:174103, 2014.

[76] Mahsa Afsari, Arash Boochani, Mohammadreza Hantezadeh, and Seyed Mohammad Elahi. Topological nature in cubic phase of perovskite CsPbI₃: By DFT. *Solid State Commun.*, 259:10–15, 2017.

[77] Yifan Li, Chenhui Zhang, Xixiang Zhang, Dan Huang, Qian Shen, Yingchun Cheng, and Wei Huang. Intrinsic point defects in inorganic perovskite CsPbI₃ from first-principles prediction. *Appl. Phys. Lett.*, 111:162106, 2017.

[78] Christopher Grote and Robert F. Berger. Strain Tuning of Tin-Halide and Lead-Halide Perovskites: A First-Principles Atomic and Electronic Structure Study. *J. Phys. Chem. C*, 119:22832–22837, 2015.

[79] Jacky Even, Laurent Pedesseau, Jean-Marc Jancu, and Claudine Katan. Importance of spin–orbit coupling in hybrid organic/inorganic perovskites for photovoltaic applications. *J. Phys. Chem. Lett.*, 4:2999–3005, 2013.

[80] Christopher H. Hendon, Ruo Xi Yang, Lee A. Burton, and Aron Walsh. Assessment of polyanion (BF_4^- and PF_6^-) substitutions in hybrid halide perovskites. *J. Mater. Chem. A*, 3:9067–9070, 2015.

[81] L. Debbichi, S. Lee, H. Cho, A. M. Rappe, K.-H. Hong, M. S. Jang, and H. Kim. Mixed valence perovskite $Cs_2Au_2I_6$: A potential material for thin-film Pb-free photovoltaic cells with ultrahigh efficiency. *Adv. Mater.*, 30:1707001, 2018.

[82] P.-P. Sun, Q.-S. Li, L.-N. Yang, and Z.-S. Li. Theoretical insights into a potential lead-free hybrid perovskite: substituting Pb^{2+} with Ge^{2+}. *Nanoscale*, 8:1503–1512, 2016.

[83] A. Poglitsch and D. Weber. Dynamic disorder in methylammoniumtrihalogenoplumbates (II) observed by millimeter-wave spectroscopy. *J. Chem. Phys.*, 87:6373, 1987.

[84] S. S. Gokhale, L. Stand, A. Lindsey, M. Koschan, M. Zhuravleva, and C. L. Melcher. Improvement in the optical quality and energy resolution of $CsSrBr_3$: Eu scintillator crystals. *J. Cryst. Growth*, 445:1–8, 2016.

[85] Lekha Peedikakkandy and Parag Bhargava. Composition dependent optical, structural and photoluminescence characteristics of cesium tin halide perovskites. *RSC Adv.*, 6:19857–19860, 2016.

[86] Bo Wu, Yuanyuan Zhou, Guichuan Xing, Qiang Xu, Hector F. Garces, Ankur Solanki, Teck Wee Goh, Nitin P. Padture, and Tze Chien Sum. Long minority-carrier diffusion length and low surface-recombination velocity in inorganic lead-free $CsSnI_3$ perovskite crystal for solar cells. *Adv. Funct. Mater.*, 27(7):1604818, 2017.

[87] D. Sabba, H. K. Mulmudi, R. R. Prabhakar, T. Krishnamoorthy, T. Baikie, P. P. Boix, S. Mhaisalkar, and N. Mathews. Impact of anionic br– substitution on open circuit voltage in lead free perovskite $CsSnI_{3-x}Br_x$ solar cells. *J. Phys. Chem. C*, 119(4):1763–1767, 2015.

[88] Mulmudi Hemant Kumar, Sabba Dharani, Wei Lin Leong, Pablo P. Boix, Rajiv Ramanujam Prabhakar, Tom Baikie, Chen Shi, Hong Ding, Ramamoorthy Ramesh, Mark Asta, Michael Graetzel, Subodh G. Mhaisalkar, and Nripan Mathews. Lead-free halide perovskite solar cells with high photocurrents realized through vacancy modulation. *Adv. Mater.*, 26(41):7122–7127, 2014.

[89] Kai Shum, Zhuo Chen, Jawad Qureshi, Chonglong Yu, Jian J. Wang, William Pfenninger, Nemanja Vockic, John Midgley, and John T. Kenney. Synthesis and characterization of cssni$_3$ thin films. *Appl. Phys. Lett.*, 96(22):221903, 2010.

[90] R. J. Sutton, G. E. Eperon, L. Miranda, E. S. Parrott, B. A. Kamino, J. B. Patel, M. T. Hörantner, M. B. Johnston, A. Abbas Haghighirad, D. T. Moore, and H. J. Snaith. Bandgap-tunable cesium lead halide perovskites with high thermal stability for efficient solar cells. *Adv. Energy Mater.*, 6(8):1502458, 2016.

[91] A. Swarnkar, A. R. Marshall, E. M. Sanehira, B. D. Chernomordik, D. T. Moore, J. A. Christians, T. Chakrabarti, and J. M. Luther. Quantum Dot–induced Phase Stabilization of α-CsPbI$_3$ Perovskite for High-Efficiency Photovoltaics. *Science*, 354:92–95, 2016.

[92] Paifeng Luo, Wei Xia, Shengwen Zhou, Lin Sun, Jigui Cheng, Chenxi Xu, and Yingwei Lu. Solvent engineering for ambient-air-processed, phase-stable cspbi$_3$ in perovskite solar cells. *J. Phys. Chem. Lett.*, 7(18):3603–3608, 2016.

[93] L. Protesescu, S. Yakunin, M. I. Bodnarchuk, F. Krieg, R. Caputo, C. H. Hendon, R. X. Yang, A. Walsh, and M. V. Kovalenko. Nanocrystals of cesium lead halide perovskites ($CsPbX_3$, X = Cl, Br, and I): Novel optoelectronic materials showing bright emission with wide color gamut. *Nano Letters*, 15(6):3692–3696, 2015.

[94] Parthiban Ramasamy, Da-Hye Lim, Bumjin Kim, Seung-Ho Lee, Min-Sang Lee, and Jong-Soo Lee. All-inorganic cesium lead halide perovskite nanocrystals for photodetector applications. *Chem. Commun.*, 52:2067–2070, 2016.

[95] H. Wei, M. Zhuravleva, K. Yang, B. Blalock, and C. L. Melcher. Effect of Ba substitution in $CsSrI_3:Eu^{2+}$. *J. Cryst. Growth*, 384:27–32, 2013.

[96] M. Zhuravleva, B. Blalock, K. Yang, M. Koschan, and C. L. Melcher. New single crystal scintillators: $CsCaCl_3$:Eu and $CsCaI_3$:Eu. *J. Cryst. Growth*, 352(1):115–119, 2012. The Proceedings of the 18th American Conference on Crystal Growth and Epitaxy.

[97] E. Beurer, J. Grimm, P. Gerner, and H. U. Güdel. New type of near-infrared to visible photon upconversion in Tm^{2+}-doped $CsCaI_3$. *J. Am. Chem. Soc.*, 128(10):3110–3111, 2006.

[98] M. Tyagi, M. Zhuravleva, and C. L. Melcher. Theoretical and experimental characterization of promising new scintillators: Eu^{2+} doped $CsCaCl_3$ and $CsCaI_3$. *J. Appl. Phys.*, 113(20):203504, 2013.

[99] S.S. Gokhale, M. Loyd, L. Stand, A. Lindsey, S. Swider, M. Zhuravleva, and C.L. Melcher. Investigation of the unique degradation phenomenon observed in $CsSrBr_3$: Eu 5% scintillator crystals. *J. Cryst. Growth*, 452:89–94, 2016.

[100] Kan Yang, Mariya Zhuravleva, and Charles L. Melcher. Crystal growth and characterization of $CsSr_{1-x}Eu_xI_3$ high light yield scintillators. *Physica Status Solidi*, 5(1):43–45, 2011.

[101] Markus Suta and Claudia Wickleder. Photoluminescence of $CsMI_3$:Eu^{2+} (M = Mg, Ca, and Sr) – a spectroscopic probe on structural distortions. *J. Mater. Chem. C*, 3:5233–5245, 2015.

[102] Chonghea Li, Xionggang Lu, Weizhong Ding, Liming Feng, Yonghui Gao, and Ziming Guo. Formability of ABX_3 (X = F, Cl, Br, I) halide perovskites. *Acta Crystallographica Section B*, 64(6):702–707, Dec 2008.

[103] Gary L. McPherson, Arlene M. McPherson, and Jerry L. Atwood. Structures of $CsMgBr_3$, $CsCdBr_3$ and $CsMgI_3$— diamagnetic linear chain lattices. *J. Phys. Chem. Solids*, 41(5):495–499, 1980.

[104] A. Kumar, K. R. Balasubramaniam, J. Kangsabanik, Vikram, and A. Alam. Crystal structure, stability, and optoelectronic properties of the organic-inorganic wide-band-gap perovskite $CH_3NH_3BaI_3$: Candidate for transparent conductor applications. *Phys. Rev. B*, 94:180105, 2016.

[105] U. Shirwadkar, E. V. D. van Loef, R. Hawrami, S. Mukhopadhyay, J. Glodo, and K. S. Shah. New promising scintillators for gamma-ray spectroscopy: Cs(Ba,Sr)(Br,I)$_3$. In *2011 IEEE Nuclear Science Symposium Conference Record*, pages 1583–1585, 2011.

[106] Konrad Wojciechowski, Michael Saliba, Tomas Leijtens, Antonio Abate, and Henry J. Snaith. Sub-150 ℃ processed meso-superstructured perovskite solar cells with enhanced efficiency. *Energy Environ. Sci.*, 7:1142–1147, 2014.

[107] W. Zhang, M. Saliba, D. T. Moore, S. K. Pathak, M. T. Hörantner, T. Stergiopoulos, S. D. Stranks, G. E. Eperon, J. A. Alexander-Webber, A. Abate, A. Aditya Sadhanala, S. Yao, Y. Chen, R.H. Friend, L. A. Estroff, U. Wiesner, and H. J. Snaith. Ultrasmooth organic–inorganic perovskite thin-filmformation and crystallization for efficient planarheterojunction solar cells. *Nat. Commun.*, 6:6142–6151, 2015.

[108] J. Burschka, N. Pellet, S.-J. Moon, R. Humphry-Baker, P. Gao, M. K. Nazeeruddin, and M. Grätzel. Sequential deposition as a route to high-performance perovskite-sensitized solar cells. *Nature*, 499:316–319, 2013.

[109] Y.-H. Chiang, H.-M. Cheng, M.-H. Li, T.-F. Guo, and P. Chen. Low-pressure vapor-assisted solution process for thiocyanate-based pseudohalide perovskite solar cells. *ChemSusChem*, 9:2620–2627, 2016.

[110] Q. Chen, H. Zhou, Z. Hong, S. Luo, H.-S. Duan, H.-H. Wang, Y. Liu, G. Li, and Y. Yang. Planar heterojunction perovskite solar cells via vapor-assisted solution process. *J. Am. Chem. Soc.*, 136:622–625, 2014.

[111] E. Rowe, E. Tupitsyn, B. Wiggins, P. Bhattacharya, L. Matei, M. Groza, V. Buliga, A. Burger, P. Beck, N.J. Cherepy, and S.A. Payne. Double salts iodide scintillators: Cesium barium iodide, cesium calcium iodide, and barium bromine iodide. *Crystal Research and Technology*, 48(4):227–235, 2013.

[112] Ki-Ha Hong, Jongseob Kim, Lamjed Debbichi, Hyungjun Kim, and Sang Hyuk Im. Band gap engineering of $Cs_3Bi_2I_9$ perovskites with trivalent atoms using a dual metal cation. *J. Phys. Chem. C*, 121:969–974, 2017.

[113] C. M. Fang and Koushik Biswas. Quaternary Iodides A(BaSr)I_5:Eu^{2+}(A = K, Cs) as Scintillators for Radiation Detection. *J. Phys. Chem. C*, 120:1225–1236, 2016.

[114] A. Ennaoui and H. Tributsch. Energetic characterization of the photoactive FeS_2 (pyrite) interface. *Sol. Energy Mater.*, 14:461, 1986.

[115] William Shockley and Hans J. Queisser. Detailed balance limit of efficiency of p-n junction solar cells. *J. Appl. Phys.*, 32:510, 1961.

[116] Moritz Limpinsel, Nima Farhi, Nicholas Berry, Jeffrey Lindemuth, Craig L. Perkins, Qiyin Lin, and Matt Law. An inversion layer at the surface of n-type iron pyrite. *Energ. Environ. Sci.*, 7:1974, 2014.

[117] Jeff Walter, Xin Zhang, Bryan Voigt, Ryan Hool, Mike Manno, Frazier Mork, Eray S. Aydil, and Chris Leighton. Surface conduction in n -type pyrite FeS_2 single crystals. *Physi. Rev. Mater.*, 1:065403, 2017.

[118] Bryan Voigt, William Moore, Michael Manno, Jeff Walter, Jeff D. Jeremiason, Eray S. Aydil, and Chris Leighton. Transport Evidence for Sulfur Vacancies as the Origin of Unintentional n-Type Doping in Pyrite FeS_2. *ACS Appl. Mater. interfaces*, 11:15552, 2019.

[119] M. Bronold, Y. Tomm, and W. Jaegermann. Surface states on cubic d-band semiconductor pyrite (FeS_2). *Surf. Sci.*, 314:L931, 1994.

[120] A. Ennaoui, S. Fiechter, W. Jaegermann, and H. Tributsch. Photoelectrochemistry of Highly Quantum Efficient Single-Crystalline n-FeS_2 (Pyrite). *J. Electrochem. Soc.*, 133:97, 1986.

[121] M. Bronold, K. Büker, S. Kubala, C. Pettenkofer, and H. Tributsch. Surface Preparation of FeS_2 via Electrochemical Etching and Interface Formation with Metals. *Phys. Status Solidi A*, 135:231, 1993.

[122] K. Büker, N. Alonso-Vante, and H. Tributsch. Photovoltaic output limitation of n-FeS_2 (pyrite) Schottky barriers: A temperature-dependent characterization. *J. Appl. Phys.*, 72:5721, 1992.

[123] Bryan Voigt, William Moore, Moumita Maiti, Jeff Walter, Bhaskar Das, Michael Manno, Chris Leighton, and Eray S. Aydil. Observation of an internal p–n junction in pyrite fes_2 single crystals: Potential origin of the low open circuit voltage in pyrite solar cells. *ACS Materials Letters*, 2(7):861–868, 2020.

[124] A. Krishnamoorthy, F. W. Herbert, S. Yip, K. J V. Vliet, and B. Yildiz. Electronic states of intrinsic surface and bulk vacancies in FeS_2. *J. Phys.: Condens. Mater.*, 25:045004, 2013.

[125] Jun Hu, Yanning Zhang, Matt Law, and Ruqian Wu. First-principles studies of the electronic properties of native and substitutional anionic defects in bulk iron pyrite. *Phys. Rev. B*, 85:085203, 2012.

[126] Liping Yu, Stephan Lany, Robert Kykyneshi, Vorranutch Jieratum, Ram Ravichandran, Brian Pelatt, Emmeline Altschul, Heather A. S. Platt, John F. Wager, Douglas A. Keszler, and Alex Zunger. Iron chalcogenide photovoltaic absorbers. *Adv. Energy Mater.*, 1(5):748–753, 2011.

[127] J. Hu, Y. Zhang, M. Law, and R. Wu. Increasing the band gap of iron pyrite by alloying with oxygen. *J. Am. Chem. Soc.*, 134:13216, 2012.

[128] M. Verónica Ganduglia-Pirovano, Alexander Hofmann, and Joachim Sauer. Oxygen vacancies in transition metal and rare earth oxides: Current state of understanding and remaining challenges. *Surf. Sci. Rep.*, 62:219, 2007.

[129] Y. N. Zhang, M. Law, and R. Q. Wu. Atomistic Modeling of Sulfur Vacancy Diffusion Near Iron Pyrite Surfaces. *J. Phys. Chem. C*, 119:24859, 2015.

[130] F W Herbert, A Krishnamoorthy, W Ma, K J Van Vliet, and B Yildiz. Electrochimica Acta Dynamics of point defect formation , clustering and pit initiation on the pyrite surface. *Electrochim. Acta*, 127:416, 2014.

[131] A Rohrbach, J Hafner, and G Kresse. Electronic correlation effects in transition-metal sulfides. *J. Phys. Condens. Mater.*, 15:979–996, 2003.

[132] Aleksandr V. Marenich, Steven V. Jerome, Christopher J. Cramer, and Donald G. Truhlar. Charge model 5: An extension of hirshfeld population analysis for the accurate description of molecular interactions in gaseous and condensed phases. *J. Chem. Theory Comput.*, 8:527, 2012.

[133] B. Wang, S. L. Li, and D. G. Truhlar. Modeling the partial atomic charges in inorganometallic molecules and solids and charge redistribution in lithium-ion cathodes. *J. Chem. Theory Comput.*, 10:5640, 2014.

[134] Graeme Henkelman, Andri Arnaldsson, and Hannes Jónsson. A fast and robust algorithm for Bader decomposition of charge density. *Comput. Mater. Sci.*, 36:354–360, 2006.

[135] W. Tang, E. Sanville, and G. Henkelman. A grid-based Bader analysis algorithm without lattice bias. *J. Phys. Condens. Matter*, 21:084204, 2009.

[136] Min Yu and Dallas R. Trinkle. Accurate and efficient algorithm for Bader charge integration. *J. Chem. Phys.*, 134:064111, 2011, 1010.4916.

[137] Edward Sanville, Steven D. Kenny, Roger Smith, and Graeme Henkelman. Improved grid-based algorithm for bader charge allocation. *J. Comput. Chem.*, 28(5):899–908, 2007.

[138] Chris G. Van de Walle and Jörg Neugebauer. First-principles calculations for defects and impurities: Applications to III-nitrides. *J. Appl. Phys.*, 95:3851, 2004, 1106.1618.

[139] J. Buckeridge. sc-fermi.

[140] Ji Hui Yang, Wan Jian Yin, Ji Sang Park, and Su Huai Wei. Self-regulation of charged defect compensation and formation energy pinning in semiconductors. *Sci. Rep.*, 5:16977, 2015.

[141] Christoph Freysoldt, Jörg Neugebauer, and Chris G. Van De Walle. Fully Ab initio finite-size corrections for charged-defect supercell calculations. *Phys. Rev. Lett.*, 102:016402, 2009.

[142] Christoph Freysoldt, Jörg Neugebauer, and Chris G. Van de Walle. Electrostatic interactions between charged defects in supercells. *Phys. Status Solidi B*, 248:1067, 2011.

[143] A. M. Karguppikar and A. G. Vedeshwar. Transport properties of thin iron pyrite films. *Phys. Status Solidi A*, 95:717, 1986.

[144] N. Hamdadou, A. Khelil, and J. C. Bernède. Pyrite FeS_2 films obtained by sulphuration of iron pre-deposited films. *Mater. Chem. Phys.*, 78:591, 2003.

[145] Ruoshi Sun, M. K. Y. Chan, and G. Ceder. First-principles electronic structure and relative stability of pyrite and marcasite: Implications for photovoltaic performance. *Phys. Rev. B*, 83:235311, 2011.

[146] V. N. Antonov, L. P. Germash, A. P. Shpak, and A. N. Yaresko. Electronic structure, optical and x-ray emission spectra in fes_2. *physica status solidi (b)*, 246(2):411–416, 2009.

[147] Tzuen Rong Yang, Jiang Tsu, Yu Jeng, Kuang Huang, Shinn Horng Chen, Ming Yih Tsay, and Ying Sheng. Optical-absorption study of synthetic pyrite FeS_2 single crystals Optical-absorption study of synthetic pyrite Fe & single crystals. *J. Appl. Phys.*, 77:1710, 1995.

[148] William W. Kou and Mohindar S. Seehra. Optical absorption in iron pyrite (FeS_2. *Phys. Rev. B*, 18:7062–7068, 1978.

[149] Ming-Yih Tsay, Ying-Sheng Huang, and Yang-Fang Chen. Photoconduction of synthetic pyrite FeS_2 single crystals. *J. Appl. Phys.*, 74(4):2786–2789, 1993.

[150] A. M. Karguppikar and A. G. Vedeshwar. Electrical and optical properties of natural iron pyrite (FeS_2). *physica status solidi (a)*, 109(2):549–558, 1988.

[151] A. K. Abass, Z. A. Ahmed, and R. E. Tahir. Absorption edge measurements in chemically deposited pyrite FeS_2 thin layers. *J. Appl. Phys.*, 61(6):2339–2341, 1987.

[152] A Schlegel and P Wachter. Optical properties, phonons and electronic structure of iron pyrite (FeS_2). *J. Phys. C: Sol. State Phys.*, 9:3363–3369, 1976.

[153] M. S. Seehra and S. S. Seehra. Temperature dependence of the band gap of FeS_2. *Phys. Rev. B*, 19:6620–6621, 1979.

[154] P Lazić, R Armiento, F W Herbert, R Chakraborty, R Sun, M K Y Chan, K Hartman, T Buonassisi, B Yildiz, and G Ceder. Low intensity conduction states in FeS2: implications for absorption, open-circuit voltage and surface recombination. *J. Phys. Condens. Mater.*, 25:465801, 2013.

[155] S. Miyahara and T. Teranishi. Magnetic properties of FeS_2 and CoS_2. *J. Appl. Phys.*, 39(2):896–897, 1968.

[156] Xin Zhang, Tom Scott, Tyler Socha, David Nielsen, Michael Manno, Melissa Johnson, Yuqi Yan, Yaroslav Losovyj, Peter Dowben, Eray S. Aydil, and Chris Leighton. Phase stability and stoichiometry in thin film iron pyrite: Impact on electronic transport properties. *ACS Appl. Mater. Interfaces*, 7(25):14130–14139, 2015.

[157] Werner Puff, M. Birkholz, Adam G. Balogh, and S. Fiechter. Vacancy-Type Defects in Iron-Pyrite FeS_{2-x}. *Mater. Sci. Forum*, 255-257:342, 1997.

[158] E. Watson, D. Cherniak, and E. Frank. Retention of biosignatures and mass-independent fractionations in pyrite: Self-diffusion of sulfur. *Geochimica et Cosmochimica Acta*, 73:4792–4802, 2009.

[159] Debmalya Ray, Bryan Voigt, Michael Manno, Chris Leighton, Eray S. Aydil, and Laura Gagliardi. Sulfur vacancy clustering and its impact on electronic properties in pyrite FeS_2. *Chem. Mater.*, 32(11):4820–4831, 2020.

[160] Bryan Voigt, Bhaskar Das, David M. Carr, Debmalya Ray, Moumita Maiti, William Moore, Michael Manno, Jeff Walter, Eray S. Aydil, and Chris Leighton. Mitigation of the internal p-n junction in CoS_2-contacted FeS_2 single crystals: Accessing bulk semiconducting transport. *Phys. Rev. Materials*, 5:025405, 2021.

[161] Omar K. Farha, A. Özgür Yazaydin, Ibrahim Eryazici, Christos D. Malliakas, Brad G. Hauser, Mercouri G. Kanatzidis, Sonbinh T. Nguyen, Randall Q. Snurr, and Joseph T. Hupp. De novo synthesis of a metal-organic framework material featuring ultrahigh surface area and gas storage capacities. *Nat. Chem.*, 2:944–948, 2010.

[162] Mircea Dincă and Jeffrey R. Long. Hydrogen storage in microporous metal-organic frameworks with exposed metal sites. *Angew. Chem. Int. Ed.*, 47:6766–6779, 2008.

[163] Zongbi Bao, Ganggang Chang, Huabin Xing, Rajamani Krishna, Qilong Ren, and Banglin Chen. Potential of microporous metal-organic frameworks for separation of hydrocarbon mixtures. *Energ. Environ. Sci.*, 9:3612–3641, 2016.

[164] Jian Rong Li, Ryan J. Kuppler, and Hong Cai Zhou. Selective gas adsorption and separation in metal-organic frameworks. *Chem. Soc. Rev.*, 38:1477–1504, 2009.

[165] Hakan Demir, Samuel J. Stoneburner, Wooseok Jeong, Debmalya Ray, Xuan Zhang, Omar K. Farha, Christopher J. Cramer, J. Ilja Siepmann, and Laura Gagliardi. Metal-Organic Frameworks with Metal-Catecholates for O2/N2 Separation. *J. Phys. Chem. C*, 123:12935–12946, 2019.

[166] Jeongyong Lee, Omar K. Farha, John Roberts, Karl A. Scheidt, Sonbinh T. Nguyen, and Joseph T. Hupp. Metal-organic framework materials as catalysts. *Chem. Soc. Rev.*, 38:1450–1459, 2009.

[167] Jorge Gascon, Avelino Corma, Freek Kapteijn, and Francesc X. Llabrés I Xamena. Metal organic framework catalysis: Quo vadis? *ACS Catal.*, 4:361–378, 2014.

[168] Takaaki Ikuno, Jian Zheng, Aleksei Vjunov, Maricruz Sanchez-Sanchez, Manuel A. Ortuño, Dale R. Pahls, John L. Fulton, Donald M. Camaioni, Zhanyong Li, Debmalya Ray, B. Layla Mehdi, Nigel D. Browning, Omar K. Farha, Joseph T. Hupp, Christopher J. Cramer, Laura Gagliardi, and Johannes A. Lercher. Methane oxidation to methanol catalyzed by cu-oxo clusters stabilized in nu-1000 metal–organic framework. *J. Am. Chem. Soc.*, 139(30):10294–10301, 2017.

[169] V. Bernales, M. A. Ortuño, D. G. Truhlar, C. J. Cramer, and L. Gagliardi. Computational design of functionalized metal-organic framework nodes for catalysis. *ACS Cent. Sci.*, 4:5–19, 2018.

[170] Dong Yang, Carlo Alberto Gaggioli, Debmalya Ray, Melike Babucci, Laura Gagliardi, and Bruce C. Gates. Tuning Catalytic Sites on Zr_6O_8 Metal-Organic Framework Nodes via Ligand and Defect Chemistry Probed with tert-Butyl Alcohol Dehydration to Isobutylene. *J. Am. Chem. Soc.*, 142:8044–8056, 2020.

[171] Patricia Horcajada, Tamim Chalati, Christian Serre, Brigitte Gillet, Catherine Sebrie, Tarek Baati, Jarrod F. Eubank, Daniela Heurtaux, Pascal Clayette, Christine Kreuz, Jong San Chang, Young Kyu Hwang, Veronique Marsaud, Phuong Nhi Bories, Luc Cynober, Sophie Gil, Gérard Férey, Patrick Couvreur, and Ruxandra Gref. Porous metal-organic-framework nanoscale carriers as a potential platform for drug deliveryand imaging. *Nat. Mater.*, 9:172–178, 2010.

[172] Lauren E. Kreno, Kirsty Leong, Omar K. Farha, Mark Allendorf, Richard P. Van Duyne, and Joseph T. Hupp. Metal-organic framework materials as chemical sensors. *Chem. Rev.*, 112:1105–1125, 2012.

[173] Caleb A. Kent, Brian P. Mehl, Liqing Ma, John M. Papanikolas, Thomas J. Meyer, and Wenbin Lin. Energy transfer dynamics in metal-organic frameworks. *J. Am. Chem. Soc.*, 132:12767–12769, 2010.

[174] Subhadip Goswami, Lin Ma, Alex B.F. Martinson, Michael R. Wasielewski, Omar K. Farha, and Joseph T. Hupp. Toward Metal-Organic Framework-Based Solar Cells: Enhancing Directional Exciton Transport by Collapsing Three-Dimensional Film Structures. *ACS Appl. Mater. interfaces*, 8:30863–30870, 2016.

[175] William A. Maza, Roberto Padilla, and Amanda J. Morris. Concentration Dependent Dimensionality of Resonance Energy Transfer in a Postsynthetically Doped Morphologically Homologous Analogue of UiO-67 MOF with a Ruthenium(II) Polypyridyl Complex. *J. Am. Chem. Soc.*, 137:8161–8168, 2015.

[176] Jin Liang Wang, Cheng Wang, and Wenbin Lin. Metal-organic frameworks for light harvesting and photocatalysis. *ACS Catal.*, 2:2630–2640, 2012.

[177] Idan Hod, Matthew D. Sampson, Pravas Deria, Clifford P. Kubiak, Omar K. Farha, and Joseph T. Hupp. Fe-Porphyrin-Based Metal-Organic Framework Films as High-Surface Concentration, Heterogeneous Catalysts for Electrochemical Reduction of CO2. *ACS Catal.*, 5:6302–6309, 2015.

[178] Nikolay Kornienko, Yingbo Zhao, Christopher S. Kley, Chenhui Zhu, Dohyung Kim, Song Lin, Christopher J. Chang, Omar M. Yaghi, and Peidong Yang. Metal-Organic Frameworks for Electrocatalytic Reduction of Carbon Dioxide. *J. Am. Chem. Soc.*, 137:14129–14135, 2015.

[179] Guodong Wu, Jiahong Huang, Ying Zang, Jun He, and Gang Xu. Porous field-effect transistors based on a semiconductive metal-organic framework. *J. Am. Chem. Soc.*, 139:1360–1363, 2017.

[180] Doufeng Wu, Ziyang Guo, Xinbo Yin, Qingqing Pang, Binbin Tu, Lijuan Zhang, Yong Gang Wang, and Qiaowei Li. Metal-organic frameworks as cathode materials for Li-O 2 batteries. *Adv. Mater.*, 26:3258–3262, 2014.

[181] Michael G. Campbell, Sophie F. Liu, Timothy M. Swager, and Mircea Dincă. Chemiresistive Sensor Arrays from Conductive 2D Metal-Organic Frameworks. *J. Am. Chem. Soc.*, 137:13780–13783, 2015.

[182] Khalid AlKaabi, Casey R. Wade, and Mircea Dincă. Transparent-to-Dark Electrochromic Behavior in Naphthalene-Diimide-Based Mesoporous MOF-74 Analogs. *Chem*, 1:264–272, 2016.

[183] Chung Wei Kung, Timothy Chiaan Wang, Joseph E. Mondloch, David Fairen-Jimenez, Daniel M. Gardner, Wojciech Bury, Jordan Matthew Klingsporn, Jonathan C. Barnes, Richard Van Duyne, J. Fraser Stoddart, Michael R. Wasielewski, Omar K. Farha, and Joseph T. Hupp. Metal-organic framework thin films composed of free-standing acicular nanorods exhibiting reversible electrochromism. *Chem. Mater.*, 25:5012–5017, 2013.

[184] D. Sheberla, J. C. Bachman, J. S. Elias, C. J. Sun, Y. Shao-Horn, and M. Dincă. Conductive MOF electrodes for stable supercapacitors with high areal capacitance. *Nat. Mater.*, 16:220–224, 2017.

[185] Kyung Min Choi, Hyung Mo Jeong, Jung Hyo Park, Yue Biao Zhang, Jeung Ku Kang, and Omar M. Yaghi. Supercapacitors of nanocrystalline metal-organic frameworks. *ACS Nano*, 8:7451–7457, 2014.

[186] Lei Sun, Michael G. Campbell, and Mircea Dincă. Electrically Conductive Porous Metal-Organic Frameworks. *Angew. Chem. Int. Ed.*, 55:3566–3579, 2016.

[187] Sanjeev K. Bhardwaj, Neha Bhardwaj, Rajnish Kaur, Jyotsana Mehta, Amit L. Sharma, Ki Hyun Kim, and Akash Deep. An overview of different strategies to introduce conductivity in metal-organic frameworks and miscellaneous applications thereof. *J. Mater. Chem. A*, 6:14992–15009, 2018.

[188] C. W. Kung, K. Otake, C. T. Buru, S. Goswami, Y. Cui, J. T. Hupp, A. M. Spokoyny, and O. K. Farha. Increased electrical conductivity in a mesoporous metal-organic framework featuring metallacarboranes guests. *J. Am. Chem. Soc.*, 140:3871–3875, 2018.

[189] A. A. Talin, A. Centrone, A. C. Ford, M. E. Foster, V. Stavila, P. Haney, A. R. Kinney, V. Szalai, F. El Gabaly, H. P. Yoon, F. Léonard, and M. D Allendorf. Tunable electrical conductivity in metal-organic framework thin-film devices. *Science*, 343:66–69, 2014.

[190] Lilia S. Xie, Grigorii Skorupskii, and Mircea Dincă. Electrically Conductive Metal-Organic Frameworks. *Chem. Rev.*, 120:8536–8580, 2020.

[191] D. M. D'Alessandro. Exploiting redox activity in metal-organic frameworks: Concepts, trends and perspectives. *Chem. Commun.*, 52:8957–8971, 2016.

[192] Idan Hod, Wojciech Bury, Daniel M. Gardner, Pravas Deria, Vladimir Roznyatovskiy, Michael R. Wasielewski, Omar K. Farha, and Joseph T. Hupp. Bias-switchable permselectivity and redox catalytic activity of a ferrocene-functionalized, thin-film metal-organic framework compound. *J. Phys. Chem. Lett.*, 6:586–591, 2015.

[193] Karan Maindan, Xinlin Li, Jierui Yu, and Pravas Deria. Controlling Charge-Transport in Metal-Organic Frameworks: Contribution of Topological and Spin-State Variation on the Iron-Porphyrin Centered Redox Hopping Rate. *J. Phys. Chem. B*, 123:8814–8822, 2019.

[194] Shaoyang Lin, Pavel M. Usov, and Amanda J. Morris. The role of redox hopping in metal-organic framework electrocatalysis. *Chem. Commun.*, 54:6965–6974, 2018.

[195] Yoji Kobayashi, Benjamin Jacobs, Mark D. Allendorf, and Jeffrey R. Long. Conductivity, doping, and redox chemistry of a microporous dithiolene-based metal-organic framework. *Chem. Mater.*, 22:4120–4122, 2010.

[196] Jesse G. Park, Michael L. Aubrey, Julia Oktawiec, Khetpakorn Chakarawet, Lucy E. Darago, Fernande Grandjean, Gary J. Long, and Jeffrey R. Long. Charge delocalization and bulk electronic conductivity in the mixed-valence metal-organic framework Fe(1,2,3-triazolate)$_2$(BF_4)$_x$. *J. Am. Chem. Soc.*, 140:8526–8534, 2018.

[197] Lilia S. Xie, Lei Sun, Ruomeng Wan, Sarah S. Park, Jordan A. Degayner, Christopher H. Hendon, and Mircea Dincă. Tunable Mixed-Valence Doping toward Record Electrical Conductivity in a Three-Dimensional Metal-Organic Framework. *J. Am. Chem. Soc.*, 140:7411–7414, 2018.

[198] Michael L. Aubrey, Brian M. Wiers, Sean C. Andrews, Tsuneaki Sakurai, Sebastian E. Reyes-Lillo, Samia M. Hamed, Chung Jui Yu, Lucy E. Darago, Jarad A. Mason, Jin Ook Baeg, Fernande Grandjean, Gary J. Long, Shu Seki, Jeffrey B. Neaton, Peidong Yang, and Jeffrey R. Long. Electron delocalization and charge mobility as a function of reduction in a metal-organic framework. *Nat. Mater.*, 17:625–632, 2018.

[199] Xiaowa Nie, Ambarish Kulkarni, and David S. Sholl. Computational prediction of metal organic frameworks suitable for molecular infiltration as a route to development of conductive materials. *J. Phys. Chem. Lett.*, 6:1586–1591, 2015.

[200] Lei Sun, Tomoyo Miyakai, Shu Seki, and Mircea Dincă. Mn2(2,5-disulfhydrylbenzene-1,4-dicarboxylate): A microporous metal-organic framework with infinite (-Mn-S-)∞ chains and high intrinsic charge mobility. *J. Am. Chem. Soc.*, 135:8185–8188, 2013.

[201] H.W. Kroto, J.R. Heath, S.C. O'Brien, R.F. Curl, and R E Smalley. Kroto Et Al 1985. *Nature*, 318:162–163, 1985.

[202] H. K. Chae, D. Y. Siberio-Pérez, J. Kim, Y. Go, M. Eddaoudi, A. J. Matzger, M. O'Keeffe, and O. M. Yaghi. A route to high surface area, porosity and inclusion of large molecules in crystals. *Nature*, 427:523–527, 2004.

[203] Haibing Meng, Chong Zhao, Mingzhe Nie, Chunru Wang, and Taishan Wang. Changing the Hydrophobic MOF Pores through Encapsulating Fullerene C_{60} and Metallofullerene $Sc_3C_2@C_{80}$. *J. Phys. Chem. C*, 123:6265–6269, 2019.

[204] Xiaojing Liu, Mariana Kozlowska, Timur Okkali, Danny Wagner, Tomohiro Higashino, Gerald Brenner-Weiß, Stefan M. Marschner, Zhihua Fu, Qiang Zhang, Hiroshi Imahori, Stefan Bräse, Wolfgang Wenzel, Christof Wöll, and Lars Heinke. Photoconductivity in

Metal–Organic Framework (MOF) Thin Films. *Angew. Chem. Int. Ed.*, 58:9590–9595, 2019.

[205] Yongqiang Feng, Taishan Wang, Yongjian Li, Jie Li, Jingyi Wu, Bo Wu, Li Jiang, and Chunru Wang. Steering Metallofullerene Electron Spin in Porous Metal-Organic Framework. *J. Am. Chem. Soc.*, 137:15055–15060, 2015.

[206] Manuel Souto, Joaquín Calbo, Samuel Mañas-Valero, Aron Walsh, and Guillermo Mínguez Espallargas. Charge-transfer interactions between fullerenes and a mesoporous tetrathiafulvalene-based metal-organic framework. *Beilstein J. Nanotechnol.*, 10:1883–1893, 2019.

[207] Saied Md Pratik, Laura Gagliardi, and Christopher J. Cramer. Boosting photoelectric conductivity in porphyrin-based mofs incorporating C_{60}. *J. Phys. Chem. C*, 124:1878–1887, 2020.

[208] Nazario Martín. New challenges in fullerene chemistry. *Chem. Commun.*, 20:2093–2104, 2006.

[209] Francesco Giacalone and Nazario Martín. Fullerene polymers: Synthesis and properties. *Chem. Rev.*, 106:5136–5190, 2006.

[210] A. Zieleniewska, F. Lodermeyer, A. Roth, and D. M. Guldi. Fullerenes-how 25 years of charge transfer chemistry have shaped our understanding of (interfacial) interactions. *Chem. Soc. Rev.*, 47:702–714, 2018.

[211] O. Vostrowsky and A. Hirsch. Heterofullerenes. *Chem. Rev.*, 106:5191–5207, 2006.

[212] Dana L. Caulder and Kenneth N. Raymond. Supermolecules by design. *Acc. Chem. Res.*, 32:975–982, 1999.

[213] Xiao Yuan Ren and Zi Yang Liu. Structural and electronic properties of S-doped fullerene C_{58} : Where is the S atom situated? *J. Chem. Phys.*, 122:1–5, 2005.

[214] Yan Chai, Ting Guo, Changming Jin, Robert E. Haufler, L. P.Felipe Chibante, Jan Fure, Lihong Wang, J. Michael Alford, and Richard E. Smalley. Fullerenes with metals inside. *J. Phys. Chem.*, 95:7564–7568, 1991.

[215] H. J. Muhr, R. Nesper, B. Schnyder, and R. Kötz. The boron heterofullerenes $C_{59}B$ and $C_{69}B$: Generation, extraction, mass spectrometric and XPS characterization. *Chem. Phys. Lett.*, 249:399–405, 1996.

[216] Paul W. Dunk, Antonio Rodríguez-Fortea, Nathan K. Kaiser, Hisanori Shinohara, Josep M. Poblet, and Harold W. Kroto. Formation of heterofullerenes by direct exposure of C_{60} to boron vapor. *Angew. Chem. Int. Ed.*, 52:315–319, 2013.

[217] Tsutomu Ohtsuki, Kaoru Ohno, Keiichiro Shiga, Yoshiyuki Kawazoe, Yutaka Maruyama, and Kazuyoshi Masumoto. Formation of As- and Ge-doped heterofullerenes. *Phys. Rev. B*, 60:1531–1534, 1999.

[218] Iris Lamparth, Berthold Nuber, Georg Schick, Andreas Skiebe, Thomas Grösser, and Andreas Hirsch. $C_{59}N^+$ and $C_{69}N^+$: isoelectronic heteroanalogues of C_{60} and C_{70}. *Angew. Chem. Int. Ed.*, 34:2257–2259, 1995.

[219] Johannes Averdung, Heinrich Luftmann, Ingo Schlachter, and Jochen Mattay. Aza-dihydro[60]fullerene in the gas phase. A mass-spectrometric and quantumchemical study. *Tetrahedron*, 51:6977–6982, 1995.

[220] Wei Guang Liu and Donald G. Truhlar. Computational Linker Design for Highly Crystalline Metal-Organic Framework NU-1000. *Chem. Mater.*, 29:8073–8081, 2017.

[221] A. D. Becke and E. R. Johnson. A density-functional model of the dispersion interaction. *J. Chem. Phys.*, 123:154101, 2005.

[222] C Fonseca Guerra, JG Snijders, G t tegatteschi2006molecular Velde, and E Jan Baerends. Towards an order-n dft method. *Theor. Chem. Acc.*, 99(6):391–403, 1998.

[223] G t Te Velde, F Matthias Bickelhaupt, Evert Jan Baerends, C Fonseca Guerra, Stan JA van Gisbergen, Jaap G Snijders, and Tom Ziegler. Chemistry with adf. *J. Comput. Chem.*, 22(9):931–967, 2001.

[224] Evert Jan Baerends, Tom Ziegler, A. J. Atkins, Jochen Autschbach, Donald Bashford, A. Bérces, F. Matthias Bickelhaupt, C. Bo, P. M. Boerritger, Luigi Cavallo, D. P. Chong, D. V. Chulhai, L. Deng, R. M. Dickson, J. M. Dieterich, D. E. Ellis, M. van Faassen, A. Ghysels, A. Giammona, Stan J. A. van Gisbergen, A. W. Götz, S. Gusarov, F. E. Harris, P. van den Hoek, Christoph R. Jacob, H. Jacobsen, L. Jensen, J. W. Kaminski, G. van Kessel, F. Kootstra, A. Kovalenko, Mykhaylo Krykunov, Erik van Lenthe, D. A. McCormack, A. Michalak, M. Mitoraj, S. M. Morton, Johannes Neugebauer, V. P. Nicu, Louis Noodleman, V. P. Osinga, S. Patchkovskii, Michele Pavanello, C. A. Peeples, Pierre Herman Theodoor Philipsen, D. Post, Cory C. Pye, W. Ravenek, J. I. Rodríguez, P. Ros, R. Rüger, P. R. T. Schipper, H. van Schoot, G. Schreckenbach, J. S. Seldenthuis, Mike Seth, Jaap G. Snijders, Miquel Solà, M. Swart, D. Swerhone, G. te Velde, P. Vernooijs, L. Versluis, Lucas Visscher, O. Visser, Fan Wang, T. A. Wesolowski, E. M. van Wezenbeek, G. Wiesenekker, S. K. Wolff, T. K. Woo, and A. L. Yakovlev. ADF2016, SCM, Theoretical Chemistry, Vrije Universiteit, Amsterdam, The Netherlands, https://www.scm.com.

[225] Y. Zhao and D. G. Truhlar. The M06 suite of density functionals for main group thermochemistry, thermochemical kinetics, noncovalent interactions, excited states, and transition elements: two new functionals and systematic testing of four M06-class functionals and 12 other functionals. *Theor. Chem. Acc.*, 120:215–241, 2008.

[226] Sameer Patwardhan and George C. Schatz. Theoretical Investigation of Charge Transfer in Metal Organic Frameworks for Electrochemical Device Applications. *J. Phys. Chem. C*, 119:24238–24247, 2015.

[227] Chung Wei Kung, Subhadip Goswami, Idan Hod, Timothy C. Wang, Jiaxin Duan, Omar K. Farha, and Joseph T. Hupp. Charge Transport in Zirconium-Based Metal-Organic Frameworks. *Acc. Chem. Res.*, 53:1187–1195, 2020.

[228] Hongcun Bai, Wenxin Ji, Xiangyu Liu, Liqiong Wang, Nini Yuan, and Yongqiang Ji. Doping the buckminsterfullerene by substitution: Density functional theory studies of $C_{59}X$ (X = B, N, Al, Si, P, Ga, Ge, and As). *J. Chem.*, 2013:1–9, 2012.

[229] Dante Gatteschi, Roberta Sessoli, and Jacques Villain. *Molecular nanomagnets*, volume 5. Oxford University Press on Demand, 2006.

[230] Frank Neese and Dimitrios A Pantazis. What is not required to make a single molecule magnet. *Faraday discussions*, 148:229–238, 2011.

[231] A. Caneschi, D. Gatteschi, R. Sessoli, A. L. Barra, L. C. Brunel, and M. Guillot. Alternating current susceptibility, high field magnetization, and millimeter band epr evidence for a ground s= 10 state in $[Mn_{12}O_{12}(CH_3COO)_{16}(H_2O)_4]$. $2CH_3COOH.4H_2O$. *J. Am. Chem. Soc.*, 113(15):5873–5874, 1991.

[232] Roberta Sessoli, Hui Lien Tsai, Ann R Schake, Sheyi Wang, John B Vincent, Kirsten Folting, Dante Gatteschi, George Christou, and David N Hendrickson. High-spin molecules:[mn12o12 (o2cr) 16 (h2o) 4]. *J. Am. Chem. Soc.*, 115(5):1804–1816, 1993.

[233] Roberta Sessoli, Dante Gatteschi, Andrea Caneschi, and MA Novak. Magnetic bistability in a metal-ion cluster. *Nature*, 365(6442):141–143, 1993.

[234] Anatole Abragam and Brebis Bleaney. *Electron paramagnetic resonance of transition ions*. OUP Oxford, 2012.

[235] Jun-Liang Liu, Yan-Cong Chen, Yan-Zhen Zheng, Wei-Quan Lin, Liviu Ungur, Wolfgang Wernsdorfer, Liviu F Chibotaru, and Ming-Liang Tong. Switching the anisotropy barrier of a single-ion magnet by symmetry change from quasi-d 5h to quasi-o h. *Chem. Sci.*, 4(8):3310–3316, 2013.

[236] Katie R Meihaus and Jeffrey R Long. Magnetic blocking at 10 k and a dipolar-mediated avalanche in salts of the bis (η8-cyclooctatetraenide) complex [er (cot) 2]-. *J. Am. Chem. Soc.*, 135(47):17952–17957, 2013.

[237] Liviu Ungur, Jennifer J Le Roy, Ilia Korobkov, Muralee Murugesu, and Liviu F Chibotaru. Fine-tuning the local symmetry to attain record blocking temperature and magnetic remanence in a single-ion magnet. *Angewandte Chemie*, 126(17):4502–4506, 2014.

[238] Jennifer J Le Roy, Liviu Ungur, Ilia Korobkov, Liviu F Chibotaru, and Muralee Murugesu. Coupling strategies to enhance single-molecule magnet properties of erbium–cyclooctatetraenyl complexes. *J. Am. Chem. Soc.*, 136(22):8003–8010, 2014.

[239] Conrad AP Goodwin, Fabrizio Ortu, Daniel Reta, Nicholas F Chilton, and David P Mills. Molecular magnetic hysteresis at 60 kelvin in dysprosocenium. *Nature*, 548(7668):439–442, 2017.

[240] Conrad AP Goodwin, Daniel Reta, Fabrizio Ortu, Nicholas F Chilton, and David P Mills. Synthesis and electronic structures of heavy lanthanide metallocenium cations. *J. Am. Chem. Soc.*, 139(51):18714–18724, 2017.

[241] Fu-Sheng Guo, Benjamin M Day, Yan-Cong Chen, Ming-Liang Tong, Akseli Mansikkamäki, and Richard A Layfield. A dysprosium metallocene single-molecule magnet functioning at the axial limit. *Angewandte Chemie*, 129(38):11603–11607, 2017.

[242] Fu-Sheng Guo, Benjamin M Day, Yan-Cong Chen, Ming-Liang Tong, Akseli Mansikkamäki, and Richard A Layfield. Magnetic hysteresis up to 80 kelvin in a dysprosium metallocene single-molecule magnet. *Science*, 362(6421):1400–1403, 2018.

[243] Javier Luzon and Roberta Sessoli. Lanthanides in molecular magnetism: so fascinating, so challenging. *Dalton Trans.*, 41(44):13556–13567, 2012.

[244] Franziska Völcker, Yanhua Lan, Annie K Powell, and Peter W Roesky. Slow magnetic relaxation in tris (diphosphanylamido) and tetra (phosphanoamido) dysprosium complexes. *Dalton Trans.*, 42(32):11471–11475, 2013.

[245] Peng Zhang, Li Zhang, and Jinkui Tang. Lanthanide single molecule magnets: progress and perspective. *Dalton Trans.*, 44(9):3923–3929, 2015.

[246] Conrad AP Goodwin. Blocking like it's hot: a synthetic chemists' path to high-temperature lanthanide single molecule magnets. *Dalton Trans.*, 49(41):14320–14337, 2020.

[247] Norman M Edelstein. Comparison of the electronic structure of the lanthanides and actinides. *J. alloys compds.*, 223(2):197–203, 1995.

[248] HM Crosswhite, H Crosswhite, WT Carnall, and AP Paszek. Spectrum analysis of u3+: Lacl3. *J. Chem. Phys.*, 72(9):5103–5117, 1980.

[249] N Magnani, E Colineau, R Eloirdi, J-C Griveau, R Caciuffo, SM Cornet, I May, CA Sharrad, D Collison, and REP Winpenny. Superexchange coupling and slow magnetic relaxation in a transuranium polymetallic complex. *Physical review letters*, 104(19):197202, 2010.

[250] Luis Escalera-Moreno, José J Baldoví, Alejandro Gaita-Ariño, and Eugenio Coronado. Exploring the high-temperature frontier in molecular nanomagnets: from lanthanides to actinides. *Inorg. Chem.*, 58(18):11883–11892, 2019.

[251] Daniel Reta, Fabrizio Ortu, Simon Randall, David P Mills, Nicholas F Chilton, Richard EP Winpenny, Louise Natrajan, Bryan Edwards, and Nikolas Kaltsoyannis. The performance of density functional theory for the description of ground and excited state properties of inorganic and organometallic uranium compounds. *J. Orgmet. Chem.*, 857:58–74, 2018.

[252] Mariano Spivak, Konstantinos D Vogiatzis, Christopher J Cramer, Coen de Graaf, and Laura Gagliardi. Quantum chemical characterization of single molecule magnets based on uranium. *J. Phys. Chem. A*, 121(8):1726–1733, 2017.

[253] Carlo Alberto Gaggioli and Laura Gagliardi. Theoretical investigation of plutonium-based single-molecule magnets. *Inorg. Chem.*, 57(14):8098–8105, 2018.

[254] Saurabh Kumar Singh, Christopher J Cramer, and Laura Gagliardi. Correlating electronic structure and magnetic anisotropy in actinide complexes [an (cot) 2], aniii/iv= u, np, and pu. *Inorg. Chem.*, 59(10):6815–6825, 2020.

[255] Matthew J. Polinski, E. B. Garner III, R. Maurice, N. Planas, J. T. Stritzinger, T. G. Parker, J. N. Cross, T. D. Green, E. V. Alekseev, S. M. Van Cleve, W. Depmeier, L. Gagliardi, M. Shatruk, K. L. Knappenberger, G. Liu, S. Skanthakumar, Lynda Soderholm, David A. Dixon, and Thomas E. Albrecht-Schmitt. Unusual structure, bonding and properties in a californium borate. *Nat. Chem.*, 6:387–392, 2014.

[256] Frankie D. White, David Dan, and Thomas E. Albrecht-Schmitt. Contemporary chemistry of berkelium and californium. *Chem. Eur. J.*, 25(44):10251–10261, 2019.

[257] S. K. Cary, M. Vasiliu, R. E. Baumbach, J. T. Stritzinger, T. D. Green, K. Diefenbach, J. N. Cross, K. L. Knappenberger, G. Liu, M. A. Silver, E. A. DePrince, M. J. Polinski, S. M. Van Cleve, J. H. House, N. Kikugawa, A. Gallagher, A. A. Arico, David A. Dixon, and Thomas E. Albrecht-Schmitt. Unusual structure, bonding and properties in a californium borate. *Nat. Commun.*, 16(6):6827–6834, 2015.

[258] Shane S. Galley, Carlo Alberto Gaggioli, Matthias Zeller, Cristian Celis-Barros, Thomas E. Albrecht-Schmitt, Laura Gagliardi, and Suzanne C. Bart. Evidence of alpha radiolysis in the formation of a californium nitrate complex. *Chem. Eur. J.*, 26(41):8885–8888, 2020.

[259] Shane S. Galley, Scott A. Pattenaude, Carlo Alberto Gaggioli, Yusen Qiao, Joseph M. Sperling, Matthias Zeller, Srimanta Pakhira, Jose L. Mendoza-Cortes, Eric J. Schelter, Thomas E. Albrecht-Schmitt, Laura Gagliardi, and Suzanne C. Bart. Synthesis and characterization of tris-chelate complexes for understanding f-orbital bonding in later actinides. *J. Am. Chem. Soc.*, 141(6):2356–2366, 2019, https://doi.org/10.1021/jacs.8b10251.

[260] C. Gao, A. Genoni, S. Gao, S. Jiang, A Soncini, and J. Overgaard. Observation of the asphericity of 4f-electron density and its relation to the magnetic anisotropy axis in single-molecule magnets. *Nat. Chem.*, 12(213-219):387–392, 2014.

[261] Axel D Becke. Density-functional thermochemistry. iv. a new dynamical correlation functional and implications for exact-exchange mixing. *J. Chem. Phys.*, 104(3):1040–1046, 1996.

[262] Erik Van Lenthe and Evert Jan Baerends. Optimized slater-type basis sets for the elements 1–118. *J. Comput. Chem.*, 24(9):1142–1156, 2003.

[263] E van Lenthe, Evert-Jan Baerends, and Jaap G Snijders. Relativistic regular two-component hamiltonians. *J. Chem. Phys.*, 99(6):4597–4610, 1993.

[264] Erik van Lenthe, Evert-Jan Baerends, and Jaap G Snijders. Relativistic total energy using regular approximations. *J. Chem. Phys.*, 101(11):9783–9792, 1994.

[265] Erik van Lenthe, Andreas Ehlers, and Evert-Jan Baerends. Geometry optimizations in the zero order regular approximation for relativistic effects. *J. Chem. Phys.*, 110(18):8943–8953, 1999.

[266] Björn O Roos, Peter R Taylor, and Per E M Siegbahn. A complete active space SCF method (CASSCF) using a density matrix formulated super-ci approach. *Chemical Physics*, 48(2):157–173, 1980.

[267] Björn O Roos. The complete active space self-consistent field method and its applications in electronic structure calculations. *Advances in Chemical Physics: Ab Initio Methods in Quantum Chemistry Part 2*, 69:399–445, 1987.

[268] Francesco Aquilante, Jochen Autschbach, Alberto Baiardi, Stefano Battaglia, Veniamin A Borin, Liviu F Chibotaru, Irene Conti, Luca De Vico, Mickaël Delcey, Ignacio Fdez. Galván, et al. Modern quantum chemistry with [open] molcas. *J. Chem. Phys.*, 152(21):214117, 2020.

[269] Per-Åke Malmqvist and Björn O Roos. The casscf state interaction method. *Chemical physics letters*, 155(2):189–194, 1989.

[270] Per Åke Malmqvist, Björn O Roos, and Bernd Schimmelpfennig. The restricted active space (ras) state interaction approach with spin–orbit coupling. *Chemical physics letters*, 357(3-4):230–240, 2002.

[271] Liviu F Chibotaru, Liviu Ungur, and Alessandro Soncini. The origin of nonmagnetic kramers doublets in the ground state of dysprosium triangles: evidence for a toroidal magnetic moment. *Angewandte Chemie*, 120(22):4194–4197, 2008.

[272] Liviu F Chibotaru, Liviu Ungur, Christophe Aronica, Hani Elmoll, Guillaume Pilet, and Dominique Luneau. Structure, magnetism, and theoretical study of a mixed-valence $Co(II)_3Co(III)_4$ heptanuclear wheel: Lack of smm behavior despite negative magnetic anisotropy. *J. Am. Chem. Soc.*, 130(37):12445–12455, 2008.

[273] Liviu F Chibotaru and Liviu Ungur. Ab initio calculation of anisotropic magnetic properties of complexes. i. unique definition of pseudospin hamiltonians and their derivation. *J. Chem. Phys.*, 137(6):064112, 2012.

[274] Francesco Aquilante, Roland Lindh, and Thomas Bondo Pedersen. Unbiased auxiliary basis sets for accurate two-electron integral approximations. *J. Chem. Phys.*, 127(11):114107, 2007.

[275] Qing Lu and Kirk A Peterson. Correlation consistent basis sets for lanthanides: The atoms La–Lu. *J. Chem. Phys.*, 145(5):054111, 2016.

[276] Rulin Feng and Kirk A Peterson. Correlation consistent basis sets for actinides. II. the atoms Ac and Np–Lr. *J. Chem. Phys.*, 147(8):084108, 2017.

[277] Thom H Dunning Jr. Gaussian basis sets for use in correlated molecular calculations. i. the atoms boron through neon and hydrogen. *J. Chem. Phys.*, 90(2):1007–1023, 1989.

[278] Wibe A De Jong, Robert J Harrison, and David A Dixon. Parallel douglas–kroll energy and gradients in nwchem: estimating scalar relativistic effects using douglas–kroll contracted basis sets. *J. Chem. Phys.*, 114(1):48–53, 2001.

[279] Alexander A. Granovsky. Extended Multi-configuration Quasi-degenerate Perturbation Theory: The New Approach to Multi-state Multi-reference Perturbation Theory. *J. Chem. Phys.*, 134(21):214113, 2011.

[280] Toru Shiozaki, Werner Győrffy, Paolo Celani, and Hans-Joachim Werner. Communication: Extended multi-state complete active space second-order perturbation theory: Energy and nuclear gradients. *J. Chem. Phys.*, 135(8):081106, 2011.

[281] Stefano Battaglia and Roland Lindh. Extended Dynamically Weighted CASPT2: The Best of Two Worlds. *J. Chem. Theory Comput.*, 16(3):1555–1567, 2020.

[282] Daniel Reta, Jon G. C. Kragskow, and Nicholas F. Chilton. Ab Initio Prediction of High-Temperature Magnetic Relaxation Rates in Single-Molecule Magnets. *J. Am. Chem. Soc.*, 143(15):5943–5950, 2021.

[283] Xixi Meng, Mengmeng Wang, Xiaoshuang Gou, Wenlong Lan, Kexin Jia, Yu-Xia Wang, Yi-Quan Zhang, Wei Shi, and Peng Cheng. Two C_{2v} Symmetry Dysprosium(III) Single-molecule Magnets With Effective Energy Barriers Over 600 K. *Inorg. Chem. Front.*, 3:2349–2355, 2021.

[284] B. Hammer, L. B. Hansen, and J. K. Nørskov. Improved Adsorption Energetics within Density-Functional Theory using Revised Perdew-Burke-Ernzerhof Functionals. *Phys. Rev. B*, 59:7413–7421, 1999.

[285] J. P. Perdew, J. A. Chevary, S. H. Vosko, K. A. Jackson, M. R. Pederson, D. J. Singh, and C. Fiolhais. Atoms, Molecules, Solids, and Surfaces: Applications of the Generalized Gradient Approximation for Exchange and Correlation. *Phys. Rev. B*, 46:6671–6687, 1992.

[286] R. Armiento and A. E. Mattsson. Functional designed to include surface effects in self-consistent density functional theory. *Phys. Rev. B*, 72:085108, 2005.

[287] A. E. Mattsson and R. Armiento. Implementing and testing the am05 spin density functional. *Phys. Rev. B*, 79:155101, 2009.

[288] A. E. Mattsson, R. Armiento, J. Paier, G. Kresse, J. M. Wills, and T. R. Mattsson. The am05 density functional applied to solids. *J. Chem. Phys.*, 128:084714, 2008.

[289] J. Tao, J. P. Perdew, V. N. Staroverov, and G. E. Scuseria. Climbing the Density Functional Ladder: Nonempirical meta generalized gradient approximation designed for molecules and solids. *Phys. Rev. Lett.*, 91:146401, 2003.

[290] Xavier Gonze and Changyol Lee. Dynamical matrices, born effective charges, dielectric permittivity tensors, and interatomic force constants from density-functional perturbation theory. *Phys. Rev. B*, 55:10355–10368, 1997.

Appendix A

Supporting Information of Chapter 2

Table A.1: Optimized lattice parameter values (in Å) of $CsPbI_3$ using PBE-D3, PBE, PBEsol, GAM, HSE06 functionals. In the platonic model of perovskites, the cells considered in the calculation are orthorhombic. Thus, for cubic phases we have three lattice parameters.

$CsPbI_3$			
Cubic	a	b	c
PBE-D3	8.89	8.89	12.57
PBE	9.04	9.04	12.80
PBEsol	8.81	8.81	12.48
GAM	9.03	9.03	12.75
HSE06	8.99	8.99	12.72
Tetragonal 1	a	b	c
PBE-D3	8.65	8.65	12.85
PBE	8.80	8.80	13.03
PBEsol	8.57	8.57	12.77
GAM	8.77	8.77	13.04
HSE06	8.79	8.79	12.89
Tetragonal 2	a	b	c
PBE-D3	8.64	8.64	12.84
PBE	8.82	8.82	12.99
PBEsol	8.61	8.61	12.68
GAM	8.78	8.78	13.05
HSE06	8.77	8.77	12.90
Orthorhombic 1	a	b	c
PBE-D3	8.72	9.00	12.30
PBE	8.89	9.11	12.55
PBEsol	8.64	8.93	12.25
GAM	8.88	9.10	12.52
HSE06	8.83	9.03	12.50
Orthorhombic 2	a	b	c
PBE-D3	8.88	8.61	12.53
PBE	9.03	8.86	12.69
PBEsol	8.87	8.54	12.45
GAM	8.99	8.77	12.66
HSE06	9.02	8.66	12.62

Table A.2: Optimized lattice parameter values (in Å) of $CsSnI_3$ using PBE-D3, PBE, PBEsol, GAM, HSE06 functionals. In the platonic model of perovskites, the cells considered in the calculation are orthorhombic. Thus, for cubic phases we have three lattice parameters.

$CsSnI_3$			
Cubic	a	b	c
PBE-D3	8.73	8.73	12.37
PBE	8.89	8.89	12.54
PBEsol	8.69	8.69	12.28
GAM	8.90	8.90	12.59
HSE06	8.81	8.81	12.47
Tetragonal 1	a	b	c
PBE-D3	8.54	8.54	12.64
PBE	8.72	8.72	12.79
PBEsol	8.52	8.52	12.44
GAM	8.70	8.70	12.90
HSE06	8.67	8.67	12.64
Tetragonal 2	a	b	c
PBE-D3	8.61	8.61	12.52
PBE	8.71	8.71	12.80
PBEsol	8.52	8.52	12.45
GAM	8.70	8.70	12.86
HSE06	8.69	8.69	12.62
Orthorhombic 1	a	b	c
PBE-D3	8.62	8.84	12.18
PBE	8.83	8.93	12.42
PBEsol	8.56	8.76	12.10
GAM	8.81	8.99	12.39
HSE06	8.77	8.86	12.34
Orthorhombic 2	a	b	c
PBE-D3	8.75	8.55	12.36
PBE	8.88	8.74	12.53
PBEsol	8.69	8.50	12.24
GAM	8.96	8.70	12.49
HSE06	8.89	8.61	12.45

Table A.3: Optimized lattice parameter values (in Å) of $CsGeI_3$ using PBE-D3, PBE, PBEsol, GAM, HSE06 functionals. In the platonic model of perovskites, the cells considered in the calculation are orthorhombic. Thus, for cubic phases we have three lattice parameters.

$CsGeI_3$			
Cubic	a	b	c
PBE-D3	8.32	8.32	11.78
PBE	8.49	8.49	11.99
PBEsol	8.24	8.24	11.70
GAM	8.53	8.53	12.04
HSE06	8.40	8.40	11.88
Tetragonal 1	a	b	c
PBE-D3	8.33	8.33	11.83
PBE	8.43	8.43	12.11
PBEsol	8.22	8.22	11.78
GAM	8.46	8.46	12.19
HSE06	8.39	8.39	11.91
Tetragonal 2	a	b	c
PBE-D3	8.29	8.29	11.87
PBE	8.40	8.40	12.19
PBEsol	8.22	8.22	11.77
GAM	8.43	8.43	12.27
HSE06	8.38	8.38	11.94
Orthorhombic 1	a	b	c
PBE-D3	8.30	8.38	11.75
PBE	8.45	8.52	11.96
PBEsol	8.23	8.31	11.65
GAM	8.48	8.6	11.96
HSE06	8.38	8.43	11.86
Orthorhombic 2	a	b	c
PBE-D3	8.31	8.30	11.84
PBE	8.49	8.44	12.01
PBEsol	8.27	8.21	11.74
GAM	8.54	8.43	12.10
HSE06	8.40	8.38	11.91

Table A.4: Optimized lattice parameter values (in Å) of $CsMgI_3$ using PBE-D3, PBE, PBEsol, GAM, HSE06 functionals. In the platonic model of perovskites, the cells considered in the calculation are orthorhombic. Thus, for cubic phases we have three lattice parameters.

$CsMgI_3$			
Cubic	a	b	c
PBE-D3	8.21	8.21	11.63
PBE	8.33	8.33	11.84
PBEsol	8.19	8.19	11.58
GAM	8.30	8.30	11.72
HSE06	8.29	8.29	11.75
Tetragonal 1	a	b	c
PBE-D3	8.04	8.04	12.10
PBE	8.26	8.26	12.12
PBEsol	8.00	8.00	12.06
GAM	8.14	8.14	12.13
HSE06	8.20	8.20	12.00
Tetragonal 2	a	b	c
PBE-D3	8.04	8.04	12.07
PBE	8.23	8.23	12.16
PBEsol	8.01	8.01	11.96
GAM	8.14	8.14	12.16
HSE06	8.22	8.22	11.94
Orthorhombic 1	a	b	c
PBE-D3	8.18	8.30	11.52
PBE	8.33	8.44	11.73
PBEsol	8.16	8.27	11.49
GAM	8.28	8.37	11.65
HSE06	8.28	8.37	11.63
Orthorhombic 2	a	b	c
PBE-D3	8.18	8.17	11.70
PBE	8.33	8.3	11.92
PBEsol	8.17	8.13	11.64
GAM	8.27	8.24	11.82
HSE06	8.27	8.24	11.82

Table A.5: Optimized lattice parameter values (in Å) of $CsCaI_3$ using PBE-D3, PBE, PBEsol, GAM, HSE06 functionals. In the platonic model of perovskites, the cells considered in the calculation are orthorhombic. Thus, for cubic phases we have three lattice parameters.

$CsCaI_3$			
Cubic	a	b	c
PBE-D3	8.67	8.67	12.22
PBE	8.78	8.78	12.46
PBEsol	8.60	8.60	12.15
GAM	8.72	8.72	12.32
HSE06	8.77	8.77	12.40
Tetragonal 1	a	b	c
PBE-D3	8.44	8.44	12.52
PBE	8.64	8.64	12.75
PBEsol	8.44	8.44	12.41
GAM	8.57	8.57	12.61
HSE06	8.60	8.6	12.66
Tetragonal 2	a	b	c
PBE-D3	8.46	8.46	12.50
PBE	8.64	8.64	12.72
PBEsol	8.41	8.41	12.43
GAM	8.56	8.56	12.62
HSE06	8.59	8.59	12.65
Orthorhombic 1	a	b	c
PBE-D3	8.54	8.75	12.03
PBE	8.71	8.87	12.29
PBEsol	8.47	8.70	11.99
GAM	8.66	8.79	12.20
HSE06	8.67	8.84	12.22
Orthorhombic 2	a	b	c
PBE-D3	8.61	8.50	12.22
PBE	8.81	8.64	12.44
PBEsol	8.61	8.41	12.16
GAM	8.74	8.58	12.33
HSE06	8.75	8.61	12.39

Table A.6: Optimized lattice parameter values (in Å) of $CsSrI_3$ using PBE-D3, PBE, PBEsol, GAM, HSE06 functionals. In the platonic model of perovskites, the cells considered in the calculation are orthorhombic. Thus, for cubic phases we have three lattice parameters.

$CsSrI_3$			
Cubic	a	b	c
PBE-D3	9.02	9.02	12.77
PBE	9.18	9.18	12.95
PBEsol	8.98	8.98	12.72
GAM	9.05	9.05	12.8
HSE06	9.09	9.09	12.88
Tetragonal 1	a	b	c
PBE-D3	8.69	8.69	13.02
PBE	8.89	8.89	13.19
PBEsol	8.67	8.67	12.96
GAM	8.79	8.79	13.07
HSE06	8.87	8.87	13.08
Tetragonal 2	a	b	c
PBE-D3	8.70	8.70	13.02
PBE	8.9	8.9	13.19
PBEsol	8.66	8.66	12.93
GAM	8.81	8.81	13.05
HSE06	8.85	8.85	13.11
Orthorhombic 1	a	b	c
PBE-D3	8.81	9.09	12.43
PBE	9.05	9.14	12.68
PBEsol	8.79	9.01	12.4
GAM	8.93	9.07	12.55
HSE06	9.02	9.09	12.62
Orthorhombic 2	a	b	c
PBE-D3	9.05	8.59	12.61
PBE	9.15	8.89	12.83
PBEsol	9.01	8.56	12.54
GAM	9.02	8.80	12.70
HSE06	9.17	8.72	12.74

Table A.7: Optimized lattice parameter values (in Å) of $CsBaI_3$ using PBE-D3, PBE, PBEsol, GAM, HSE06 functionals. In the platonic model of perovskites, the cells considered in the calculation are orthorhombic. Thus, for cubic phases we have three lattice parameters.

$CsBaI_3$			
Cubic	a	b	c
PBE-D3	9.43	9.43	13.35
PBE	9.61	9.61	13.64
PBEsol	9.40	9.40	13.31
GAM	9.46	9.46	13.38
HSE06	9.57	9.57	13.52
Tetragonal 1	a	b	c
PBE-D3	9.05	9.05	13.52
PBE	9.23	9.23	13.75
PBEsol	9.02	9.02	13.4
GAM	9.12	9.12	13.55
HSE06	9.17	9.17	13.67
Tetragonal 2	a	b	c
PBE-D3	9.05	9.05	13.50
PBE	9.27	9.27	13.71
PBEsol	9.02	9.02	13.40
GAM	9.13	9.13	13.54
HSE06	9.18	9.18	13.66
Orthorhombic 1	a	b	c
PBE-D3	9.16	9.41	12.90
PBE	9.47	9.42	13.19
PBEsol	9.14	9.3	12.85
GAM	9.32	9.31	12.92
HSE06	9.40	9.40	13.11
Orthorhombic 2	a	b	c
PBE-D3	9.48	8.76	13.04
PBE	9.47	9.23	13.30
PBEsol	9.35	8.89	12.95
GAM	9.40	9.00	13.05
HSE06	9.60	8.90	13.17

Table A.8: Predicted bandgaps (in eV) of $CsMI_3$ (M= Ge, Sn, Pb, Mg, Ca, Sr,Ba) using different functionals.D indicates direct band gap, while I indicates indirect band gap.

$CsPbI_3$						
Structure	PBE	PBE-D3	PBEsol	GAM	HSE06	HSE06+SOC
Cubic	1.485(D)	1.334(D)	1.161(D)	1.976(D)	1.938(D)	0.755(D)
Tetragonal 1	1.604(D)	1.484(D)	1.333(D)	2.056(D)	2.056(D)	1.095(D)
Tetragonal 2	1.596(D)	1.471(D)	1.340(D)	2.058(D)	2.096(D)	1.215(D)
Orthorhombic 1	1.755(D)	1.656(D)	1.531(D)	2.224(D)	2.244(D)	1.208(D)
Orthorhombic 2	1.831(D)	1.732(D)	1.556(D)	2.289(D)	2.322(D)	1.262(D)
$CsSnI_3$						
Cubic	0.459(D)	0.242(D)	0.003(I)	1.076(D)	0.694(D)	0.344(D)
Tetragonal 1	0.682(D)	0.475(D)	0.271(D)	1.250(D)	0.923(D)	0.709(D)
Tetragonal 2	0.677(D)	0.424(D)	0.296(D)	1.248(D)	0.899(D)	0.693(D)
Orthorhombic 1	0.747(D)	0.553(D)	0.416(D)	1.407(D)	1.000(D)	0.725(D)
Orthorhombic 2	0.817(D)	0.635(D)	0.504(D)	1.469(D)	1.127(D)	0.804(D)
$CsGeI_3$						
Cubic	0.647(D)	0.433(D)	0.274(D)	1.241(D)	0.872(D)	0.691(D)
Tetragonal 1	0.688(D)	0.468(D)	0.359(D)	1.282(D)	0.895(D)	0.732(D)
Tetragonal 2	0.709(D)	0.485(D)	0.347(D)	1.304(D)	0.920(D)	0.780(D)
Orthorhombic 1	0.720(D)	0.506(D)	0.383(D)	1.376(D)	0.946(D)	0.784(D)
Orthorhombic 2	0.778(D)	0.637(D)	0.462(D)	1.448(D)	1.016(D)	0.849(D)
$CsMgI_3$						
Cubic	1.146(D)	1.239(D)	1.221(D)	1.493(D)	2.074(D)	1.839(D)
Tetragonal 1	1.482(D)	1.776(D)	1.812(D)	1.847(D)	2.394(D)	2.152(D)
Tetragonal 2	1.583(D)	1.835(D)	1.832(D)	1.889(D)	2.362(I)	2.124(D)
Orthorhombic 1	1.4411(D)	1.551(D)	1.544(D)	1.731(D)	2.341(D)	2.130(D)
Orthorhombic 2	1.626(D)	1.744(D)	1.768(I)	1.930(I)	2.428(D)	2.204(D)
$CsCaI_3$						
Cubic	3.707(D)	3.675(D)	3.573(D)	3.879(D)	4.755(D)	4.528(D)
Tetragonal 1	3.788(D)	3.755(D)	3.655(D)	3.947(D)	4.893(D)	4.669(D)
Tetragonal 2	3.916(I)	3.918(I)	3.847(I)	4.076(I)	4.957(I)	4.704(D)
Orthorhombic 1	3.812(D)	3.787(D)	3.697(D)	3.962(D)	4.892(D)	4.701(D)
Orthorhombic 2	3.940(I)	3.934(I)	3.848(I)	4.092(I)	5.029(I)	4.771(D)
$CsSrI_3$						
Cubic	3.605(D)	3.684(D)	3.575(D)	3.638(D)	4.612(D)	4.389(D)
Tetragonal 1	3.816(D)	3.898(D)	3.765(D)	3.891(D)	4.839(D)	4.519(D)
Tetragonal 2	3.845(D)	3.918(D)	3.800(D)	3.931(D)	4.879(D)	4.547(D)
Orthorhombic 1	3.868(D)	3.937(D)	3.848(D)	3.937(D)	4.905(D)	4.649(D)
Orthorhombic 2	3.986(I)	4.147(D)	4.010(D)	4.133(I)	5.050(D)	4.724(D)

$CsBaI_3$						
Cubic	3.491(D)	3.563(D)	3.489(D)	3.417(D)	4.467(D)	4.246(D)
Tetragonal 1	3.665(D)	3.745(D)	3.659(D)	3.629(D)	4.657(D)	4.346(D)
Tetragonal 2	3.739(D)	3.769(D)	3.677(D)	3.646(D)	4.676(D)	4.370(D)
Orthorhombic 1	3.900(D)	3.908(D)	3.838(D)	3.873(D)	4.913(D)	4.592(D)
Orthorhombic 2	3.993(D)	4.116(D)	3.998(D)	4.060(D)	5.044(D)	4.722(D)

Table A.9: Predicted effective masses of holes in $CsMI_3$ (M= Ge, Sn, Pb, Mg, Ca, Sr, Ba) along Y-Γ paths using HSE06 functionals.

Effective masses of hole							
	Ge	Sn	Pb	Mg	Ca	Sr	Ba
Cubic	0.119	0.102	0.188	1.456	2.037	2.115	2.883
Tetragonal 1	0.125	0.157	0.262	1.927	2.275	2.445	2.796
Tetragonal 2	0.132	0.153	0.295	2.19	ND	2.107	2.963
Orthorhombic 1	0.126	0.129	0.243	0.98	1.302	1.57	1.488
Orthorhombic 2	0.136	0.148	0.264	2.079	2.922	1.483	0.805

Table A.10: Predicted effective masses of electrons in $CsMI_3$ (M= Ge, Sn, Pb, Mg, Ca, Sr, Ba) along Y-Γ paths using HSE06 functionals.

Effective masses of electrons							
	Ge	Sn	Pb	Mg	Ca	Sr	Ba
Cubic	0.778	0.776	0.791	0.242	0.389	0.354	0.397
Tetragonal 1	0.784	0.888	0.908	0.306	0.389	0.338	0.374
Tetragonal 2	0.804	0.92	1.011	0.303	0.331	0.342	0.375
Orthorhombic 1	0.477	0.245	0.271	0.31	0.314	0.324	0.369
Orthorhombic 2	0.874	0.959	0.709	0.32	0.33	0.305	0.323

Table A.11: Predicted effective masses of holes in $CsMI_3$ (M= Ge, Sn, Pb, Mg, Ca, Sr, Ba) along Γ-Z paths using HSE06 functionals.

Effective masses of holes							
	Ge	Sn	Pb	Mg	Ca	Sr	Ba
Cubic	0.114	0.094	0.19	ND	ND	ND	ND
Tetragonal 1	0.117	0.114	0.223	0.522	0.665	1.508	ND
Tetragonal 2	0.121	0.112	0.227	0.794	1.178	ND	ND
Orthorhombic 1	0.125	0.138	0.259	ND	ND	ND	ND
Orthorhombic 2	0.129	0.129	0.251	1.423	1.16	ND	ND

Table A.12: Predicted effective masses of electrons in $CsMI_3$ (M= Ge, Sn, Pb, Mg, Ca, Sr, Ba) along Γ-Z paths using HSE06 functionals.

Effective masses of electrons							
	Ge	Sn	Pb	Mg	Ca	Sr	Ba
Cubic	0.717	0.683	0.717	0.229	0.451	0.343	0.39
Tetragonal 1	0.348	0.083	0.089	0.263	0.285	0.322	0.363
Tetragonal 2	0.217	0.082	0.083	0.258	0.284	0.317	0.361
Orthorhombic 1	0.822	1.02	1.206	0.292	0.424	0.336	0.385
Orthorhombic 2	0.43	0.922	1.012	0.286	0.3	0.322	0.363

Table A.13: Projected valence and con+duction bands at the Γ point of the cubic phase by HSE06. Contributions by s, p and d orbitals are in $\%$.

		VB			CB		
		s	p	d	s	p	d
Ge	Cs	0	0	0	0	0	0
	Metal	41	0	0	0	80.1	0
	I	0	59	0	11.7	0	8.2
Sn	Cs	0	0	0	0	0	0.1
	Metal	45.6	0	0	0	81.6	0
	I	0	54.4	0	11	0	7.3
Pb	Cs	0	0	0	0	0	0.2
	Metal	36.5	0	0	0	80.4	0
	I	0	63.5	0	11.7	0	7.6
Mg	Cs	0	0	0	0.1	0	0
	Metal	0	0	0	67.1	0	0
	I	0	100	0	20.1	0	12.6
Ca	Cs	0	0	0	19.5	0	0
	Metal	0	0	0	12.7	0	0
	I	0	100	0	67.9	0	0
Sr	Cs	0	0	0	19.5	0	0
	Metal	0	0	0	12.7	0	0
	I	0	100	0	67.9	0	0
Ba	Cs	0	0	0	28.5	0	0
	Metal	0	0	0	8.5	0	0
	I	0	100	0	61.9	0	1.1

Table A.14: Projected valence and conduction bands at the Γ point of the tetragonal 1 phase by HSE06. Contributions by s, p and d orbitals are in $\%$.

		VB			CB		
		s	p	d	s	p	d
Ge	Cs	0	0	0	0	0	0
	Metal	40.8	0	0	0	80.2	0
	I	0	59.2	0	11.6	0	8.1
Sn	Cs	0	0	0	0	0	0.1
	Metal	43.3	0	0	0	82.8	0
	I	0	56.6	0.1	10.4	0	6.7
Pb	Cs	0	0	0	0	0	0.2
	Metal	34.3	0	0	0	81.6	0
	I	0	65.7	0	11.1	0	7.1
Mg	Cs	0	0.2	0	0	0	0.1
	Metal	0	0	0	57.7	0	0
	I	0	99.8	0	18.6	13.7	9.9
Ca	Cs	0	0.2	0	11.5	0	0.4
	Metal	0	0	0	22.8	0	0.6
	I	0	99.8	0	62.6	1.5	0.7
Sr	Cs	0	0.3	0	16.1	0	0.9
	Metal	0	0	0	16.6	0	0
	I	0	99.7	0	65.4	0.9	0
Ba	Cs	0	0.3	0	20.9	0	1.2
	Metal	0	0.7	0	14.5	0	0
	I	0.1	98.9	0	62.5	0	0.9

Table A.15: Projected valence and conduction bands at the Γ point of the tetragonal 2 phase by HSE06. Contributions by s, p and d orbitals are in $\%$.

		VB			CB		
		s	p	d	s	p	d
Ge	Cs	0	0	0	0	0	0
	Metal	40.4	0	0	0	80.4	0
	I	0	59.6	0	11.5	0	8.1
Sn	Cs	0	0	0	0	0	0.1
	Metal	43.5	0	0	0	82.7	0
	I	0	56.4	0.1	10.5	0	6.8
Pb	Cs	0	0	0	0	0	0.2
	Metal	33.8	0	0	0	81.7	0
	I	0	66.2	0	11	0	7.1
Mg	Cs	0	0	0.1	0	0	0.1
	Metal	0	0	0	58.7	0	0
	I	0	99.9	0	18.7	12.1	10.3
Ca	Cs	0	0	0.3	11.7	0	0.2
	Metal	0	0	0.1	22.3	0	0.7
	I	0	99.6	0	62.9	1.5	0.7
Sr	Cs	0	0.3	0.1	16.4	0	0.7
	Metal	0	0.7	0	16.4	0	0.2
	I	0	98.8	0	65.4	0.9	0
Ba	Cs	0	0.1	0.1	20.9	0	1.2
	Metal	0	0.7	0	14.5	0	0
	I	0.1	98.9	0	62.5	0	0.9

Table A.16: Projected valence and conduction bands at the Γ point of the orthorhombic 1 phase by HSE06. Contributions by s, p and d orbitals are in $\%$.

		VB			CB		
		s	p	d	s	p	d
Ge	Cs	0	0	0	0	0	0
	Metal	40.4	0	0	0	79.8	0
	I	0	59.6	0	11.6	0.5	8.1
Sn	Cs	0	0	0	0	0	0.1
	Metal	43.5	0	0	0	81.2	0
	I	0	56.5	0.1	10.5	1.4	6.9
Pb	Cs	0	0	0	0	0	0.1
	Metal	33.8	0	0	0	79.5	0
	I	0	66.2	0	11	2.3	7.1
Mg	Cs	0	0	0.1	0	0	0
	Metal	0	0	0	58.9	0	0
	I	0	99.9	0	18.5	12	10.5
Ca	Cs	0	0.4	0.3	9.9	0	1.2
	Metal	0	0	0.1	13.1	0	25.3
	I	0	99.2	0	44.9	1.4	4.2
Sr	Cs	0	0.7	0.3	14.4	0	0.7
	Metal	0	0	0	17.1	0	3.2
	I	0	99	0	63.2	0.9	0.5
Ba	Cs	0	0.2	0	13.5	0.3	1
	Metal	0	0.6	0	14.5	0	17.8
	I	0	99.1	0	49.6	1	2.3

Table A.17: Projected valence and conduction bands at the Γ point of the orthorhombic 2 phase by HSE06. Contributions by s, p and d orbitals are in $\%$.

		VB			CB		
		s	p	d	s	p	d
Ge	Cs	0	0	0	0	0	0
	Metal	40	0	0	0	79.5	0
	I	0	60	0	11.2	1.5	7.7
Sn	Cs	0	0	0.1	0	0	0.2
	Metal	43	0	0	0	79.1	0
	I	0	56.9	0.1	10	4.3	6.4
Pb	Cs	0	0	0.1	0	0	0.3
	Metal	33.4	0	0	0	77.1	0
	I	0	66.6	0	10.3	5.7	6.5
Mg	Cs	0	0	0.1	0	0.1	0
	Metal	0	0	0	57	0	0
	I	0	99.9	0	18.3	14.7	9.9
Ca	Cs	0.1	0	0.4	9.5	0	0
	Metal	0	0	0.1	25.8	0	0.9
	I	0	99.4	0	61.1	1.2	1.6
Sr	Cs	0	1	0.1	11.9	0	0.2
	Metal	0	0.6	0	22	0	1.3
	I	0	98.4	0	63.8	0.6	0.2
Ba	Cs	0	0.6	0.1	13.8	0	0.2
	Metal	0	0.7	0	21	0	5.5
	I	0	98.6	0	58.9	0	0.5

Table A.18: Predicted formation energies (in kcal/mol) for $CsMI_3$ (M= Ge, Sn, Pb, Mg, Ca, Sr, Ba) using various density functionals.

	PBE	PBE-D3	PBEsol	GAM	HSE06
	$CsPbI_3$				
Cubic	-0.16	9.61	4.34	4.30	-1.87
Tetragonal 1	-6.65	-0.51	-4.29	-7.03	-9.16
Tetragonal 2	-6.99	-0.60	-4.68	-7.22	-9.24
Orthorhombic 1	-7.11	-0.05	-4.14	-7.81	-9.36
Orthorhombic 2	-10.04	-3.48	-7.44	-13.47	-12.10
	$CsSnI_3$				
Cubic	-19.96	-7.10	-11.63	-11.49	-20.67
Tetragonal 1	-22.30	-10.34	-14.72	-18.42	-22.73
Tetragonal 2	-22.28	-10.84	-14.66	-18.34	-22.83
Orthorhombic 1	-22.66	-10.36	-14.25	-18.86	-22.83
Orthorhombic 2	-24.37	-12.51	-16.76	-21.21	-24.33
	$CsGeI_3$				
Cubic	-6.46	-6.70	-12.08	-7.01	-8.84
Tetragonal 1	-5.52	-6.71	-10.83	-6.58	-8.65
Tetragonal 2	-4.52	-6.08	-10.90	-6.56	-8.55
Orthorhombic 1	-5.82	-6.44	-11.10	-6.64	-8.46
Orthorhombic 2	-5.27	-5.55	-10.55	-6.45	-8.06
	$CsMgI_3$				
Cubic	13.76	-5.04	8.96	1.32	12.97
Tetragonal 1	13.14	-4.44	9.08	2.30	13.28
Tetragonal 2	13.07	-4.94	8.40	1.96	12.84
Orthorhombic 1	13.05	-5.28	8.26	1.96	13.28
Orthorhombic 2	13.33	-5.25	7.97	3.70	12.96

	PBE	PBE-D3	PBEsol	GAM	HSE06
	$CsCaI_3$				
Cubic	-2.61	1.22	-0.07	-7.75	-3.66
Tetragonal 1	-5.90	-4.17	-5.68	-11.69	-7.71
Tetragonal 2	-6.24	-4.71	-6.11	-11.84	-8.02
Orthorhombic 1	-5.93	-3.45	-5.09	-11.78	-7.53
Orthorhombic 2	-7.64	-5.56	-7.43	-12.53	-9.13
	$CsSrI_3$				
Cubic	-6.18	12.21	9.47	-4.90	-4.55
Tetragonal 1	-16.05	-1.02	-3.61	-16.38	-15.36
Tetragonal 2	-16.37	-1.35	-4.02	-16.82	-15.68
Orthorhombic 1	-16.55	-0.58	-3.65	-19.76	-15.96
Orthorhombic 2	-19.31	-4.05	-7.14	-22.99	-19.09
	$CsBaI_3$				
Cubic	19.12	53.86	46.79	22.09	22.34
Tetragonal 1	1.01	29.84	24.00	0.46	3.35
Tetragonal 2	0.78	29.57	23.65	0.19	3.10
Orthorhombic 1	-2.71	26.83	19.97	-8.20	-1.51
Orthorhombic 2	-4.61	20.41	17.56	-11.93	-4.97

A.1 Experimental Methods

A.1.1 Synthesis

All materials were purchased from Sigma Aldrich, and used as received. All synthesis steps were performed in a N_2 glovebox or a sealed N_2-filled quartz ampoule.

We attempted to synthesize $CsCaI_3$, $CsBaI_3$, and $CsSrBr_3$ by melting and reacting the liquid precursors, a technique common in the fabrication of $CsMI_3$ scintillator compounds.1–8 Desired molar ratios of the precursor compounds (CsI, CaI_2, BaI_2, CsSr, $SrBr_2$) were weighed and then ground together with a mortar and pestle for 60 seconds. This mixed powder was then loaded into a 0.5" OD quartz ampoule, which was evacuated overnight to 3 mTorr. Ampoules were then flame-sealed and heated in a furnace at 750 ℃ for 12 hours, then cooled to room temperature at a rate of 25 ℃/hr.

A.1.2 X-ray Diffraction

X-ray diffraction was collected from powder samples using either a Bruker D8 Discover 2D diffractometer (Co Kα radiation, λ=1.7889 Å) or a PANalytical X'pert PRO diffractometer (Co Kα radiation, λ=1.7889 Å). Powder samples were prepared by grinding large chunks of the synthesized material in a mortar and pestle for 1 minute.

To prevent the ingress of moisture, powder samples were sealed prior to measurement in either a home-made sample holder with a 3.6 μm thick mylar window (used in the Bruker diffractometer) or inside of an Anton Paar polycarbonate domed sample holder (used in the PANalytical diffractometer). All samples were prepared and loaded in a nitrogen glovebox and measured less than an hour after preparation.

Both sample holders generated a background signal, which was subtracted from all XRD patterns for clarity.

A.1.3 Optical Absorbance

Finely ground powder of $CsSrBr_3$ was suspended in silicone oil and loaded into a quartz cuvette in a glovebox. The cuvette was closed with a stopper and sealed with several layers of parafilm. The cuvette was taken to the spectrophotometer and measured within 5 minutes. Transmittance spectra were recorded using a Spectronic Genesys 5 Spectrophotometer at a scan rate of 1 pt / nm. Absorbance was calculated using $A = -log_{10}T$, where A is absorbance and T is transmittance.

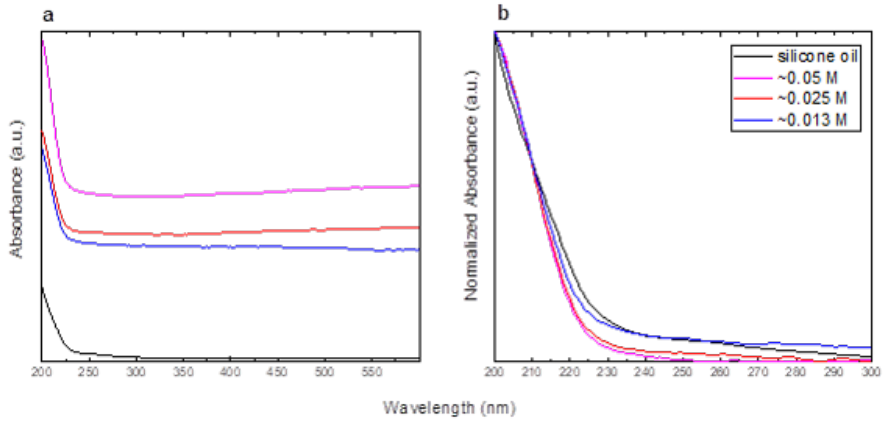

Figure A.1: Absorption data for several concentrations of $CsSrBr_3$ suspended in silicone oil. a) Raw absorbance data, which shows significant scattering at long wavelengths for large concentrations. b) Normalized absorbance data, which shows there is no significant absorption above the background silicone oil signal down to 200 nm (instrument limit). This indicates that the optical bandgap of $CsSrBr_3$ could be >6.2 eV.

A.1.4 Air Sensitivity Measurements

To assess the stability of $CsSrBr_3$, a powdered sample was exposed to ambient conditions and XRD patterns were taken periodically using a Bruker D8 Advance theta-theta diffractometer (Cu Kα radiation, λ=1.54059 Å). For the initial measurement, samples were sealed in a home-made sample holder with a 3.6 μm thick mylar window. This mylar window was then removed and XRD patterns were collected as a function of time.

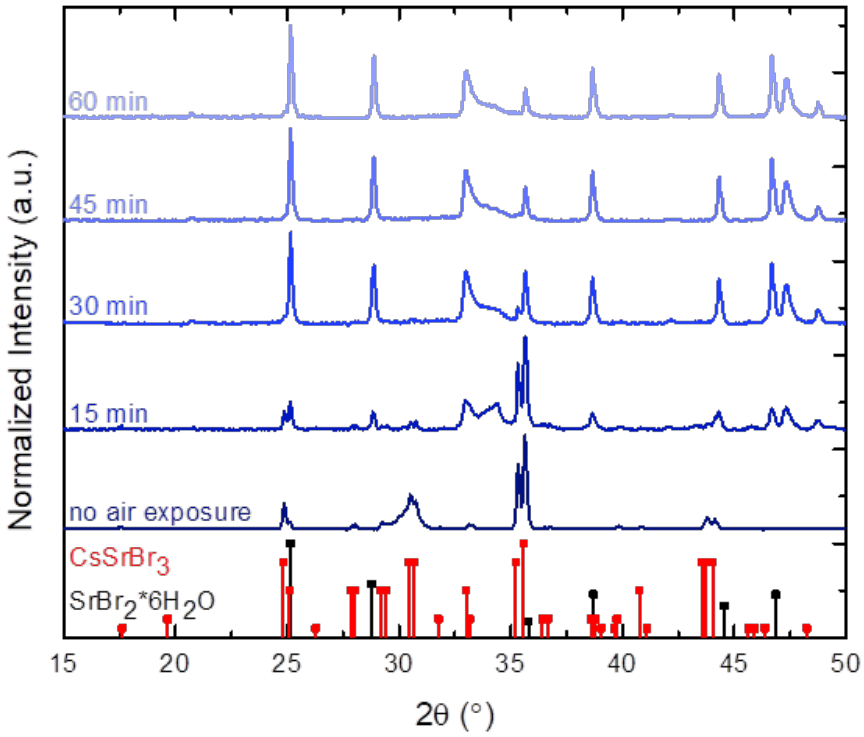

Figure A.2: X-ray diffraction patterns of $CsSrBr_3$ as a function of air exposure time. Initially, a diffraction pattern was taken with the protective mylar film (darkest blue trace), which matches $CsSrBr_3$ (red sticks) as expected. After 15 minutes of the mylar film being removed, a significant change in the diffraction pattern was observed. Within 60 minutes, the XRD pattern was almost completely $SrBr_2*6H_2O$ (black sticks). This rapid degradation in the presence of moisture, along with its large optical bandgap, indicates this material is unlikely to be useful in PV applications.

Table A.19: Comparison of lattice parameters (in Å), Formation Energy (in kcal/mol) and bandgap (in eV) of $CsBa_2I_5$ using different functionals.

$CsBa_2I_5$	a	b	c	Formation Energy	Bandgap
PBE-D3	10.56	9.29	14.77	-12.09	3.731
PBE	10.71	9.51	15.23	-24.35	3.825
PBEsol	10.48	9.24	14.70	-15.16	3.630
GAM	10.59	9.46	15.16	-25.37	3.931
HSE06	10.66	9.46	15.15	-24.46	4.801
Experimental	10.541a	9.256a	14.637a	-	5.3-5.5c
	10.617b	9.304b	14.699b	-	

Table A.20: Comparison of lattice parameters (in Å), Formation Energy (in kcal/mol) and bandgap (in eV) of $CsSrBr_3$ using different functionals.

$CsSrBr_3$	a	b	c	Formation Energy	Bandgap
PBE-D3	8.35	11.83	8.23	-7.30	4.599
PBE	8.49	11.97	8.34	-23.44	4.481
PBEsol	8.40	11.82	8.21	-7.86	4.638
GAM	8.30	11.72	8.18	-26.16	4.502
HSE06	8.45	11.92	8.30	-21.77	5.699
Experimental	8.3344	11.8238	8.2417		

Appendix B

Supporting Information of Chapter 3

B.1 Computational Methods

Spin-polarized density functional theory (DFT) calculations were performed for a unit cell of pyrite using the Vienna ab-initio Simulation Package (VASP)[54, 55, 56, 57] and projected augmented wave (PAW) potentials.[66, 67] A kinetic energy cutoff of 350 eV and Γ-centered 7×7×7 k-point grid was used for structure optimizations and electronic property calculations. Energy convergence criteria of 10^{-5} eV and force convergence criteria of 0.02 eV/Å were used for all calculations. We tested various DFT functionals such as PBE,[58, 59] PBE-D3,[60, 221] PBEsol,[61] revPBE,[284] PW91,[285] AM05,[286, 287, 288] GAM,[62] TPSS,[289] PBE+U (U = 1.6, 1.8 and 2.0 eV),[131] HSE06 (a = 0.05, 0.07, 0.10, 0.15, 0.20, 0.25, where a is the Hartree-Fock exchange parameter)[63, 64, 65] and benchmarked their results with respect to experimental lattice parameter, Fe-S bond distance, S-S bond distance, and band gap. We found that PBE+U with a Hubbard U value of 1.8 eV, and the HSE06 functional with a = 0.07, best describe the structural and electronic properties of pyrite.

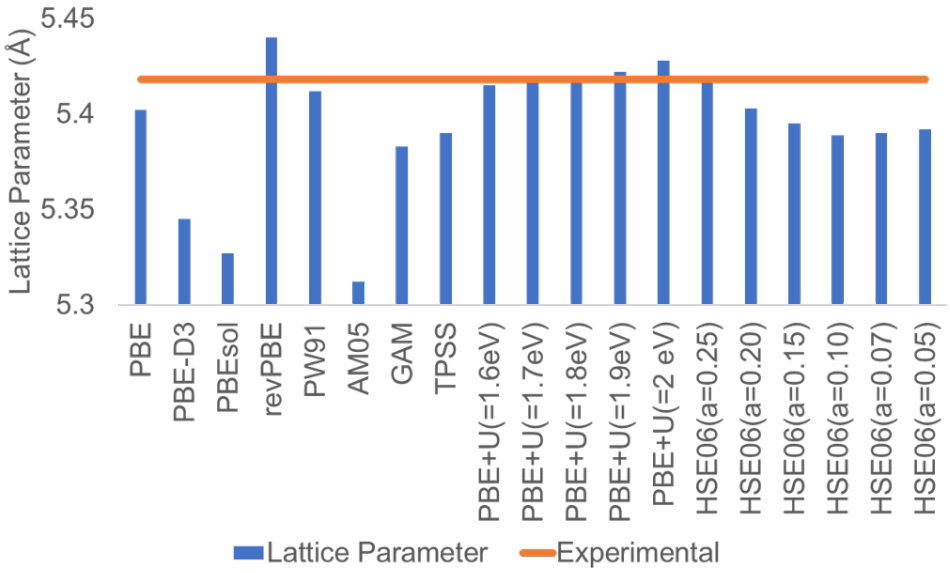

Figure B.1: Comparison of experimental and computed pyrite lattice parameter (in Å) using various DFT functionals.

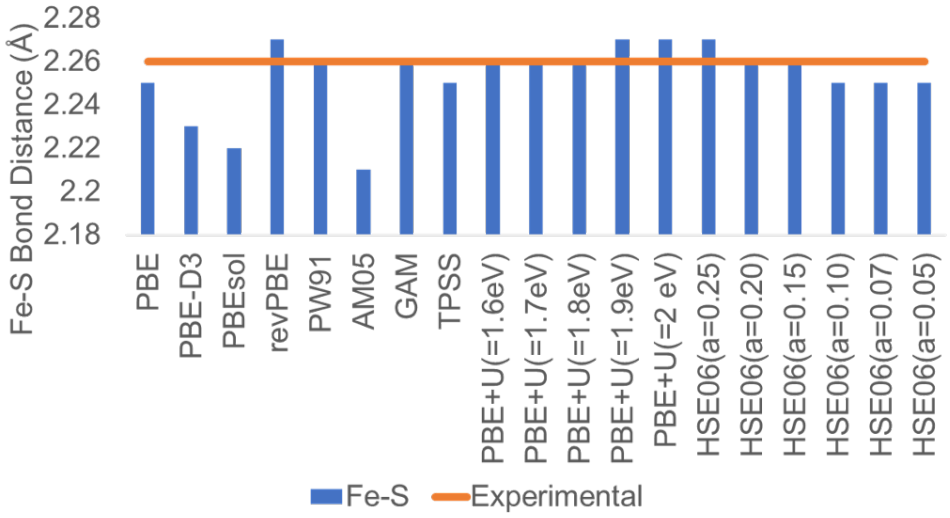

Figure B.2: Comparison of experimental and computed pyrite Fe-S bond distance (in Å) using various DFT functionals.

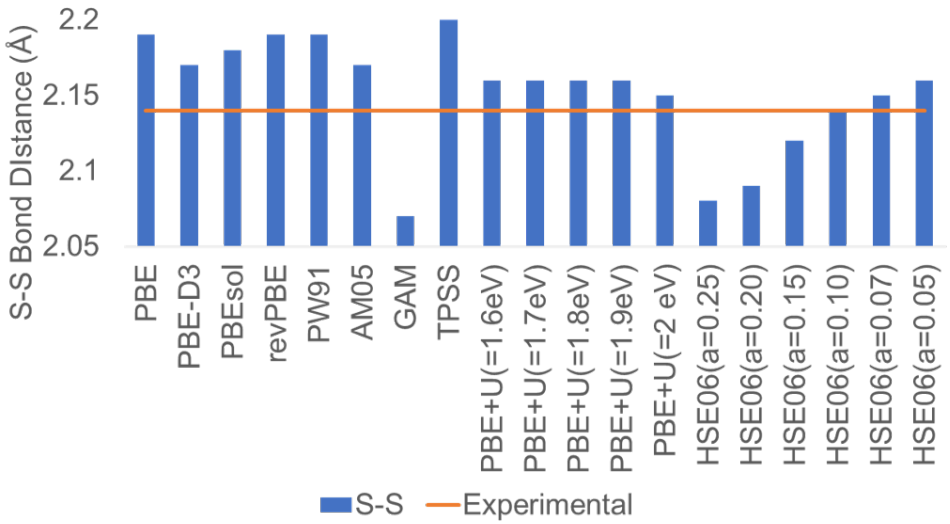

Figure B.3: Comparison of experimental and computed pyrite S-S bond distance (in Å) using various DFT functionals.

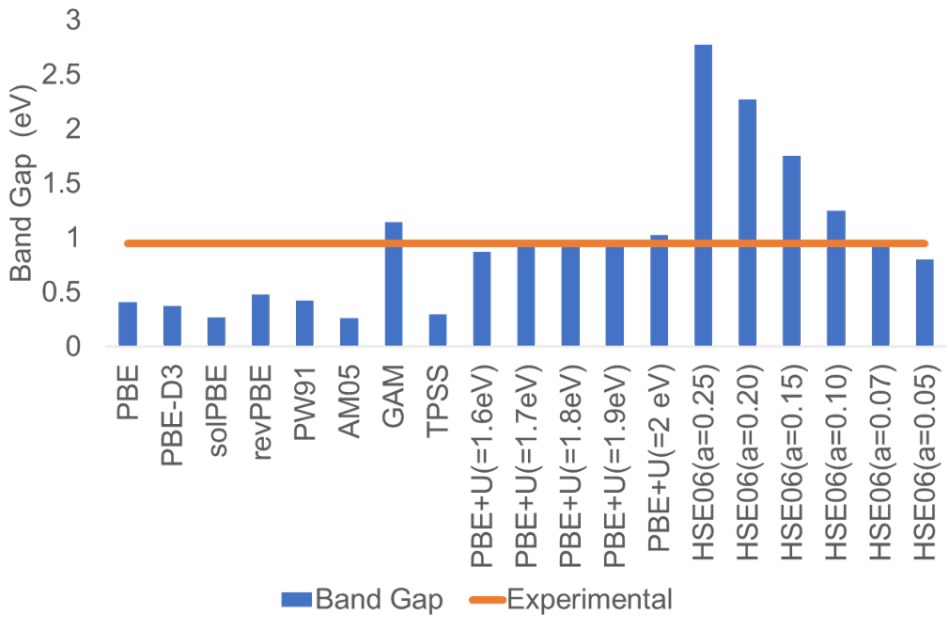

Figure B.4: Comparison of experimental and computed band gap (in eV) of pyrite using various DFT functionals.

B.2 Effects of Lattice Expansion, Zero-point Energy Corrections, Vibrational Entropy, and Configurational Entropy on Defect Formation and Binding Energies

The total free energy of a system, incorporating effects such as lattice expansion, zero-point energy corrections, vibrational entropy, and configurational entropy, can be written as follows:

$$G = E + E_{ZPE} - TS_{vib} - TS_{config} + \Delta G_{lattice-expansion} \tag{B.1}$$

where G is the free energy of the system, E is the electronic energy of the system, E_{ZPE} is the zero-point energy correction and is defined as $\sum_{i=3z} = 0.5\hbar\omega_i$ (where Z is the number of atoms in the supercell, $\hbar$ is the reduced Planck constant and ω_i is the vibration frequency), S_{vib} and S_{config} are vibrational and configurational entropy, respectively, and T is temperature. S_{vib} is defined as follows:

$$S_{vib} = k_B \sum_{i=3z-6} \frac{\frac{\hbar\omega_i}{k_B T}}{\exp^{\frac{\hbar\omega_i}{k_B T}} - 1} - \ln\left(1 - \exp^{\frac{\hbar\omega_i}{k_B T}}\right) \tag{B.2}$$

and $\Delta G_{\text{lattice-expansion}}$ is the total change in vibrational energy due to thermal expansion.

Evaluation of E_{ZPE}, S_{vib}, and $\Delta G_{lattice-expansion}$ all require vibrational frequency calculations. We performed such vibrational frequency calculations using VASP and the density functional perturbation theory (DFPT)[290] approximation. Due to computational cost, however, we restricted these calculations to 2×2×2 supercells of defect-free pyrite, the S mono-vacancy, the S-S dimer and the S tetra-vacancy.

Incorporating these effects into the defect formation energy (which is calculated from equation 3.1 of Chapter 3) we can obtain a total free energy for defect formation as

$$\Delta G_{formation} = \Delta E_{formation} + \Delta E_{ZPE} - T\Delta S_{vib} - T\Delta S_{config} + \Delta\Delta G_{lattice-expansion} \tag{B.3}$$

Where $\Delta G_{formation}$ is the total free energy of defect formation, $\Delta G_{formation}$ is the defect formation energy without thermal and configurational entropy effects (as calculated by equation

3.1 in the main text), $\Delta S_{vib}$and ΔS_{config} are vibrational and configurational entropy corrections, respectively, T is temperature, and $\Delta\Delta G_{\text{lattice-expansion}}$ is the difference in the change in free energy due to lattice (thermal) expansion for supercells with and without a defect.

The binding energy (equation 3.3 of Chapter 3) will also be affected by incorporating these effects, as

$$E_b = \sum_i \Delta G_{formation}(i) - \Delta G_{formation}(defect - cluster) \tag{B.4}$$

where E_{b} is now the total free energy for binding a defect. In the following sections, we will discuss each effect and how it influences $\Delta G_{\text{formation}}$ and E_{b}.

B.2.1 Zero-point Energy and Vibrational Entropy

The free energies of the S mono-vacancy, S-S-dimer vacancy and tetra S-vacancy were calculated at 300 K. Fully relaxed structures (both lattice parameter and atomic positions) were used in the frequency calculations. The effect of zero-point energy and vibrational entropy corrections on the defect formation energy and binding energy of these defects are summarized in Table B.7. The zero-point energy and vibrational entropy corrections change the binding energy by less than 0.1 eV. Thus, we ignore these when reporting the binding energy.

B.2.2 Lattice Expansion

To address this issue, we first started with the DFT-relaxed lattice parameter of supercells containing either the S mono-vacancy or the S-S dimer vacancy, at 0 K, and used the experimental thermal expansion coefficient23 of 4.5 × 10^{-6} K^{-1} to get the lattice parameter at 300 K. Vibrational frequencies were calculated using DFPT, and we then took the difference in total vibrational energy between 300 K and 0 K to be an energy correction for lattice expansion (i.e., $\Delta G_{\text{lattice-expansion}}$). For both the S mono-vacancy and S-S dimer vacancy, we find $\Delta\Delta G_{\text{lattice-expansion}} \approx$ 2 meV, which is significantly lower than the formation and binding energies, and we thus neglect this term when reporting these quantities.

B.2.3 Configurational Entropy

For a S mono-vacancy in a given supercell,

$$S_{config} = k_B \ln N \tag{B.5}$$

where S_{config} is the configurational entropy and N is the number of equivalent, or possible, defect sites in the pyrite supercell (64 for a 2×2×2 supercell and 216 for a 3×3×3 supercell), and k_B is Boltzmann constant. Using simple arguments, for two isolated S mono-vacancies we find,

$$S_{config} = k_B \ln \frac{N(N-1)}{2} \tag{B.6}$$

For the cis-S di-vacancy we find,

$$S_{config} = k_B \ln 2N \tag{B.7}$$

and for the S-S dimer vacancy, trans-S di-vacancy and S tetra-vacancy,

$$S_{config} = k_B \ln \frac{N}{2} \tag{B.8}$$

Thus, at T = 300 K, the change in free energy due to configurational entropy will be $-TS_{config}$ (see Table B.8 for values). The value of the configurational entropy will, of course, depend on the supercell size, as a bigger supercell will have higher configurational freedom for defect formation. Any change in defect formation energy will in turn influence the defect binding energy; these values are reported in Table B.10. The overall change in defect formation and binding energies due to configurational entropy effects are reported in Tables B.9 and Table B.11, respectively.

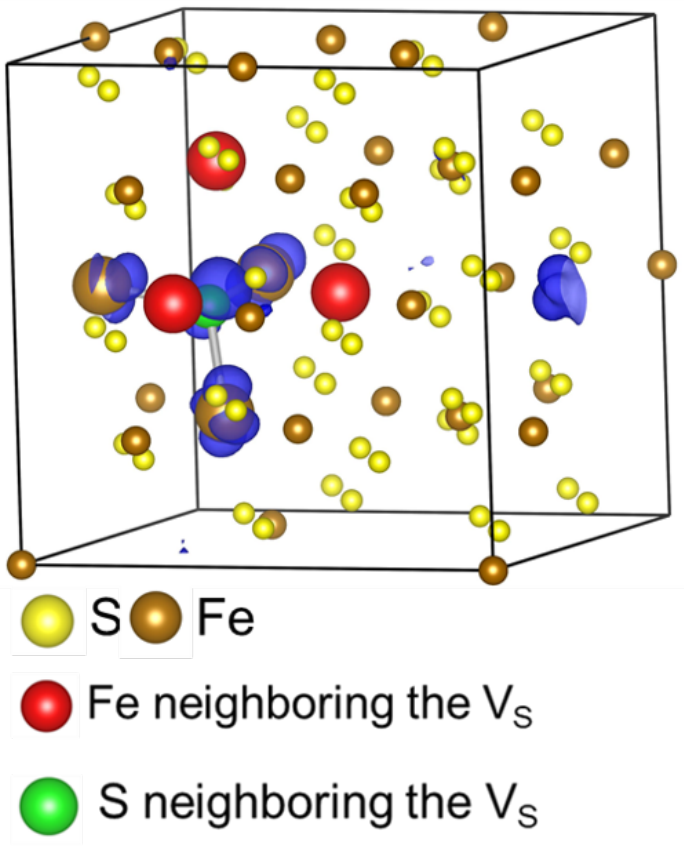

Figure B.5: Partial charge density (shown in blue) analysis of the highest occupied orbital of a 2×2×2 pyrite supercell containing one S mono-vacancy, calculated using the PBE+U (U = 1.8 eV) level of theory.

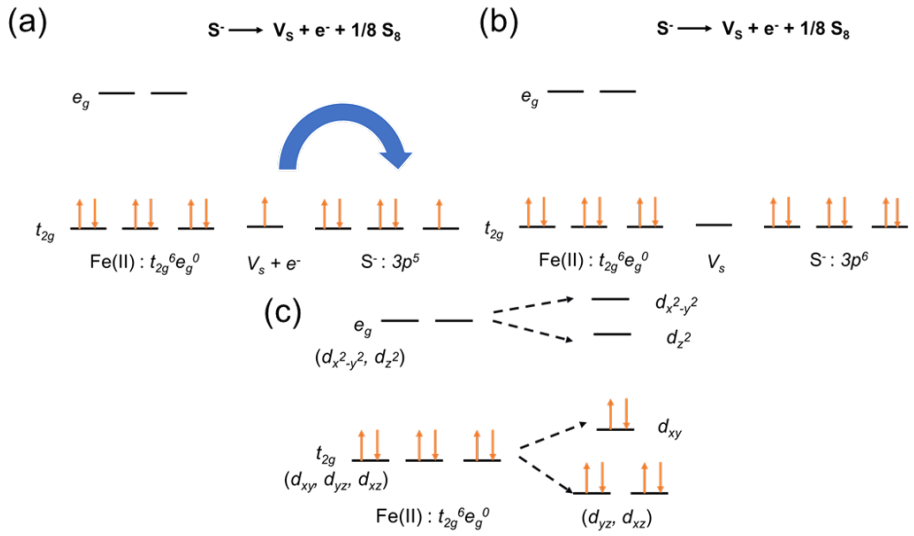

Figure B.6: (a-b) Schematic representation of electron transfer from the S mono-vacancy site to the remaining S in the dimer, effectively doubling its negative charge and, in a simple ionic picture, making it S^{2-}. (c) Schematic representation of how the crystal field splitting of the 3 Fe atoms coordinated to this S^{2-} atom changes upon introduction of the neighboring S mono-vacancy. In defect-free pyrite, all Fe atoms are in an octahedral crystal field (left) with the region near the valence band maximum largely derived from Fe t_{2g} states. Upon introduction of a S mono-vacancy, which induces mild elongation of the Fe–S^{2-} bond as the remaining S moves to occupy the original dimer center-of-mass, these 3 Fe centers are now in a distorted octahedral crystal field (right), creating a t_{2g}-derived donor state close to, but just above, the valence band maximum, thus explaining why the S mono-vacancy produces a very deep donor state in pyrite.

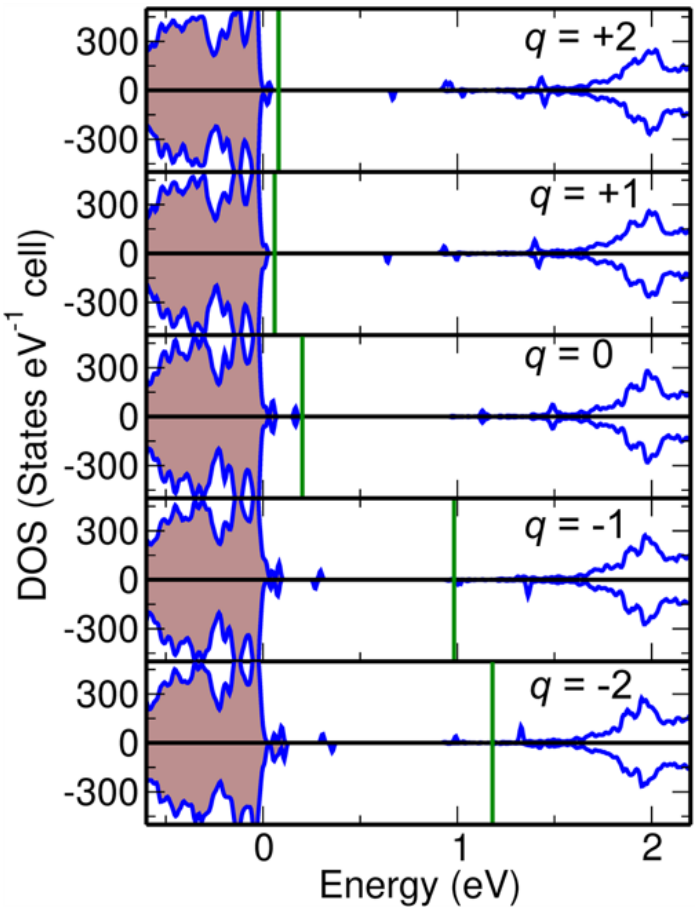

Figure B.7: Density-of-states (DOS) comparison of various charge states of the S mono-vacancy in a 3×3×3 pyrite supercell, calculated using the PBE+U (U = 1.8 eV) level of theory. The vertical green lines represent the Fermi energy.

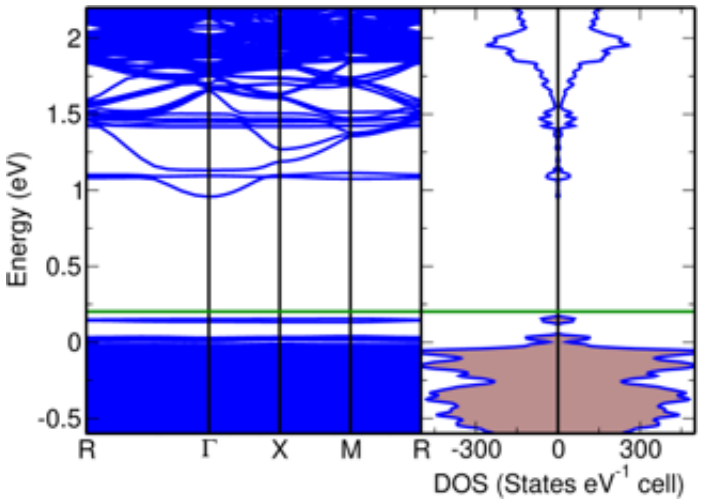

Figure B.8: Band structure and DOS of two S mono-vacancies in a 3×3×3 pyrite supercell, calculated using PBE+U (=1.8 eV) level of theory. The horizontal green line represents the Fermi energy. The band structure and DOS are quite similar to that of a single S mono-vacancy, suggesting these two vacancies are essentially non-interacting, and thus this supercell merely contains twice the concentration of defects examined in the case of the single S mono-vacancy.

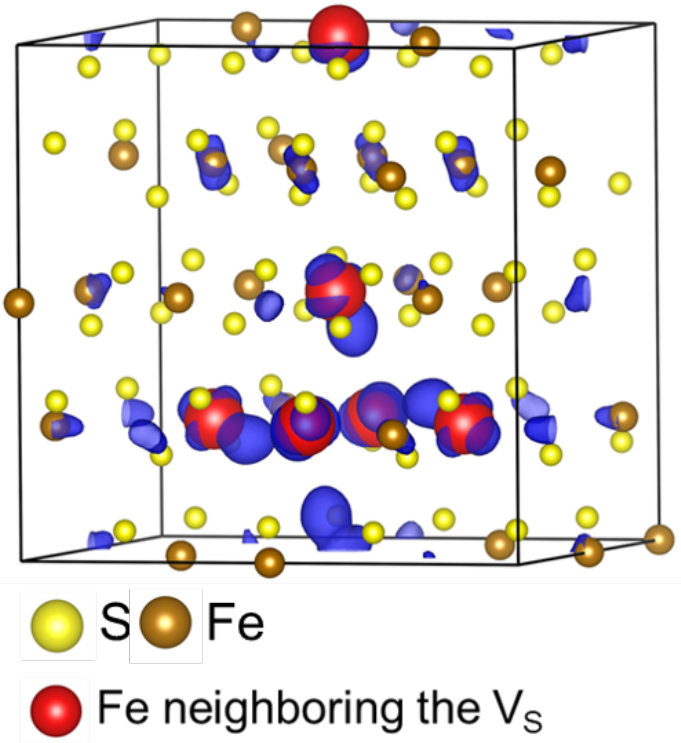

Figure B.9: Partial charge density (shown in blue) analysis of the highest occupied defect state in a 2×2×2 pyrite supercell containing a S-S-dimer vacancy, calculated using PBE+U (U = 1.8 eV) level of theory.

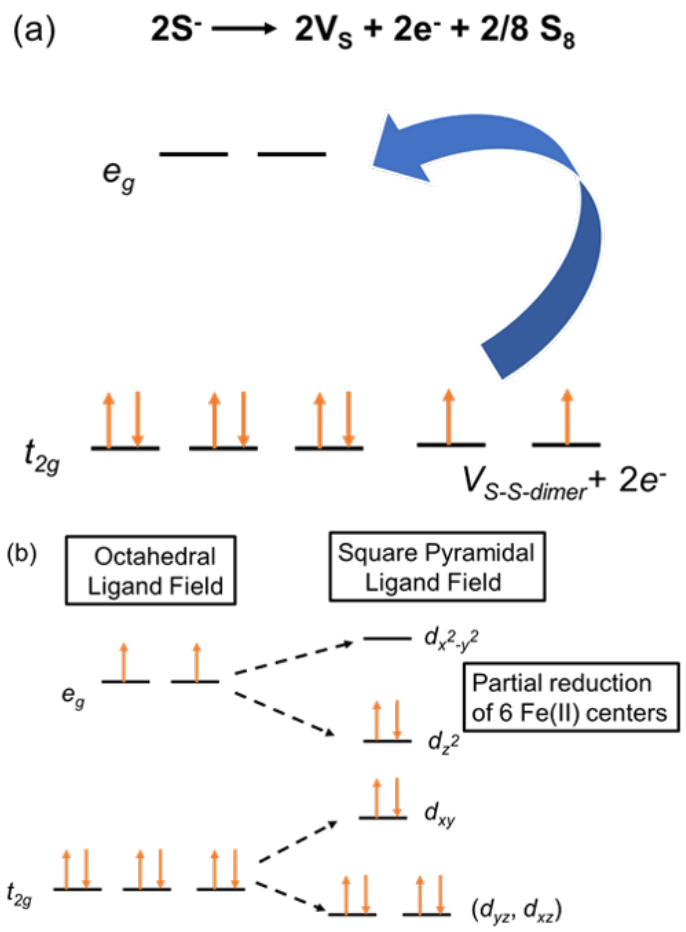

Figure B.10: (a) Schematic representing the movement of electrons from the S-S dimer site to the six neighboring Fe centers upon creation of a dimer vacancy. Unlike in the case of the S mono-vacancy, the S-S-dimer vacancy does not have a nearest-neighbor S atom where electrons can transfer, thus they move to the six Fe centers coordinated with one of the S vacancies. (b) Schematic representation of how the crystal field splitting of the six Fe centers reorganizes after a S-S-dimer vacancy is introduced. Due to the creation of the dimer vacancy, these six Fe centers change from octahedral coordination (left) to square planar (right).

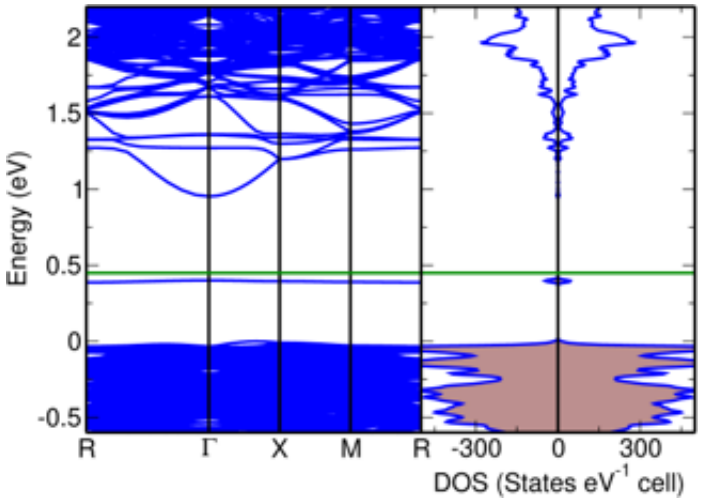

Figure B.11: Band structure and DOS of S-S-dimer vacancy in a 3×3×3 pyrite supercell, calculated using PBE+U (U = 1.8 eV) level of theory. The horizontal green line represents the Fermi energy.

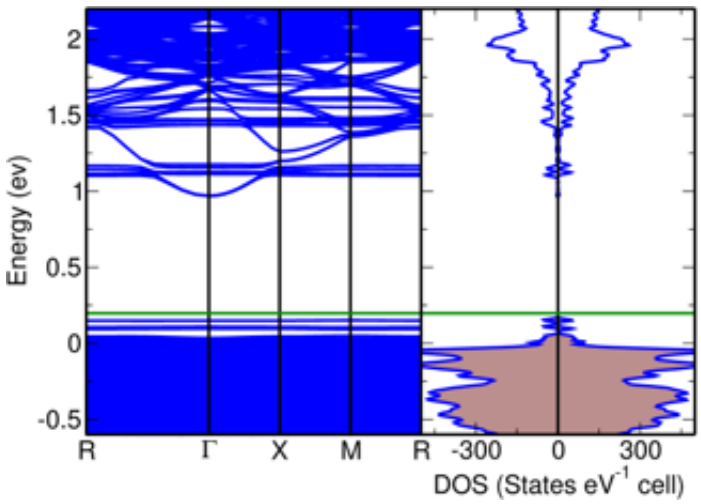

Figure B.12: Band structure and DOS of cis-S di-vacancy in a 3×3×3 pyrite supercell calculated, using PBE+U (U = 1.8 eV) level of theory. The horizontal green line represents the Fermi energy.

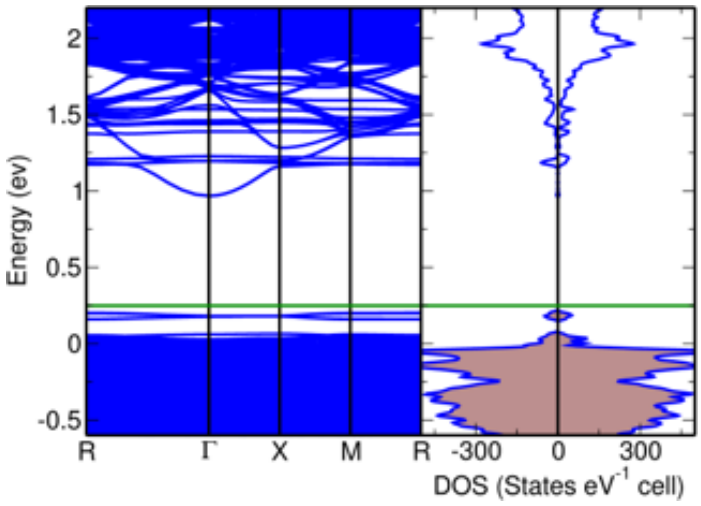

Figure B.13: . Band structure and DOS of trans-S di-vacancy in a 3×3×3 pyrite supercell calculated, using PBE+U (U = 1.8 eV) level of theory. The horizontal green line represents the Fermi energy.

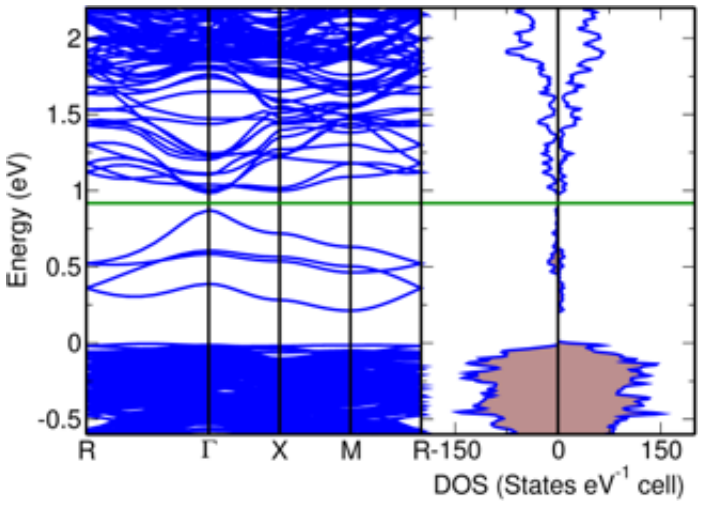

Figure B.14: Band structure and DOS of a tetra S-vacancy in a 2×2×2 pyrite supercell, calculated using PBE+U (U = 1.8 eV) level of theory. The horizontal green line represents the Fermi energy.

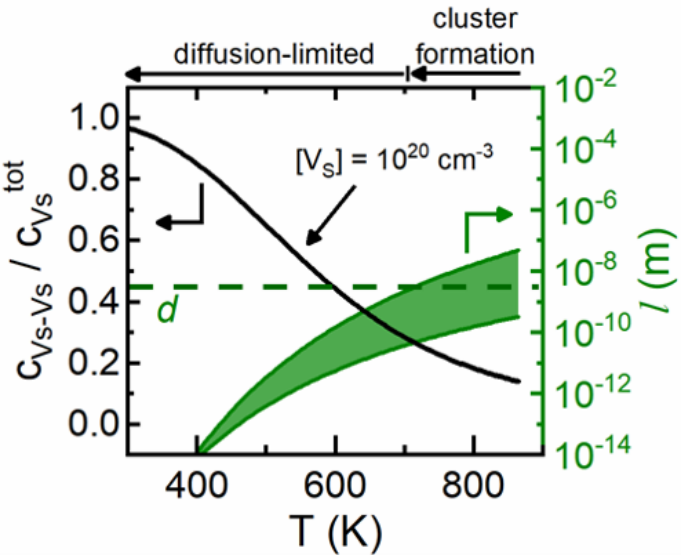

Figure B.15: The temperature (T) dependence of (left axis) the fraction of S mono-vacancies (V_S) participating in a S-S dimer vacancy for total S vacancy concentration 10^{20} cm^{-3}, assuming a binding energy of 0.34 eV. Also plotted (right axis, green) is the T-dependence of a range of S vacancy diffusion lengths (l) estimated assuming $l = \sqrt{Dt}$, where D is the vacancy diffusion coefficient and t is time (10 min). As upper and lower bounds, DFT-calculated V_S diffusion and experimental S self-diffusion coefficients were used, respectively. The average separation between V_S (assuming a concentration of 10^{19}-10^{20} cm^{-3}) is 2-5 nm, and is marked with a green dashed line. The T ($\sim$ 710 K) where the range of diffusion lengths falls below this separation distance marks the point where clustering events can no longer occur as the crystal cools, because diffusion is insufficient.

Table B.1: Total electronic energy of the pyrite unit cell with respect to kinetic energy cutoff.

Energy Cut off (eV)	Total Electronic Energy (eV)	Change in Electronic Energy per atom (eV/atom)
300	-64.9324131	-
325	-64.9578879	-0.0021
350	-64.9614187	-0.0003
375	-64.9643023	-0.0002
400	-64.9671692	-0.0002
425	-64.9654424	0.0001
450	-64.9786569	-0.0011

Table B.2: Convergence of activation energy ($\Delta E_{\text{activation}}$) and defect formation energy ($\Delta E_{formation}$) with respect to kinetic energy cutoff, using a 2×2×2 supercell and cutoffs of 350 eV and 400 eV. The $\Delta E_{formation}$ reported here does not include contributions from configurational entropy.

Type of Defect	$\Delta E_{activation}$ using PBE+U and a 2×2×2 supercell (eV)		$\Delta E_{formation}$ using PBE+U and a 2×2×2 supercell (eV)	
	350 eV	400 eV	350 eV	400 eV
S mono-vacany	0.83	0.84	2.09-2.99	2.09-2.99
S-S-dimer vacancy	0.54	0.55	3.52-5.52	3.50-5.50

Table B.3: Comparison of activation energy ($\Delta E_{activation}$) for various defects with respect to supercell size and functional.

Type of Defect	$\Delta E_{activation}$ using PBE+U and a 3×3×3 supercell (eV)	$\Delta E_{activation}$ using PBE+U and a 2×2×2 supercell (eV)	$\Delta E_{activation}$ using PBE+U and a 2×2×2 supercell (eV)
S mono-vacancy	0.80	0.83	0.91
Two S mono-vacancies	0.80	0.78	0.86
S-S-dimer vacancy	0.55	0.54	0.68
cis-S di-vacancy	0.82	0.89	0.97
trans-S di-vacancy	0.76	0.71	0.76
S tetra vacancy	0.41	0.11	0.21

Table B.4: Comparison of defect formation energy ($\Delta E_{formation}$) for various S vacancies with respect to supercell size and functional. This does not include contributions from configurational entropy.

Type of Defect	$\Delta E_{formation}$ using PBE+U and a 3×3×3 supercell (eV)	$\Delta E_{formation}$ using PBE+U and a 2×2×2 supercell (eV)	$\Delta E_{formation}$ using PBE+U and a 2×2×2 supercell (eV)
S mono-vacancy	2.12-3.02	2.09-2.99	2.26-3.16
Two S mono-vacancies	4.26-6.06	4.00-5.80	4.26-6.06
S-S-dimer vacancy	3.74-5.54	3.72-5.52	3.68-5.48
cis-S di-vacancy	4.14-5.94	4.10-5.90	4.18-5.98
trans-S di-vacancy	3.50-5.30	3.48-5.28	3.84-5.64
S tetra vacancy	6.96-10.56	6.44-10.04	7.20-10.80

Table B.5: Comparison of binding energy (E_b) for various defects with respect to supercell size and functional. This does not include contributions from configurational entropy.

Type of Defect	E_b using PBE+U and a 3×3×3 supercell (eV)	E_b using PBE+U and a 2×2×2 supercell (eV)	E_b using PBE+U and a 2×2×2 supercell (eV)
Two S mono-vacancies	-0.02	0.18	0.26
S-S-dimer vacancy	0.50	0.46	0.84
cis-S di-vacancy	0.10	0.08	0.34
trans-S di-vacancy	0.74	0.70	0.68
S tetra vacancy	1.52	1.92	1.84

Table B.6: The donor activation energy ($\Delta E_{activation}$) of S vacancy-related defects, calculated by fixing (at 5.418 Å) or relaxing the lattice parameter (a). Atomic positions were always relaxed, and the PBE+U (U = 1.8 eV) functional and a 3×3×3 supercell were used for all calculations.

Type of Defect	$\Delta E_{activation}$ when relaxing a (eV)	$\Delta E_{activation}$ when fixing a (eV)
S mono-vacancy	0.80	0.80
Two S mono-vacancies	0.80	0.80
S-S-dimer vacancy	0.55	0.55
cis-S di-vacancy	0.82	0.82
trans-S di-vacancy	0.76	0.77
S tetra vacancy	0.41	0.41

Table B.7: Effect of zero-point energy and vibrational entropy on the formation energy ($\Delta E_{formation}$) and binding energy (E_b) for various defects using a 2×2×2 pyrite supercell.

Type of Defect	Change in Formation Energy (eV)	Change in Binding Energy (eV)
S mono-vacancy	-0.05	-
S-S-dimer vacancy	-0.02	-0.08
S tetra vacancy	-0.16	-0.04

Table B.8: Effect of configurational entropy on the formation energy ($\Delta E_{formation}$) for various defects with respect to supercell size.

Type of Defect	-TS_{config} (2×2×2 supercell (eV)	-TS_{config} (3×3×3 supercell (eV)
S mono-vacancy	-0.11	-0.14
Two S mono-vacancies	-0.20	-0.25
S-S-dimer vacancy	-0.09	-0.12
cis-S di-vacancy	-0.12	-0.16
trans-S di-vacancy	-0.09	-0.12
S tetra vacancy	-0.09	-0.12

Table B.9: Comparison of the defect formation energy ($\Delta G_{formation}$) for various defects (incorporating configurational entropy only).

Type of Defect	$\Delta G_{formation}$ using PBE+U and a 3×3×3 supercell (eV)	$\Delta G_{formation}$ using PBE+U and a 2×2×2 supercell (eV)
S mono-vacancy	1.98-2.88	1.98-2.88
Two S mono-vacancies	4.01-5.81	3.80-5.60
S-S-dimer vacancy	3.62-5.42	3.63-5.43
cis-S di-vacancy	3.98-5.78	3.98-5.78
trans-S di-vacancy	3.38-5.18	3.39-5.19
S tetra vacancy	6.84-10.44	6.35-9.95

Table B.10: Effect of configurational entropy on binding energy (E_b) for various defects with respect to supercell size.

Type of Defect	Decrease in E_b (2×2×2 supercell) (eV)	Decrease in E_b (3×3×3 supercell) (eV)
Two S mono-vacancies	-0.02	-0.03
S-S-dimer vacancy	-0.13	-0.16
cis-S di-vacancy	-0.10	-0.12
trans-S di-vacancy	-0.13	-0.16
S tetra vacancy	-0.35	-0.44

Table B.11: Comparison of binding energy (E_b) for various defects (incorporating configurational entropy only).

Type of Defect	E_b using PBE+U and a 3×3×3 supercell (eV)	E_b using PBE+U and a 2×2×2 supercell (eV)
Two S mono-vacancies	-0.05	0.16
S-S-dimer vacancy	0.34	0.33
cis-S di-vacancy	-0.02	-0.02
trans-S di-vacancy	0.58	0.57
S tetra vacancy	1.08	1.57

Table B.12: Comparison of PBE+U (U = 1.8 eV)-calculated effective masses with past theory and experiment.

Effective Mass	This Work	Previous Theoretical Work	Experimental Work
Holes	1.46 (VBM→ Γ 1.95 (VBM→ X)	1.23-1.98	2.2±0.7 [26]
Electrons	0.56	0.49[125]	0.45 [143, 149]

Appendix C

Supporting Information of Chapter 4

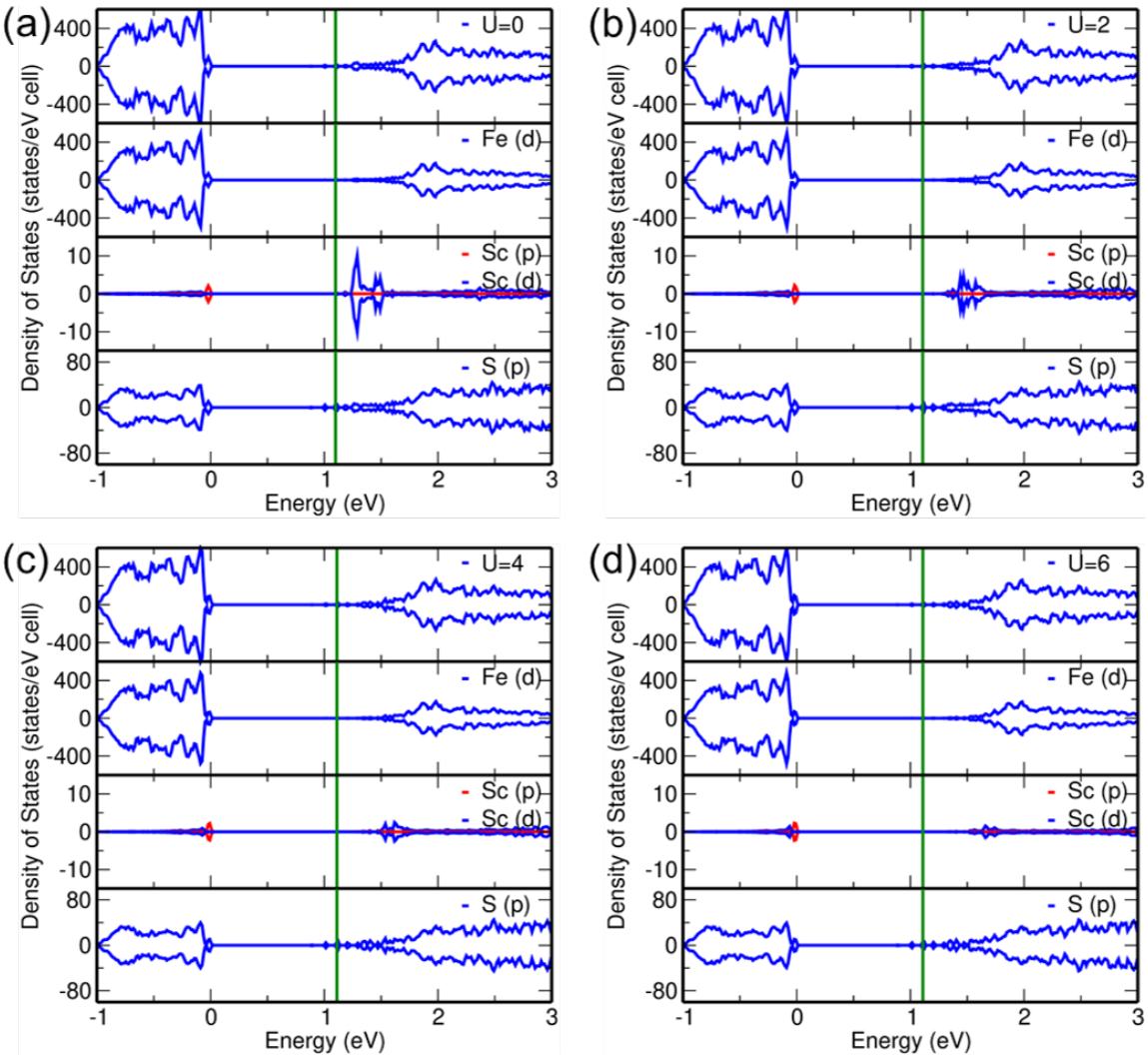

Figure C.1: Comparison of PDOS of Sc doped Pyrite as a function of Hubbard U value.

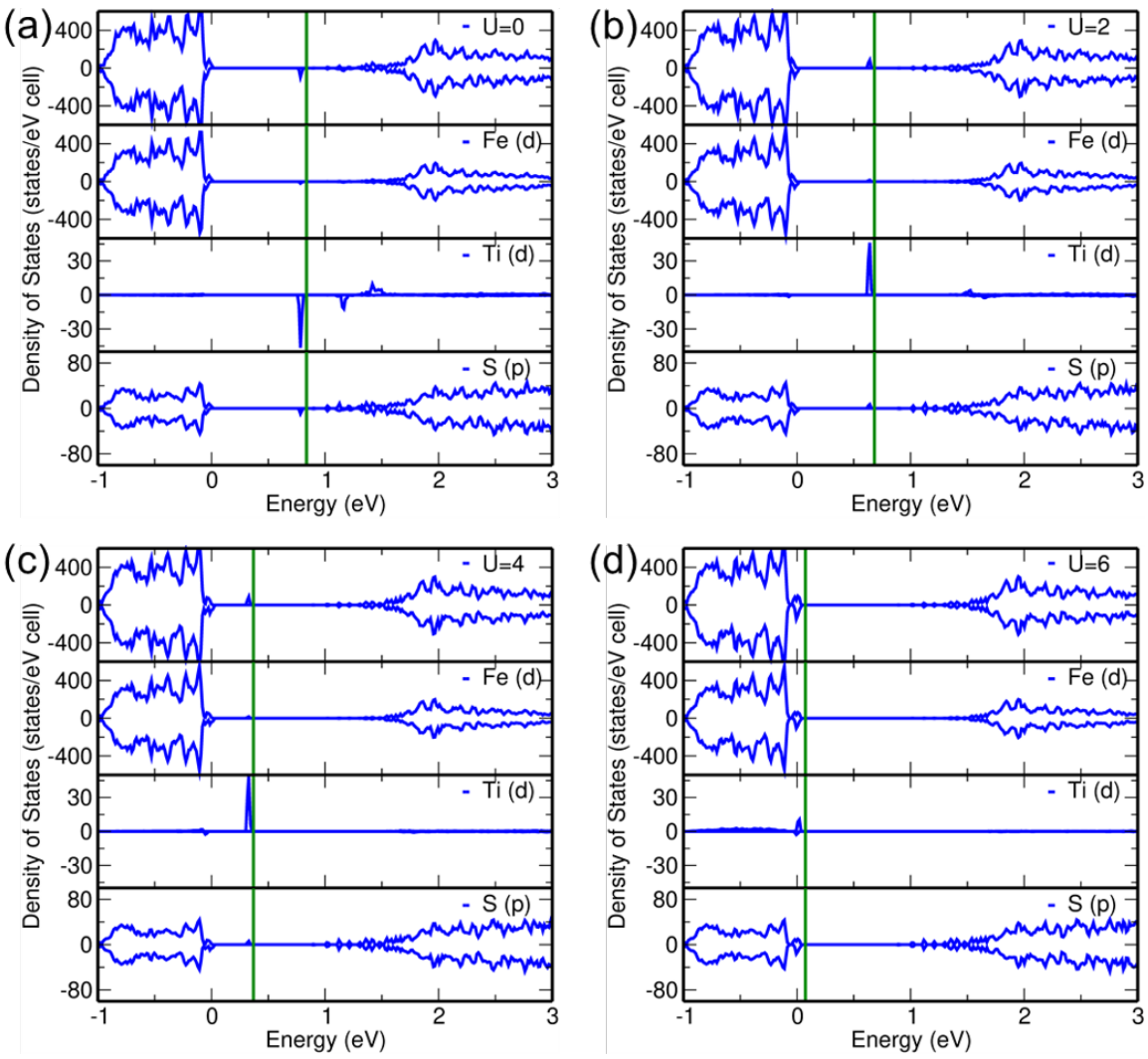

Figure C.2: Comparison of PDOS of Ti doped Pyrite as a function of Hubbard U value.

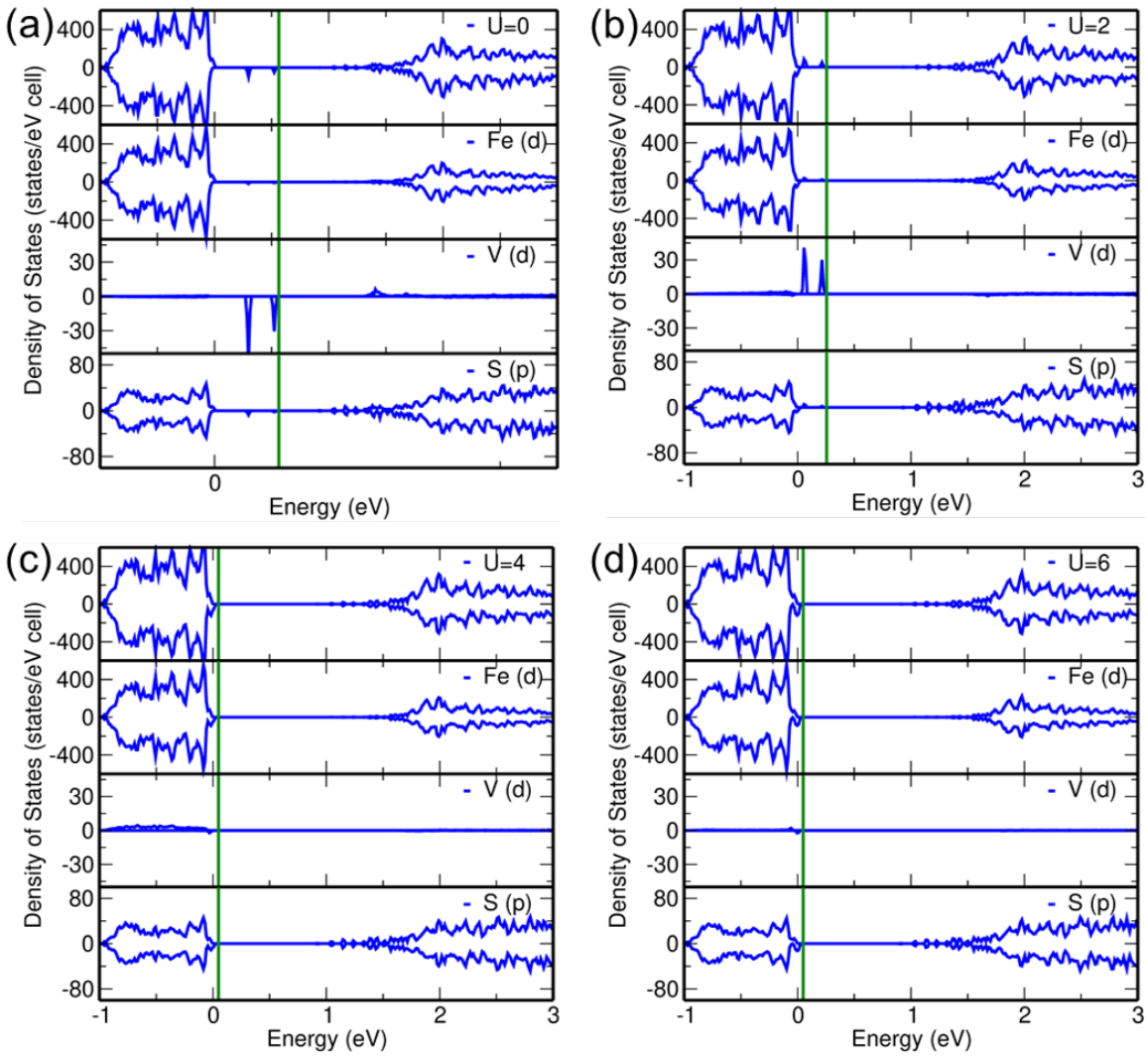

Figure C.3: Comparison of PDOS of V doped Pyrite as a function of Hubbard U value.

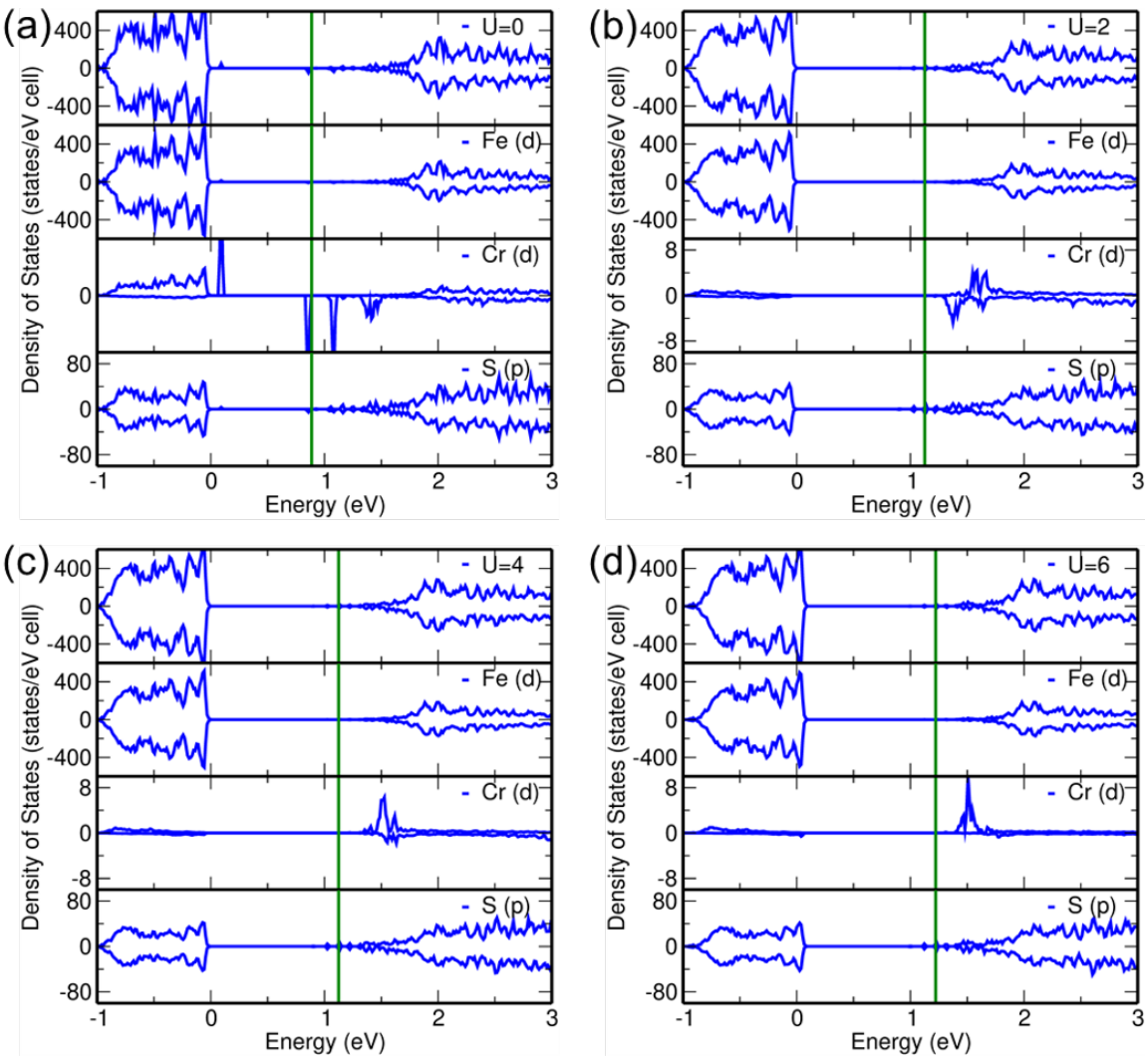

Figure C.4: Comparison of PDOS of Cr doped Pyrite as a function of Hubbard U value.

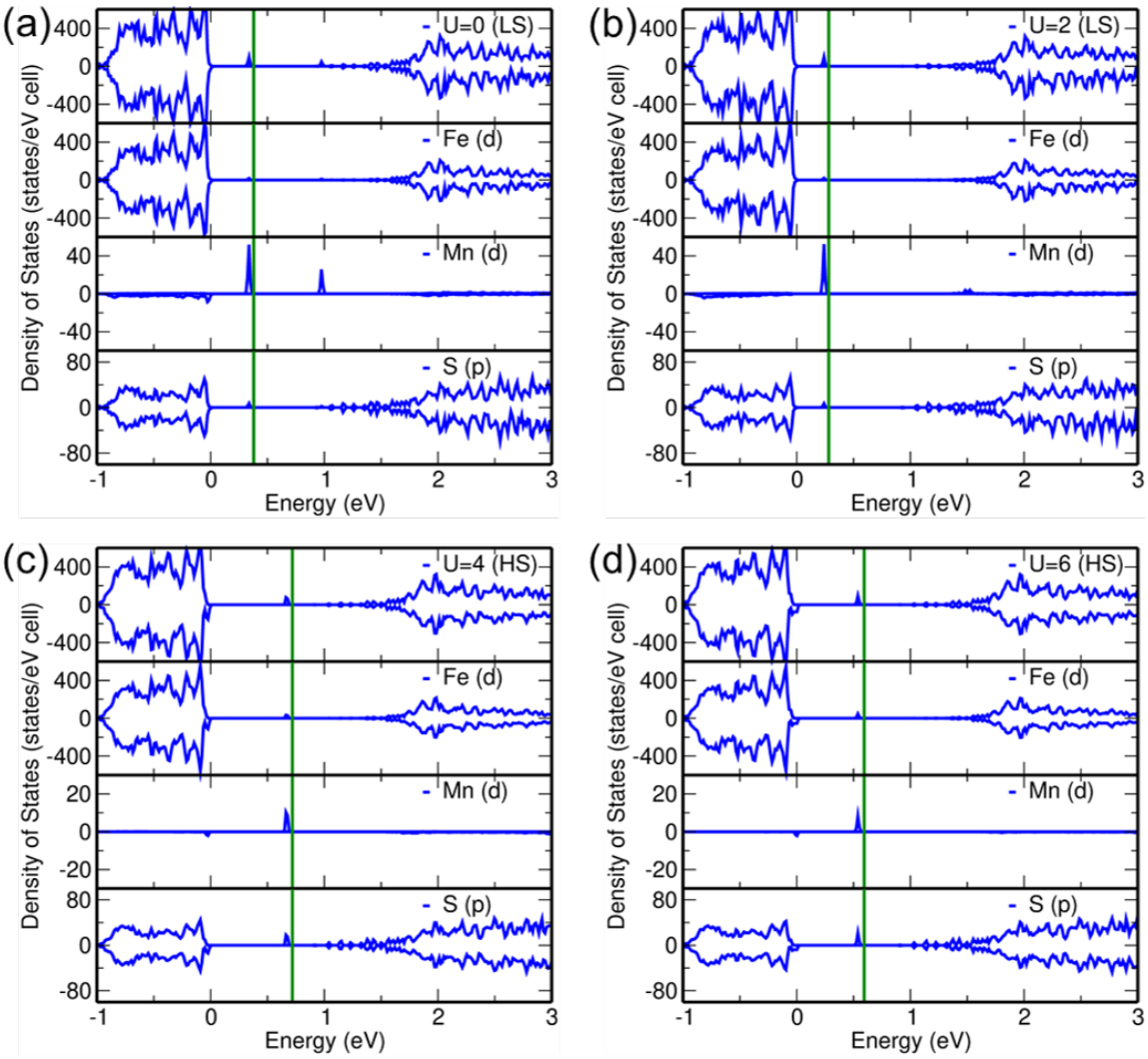

Figure C.5: Comparison of PDOS of Mn doped Pyrite as a function of Hubbard U value.

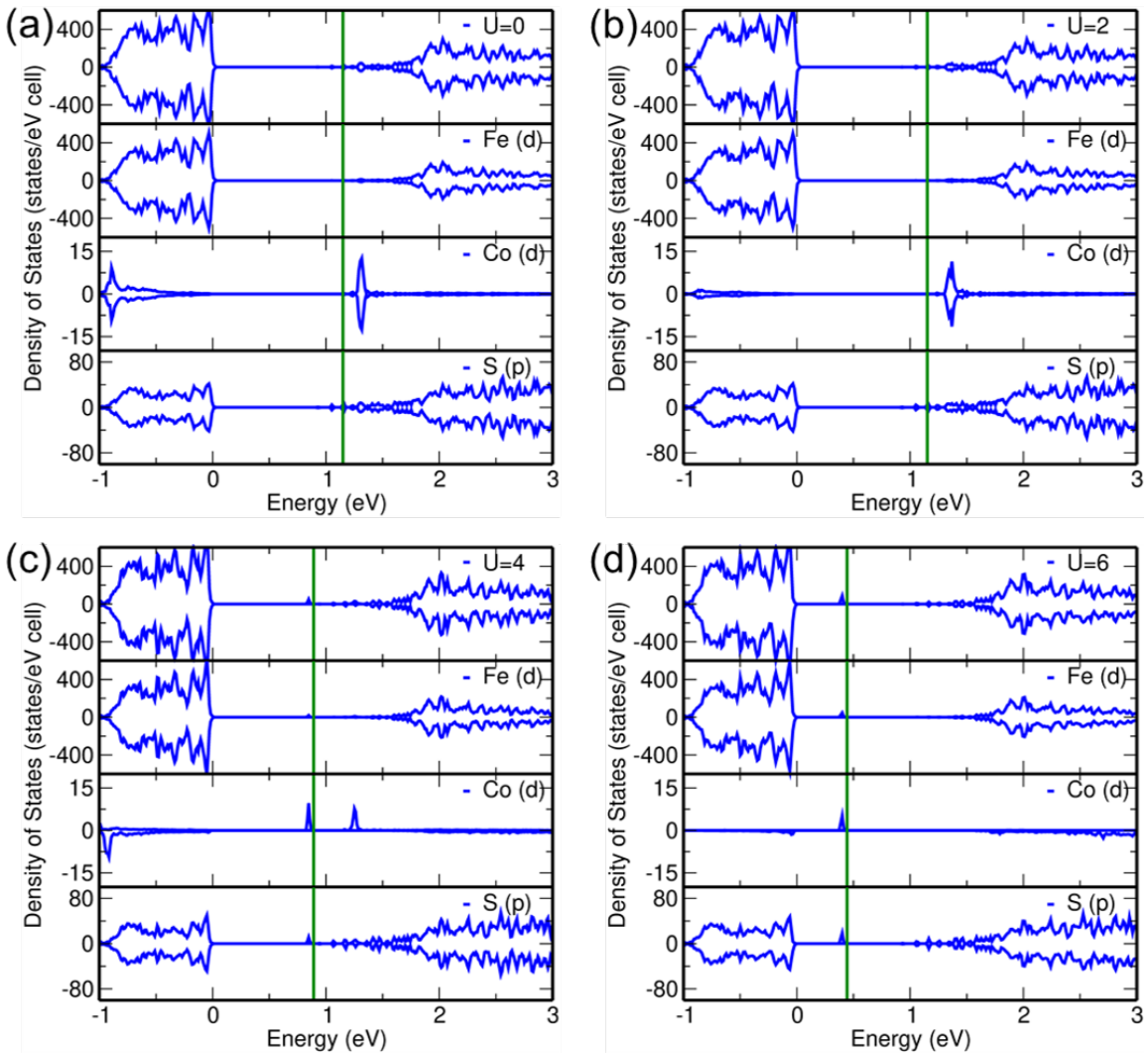

Figure C.6: Comparison of PDOS of Co doped Pyrite as a function of Hubbard U value.

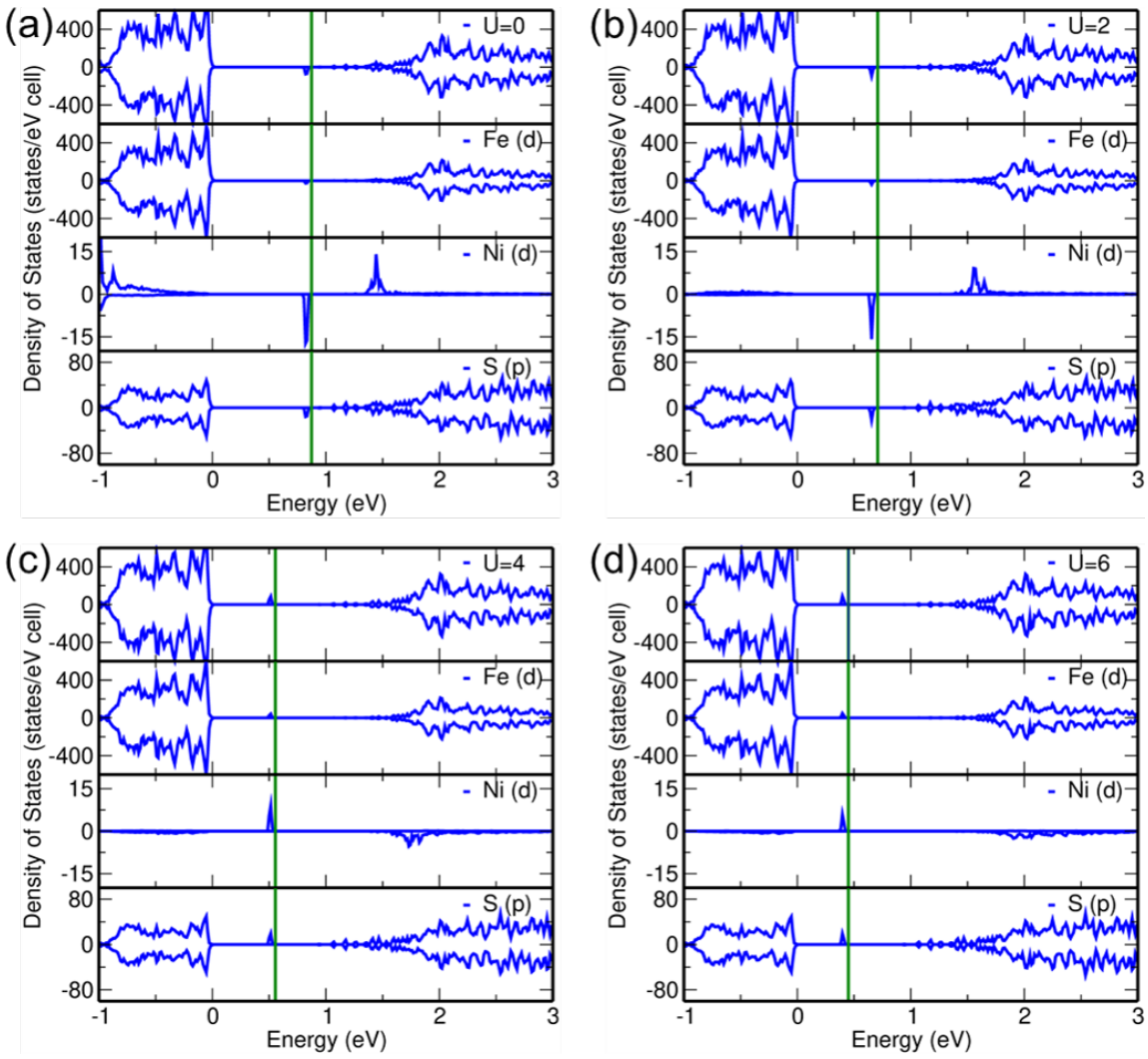

Figure C.7: Comparison of PDOS of Ni doped Pyrite as a function of Hubbard U value.

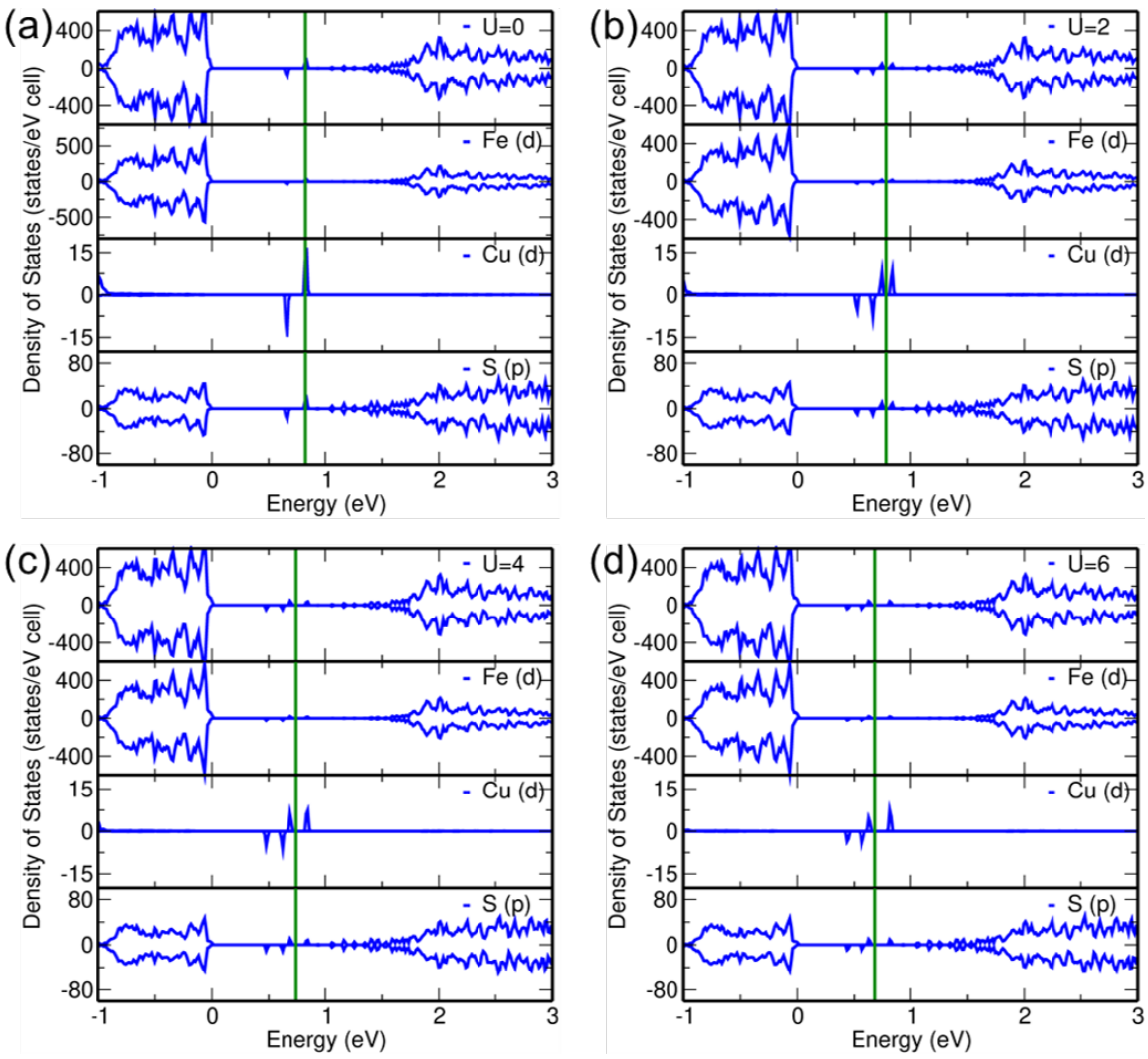

Figure C.8: Comparison of PDOS of Cu doped Pyrite as a function of Hubbard U value.

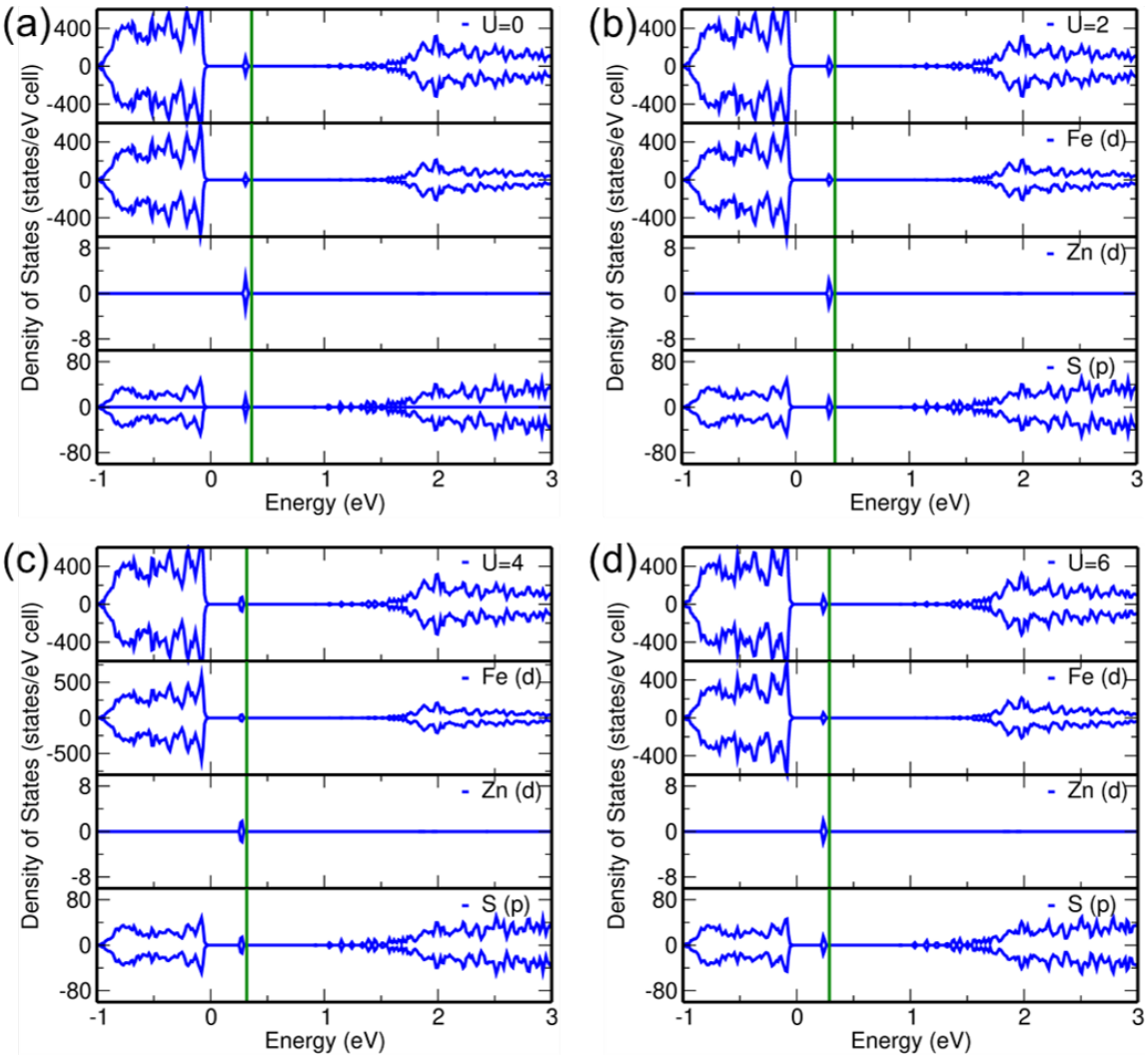

Figure C.9: Comparison of PDOS of Zn doped Pyrite as a function of Hubbard U value.

Appendix D

Supporting Information of Chapter 5

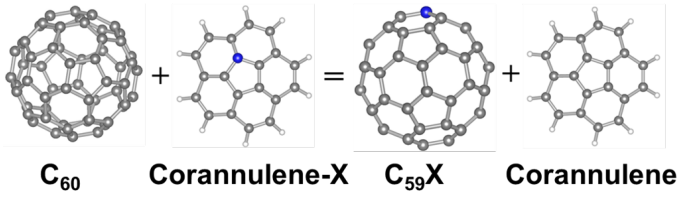

Figure D.1: Schematic representation of formation of $C_{59}X$ from Corannulene-X and C_{60}

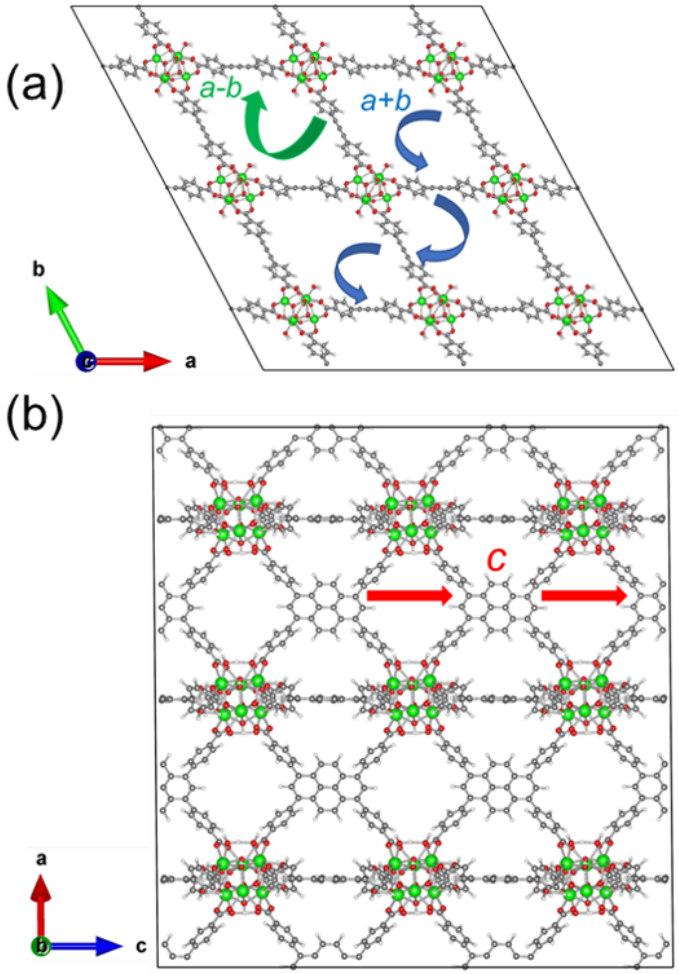

Figure D.2: Schematic representation of various charge-transfer directions in the pristine NU-901 MOF. The blue and green arrows represent the charge transfer in ab plane along a+b and a-b direction. The red arrow represents the charge transfer along the c-direction.

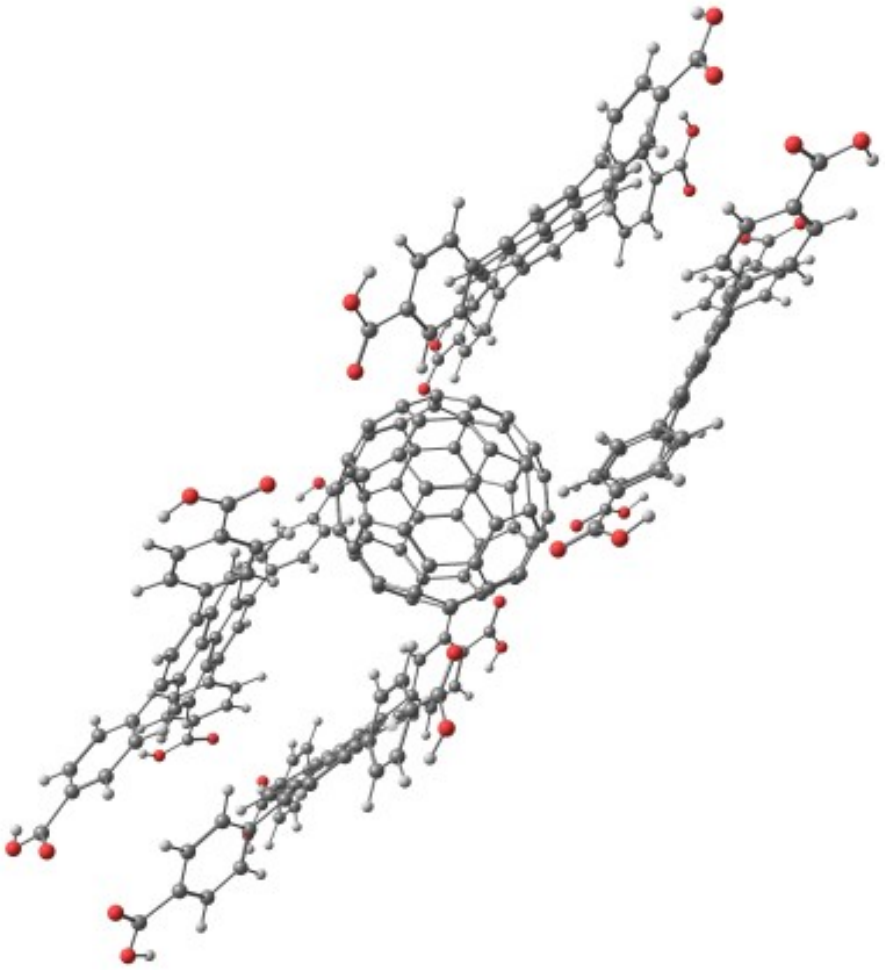

Figure D.3: Schematic representation of charge transfer between linkers and fullerene in the C60@NU-901 (ST) structure.

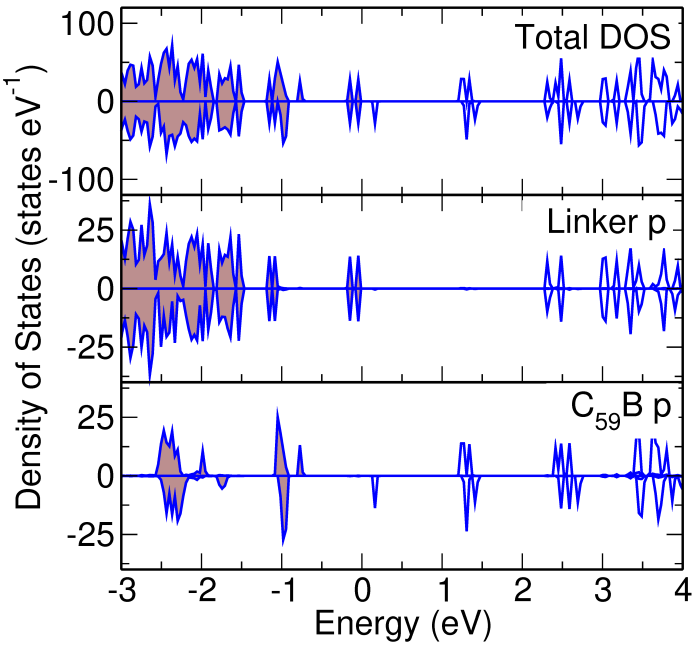

Figure D.4: Total DOS and projected DOS of $C_{59}B$@NU-901 conformation 1

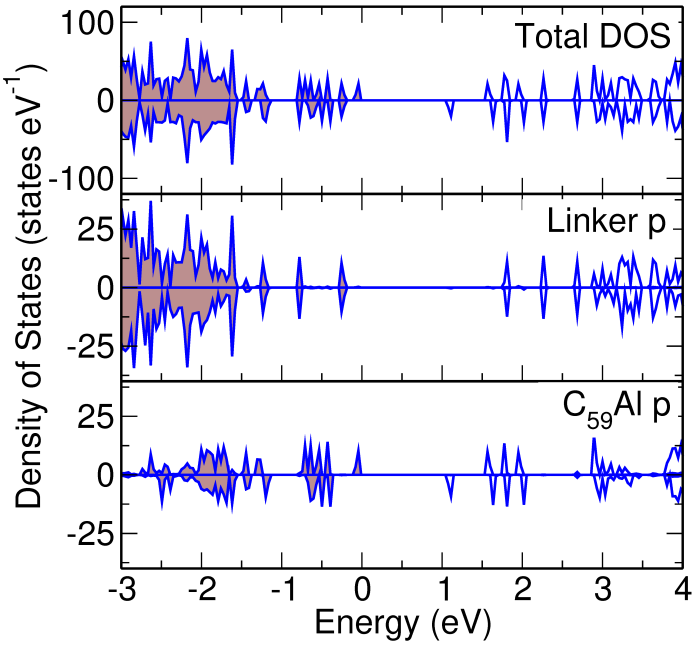

Figure D.5: Total DOS and projected DOS of $C_{59}Al$@NU-901 conformation 1

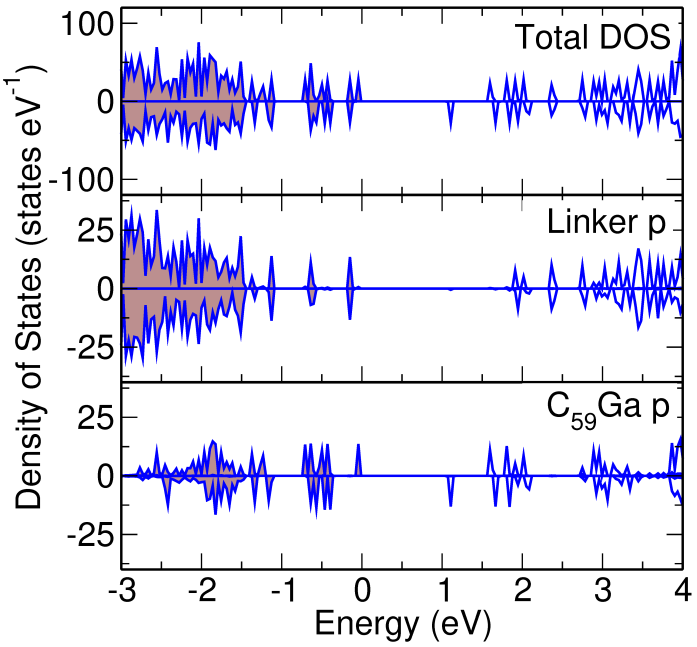

Figure D.6: Total DOS and projected DOS of C_{59}Ga@NU-901 conformation 1

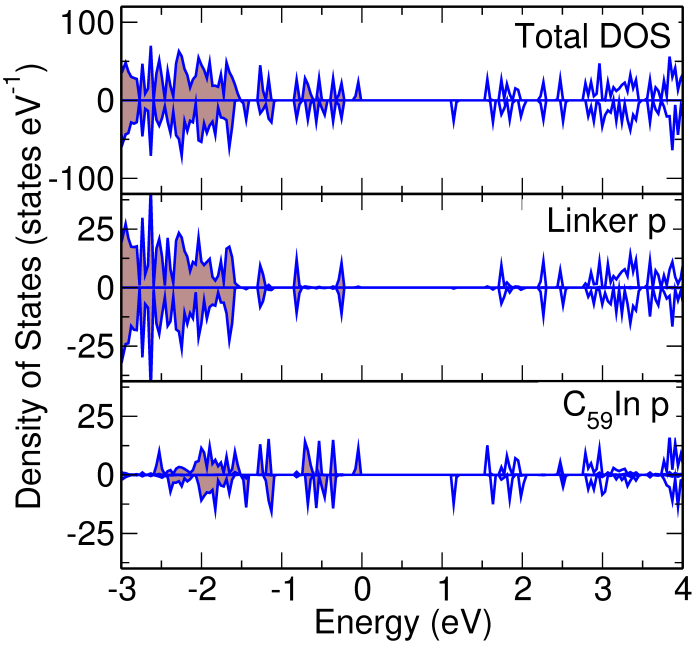

Figure D.7: Total DOS and projected DOS of C_{59}In@NU-901 conformation 1

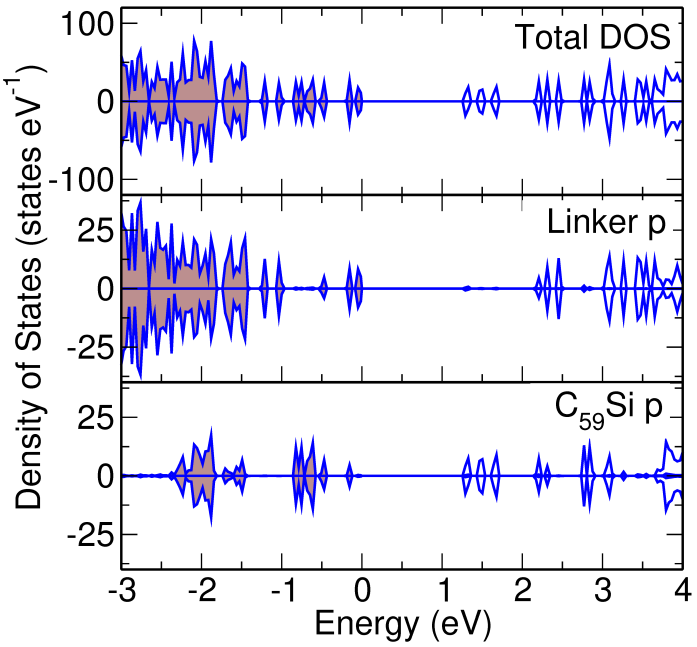

Figure D.8: Total DOS and projected DOS of C_{59}Si@NU-901 conformation 1

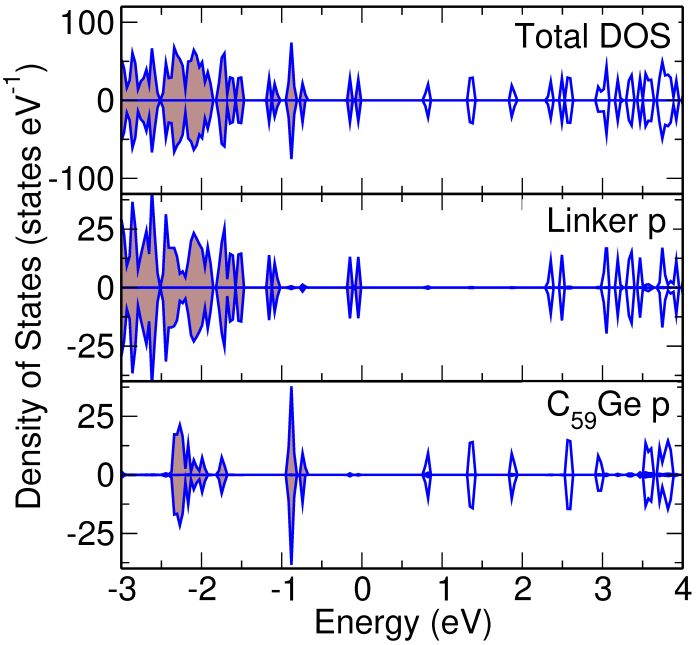

Figure D.9: Total DOS and projected DOS of C_{59}Ge@NU-901 conformation 1

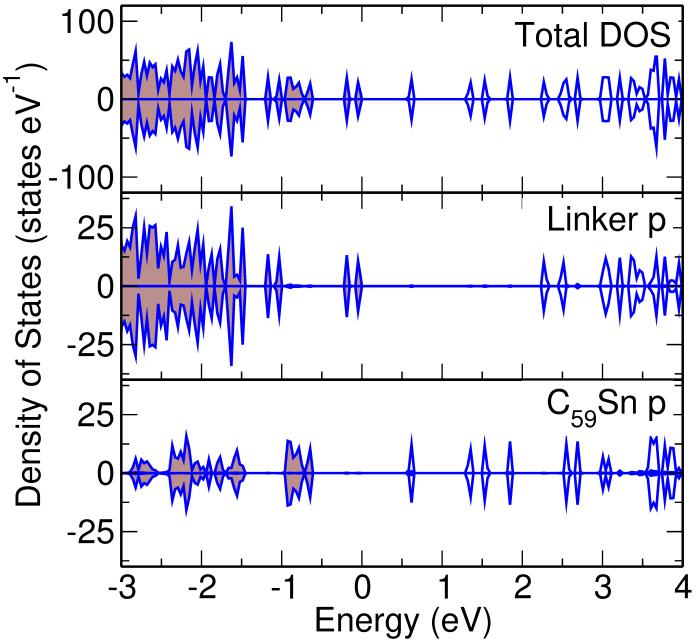

Figure D.10: Total DOS and projected DOS of $C_{59}Sn$@NU-901 conformation 1

Table D.1: Comparison of PBE-D3-BJ lattice parameter with experimental and previous theoretical lattice parameter of NU-901.

NU-901	a(Å)	b(Å)	c(Å)	α	β	γ
This Work	19.83	19.83	16.71	90.4	90.3	117.9
Previous Theoretical Work[220]	19.84	19.84	16.70	90.4	90.3	117.8
Experimental Work [183]	19.146	19.146	16.053	90.0	90.0	120.0

Table D.2: Hole-transfer integrals (eV) from linker to linker (in pristine NU-901) and from linker to fullerene (in C_{60}@NU-901 (ST)) computed using the M06-2X functional.

NU-901	Hole Transfer Integral (eV)	C_{60}@NU-901 (ST	Hole Transfer Integral (eV)
$a+b$	0.00261	L1-C_{60}	0.00379
$a-b$	0.00002	L2-C_{60}	0.00330
c	0.00232	L3-C_{60}	0.01306
-		L4-C_{60}	0.00853

Table D.3: Comparison of relative stability (kcal/mol) of conformation 1 and conformation 2 of C_{59}X@NU-901, and C_{59}X@NU-901 (NST) using the PBE-D3-BJ functional.

C_{59}X	C_{59}B	C_{59}Al	C_{59}Ga	C_{59}In	C_{59}Si	C_{59}Ge	C_{59}Sn
Conformation 1	0.6	29.9	4.2	21.2	0.0	0.5	0.0
Conformation 2	0.0	0.0	0.0	0.0	9.3	0.0	4.6
C_{59}X@NU-901 (NST)	20.7	76.7	47.3	68.0	31.9	20.9	27.0

Table D.4: Computed formation energy (kcal/mol) of C_{59}X using the PBE-D3-BJ functional.

C_{59}X	C_{60}	C_{59}B	C_{59}Al	C_{59}Ga	C_{59}In	C_{59}Si	C_{59}Ge	C_{59}Sn
$\Delta E_{formation}$	0	-19.6	-38.3	-37.9	30.1	-27.2	-29.0	-33.7

Appendix E

Supporting Information of Chapter 6

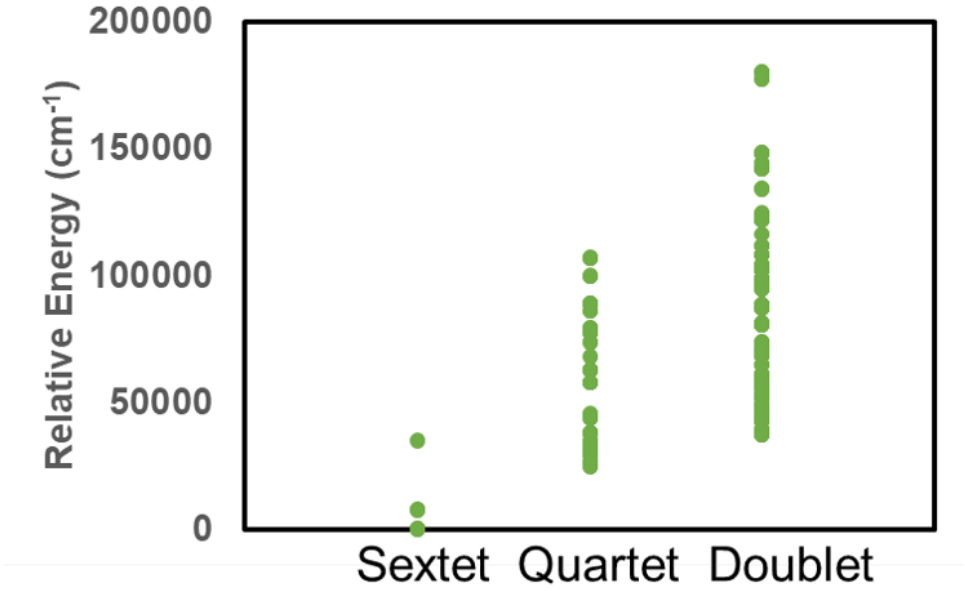

Figure E.1: Relative energies (cm^{-1}) of various roots of Dy-Ph (expt.) complex computed using SA-CASSCF method. Basis set choice of BS2 was used for these calculations. The first sextet root is taken as the ground state.

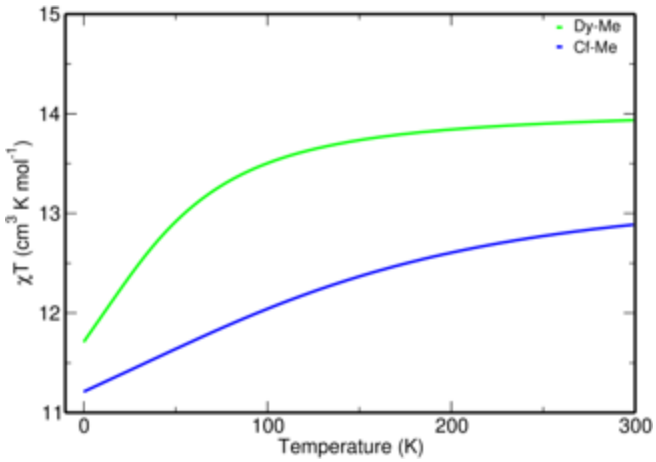

Figure E.2: Comparison of computed χT vs T curve using DFT optimized geometry of Dy-Me and Cf-Me at SA-CASSCF-SO level of theory and BS1 basis set combinations.

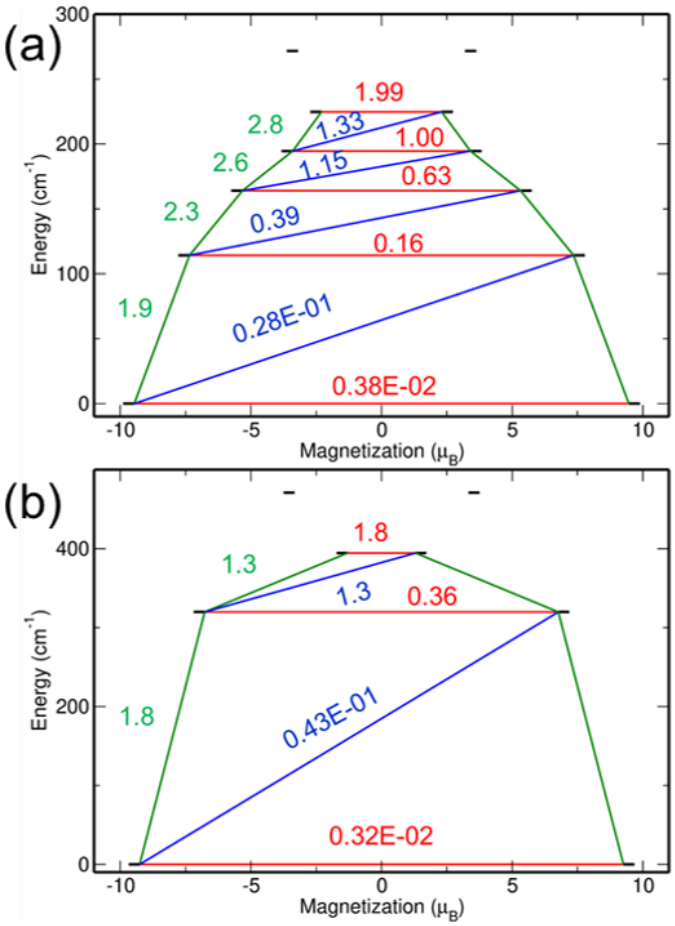

Figure E.3: Comparison of blocking barrier of (a) Dy-Me and (b) Cf-Me computed using SA-CASSCF-SO level of theory and BS1 basis set combinations and singleaniso package. The red line indicates QTM between $\pm m_J$ states. The green line indicates the transitions between $\pm m_J$ to $\pm m_{J+1}$ states which will assist TA-QTM mechanism in the excited states. The blue line represents possible Orbach processes.

Table E.1: Relative energies (cm^{-1}) of first 9 Kraemer's doublet of Dy-Ph (expt.) and Dy-Ph (DFT) using SA-CASSCF-SO using BS1 set of basis sets.

	Dy-Ph (expt)	Dy-Ph (DFT)
KD1	0.0	0.0
KD2	156.7	113.9
KD3	214.4	151.2
KD4	243.0	192.5
KD5	289.1	228.0
KD6	339.7	284.9
KD7	392.2	366.4
KD8	469.5	476.0
KD9	3641.9	3595.2

Table E.2: Comparison of g-tensor values for Dy-Ph (expt.) and Dy-Ph (DFT) at the SA-CASSCF-SO level of theory using BS1 set of basis sets.

	Dy-Ph (expt.)			Dy-Ph (DFT)		
	g_x	g_y	g_z	g_x	g_y	g_z
KD1	0.01	0.01	19.42	0.00	0.00	19.57
KD2	0.28	0.40	15.58	0.63	0.83	16.85
KD3	3.09	4.30	13.39	1.03	1.81	13.38
KD4	9.32	5.23	0.36	3.43	4.84	8.10
KD5	2.16	3.26	13.61	2.55	4.45	10.02
KD6	0.59	0.89	17.71	0.01	0.19	17.49
KD7	0.13	0.43	18.40	0.08	0.15	18.41
KD8	0.03	0.07	19.38	0.01	0.02	19.48

Table E.3: Relative energies (cm^{-1}) of first 9 Kraemer's doublet of Dy-Ph (DFT) and Dy-Me using SA-CASSCF-SO level of theory using BS1 and BS2 set of basis sets.

	BS1		BS2	
	Dy-Ph (DFT)	Dy-Me	Dy-Ph (DFT)	Dy-Me
KD1	0.0	0.0	0.0	0.0
KD2	113.9	114.3	117.3	118.3
KD3	151.2	164.0	155.7	169.6
KD4	192.5	194.5	197.6	199.9
KD5	228.0	224.7	235.6	232.0
KD6	284.9	271.7	288.8	278.3
KD7	366.4	343.3	380.1	356.7
KD8	476.0	475.8	496.1	490.8
KD9	3595.2	3603.7	3590.1	3599.4

Table E.4: Comparison of g-tensor values for Dy-Ph (DFT) and Dy-Me at the SA-CASSCF-SO level of theory using BS1 set of basis sets.

	Dy-Ph (DFT)			Dy-Me		
	g_x	g_y	g_z	g_x	g_y	g_z
KD1	0	0	19.57	0.01	0.01	19.35
KD2	0.63	0.83	16.85	0.42	0.52	15.93
KD3	1.03	1.81	13.38	1.43	1.85	14.24
KD4	3.43	4.84	8.1	1.39	3.91	8.88
KD5	2.55	4.45	10.02	3.14	5.81	9.75
KD6	0.01	0.19	17.49	0.21	0.4	18.39
KD7	0.08	0.15	18.41	0.03	0.06	19.03
KD8	0.01	0.02	19.48	0	0.01	19.69

Table E.5: Comparison of g-tensor values for Dy-Ph (DFT) and Dy-Me at the SA-CASSCF-SO level of theory using BS2 set of basis sets.

	Dy-Ph (DFT)			Dy-Me		
	g_x	g_y	g_z	g_x	g_y	g_z
KD1	0	0	19.58	0.01	0.01	19.37
KD2	0.62	0.8	16.84	0.43	0.53	15.93
KD3	0.97	1.78	13.52	1.35	1.8	14.25
KD4	3.47	4.94	8.11	1.79	4.22	8.78
KD5	2.69	4.21	9.88	3.07	5.25	9.99
KD6	0.12	0.32	17.39	0.24	0.45	18.34
KD7	0.07	0.13	18.43	0.02	0.05	19.02
KD8	0.01	0.02	19.48	0	0	19.68

Table E.6: Relative energies (cm^{-1}) of first 9 Kraemer's doublet of Dy-Me and Cf-Me using SA-CASSCF-SO level of theory using BS1 set of basis sets.

	Dy-Me	Cf-Me
KD1	0.0	0.0
KD2	114.3	319.8
KD3	164.0	394.5
KD4	194.5	470.8
KD5	224.7	531.6
KD6	271.7	655.6
KD7	343.3	790.6
KD8	475.8	1092.4
KD9	3603.7	8294.5

Table E.7: Comparison of g-tensor values for Dy-Me and Cf-Me at the SA-CASSCF-SO level of theory using BS1 set of basis sets.

	Dy-Me			Cf-Me		
	g_x	g_y	g_z	g_x	g_y	g_z
KD1	0.01	0.01	19.35	0.00	0.01	18.93
KD2	0.42	0.52	15.93	0.82	1.26	14.71
KD3	1.43	1.85	14.24	1.49	2.46	14.87
KD4	1.39	3.91	8.88	8.58	4.80	0.54
KD5	3.14	5.81	9.75	3.23	4.51	9.93
KD6	0.21	0.40	18.39	0.22	0.35	17.81
KD7	0.03	0.06	19.03	0.03	0.04	18.27
KD8	0.00	0.01	19.69	0.01	0.01	19.06

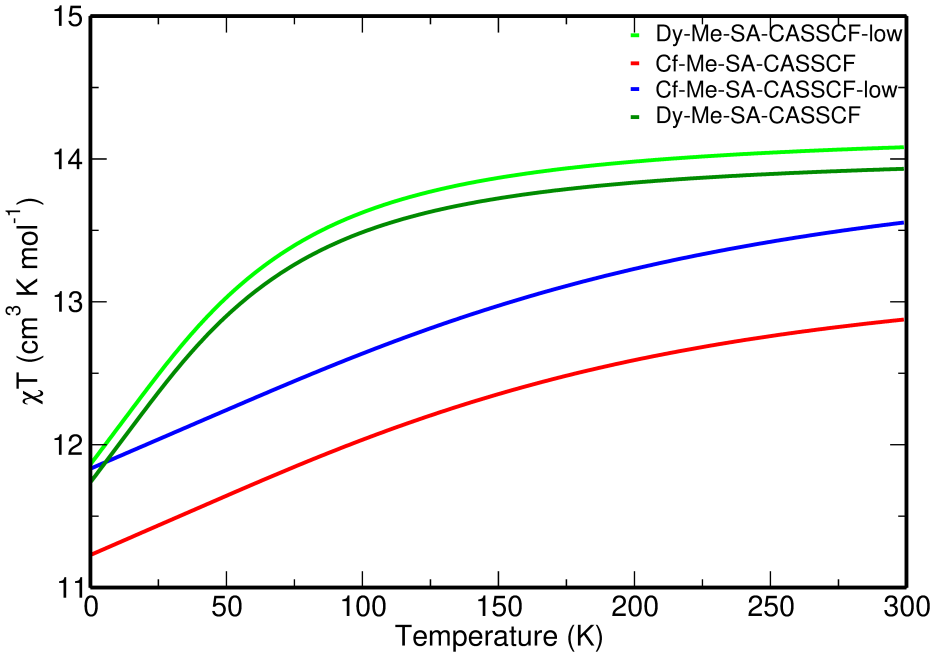

Figure E.4: Comparison of the computed χT vs T curves of Dy-Me and Cf-Me complexes using SA-CASSCF-SO and SA-CASSCF-SO-low level of theory and the BS2 basis set.

Table E.8: Relative energy (cm^{-1}) of first 9 KDs of Dy-Me and Cf-Me using SA-CASSCF-SO and SA-CASSCF-SO-low level of theory.

	Dy-Me		Cf-Me	
	SA-CASSCF-SO-low	SA-CASSCF-SO	SA-CASSCF-SO-low	SA-CASSCF-SO
KD1	0.0	0.0	0.0	0.0
KD2	120.1	118.3	363.1	329.0
KD3	171.3	169.6	406.3	398.9
KD4	201.9	199.9	516.6	481.0
KD5	233.7	232.0	581.5	544.8
KD6	283.1	278.3	741.3	664.2
KD7	363.0	356.7	911.2	813.7
KD8	499.2	490.8	1238.6	1107.7
KD9	3045.4	3599.4	5864.6	8280.9

Table E.9: Comparison of relative energy (cm^{-1}) of 21 sextet roots of Dy-Me and Cf-Me complex using SA-CASSCF and XMS-CASPT2 level of theory.

	Dy-Me		Cf-Me	
Root No.	SA-CASSCF	XMS-CASPT2	SA-CASSCF	XMS-CASPT2
1	0.0	0.0	0.0	0.0
2	5.7	7.6	32.5	73.7
3	153.1	210.6	373.8	476.9
4	177.8	231.1	454.3	543.0
5	208.2	301.7	667.2	808.4
6	309.5	413.1	840.9	1019.8
7	329.0	435.4	885.9	1013.5
8	383.1	488.9	964.0	1140.7
9	396.5	514.7	1015.2	1214.0
10	553.4	689.6	1413.0	1613.8
11	556.7	695.9	1437.8	1655.6
12	7606.0	6073.9	5659.6	4030.2
13	7634.8	6106.3	5820.1	4236.7
14	7759.5	6273.9	6106.3	4544.7
15	7776.3	6302.8	6213.2	4633.9
16	7792.8	6321.5	6304.1	4813.1
17	7839.3	6379.8	6366.7	4900.0
18	7864.6	6394.0	6510.3	4975.8
19	34904.1	27926.4	25177.8	18625.7
20	35142.2	28236.7	25709.2	19307.3
21	35315.9	28432.9	25981.2	19645.9